Emergent Quantum Order in the Strongly Coupled Moiré-Hofstadter Regime

by

Stefan Divic

A dissertation submitted in partial satisfaction of the

requirements for the degree of

Doctor of Philosophy

in

Physics

in the

Graduate Division

of the

University of California, Berkeley

Committee in charge:

Professor Michael P. Zaletel, Chair
Professor Ehud Altman
Professor Lin Lin

Summer 2025

Emergent Quantum Order in the Strongly Coupled Moiré-Hofstadter Regime

Abstract

Emergent Quantum Order in the Strongly Coupled Moiré-Hofstadter Regime

by

Stefan Divic

Doctor of Philosophy in Physics

University of California, Berkeley

Professor Michael P. Zaletel, Chair

A collection of many coordinated degrees of freedom can exhibit macroscopic behaviour bearing little resemblance to that of its constituent parts, a phenomenon known as emergence. In quantum materials, intricate correlations between electrons and ions produce a zoo of emergent behaviours that physicists seek to characterize and control. The past decade has seen rapid development in the synthesis and manipulation of moiré heterostructures, a new family of highly-tunable materials consisting of layered 2D sheets of atoms. Under the application of a perpendicular magnetic field, these devices provide unprecedented access to the Hofstadter flux regime, in which the movement of electrons is sensitive to both cyclotron motion and the effective moiré lattice, leading to quantized response and topological obstructions to wavefunction localization. In some moiré systems with no applied field, pairs of low-energy electronic degrees of freedom behave as though subjected to opposite internal magnetic fields, permitting an effective Hofstadter description of these systems as well.

This dissertation investigates the correlated behaviour of moiré-Hofstadter electrons under the influence of strong repulsive interactions. In Chapter 2, we study a lattice model inspired by magic-angle twisted bilayer graphene where the tension between these localizing forces and the intrinsic delocalization of low-energy electronic states stabilizes a correlated topological insulator, with evidence that hole doping leads to unconventional superconductivity. In Chapter 3, we reveal and characterize a quantum phase transition between integer quantum Hall and chiral spin liquid phases in a Hofstadter-Hubbard model of moiré transition metal dichalcogenides, exposing a hidden particle-hole symmetry and the structure of critical current fluctuations. Finally, Chapter 4 argues that the energetic properties of fractionalized excitations in the spin liquid phase near this quantum critical point are ideal for the microscopic realization of Laughlin's anyon superconductivity proposal.

for Miloš

Contents

Acknowledgments

I extend my sincere gratitude to everyone who has supported me through this circuitous doctoral journey and all that preceded it. I have benefited greatly from being surrounded by brilliant people who are so willing to share their knowledge and ideas. I first want to acknowledge the vibrant and ever-changing community of 5th floor Birge, namely Sam Garratt, Jaewon Kim, Lizzy Dresselhaus, Ethan Lake, Méabh Allen, Koh Yamakawa, Chunxiao Liu, Marcus Bintz, Zhihuan Dong, Yimu Bao and Yu-Ping Lin. My appreciation goes out to all generations of the Zaletel group — Tomohiro Soejima, Dan Parker, Ruihua Fan, Zhehao Dai, Yantao Wu, Bart Andrews, Nick Bultinck, Karthik Siva, Amir Mohammadi, Shahin Jahanbani, Gabriel Woolls, Jiechao Feng, Adarsh Iyer and Vibhu Ravindran — for providing endless entertainment and for helping clarify many misshapen ideas. To Ehud Altman, Dung-Hai Lee, Joel Moore, for your deep and inspiring knowledge and contributions.

To Andre Simoneau, for excavating my talent and curiosity when I had lost sight of them. To Camila and Lisa, for all your coaching and positivity. To Mr. Webb, for being my unlikely weekly companion, in problem-solving sessions where I eventually learned the meaning of rigour. To Arun Paramekanti, Amar Vutha, Erich Poppitz and A.W. Peet at UofT, for nurturing my confidence and ambition, and for propelling me onward to Berkeley.

To my many collaborators including Xue-Yang Song, Clemens Kuhlenkamp, Sopheak Sorn, Johannes Hauschild, Monika Aidelsburger, Henry Ling and Tami Pereg-Barnea for all your insights and efforts. Special thanks to Rahul Sahay, for every hour on Zoom, in the situation room, and every lap around campus. You've taught me a tremendous amount.

To my friends and colleagues from the Flatiron Institute, Harvard, and the Boulder School, particularly Andrew Hardy, Schulyer Moss, Jenny Coulter, Anna Dawid, Leo dos Anjos Cunha, Nicolas Morales Duran, Kyle Eskridge, Olivier Gauthé, Olivier Gingras, Thomas Hahn, Agnes Valenti, Lukas Weber, Roeland Wiersema, Fabian Kugler, Ryan Levy, Matt Fishman, Nicolas Regnault, Miles Stoudenmire, Joey Tindall, Junkai Dong, Patrick Ledwith, Saran Prembabu, Sambuddha Chattopadhyay, Ophelia Sommer, Nishad Maskara, Josephine Yu, Cristian Voinea, Yaar Vituri, Nishchhal Verma, Konstantinos Vasiliou, Tixuan Tan, Felipe Reyes-Osorio, Marvin Qi, Akshat Pandey, Matthew O'Brien, Anqi Mu, Nandagopal Manoj, Emmanouil Kokkinis, Luke Kim, Wilhelm Kadow, Mohammad Hassan, Sandeep Joy, Rafael Calderon, Joshua Covey, Noga Bashan, Amogh Anakru, and many others.

To my new research group in Philadelphia, Katherine Ding, Wyndham White, Deven Carmichael, Steven Gassner, Ben Kass, Brandon Monsen, Wai-Taing Tai, Spenser Talkington, Gene Mele, Charlie Kane, and Martin Claassen, for welcoming me into your vibrant community with open arms.

To my other dear mentors and friends, Tomohiro Soejima, Dan Parker, Shubhayu Chatterjee, and Valentin Crépel. You have provided more support than I deserve and continue to inspire me with your boundless kindness and resourcefulness. I am so happy for all your ongoing success. To Andy Millis, Norm Yao, and Ashvin Vishwanath, for your guidance and insight. I am a much better physicist for having collaborated with you.

To my advisor Mike, for letting me bear witness to your intellectual process and for giving me endless permission to cultivate my own style and interests, guided closely by many of yours. I am deeply inspired by your creativity and intuition, your ability to blend theory and method development and experiment, but also your ability to hike vigorously in sandals. Thank you for your generous support and your trust – I hope we'll stay in touch.

To my friends up north, including Mahmoud, Adam, James, Gillian, Chloe, Rob, Ben, Alex, for your love and camaraderie, however many miles or kilometers lie between us. To my Boundless™ partners in crime, Luca, Hayden, Anubhav, Hannah, Alex, Denys, Mark, Catherine, Ben, Michael, Neve, Jerry, Lisa, Madi, Josh, Cheyanne, and Jenn.

To my dear musical companions Adri and Irian, for all those extended recording sessions, chaotic demos, and meandering car rides. To Philippe, Kevin, Mary, Alex and my jazz basement friends for keeping me sharp and honest. To Isaac Harris for his unbelievable financial and culinary generosity, and to the Meal Monday community he brought together: Sophia, Dylan, Elise, Rachel, Rachael, Dmitry, Shereen, Madeline^2, Ashwin, Burhan, and many others. To the group chat, Sajant Anand, Stephen Gant, Zack Weinstein, Malcolm Spilka, and Nguyen Ho Nam, for testing the limits of humour and common sense.

Finally, this degree would simply have been impossibly without the love and understanding of my family. Thank you, Kenzo and Mari, for teaching me how to be kind and good. Braedon and Diane, for being the mature, sensible role models that I very often need. Lilian and Hanqing, for always spoiling me but keeping your expectations high. Everyone in Japan – Aya, Mirai, Toshiko, Mitsuhiro – for expanding my horizons. My grandparents, for sacrificing so much and teaching me how to lead a good life. Mama, for managing to support us against all odds and for showing me what really matters. And to Cindy, for everything.

Chapter 1

Introduction

The advent of moiré materials, particularly magic-angle twisted bilayer graphene (MATBG) and moiré transition metal dichalcogenides (TMDs), has opened an unprecedented frontier in the study of correlated quantum matter [1–3]. These systems offer uniquely tunable platforms in which interacting electrons can be studied and manipulated under conditions not accessible in traditional solids [4]. In the past several years, there has been rapid expansion of both experimental capability and theoretical understanding in this burgeoning field [5–7], leading to the discovery of both unexpected and long-sought quantum phases of matter [8, 9].

A key advantage of moiré materials, and 2D van der Waals heterostructures more broadly, is their exceptional *in situ* tunability [10]. Through electrostatic gating, experimentalists can precisely control carrier density and displacement fields, thereby tuning not only the strength of electron-electron interactions, but also the topology and quantum geometry of electronic Bloch wavefunctions [11, 12]. In addition, the large effective lattice constants of these systems—arising from long-wavelength variations in local atomic registry—enable access to the Hofstadter flux regime at laboratory-accessible magnetic field strengths [13]. The defining characteristic of this regime is that the lattice constant is an appreciable fraction of the magnetic length, so the unit cell encloses a substantial fraction of the magnetic flux quantum [14]. In contrast to continuum Landau levels, where relative kinetic energy is completely quenched by cyclotron motion [15], the lattice structure of Hofstadter systems produces a richer, strongly field-dependent spectrum of energies and electronic states [16].

In certain heterostructures, the moiré-scale patterns of strain, corrugation, and inter-layer tunneling generate topological bands at low energies, even at zero magnetic field [17–19]. The topology of isolated bands is often captured by a nonzero Chern number, detectable through quantized linear response [20–22]. In MATBG, the low-energy bands may carry a different "fragile" multi-band topological invariant [23–27]. In both cases, the underlying topological obstruction forbids a description of the low-energy subspace in terms of localized atomic orbitals [28], complicating the direct application of traditional strong coupling methods [29]. Nonetheless, it can be fruitful to view these degrees of freedom (considering all valleys and flavors collectively) as arising in an auxiliary system subject to a time reversal-symmetric combination of magnetic fields [30–32], *e.g.*, a generalized Hofstadter lattice system.

This dissertation explores the rich landscape of quantum phenomena in the strong coupling regime of these moiré-Hofstadter systems, where repulsive interactions contend directly with both kinetic energy and orbital magnetic effects [13, 33]. We investigate two distinct frontiers: one in which internal magnetic fields arise as an emergent description of a moiré system (Chapter 2), and another where an applied field strongly breaks time reversal symmetry, drastically restructuring the phase diagram and Mott transition of the familiar Hubbard model (Chapters 3 and 4). Working at the interface of the quantum Hall and Mott regimes, we uncover quantum phenomena ranging from superconductivity coexisting with unconventional magnetism, to quantum criticality associated with the dissolution of spin liquid order in a regime with prominent charge fluctuations. In particular, through the modern lens of moiré materials and with the aid of powerful tensor network methods [34–36], this dissertation sheds new light on Laughlin's paradigmatic chiral spin liquid and anyon superconductivity proposals [37–40], and grounds them in explicit Hofstadter lattice realizations.

The remainder of this chapter presents concepts, motivations, and themes relevant to subsequent chapters in this dissertation, followed by a detailed overview.

1.1 Integer Quantum Hall Effect and its Flavorful Variants

The integer quantum Hall effect (IQHE) is a remarkable collective behavior of electrons arising when a continuum two-dimensional electron gas (or 2DEG) is placed in a strong perpendicular magnetic field. In its non-interacting idealization, electrons enter into quantized "Landau" energy levels as a consequence of quantum cyclotron motion, in which their relative kinetic energy is completely quantized [15]. The crucial observable associated with the quantum Hall effects is the Hall resistivity ρ_H, a response quantity relating current flow to a transverse electric field. From the idealized Landau level wavefunctions, it can be calculated that $\rho_H = \nu^{-1} h/e^2$ (where $\nu = n_e/n_\phi$ is the ratio of electron density to flux density) when an integer number of Landa levels ν is fully occupied [41].

It is an astonishing experimental fact, first discovered in 1980 by Klaus von Klitzing *et al.*, that ρ_H is not only perfectly quantized *at* integer values of ν, but remains quantized across a broad plateau of magnetic field strengths [42]. The presence of these plateaus immediately signals the presence of some amount of disorder, for otherwise Galilean invariance demands that ρ_H be linear in the magnetic field [43]. Nonetheless, the remarkably-quantized values of the Hall resistance within these plateaus hints at a deeper, topological organizing principle which identifies the idealized filled Landau level with a broader class of quantum states.

This view of the IQH phase is clarified by the following thought experiment due to Laughlin [44], adapted by Halperin in Ref. [45]. Consider a 2D annular sample delimited by an inner and outer edge, whose bulk is penetrated by a uniform magnetic field and bears a gap to all mobile electronic excitations. Now imagine that an additional magnetic flux is threaded adiabatically slowly through the region enclosed by the inner edge. If the final

enclosed flux is the elementary flux quantum, then the initial and final Hamiltonians within the annulus differ only by a gauge transformation, meaning their full energy eigenspectra are equivalent. An analysis of the idealized Landau level orbitals reveals that the net result of this adiabatic cycle is for exactly one electron to be funneled from the inner edge to the outer edge. This process is robust to both disorder and weak interactions that preserve the integrity of the mobility gap [44, 46]. It has therefore been said that "the quantum Hall effect is an emergent phenomenon characterized by the ability of the matter in question to pump an integral number of electrons across the sample in a flux-winding experiment" [41].

Since this pivotal discovery, many materials and model systems of very different nature have been found to exhibit the same phenomenon of quantized integral Hall response [20]. When translation invariance is broken by an underlying lattice, this phase is known as a "Chern insulator", observed for instance in graphene subjected to an hBN moiré potential [47–49]. The quantum anomalous Hall effect (QAHE) is the even more exotic realization of quantized Hall conductance at *zero* magnetic field [50, 51], first observed in a magnetic topological insulator [52, 53]. Moiré realizations are now numerous and include TBG with an aligned hBN subtrate [17, 18] and heterobilayer $MoTe_2/WSe_2$ tuned by an out-of-plane displacement field [19]. For the first time, a higher-Chern insulator has also been observed at zero field [54], associated with wavefunction topology and Hall response not realized in the Landau levels of any 2DEG. These experiments demonstrate the utility of moiré materials for realizing novel, often long-theorized phases of matter in a highly-configurable setting.

Spin and Layer Quantum Hall Magnets

We now discuss the minimal setting in which interactions play a crucial role in the quantum Hall effect. When the electronic system carries multiple internal "flavor" degrees of freedom (such as spin, valley, or layer pseudospin), the IQHE admits a natural extension known as generalized quantum Hall ferromagnetism (QHFM).

In gallium arsenide (GaAs) quantum wells, spin-orbit coupling substantially reduces the effective g factor compared to its free electron value, making the spin splitting much smaller than the cyclotron gap [43]. Nonetheless, at a total electron filling of $\nu = \nu_\uparrow + \nu_\downarrow = 1$, the lowest Landau level (LLL) can spontaneously polarize in spin due to exchange interactions. Indeed, the system lowers its energy by spin alignment like in a conventional ferromagnet, yet retains a net quantized Hall conductance arising from the underlying orbital structure of the LLL. As a result, the experimentally observed spin gap, of order $e^2/\epsilon\ell_B$, exceeds the bare Zeeman gap by orders of magnitude [43]. This spontaneous breaking of spin-rotational symmetry supports spin wave excitations and "skyrmion" textures, hedgehogs of spin whose topological charge density and electric charge density are tied together [55–57].

Closely related phenomena occur in bilayer quantum Hall systems, such as GaAs double wells [58]. Here, the layer pseudospin remains soft even if the true spin is polarized by Zeeman or exchange effects. These bilayer systems exhibit strong interlayer coherence, even when the microscopic interlayer tunneling is weak or vanishes entirely, which can be detected by counterflow experiments [59]. Finally, similar behavior is exhibited by graphene in a

magnetic field, where the valley index acts as yet another flavor degree of freedom [60, 61], leading to spontaneous breaking of an approximate SU(4) symmetry [62].

Twisted Bilayer Graphene as a Flavor Ferromagnet

Moiré systems extend these ideas in various striking ways. The QAHE discussed above exemplifies that moiré bands can inherit nontrivial topology from the underlying superlattice geometry rather than a magnetic field. In this section, we provide a brief review of theoretical proposals that generalized QHFM emerges in MATBG at zero field, owing to the structure of its nearly degenerate low-energy bands [30, 31, 63].

We begin by recalling that the single-particle spectrum of monolayer graphene at charge neutrality is concentrated in two regions in momentum space, called valleys and denoted by $\tau = K, K'$ [64]. At generic small twist angle, the moiré-modulated pattern of hopping (both in layer and between layers) causes a folding of the Brillouin zone and of the graphene bands, which hybridize and form mini-bands [1]. At the so-called "magic angle" of $\theta \sim 1^\circ$, numerical modeling consistent with experimental observations indicate that two intertwined bands (per spin and valley) split off from the rest at charge neutrality, exhibiting a large degree of isolation from the surrounding valence and conduction bands [65–67]. We will refer to this as the narrow band subspace.

Because these two bands necessarily exhibit energetic degeneracies [24, 68–73], there is ambiguity in how to label them, and it is *a priori* unclear what choice leads to the simplest description in the presence of interactions at some chosen filling. Refs. [30, 31, 63] advocated for the following choice: at each momentum, label the two states by the honeycomb sublattice of graphene $\sigma = A, B$ on which their weight is larger. The motivation for this choice is a putative proximity to the "chiral limit" of MATBG, defined by the approximation that the inter-layer hopping is solely between opposite graphene sublattices as a consequence of lattice relaxation [74–78]; this extends the chiral symmetry of each graphene monolayer [64]. In this limit, the states are maximally sublattice polarized [31, 79].

A surprising property of these sublattice-polarized states is that they carry nonzero Chern number [70, 73]. In particular, letting $\sigma^\alpha, \tau^\alpha, s^\alpha$ (with $\alpha = 0, x, y, z$) denote Pauli matrices for sublattice, valley, and spin, respectively, then the Chern number is $\mathcal{C} = \sigma^z\tau^z$ [30]. This motivates reorganizing the narrow band states by their Chern sector $\sigma^z\tau^z$, valley τ^z, and spin s^z. A complete set of mutually-commuting Pauli matrices can then be defined [31]:

$$\boldsymbol{\eta} = (\sigma^x\tau^x, \sigma^x\tau^y, \tau^z) \qquad \widetilde{\boldsymbol{\eta}} = (s^x, s^y, s^z) \qquad \boldsymbol{\gamma} = (\sigma^x, \sigma^y\tau^z, \sigma^z\tau^z), \tag{1.1}$$

prescribing how to independently rotate each of these degrees of freedom. They behave as a modified valley pseudospin, electronic spin, and a Chern pseudospin, respectively.

This basis is convenient for several reasons [31, 32]: (*i*) In the chiral limit, the corresponding narrow band projected Hamiltonian is Chern-diagonal and independent of spin and valley pseudospin. The projected interactions therefore have a $\mathrm{U}(4)_+ \times \mathrm{U}(4)_-$ symmetry corresponding to independent rotations of $\boldsymbol{\eta}$ and $\widetilde{\boldsymbol{\eta}}$ in each Chern sector. (*ii*) Since the

dispersion vanishes entirely in the magic-angle chiral limit [74], this enlarged symmetry is a property of the full projected Hamiltonian. (*iii*) Departing from the magic angle but retaining the chiral approximation, this basis makes manifest the residual continuous symmetry; since the dispersion is purely off-diagonal in the Chern basis, the symmetry simply reduces to U(4).

Within this framework, Refs. [30, 31, 63] analytically demonstrated the existence of generalized QHFM ground states at integer fillings of the narrow bands. However, unlike the *bona fide* quantum Hall examples presented above, the topology is generated solely from moiré interference, and any time-reversal symmetry breaking is entirely spontaneous. We further note experimental evidence for spin polarization in the vicinity of half-filling of the flat bands, occurring at temperature scales larger than those associated with correlated insulating and superconducting behavior [79–81]. This motivates further simplifying the problem by projecting to the spin polarized bands, in which the symmetry is reduced to $\mathrm{U}(2)_+ \times \mathrm{U}(2)_-$ in the chiral magic-angle limit, with a further reduction to U(2) from dispersion. In Chapter 2, we engineer a minimal lattice model inspired by these properties of MATBG in which a generalized QHFM topological insulator appears and serves as a parent state for superconductivity of purely-electronic strong coupling origin.

1.2 Fractionalization in the Quantum Hall, Mott, and Moiré Regimes

In a partly filled Landau level, interactions can give rise to an entirely new type of incompressible, "topologically ordered" fluid [82]. Shortly after the discovery of the integer quantum Hall effect, Störmer and Tsui in 1982 observed an additional Hall plateau in gallium arsenide samples at high field [83], this time at the fractional filling $\nu = n_e/n_\phi = 1/3$. As before, n_e denotes the electron density while n_ϕ denotes the flux density. This plateau is associated with a Hall conductance of $\sigma_{xy} = \frac{1}{3}e^2/h$, and a vanishing longitudinal conductance $\sigma_{xx} \to 0$ indicating a lack of dissipation. This was the first experimentally observed instance of the fractional quantum Hall effect (FQHE), a broad family of quantum behaviors occurring at different magnetic filling fractions in a 2DEG, arising intrinsically from interactions [84].

Within a year, Laughlin had conceived of a theoretical explanation [85], with continued implications for high-field physics, moiré materials, quantum computing, and beyond [86]. He proposed that this plateau was the fingerprint of a gapped quantum fluid with *fractionalized* quasi-particle excitations. The simplest way to see this is to modify the flux-threading experiment described in Sec. 1.1 above, now considering an incompressible fluid with $\sigma_{xy} = \nu e^2/h$ but ν fractional [85]. Let us imagine that the inner ring is taken to almost zero, and the outer to infinity, resulting in a punctured plane geometry. Adiabatically threading one flux quantum through the puncture yields an excitation (energy eigenstate) with additional charge $\Delta q = \sigma_{xy}\Delta\Phi = \nu e$. This charge is localized at the origin but has flowed in from infinity. This charge fractionalization is fundamentally associated with exotic anyonic exchange statistics

of these particles as argued first by Halperin [87]. It is also tied to fractionalized gapless edge excitations and ground state degeneracies dependent on the topology of the underlying spatial manifold [88].

Recent experiments in moiré materials have revealed various generalizations of continuum FQH states [9]. The first class, known as fractional Chern insulators [89], are seen at finite magnetic field in a lattice. These have been observed in bilayer graphene rotated relative to two encapsulating hBN crystals [13], as well as in MATBG [33]. The second class is even more surprising and occurs at zero magnetic field, where they are known as fractional quantum anomalous Hall (FQAH) states [50]. These were first observed in twisted $MoTe_2$ homobilayers [90–92], and subsequently in pentalayer graphene on twisted hBN [93]. Beyond these direct generalizations of the FQHE of electrons, can the tunability and engineerability of moiré materials facilitate the realization of other fractionalized quantum matter?

Kalmeyer-Laughlin Chiral Spin Liquid

We now pivot to a remarkable idea originating in the study of cuprates, namely the chiral spin liquid, a topologically-ordered phase of matter proposed by Kalmeyer and Laughlin [37, 38], with deep connections to the FQHE. They considered a triangular lattice of anti-ferromagnetically interacting spin-1/2 moments governed by the Heisenberg model

$$H = J \sum_{\langle ij \rangle} \boldsymbol{S}_i \cdot \boldsymbol{S}_j, \qquad J > 0. \tag{1.2}$$

Here, $\sum_{\langle ij \rangle}$ denotes the sum over nearest-neighbour bonds in the triangular lattice. Unlike the "frustration-free" ferromagnetic scenario $J < 0$ in which all summands may be simultaneously satisfied by spin polarizing along some direction [94, 95], the ground state of H is not solved exactly [94]. Kalmeyer and Laughlin made conceptual progress toward a plausible ground state by recasting H in terms of interacting bosons.

The mapping itself consists of treating the spin raising (lowering) operator as the creation (annihilation) operator of a "hardcore" boson $b^\dagger$, *i.e.*, one for which double occupancy is forbidden [94]: $(b_j^\dagger)^2 = b_j^2 = 0$. Associating $|\downarrow\rangle$ with the boson vacuum $|0\rangle$ and $|\uparrow\rangle$ with the single-boson occupancy state $|1\rangle$ at each site, and omitting $\hbar$, the operator mapping is

$$S_j^+ \leftrightarrow b_j^\dagger, \qquad S_j^- \leftrightarrow b_j, \qquad S_j^z \leftrightarrow b_j^\dagger b_j - \frac{1}{2}. \tag{1.3}$$

The Hamiltonian then decomposes as $H = T + V$ where the boson hopping term originates from the XY spin interaction:

$$T = \frac{J}{2} \sum_{\langle ij \rangle} b_i^\dagger b_j + \text{h.c.} \tag{1.4}$$

The $S^z S^z$ interaction instead gives rise to a nearest-neighbour repulsive density-density interaction and chemical potential. The hardcore bosons can be promoted to *bona fide* canonical

bosons by imposing the hardcore constraint energetically, namely via an additional term $H_{\text{hardcore}} = u\sum_j b_j^\dagger b_j^\dagger b_j b_j$, with u taken to be the largest energy scale in the problem.

Due to the positive sign of the hopping T, the bosons behave as though subject to a magnetic field whose flux through each triangle is $\Phi_0/2 = hc/2q$, where q denotes the U(1) charge of the boson. This is because the Peierl's substitution dictates that bosons hopping in a magnetic field $\boldsymbol{B} = \nabla \times \boldsymbol{A}$ should be governed by the kinetic Hamiltonian [16, 96]:

$$T = -\sum_{i,j} t_{ij} b_i^\dagger b_j, \qquad t_{ij} = |t| e^{\frac{2\pi i}{\Phi_0}\int_i^j \boldsymbol{A}\cdot d\boldsymbol{\ell}}. \tag{1.5}$$

The product of t_{ij} around each closed loop therefore yields the flux through that loop, modulo Φ_0. For the hardcore bosons of interest, $(-J)^3 < 0$, which confirms their experiencing $\Phi_0/2$ flux per plaquette. If the original spins are unpolarized in the ground state, then the mapping Eq. (1.3) implies that $\langle b_j^\dagger b_j\rangle = 1/2$. A corresponding density of bosons free to move in the continuum would be at magnetic filling $\nu = 1/2$ and, due to their strong hardcore interaction, would therefore enter a $m = 2$ Laughlin FQH phase [37].

The quantized Hall coefficient $\sigma_{xy} = \frac{1}{2}q^2/h$ of the boson fluid maps to a spin quantum Hall conductance (spin current in response to a transverse Zeeman gradient) of $\sigma_{xy}^s = \frac{1}{2}\hbar^2/h = 2\cdot(\hbar/2)^2/h$. Semion excitations carrying fractional charge $q/2$ instead carry $S_z = \hbar/2$, which is fractional since all local excitations carry integer spin. Finally, the putative spin ground state inherits a two-fold topological ground state degeneracy—in addition to that from spontaneously breaking time reversal symmetry—when realized on a torus or infinite cylinder [88, 97–99]. These are the defining properties of the Kalmeyer-Laughlin CSL [82].

Toward the (Electronic) Realization of the Chiral Spin Liquid

There is a good reason to venture beyond the original Kalmeyer-Laughlin proposal: the CSL fails to be the true ground state of the pure Heisenberg interaction Eq. (1.2). Instead, large-scale numerical calculations identify a long range-ordered 120° anti-ferromagnet as the ground state [100]. While the lattice and continuum bosons differ principally by the application of a deep periodic potential [37], which may plausibly have been introduced adiabatically without driving a transition between these phases, this scenario is not realized.

We are therefore left wondering whether there is a related lattice spin Hamiltonian, extending Eq. (1.2), which does realize the CSL as its ground state. This has been answered in the affirmative via the construction of exact parent Hamiltonians for the CSL [101–103]. A related, much simpler modification is to introduce a chiral three-spin interaction

$$H_\chi = J_\chi \sum_{(ijk)} \boldsymbol{S}_i \cdot \boldsymbol{S}_j \times \boldsymbol{S}_k \tag{1.6}$$

of sufficient strength [104–106], where the sum runs over all triangular plaquettes in the lattice with vertices traversed counter-clockwise as $i \to j \to k$.

Another path forward is to ask, perhaps more ambitiously, whether we can directly realize the chiral spin liquid in a lattice model of electrons [107–109], *i.e.*, without taking the Mott limit of frozen charge fluctuations. As explored in Chapters 3 and 4, this is conceptually interesting because it allows for the exploration of several inter-dependent properties: the *charged* (both conventional and fractionalized) excitations of the CSL rather than just its spin excitations [110], the structure of Mott transitions from the CSL into weak-coupling phases, and the consequences of doping charge carriers [111]. The latter is the basis for Laughlin's so-called *anyon superconductivity* proposal, whereby a "conventional" topological superconductor arises as the finite-density collective behavior of a system of charged anyons [39, 40, 112, 113]. Chapter 4 of this dissertation clarifies the energetic conditions satisfied by anyons that enable this intriguing possibility, and shows (via Chapter 3) how these requirements can be implemented, counter-intuitively in the presence of a strong orbital magnetic field in tandem with strong repulsive interactions.

To this end, we choose to view the hardcore bosonic degrees of freedom b as pairs of tightly-bound, spin-singlet molecules of fermions carrying half their charge, $e = q/2$:

$$b_j^\dagger = f_{j,\uparrow}^\dagger f_{j,\downarrow}^\dagger. \tag{1.7}$$

The tendency to form local pairs can be imposed energetically by introducing an attractive Hubbard interaction

$$H_{\text{Hub}} = -U \sum_i (n_{i\uparrow}^f - 1/2)(n_{i\downarrow}^f - 1/2), \tag{1.8}$$

with $U > 0$ sufficiently large. The flux per plaquette $\Phi_0/2$ seen by the bosons is time reversal symmetric since it is only well-defined modulo Φ_0. Thus, there are two possibilities for the flux seen by the underlying fermions; we choose $hc/4e$ (as opposed to $-hc/4e$), which explicitly breaks time reversal symmetry. The simplest fermion hopping Hamiltonian on the triangular lattice consistent with this choice is the Hofstadter model

$$h = -\sum_\sigma \sum_{i,j} h_{ij} f_{i,\sigma}^\dagger f_{j,\sigma}, \tag{1.9}$$

where h_{ij} vanishes except when i, j are nearest neighbours, and where the counter-clockwise product of h_{ij} around each triangle carries a phase $e^{i\pi/2}$.

To engineer a model for a CSL and not a bosonic FQH phase, we need $b^\dagger$ to resemble a charge-neutral spin raising operator. This can be achieved by a unitary change of basis $f_\downarrow^\dagger \to c_\downarrow$ that leaves the up-fermions unaffected, $f_\uparrow^\dagger \to c_\uparrow^\dagger$. Remarkably, the choice of flux means the form of Eq. (1.9) is identical in the c basis, up to a gauge transformation of the spin-down electrons; all plaquettes still carry $hc/4e$ flux [114, 115]. On the other hand, this particle-hole transformation flips the sign of the Hubbard interaction since $n_\downarrow^f \to 1 - n_\downarrow^c$.

At a density of one c fermion per site, and taking the Mott limit of large U, this bespoke Hofstadter model with repulsive Hubbard interactions not only perturbatively realizes the AF Heisenberg interaction Eq. (1.2) at order $\mathcal{O}(h^2/U)$, but also the chiral interaction Eq. (1.6) at

order $\mathcal{O}(h^3/U^2)$ [116, 117]. Moreover, there is direct evidence from DMRG calculations that the CSL phase is realized in the fermionic model itself [114, 118], while Refs. [118, 119] offer a compelling roadmap for its realization in moiré TMD heterostructures with an effective layer *pseudospin* degree of freedom and Zeeman-polarized spin/valley. All of this provides ample motivation for the detailed study of this Hofstadter-Hubbard model, which we undertake at both integer density (Chapter 3) and finite doping (Chapter 4), as summarized next.

1.3 Overview

The remainder of this dissertation is organized as follows:

- In Chapter 2, we investigate how basic microscopic ingredients (time reversal symmetry, band topology, and strong repulsive interactions) conspire to give rise to correlated phases of matter in moiré quantum materials. Motivated by experimental indications that combining aspects of the Fermi-Hubbard model with quantum Hall physics may foster correlated insulators and superconductivity in MATBG, we construct a minimal Hofstadter lattice model unifying these features. Using infinite-cylinder density matrix renormalization group simulations, we map out its ground state phase diagram and identify an interaction-induced topological insulator and, upon weak hole doping, present evidence for superconductivity emerging from this parent quantum spin Hall phase. To characterize this superconducting state, we develop a method to probe the gap function directly within the infinite matrix product state framework, revealing a weakly paired p-wave superconductor of holes, reminiscent of superconductivity reported in experiments on MATBG. We explicitly elucidate the structural similarities and differences between our model and those of MATBG in its chiral limit. This chapter is adapted from Ref. [120]:

  Rahul Sahay*, **Stefan Divic***, Daniel E. Parker, Tomohiro Soejima, Sajant Anand, Johannes Hauschild, Monika Aidelsburger, Ashvin Vishwanath, Shubhayu Chatterjee, Norman Y. Yao, and Michael P. Zaletel, *Superconductivity in a topological lattice model with strong repulsion* [Editor's Suggestion], Phys. Rev. B 110, 195126, (2024).

- In Chapter 3, we explore the collision of quantum Hall and Mott phenomena in the presence of a large applied field. Motivated by recent proposals for simulating the Hofstadter-Hubbard model in moiré TMD multi-layers, we focus on the regime of one-quarter flux quantum per plaquette at a density of one electron per site. Our numerical results confirm that a Kalmeyer-Laughlin chiral spin liquid emerges in the intermediate coupling regime, directly adjacent to a weak-coupling integer quantum Hall (IQH) phase. Notably, we provide the strongest evidence to date that the IQH-CSL transition is a continuous quantum phase transition featuring critical fluctuations of the electronic current. We uncover a hidden glide particle-hole symmetry operation which, we argue, is spontaneously broken at the IQH-CSL transition on odd-circumference cylinders,

shedding light on the true topological transition in 2D. More broadly, our results highlight the crucial role and structure of charge fluctuations at the phase boundary of the quantum Hall and Mott regimes. This chapter is adapted from Ref. [114]:

Stefan Divic, Tomohiro Soejima, Valentin Crépel, Michael P. Zaletel, and Andrew J. Millis, *Chiral spin liquid and quantum phase transition in the triangular lattice Hofstadter-Hubbard model*, arXiv:2406.15348.

- In Chapter 4, we argue that topological superconductivity emerges naturally upon doping in the vicinity of the IQH to CSL transition. Unlike other mechanisms driven by quantum criticality, our approach enables the numerically controlled demonstration of electron pairing, a precursor to superconductivity in this setting. We employ exact diagonalization and density matrix renormalization group methods to examine this theoretical scenario and find that electronic pairing indeed occurs on both sides of criticality over a remarkably broad range of interaction strengths. On the chiral spin liquid side, our results provide the first model realization of the long-hypothesized mechanism of anyon superconductivity. Our study thus establishes a beyond-BCS mechanism for electron pairing in a well-controlled limit, relying crucially on the interplay between electron correlations and band topology in a strongly coupled moiré-inspired lattice model. We also provide a microscopic origin for a conjectured emergent, continuous symmetry of the quantum critical point, for which we derive a low-energy parton field theory description. This chapter is adapted from Ref. [115]:

  Stefan Divic, Valentin Crépel, Tomohiro Soejima, Xue-Yang Song, Andrew J. Millis, Michael P. Zaletel, and Ashvin Vishwanath, *Anyon superconductivity from topological criticality in a Hofstadter-Hubbard model*, PNAS, vol. 122, no. 33, e2426680122, 2025.

Chapter 2

Superconductivity in a Topological Lattice Model with Strong Repulsion

Superconductors are remarkable phases of matter wherein charge-e fermions—which microscopically repel one another—instead bind into charge-$2e$ Cooper pairs that then condense. Traditionally, these phases are best understood in the context of weak interactions [121–123]. For example, in the paradigm put forth by Bardeen, Cooper, and Schrieffer (BCS), phonons mediate pairing between electrons near the Fermi surface of a weakly-correlated Fermi liquid [122]. Despite its widespread applicability, the limitations of the phonon-based theory are suggested by the experimental discovery of "unconventional" superconductors, which display a plethora of exotic phenomena ranging from high transition temperatures, to non-standard pairing symmetries, and parent states with anomalously low carrier densities [121, 124]. Such superconductors arise in surprisingly distinct settings, e.g., the cuprate compounds [125–129], iron pnictides [130–132], and possibly even in twisted bilayer graphene (TBG) [2, 133–137] and other graphene multilayers [138–144]. This diversity motivates a fundamental question that is especially relevant in the present era of highly-tunable solid-state and cold atom synthetic quantum materials. Namely, what microscopic ingredients aid the realization of unconventional superconducting ground states?

For the past several decades, investigations into unconventional superconductivity have brought to the forefront the ingredient of strong interactions. This is encapsulated in the celebrated Fermi-Hubbard model [94, 145–147], which consists of spinful fermions occupying tightly-localized orbitals coupled by strong repulsion. These minimal ingredients underlie several proposed mechanisms for unconventional superconductivity [126–129] and give rise to numerous other exotic phenomena (see e.g. [107, 148–152]). As a consequence, the Fermi-Hubbard paradigm has been the subject of decades of sustained interest in condensed matter physics, pushing the forefront of theory and motivating new experimental paradigms such as cold atom quantum simulation [153–160].

Despite their success, the simple ingredients in the Fermi-Hubbard model are insufficient to describe strongly-interacting phenomena reliant on band topology, such as the celebrated quantum hall effects [43, 84]. This setting of topological bands induced by strong magnetic

fields, with accompanying time-reversal breaking, is naively unfavorable for superconductivity in the presence of repulsive interactions. However, a number of works have suggested regimes where superconductivity may emerge in topological Hofstadter-type models, such as [161–165]. Recently, experiments on TBG and other graphene moiré multilayers—in which topology is widely believed to play a crucial role—present a related time-reversal-invariant context [68, 70] in which superconductivity can and does appear [2]. As such, various studies have sought to demonstrate the presence of an all-electronic route to superconductivity in models of TBG and, more broadly, in electronic Hamiltonians with the ingredients of time-reversal symmetry, strong repulsive interactions, and topological bands. However, owing to the complexity of the many-body problem, theoretical evidence for such a route has so far only derived from approximate or perturbative methods, e.g., mean-field theory [166, 167], large-N expansions [79], and effective continuum descriptions [79, 168, 169]. Elucidating the existence and character of superconductivity in a fully-microscopic model with these ingredients, therefore, remains an important and outstanding challenge.

In this chapter, we introduce a minimal model—the "double Hofstadter" model— that incorporates precisely these ingredients and employ unbiased matrix product state techniques to study its phase diagram on finite-circumference cylinders. Our study reveals that their interplay leads to a plethora of exotic phenomena and culminates in the numerical demonstration of an unconventional superconducting ground state at a finite circumference, with further evidence that this behavior may persist on larger cylinders.

2.1 Summary of Key Results

This chapter studies the *double Hofstadter model*, a simple lattice model with the following properties:

1. Short-range repulsive interactions (akin to the Hubbard model),
2. Narrow or "flat" topological bands (akin to quantum Hall and some moiré systems),
3. Time-reversal symmetry (facilitating superconducting phase coherence).

To bake all of these ingredients into a single Hamiltonian, we start with the familiar Harper-Hofstadter model of spinful fermions on a square lattice with a magnetic flux $\Phi = \Phi_0/q$ per plaquette [14, 16]. This is a lattice model whose lowest band carries a Chern number and limits to the lowest Landau level as $q \to \infty$, but is not time-reversal symmetric. We therefore consider a bilayer Hofstadter model (Fig. 2.1) with opposite magnetic fields in opposite layers, whereupon the model becomes time-reversal symmetric. Finally, we allow tunneling between the layers and add strong local repulsive interactions, as in the Hubbard model. We analyze the resulting *double Hofstadter model* and argue that it contains an unconventional p-wave superconductor of purely repulsive origin. After defining the model precisely in Section 2.2, our key results are five-fold and culminate in connections to contemporary experiments.

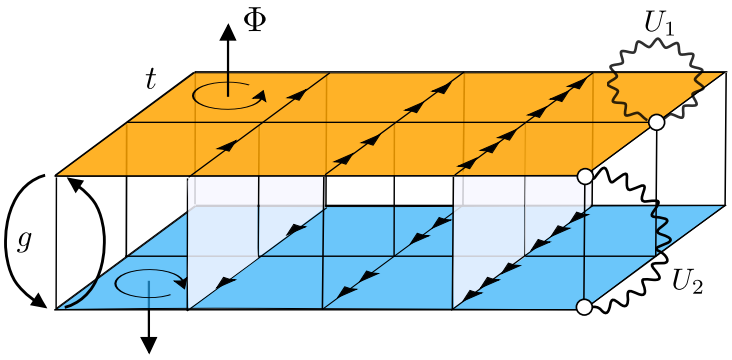

Figure 2.1: **The Double Hofstadter Model.** This chapter considers a simple lattice model with three essential ingredients: (1) narrow topological bands with (2) strong repulsive interactions and (3) time-reversal symmetry. These properties are realized in a bilayer lattice model of spinful fermions made by joining together two copies of the Harper-Hofstadter model with *opposite magnetic fields in opposite layers*. Bonds represent electron hoppings with in-layer magnitude t and inter-layer magnitude g. Peierls phases of $e^{in\pi/2}$, graphically depicted via n arrows along the direction of hopping, yield a magnetic flux of $\pm\Phi = \pm\pi/2$ per plaquette in the top and bottom layers, respectively. Finally, there are repulsive density-density interactions (wavy lines) with magnitude U_1 onsite and U_2 between the layers.

Flat Bands & Fragile Topology: First, in Section 2.2, we present the bandstructure of our model (See Fig. 2.2). Crucially, the lowest four bands are narrow and possess "fragile topology" [23–27]. Even though their total Chern number vanishes, fragile topology implies that no symmetric, exponentially-localized Wannier basis for these bands exists (without the addition of trivial filled bands to the model). This precludes any tight-binding description for the flat band subspace consisting of symmetric and exponentially-localized orbitals.

Correlated Insulator at Half-Filling: Next, in Section 2.3, we investigate the ground state phase diagram of the double Hofstadter model at half-filling of the flat band subspace. We first demonstrate analytically that the ground state at strong in-layer coupling is a generalized quantum Hall ferromagnet, which is a spontaneously-generated quantum spin Hall insulator. We refer to this state as a layer antiferromagnet ("LAF") as it is characterized by ferromagnetism within each layer but antiferromagnetism between layers [See Fig. 2.3(a)]. We confirm this analytical understanding numerically using infinite cylinder density matrix renormalization group (cylinder iDMRG) methods. Our simulation of the model is enabled by recent advances in the compression of matrix product operators [170].

Unconventional Superconductivity: Third, in Section 2.4, we provide numerical evidence that hole-doping the LAF produces an unconventional superconducting ground state. In this purely-repulsive setting, our evidence is based on state-of-the-art parallelized iDMRG numerics and is strongest at circumference $L_y = 5$. There, we conclusively demonstrate both

(algebraically) long-ranged superconducting correlations *and* a finite charge gap. Despite the exponential scaling of simulation complexity in L_y, we attempt a similar analysis on larger cylinders where we find preliminary—but ultimately inconclusive due to bond dimension limitations—evidence for a superconducting ground state. We conclude by verifying that the superconducting phase at $L_y = 5$ is robust, with stability to several perturbations including additional repulsive interactions, and always coexists with LAF order.

In Section 2.5, we devise a novel and widely applicable method to probe the superconducting gap function in charge-conserving cylinder iDMRG, which we use to systematically characterize the putative superconductor. We find that it is well-described by the weak pairing of quasi-holes above the strongly-correlated LAF insulator (i.e., it is "BCS" like) with a p-wave pairing symmetry. We emphasize that this weak-pairing phenomenology emerges in a setting where electronic repulsion dominates the kinetic energy and is, moreover, unearthed using non-perturbative numerics that do not presuppose a mean-field description. This observation then enables us to estimate the superconducting transition temperature.

Connection to Solid-State Experiments: We conclude by presenting a link between the double Hofstadter model and models of moiré materials. Explicitly, we define a mapping between the symmetries, Hamiltonian, and even some ground states of our model and those of chiral twisted bilayer graphene [31, 63, 74, 75, 171].

2.2 The Double Hofstadter Model

We now introduce the double Hofstadter model and its basic properties, showing how it incorporates repulsive interactions, narrow topological bands, and time-reversal symmetry. We define the model precisely in Sec. 2.2 and summarize its key symmetries in Sec. 2.2, focusing on time-reversal and magnetic translations. Going to momentum space in Sec. 2.2, we show that the lowest four bands of the model are energetically narrow, well-isolated, and topologically non-trivial. Finally, Sec. 2.2 describes the projected model within the flat band subspace. We identify a "layer-polarized" basis for this space, which will be the most natural basis to describe the many-body states, both numerically and analytically.

The Model

The double Hofstadter model consists of spinful fermions in a bilayer square lattice (See Fig. 2.1). At each lattice site $\mathbf{r} = (x, y) \in \mathbb{Z}^2$, define a row vector of many-body creation operators,

$$\hat{\psi}^\dagger_{\mathbf{r}} = \begin{pmatrix} \hat{\psi}^\dagger_{\mathbf{r}\mathsf{T}\uparrow} & \hat{\psi}^\dagger_{\mathbf{r}\mathsf{T}\downarrow} & \hat{\psi}^\dagger_{\mathbf{r}\mathsf{B}\uparrow} & \hat{\psi}^\dagger_{\mathbf{r}\mathsf{B}\downarrow} \end{pmatrix}. \tag{2.1}$$

We use notation $\ell \in \{\mathsf{T}, \mathsf{B}\}$ for layer and $s \in \{\uparrow, \downarrow\}$ for spin, with associated Pauli matrices $\ell^{0,x,y,z}$ and $s^{0,x,y,z}$.

The Hamiltonian has a few simple components. First, it contains nearest-neighbor hopping within each layer. Second, fermions in the top (bottom) layer experience an upwards

(downwards)-pointing magnetic field that induces a $2\pi/q$ flux per plaquette, where q is a fixed positive integer. This is implemented in a tight-binding model via the Peierls substitution with a choice of electromagnetic gauge field whose value in each layer is $\mathbf{A}_{\mathsf{T/B}} = (0, \pm(2\pi/q)x, 0)$. Concretely, the in-layer hopping Hamiltonian consists of two time-reversal-related copies of the Harper-Hofstadter model with a $1/q$ flux fraction:

$$\hat{h}_t = -t \sum_{\mathbf{r}\in\mathbb{Z}^2} \hat{\psi}^\dagger_{\mathbf{r}+\hat{\mathbf{y}}}\, e^{\frac{2\pi i x}{q}\ell^z}\, \hat{\psi}_{\mathbf{r}} + \hat{\psi}^\dagger_{\mathbf{r}+\hat{\mathbf{x}}}\hat{\psi}_{\mathbf{r}} + \text{h.c.}, \tag{2.2}$$

where we use the convention that the top and bottom layers correspond to $\ell^z = +1$ and -1, respectively. Next, electrons may tunnel vertically between the two layers:

$$\hat{h}_g = -g \sum_{\mathbf{r}\in\mathbb{Z}^2} \hat{\psi}^\dagger_{\mathbf{r}}\, \ell^x\, \hat{\psi}_{\mathbf{r}}. \tag{2.3}$$

Finally, the Hamiltonian contains both an in-layer and inter-layer Hubbard interaction, given by

$$\hat{V}_1 = \frac{U_1}{2} \sum_{\mathbf{r}\in\mathbb{Z}^2} :\hat{n}^2_{\mathbf{r}\mathsf{T}} + \hat{n}^2_{\mathbf{r}\mathsf{B}}: \qquad \hat{V}_2 = U_2 \sum_{\mathbf{r}\in\mathbb{Z}^2} :\hat{n}_{\mathbf{r}\mathsf{T}}\hat{n}_{\mathbf{r}\mathsf{B}}:, \tag{2.4}$$

where $\hat{n}_{\mathbf{r}\ell} = \sum_s \hat{n}_{\mathbf{r}\ell s}$ and where the colons indicate normal-ordering of the fermion operators. With these three ingredients, the full Hamiltonian is (see Fig. 2.1):

$$\hat{H} = \hat{h}_t + \hat{h}_g + \hat{V}_1 + \hat{V}_2 = \hat{h} + \hat{V}, \tag{2.5}$$

where $\hat{h}$ is the non-interacting portion of the model and $\hat{V}$ consists of interaction terms. In what follows, we set the magnitude of the in-layer hopping strength to $t = 1$ and scale the other couplings to be in these units. Furthermore, throughout the rest of this chapter, we will fix the flux fraction to $1/q = 1/4$ (the case depicted in Fig. 2.1). We remark that spinless variants of this model have been explored in previous works for both bosons and fermions [164, 165, 172–175]. However, we emphasize that most of the physics revealed in this chapter crucially depends on the presence of both the layer and spin degrees of freedom.

Symmetries

We now discuss the symmetries of the model beyond charge $U(1)_Q$ and spin $SU(2)_S$, which are manifest. We will find that the coupling of two opposite Hofstadter layers makes both the magnetic point group and the translation symmetries of the model slightly non-trivial.

We first note that the model, while not directly invariant under time-reversal (which would flip the magnetic field penetrating either layer), is invariant under a modified symmetry $M_z\mathcal{T}$. This operator consists of the usual time-reversal operator $\mathcal{T}$, that flips time and electronic spin, followed by an in-plane mirror flip M_z that flips the layer. Furthermore, the point group of $\hat{H}$ can be determined by considering the model's embedding into 3D space (see Fig. 2.1). In particular, the model is invariant under the dihedral group of two-fold rotations

around all three cartesian axes (though not four-fold, see below). This group is generated by π-rotations around the $\hat{\mathbf{z}}$ and $\hat{\mathbf{x}}$ axes, which we denote by C_{2z} and C_{2x}, respectively. The latter naturally exchanges the two layers and is chosen to also flip spin. The combination of the modified time-reversal symmetry with the point group defines the "magnetic point group." As its generators, we take:

$$\hat{C}_{2z}\hat{\psi}^\dagger_{\mathbf{r}}\hat{C}^{-1}_{2z} = \hat{\psi}^\dagger_{-\mathbf{r}} \tag{2.6a}$$

$$\hat{C}_{2x}\hat{\psi}^\dagger_{\mathbf{r}}\hat{C}^{-1}_{2x} = \hat{\psi}^\dagger_{C_{2x}\mathbf{r}}\ell^x s^x \tag{2.6b}$$

$$\hat{\mathcal{I}}\hat{\psi}^\dagger_{\mathbf{r}}\hat{\mathcal{I}}^{-1} = \hat{\psi}^\dagger_{-\mathbf{r}}\ell^x s^x \tag{2.6c}$$

where we have defined a *spacetime inversion* symmetry $\hat{\mathcal{I}} = \hat{C}_{2z}\cdot\hat{M}_z\hat{\mathcal{T}}$, which has the convenient property that it preserves the electronic crystal momentum, and where $C_{2x}\mathbf{r} = (x,-y)$. We remark that the spacetime inversion symmetry is anti-linear ($\hat{\mathcal{I}}i\hat{\mathcal{I}}^{-1} = -i$) while the ordinary point group symmetries are linear.

Next, the translation symmetries of $\hat{H}$ are also governed by the magnetic field. Define the operators

$$\hat{t}_x\hat{\psi}^\dagger_{\mathbf{r}}\hat{t}_x^{-1} = \hat{\psi}^\dagger_{\mathbf{r}+\hat{\mathbf{x}}}e^{\frac{2\pi i y}{q}\ell^z}, \quad \hat{t}_y\hat{\psi}^\dagger_{\mathbf{r}}\hat{t}_y^{-1} = \hat{\psi}^\dagger_{\mathbf{r}+\hat{\mathbf{y}}}. \tag{2.7}$$

These are *not* symmetries (unless $g = 0$), but will be used to define the magnetic translation group. Their non-trivial commutator $\hat{t}_y^{-1}\hat{t}_x^{-1}\hat{t}_y\hat{t}_x = e^{\frac{2\pi i}{q}\ell^z}$ encodes the layer-dependent Aharonov–Bohm phase accrued by an electron hopping counter-clockwise around a plaquette.

The translation symmetry of the Hamiltonian is substantially reduced by the inter-layer tunneling, Eq. (2.3). While the magnetic flux through each layer remains spatially uniform, the tunneling induces a flux pattern in the region *between* the layers that is non-uniform;[1] see the shaded vertical plaquettes shown in Fig. 2.1. For even q, this pattern repeats every $q/2$ sites,[2] and thus the magnetic translation symmetries of $\hat{H}$ are generated by $\hat{m}_x = (\hat{t}_x)^{q/2}$ and $\hat{m}_y = \hat{t}_y$, which anti-commute:

$$[\hat{H},\hat{m}_x] = [\hat{H},\hat{m}_y] = 0, \quad \hat{m}_x\hat{m}_y = -\hat{m}_y\hat{m}_x. \tag{2.8}$$

To define the Bravais lattice and Bloch states, we consider the largest abelian subgroup of translations. Its generators

$$\hat{T}_x = \hat{m}_x^2, \quad \hat{T}_y = \hat{m}_y, \qquad [\hat{T}_x,\hat{T}_y] = 0 \tag{2.9}$$

specify a Bravais lattice $\mathbb{L}$ with primitive lattice vectors $\mathbf{a}_x = q\hat{\mathbf{x}}$ and $\mathbf{a}_y = \hat{\mathbf{y}}$. The corresponding reciprocal lattice is then spanned by $\mathbf{G}_x = 2\pi\hat{\mathbf{x}}/q$ and $\mathbf{G}_y = 2\pi\hat{\mathbf{y}}$. Each unit

[1] We remark that this non-uniform flux pattern is precisely why our model does not have a C_{4z} symmetry in spite of the square lattice geometry.

[2] When q is instead odd, the pattern of fluxes through the vertical plaquettes repeats every q sites, and the generators are simply $(\hat{t}_x)^q$ and $\hat{t}_y$, which commute.

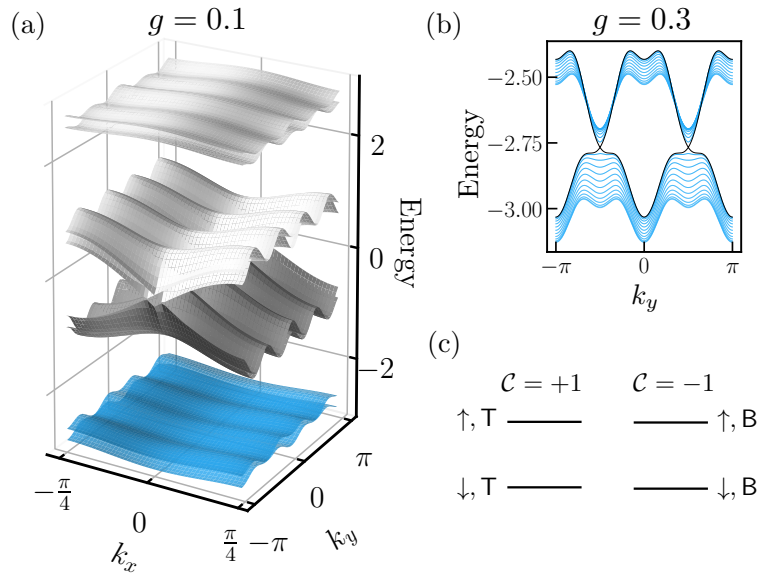

Figure 2.2: **Band Structure of the Double Hofstadter Model.** Panel (a) depicts the single-particle energy bands of the model at a flux fraction $1/q = 1/4$ and inter-layer tunneling amplitude $g = 0.1$. Including spin, there are 16 total bands. In this chapter, we focus on the lowest four (highlighted in blue), which have narrow bandwidth and are well-isolated from the remaining bands. (b) These narrow bands, shown here for $g = 0.3$ in a smaller energy window, have $w_2 = +1$ fragile topology and possess two Dirac cones that wind in the same direction. In (c), we show a schematic of the layer-polarized basis states, which span the flat band subspace and carry opposite Chern number $\mathcal{C} = \pm 1$ in opposite layers. When interactions are large, the energy difference between flat bands is irrelevant; in Section 2.2 we show that a maximally-layer polarized basis is more natural for studying ground state physics in the low-energy subspace.

cell contains q evenly-spaced sites. We describe positions in the underlying square grid by specifying a unit cell and sublattice:

$$\mathbf{r} = \mathbf{u} + \sigma\hat{\mathbf{x}} \quad (\mathbf{u} \in \mathbb{L},\ \sigma \in \{0, \ldots, q-1\}), \tag{2.10}$$

and relabel the fermion operators as $\hat{\psi}^\dagger_{\sigma\ell s}(\mathbf{u})$.

Band Structure and Topology

Combining magnetic translations Eq. (2.9) with Eqs. (2.2) and (2.3), we obtain the non-interacting band structure of the double Hofstadter model. The band structure is shown in Fig. 2.2(a) and, accounting for two-fold spin degeneracy, features $2 \times 2 \times q = 16$ total bands. The lowest four are narrow ("flat") and energetically isolated by a large band gap. Partially

filling these narrow bands in the presence of interactions will be the primary interest of this study. In what follows, it will be convenient to denote their occupation by a continuous value $0 \leq \nu \leq 4$.

In the absence of inter-layer tunneling, these narrow bands are those of the decoupled Hofstadter layers. It is known that they are topological with Chern number $\mathcal{C} = +1(-1)$ for the top (bottom) layers [20]. In fact, in the limit of small flux $1/q \to 0$, these flat bands become time-reversal related copies of the lowest Landau level [176, 177]. Introducing non-zero tunneling g hybridizes the lowest two bands in each spin sector. Although their total Chern number is zero, the bands are nonetheless topologically non-trivial. They have a fragile topological invariant $w_2 = 1 \in \mathbb{Z}_2$, protected by spacetime inversion symmetry $\mathcal{I}$ and $U(1)_Q$ [23–27]. A key implication of fragile topology is that the two $SU(2)_S$-symmetric bands possess two Dirac cones, as shown in Fig. 2.2(b), that wind in the same direction. At even q, the Dirac cones are pinned to $\mathbf{k}_\pm = \mathbf{G}_x/2 \pm \mathbf{G}_y/4$ by C_{2z}, C_{2x} and m_x (details in Appendix A).

Flat Band Hamiltonian

Let $\hat{\mathcal{P}}$ denote the many-body projection operator into the low-lying Hilbert space of the narrow bands of $\hat{h}$. Provided that the interaction scale U is smaller than the gap above the narrow Hofstadter bands, we expect the physics at $\nu \leq 4$ to be accurately captured by the projected Hamiltonian $\hat{\mathcal{P}}\hat{H}\hat{\mathcal{P}}$. This simplification is ubiquitous in studies of the quantum Hall effect at partial filling of the lowest Landau level [178]. There, one finds that interactions enhance the gap to higher bands, thereby justifying the projection assumption beyond the naive regime of applicability.

Layer-Polarized Basis for Flat Bands

When the interaction strength U greatly exceeds the bandwidth W of the low-lying bands, the single-particle energy eigenbasis is no longer a physically useful way to organize the narrow-band subspace. Drawing inspiration from the $g = 0$ limit in which layer is a good quantum number, we instead work in a basis of states that are *maximally-polarized* into either the top or bottom layer. Crucially, these states will carry a layer-dependent Chern number, a fact that will underpin our analytical and numerical understanding of the many-body phenomena. Concretely, we define a "layer-polarized" basis for the flat-band subspace as an eigenbasis of the projected layer operator:

$$\hat{\mathcal{P}}\hat{\ell}^z(\mathbf{k})\hat{\mathcal{P}}\,|v_{ls}(\mathbf{k})\rangle = \lambda_l(\mathbf{k})\,|v_{ls}(\mathbf{k})\rangle\,, \tag{2.11}$$

and demand that the (real) eigenvalues carry a consistent sign across the Brillouin zone. Here, $\hat{\ell}^z(\mathbf{k}) = \hat{\psi}^\dagger(\mathbf{k})\ell^z\hat{\psi}(\mathbf{k})$ is defined in terms of the Fourier transformed microscopic fermion operators,

$$\hat{\psi}^\dagger_{\sigma\ell s}(\mathbf{k}) = \sum_{\mathbf{u}\in\mathbb{L}} \hat{\psi}^\dagger_{\sigma\ell s}(\mathbf{u})e^{i\mathbf{k}\cdot(\mathbf{u}+\sigma\hat{\mathbf{x}})}. \tag{2.12}$$

In this basis, the creation operators for the layer-polarized orbitals take the form of Block-like states:

$$\hat{\varphi}^\dagger_{ls}(\mathbf{k}) = \sum_{\sigma,\ell} \hat{\psi}^\dagger_{\sigma\ell s}(\mathbf{k}) v_{\sigma\ell,l}(\mathbf{k}), \tag{2.13}$$

For numerical convenience, we fix the residual gauge freedom by requiring that these layer-polarized orbitals be maximally localized in x when Fourier transformed, resulting in hybrid Wannier states [179–182].

We further remark that the two eigenvalues in Eq. (2.11) are opposite in sign and equal in magnitude. For all parameters of interest, their magnitude is bounded below as $|\lambda_{\mathsf{T/B}}(\mathbf{k})| > 0.95$, very near the maximum possible value of unity. Like the Harper-Hofstadter bands of the layer-decoupled Hamiltonian $\hat{h}_t$, the layer-polarized basis states carry a Chern number $\mathcal{C} = \pm 1$ for $l = \mathsf{T/B}$ respectively. We emphasize that this holds in spite of the fact that layer is not a good quantum number in the presence of inter-layer tunneling. We therefore refer to the label l as the "dressed layer" index and remark that it is indistinguishable from the true layer index ℓ, within the low-energy subspace, in the layer-decoupled limit.

Flat Band Projected Hamiltonian

We now write the projected Hamiltonian in terms of the layer-polarized basis for the flat-band Hilbert space:

$$\hat{\mathcal{H}} = \hat{\mathcal{P}}\hat{H}\hat{\mathcal{P}} = \sum_{\mathbf{k}} \hat{\varphi}^\dagger_{\mathbf{k}} \delta h(\mathbf{k}) \hat{\varphi}_{\mathbf{k}} + \hat{\mathcal{V}}. \tag{2.14}$$

This decomposition of the Hamiltonian is chosen so that the interaction part is positive semi-definite:

$$\hat{\mathcal{V}} = \frac{1}{2} \sum_{\mathbf{q}\in \mathrm{EBZ}} V_{\ell\ell'}(\mathbf{q}) \delta\hat{\rho}_{\mathbf{q}\ell} \delta\hat{\rho}_{-\mathbf{q}\ell'}, \tag{2.15}$$

and $\delta h(\mathbf{k})$ consists of the remaining single-particle terms. The latter can be further decomposed as $\delta h_0(\mathbf{k}) + \delta h_g(\mathbf{k})$, where $\delta h_g(\mathbf{k}) \sim \mathcal{O}(g)$ is purely off-diagonal in dressed layer and $\delta h_0(\mathbf{k}) \propto l^0$ is controlled by the bandwidth of the bare Hofstadter bands, up to a constant offset and $\mathcal{O}(g^2)$ corrections.

We refer to $\hat{\mathcal{V}}$ as the "strong-coupling" form of the interaction. Explicitly, $\delta\hat{\rho}_{\mathbf{q}\ell} = \hat{\rho}_{\mathbf{q}\ell} - \bar{\rho}_{\mathbf{q}\ell}\hat{I}$ denotes the layer-resolved charge density relative to a translationally-invariant reference charge background that evenly fills the two layers, where (*c.f.* [31, 63])

$$\hat{\rho}_{\mathbf{q}\ell} = \frac{1}{\sqrt{qN}} \sum_{\mathbf{k}} \hat{\varphi}^\dagger_{\mathbf{k}} \Lambda_{\mathbf{q}\ell}(\mathbf{k}) \hat{\varphi}_{\mathbf{k}+\mathbf{q}}, \tag{2.16}$$

$$[\Lambda_{\mathbf{q}\ell}(\mathbf{k})]_{ll'} = \sum_{\sigma} v^*_{\sigma\ell,l}(\mathbf{k}) v_{\sigma\ell,l'}(\mathbf{k}+\mathbf{q}), \tag{2.17}$$

and $\bar{\rho}_{\mathbf{q}\ell} = \frac{1}{\sqrt{qN}} \sum_{\mathbf{k},\mathbf{G}} \delta_{\mathbf{q},\mathbf{G}} \mathrm{tr}\left[\Lambda_{\mathbf{G}\ell}(\mathbf{k})\right]$. For purely on-site interactions, Eq. (2.4), the interaction kernel $V(\mathbf{q})$ is a matrix in the layer indices that can be expressed as:

$$V(\mathbf{q}) = U_1 \ell^0 + U_2 \ell^x, \tag{2.18}$$

which is crucially independent of $\mathbf{q}$. Moreover, we note that the momentum $\mathbf{q}$ lives in an extended Brillouin zone, or "EBZ," which is defined relative to the microscopic square lattice as opposed to the Bravais lattice (see Appendix A for more detail).

The symmetries of the double Hofstadter model strongly constrain its form factors. Namely, spacetime inversion symmetry gives $\Lambda_{\mathbf{q}}(\mathbf{k}) = \sum_\ell \Lambda_{\mathbf{q}\ell}(\mathbf{k})$ the following functional form:[3]

$$\Lambda_{\mathbf{q}}(\mathbf{k}) = F^S_{\mathbf{q}}(\mathbf{k}) e^{i\Phi^S_{\mathbf{q}}(\mathbf{k}) l^z} + F^A_{\mathbf{q}}(\mathbf{k}) l^x e^{i\Phi^A_{\mathbf{q}}(\mathbf{k}) l^z}, \tag{2.19}$$

with real-valued functions $F^{S/A}$ and $\Phi^{S/A}$. In the 'decoupled' limit $g \to 0$, the $U(2)$ symmetry of the double Hofstadter model is enlarged to $U(2) \times U(2)$, corresponding to independent spin rotations and charge conservation in each layer. This implies F^A vanishes when $g = 0$, and in fact $F^A = \mathcal{O}(g)$ is always perturbatively small. The decoupled limit, therefore, serves as the starting point for the strong coupling theory of the double Hofstadter model that we develop in the next section.

2.3 The Layer Anti-Ferromagnet

We now investigate the phase diagram of the double Hofstadter model at electronic densities consistent with filling two of the four flat bands, i.e., $\nu = 2$. Our key finding in this section is a correlated insulating ground state, the *layer anti-ferromagnetic* (LAF) state, that will later be shown to be the parent state for superconductivity. The LAF is characterized by ferromagnetic order within each layer and anti-ferromagnetic order between layers [see Fig. 2.3(a)], thereby spontaneously breaking the $SU(2)_S$ symmetry down to $U(1)_S$. Topologically, the LAF is an interaction-induced quantum spin Hall insulator protected by a $U(1)_Q \times U(1)_S$ symmetry.

Analytic Arguments for LAF at Large U_1

Let us begin by analytically arguing that the LAF state depicted in Fig. 2.3(a) is the expected ground state when the inter-layer interaction U_1 is the dominant term in the Hamiltonian. We do so by showing that interactions favor in-layer ferromagnetic order, while additional inter-layer hopping selects for inter-layer antiferromagnetic order. We later confirm this picture numerically in Subsection 2.3, where we use extensive iDMRG computations to demonstrate the stability of the LAF and discuss a rich array of competing phases.

[3] This form is obtained by passing to the layer-polarized basis in which spacetime inversion acts as $\hat{\mathcal{I}} \hat{\varphi}^\dagger(\mathbf{k}) \hat{\mathcal{I}}^{-1} = \hat{\varphi}^\dagger(\mathbf{k}) s^x l^x$.

In-Layer Ferromagnetism

We start by working in the limit with vanishing inter-layer tunneling and inter-layer interactions, $g = U_2 = 0$, in which the two layers are completely decoupled. We further take the limit where the remaining in-layer dispersion $\delta h_0(\mathbf{k})$ [Eq. (2.14)] vanishes (up to an inconsequential momentum independent shift). At the filling fraction $\nu = 2$, the in-layer interaction Hamiltonian favors states that occupy the two layers equally. All that remains, therefore, is to determine the behavior of spin in each layer. For generic narrow, half-filled Chern bands, strong repulsive interactions will generally favor ferromagnetic spin alignment in a phenomenon known as *quantum Hall ferromagnetism* [43, 183]. Intuitively, this behavior arises from the interplay between strong interactions and the spread of Wannier functions. In a topological band, Wannier functions cannot all be atomically localized. It is therefore advantageous for the electrons to spin polarize, which forces the many-body wavefunction to vanish when two electrons are brought together and results in a favorable direct exchange energy. We remark that this is different from the paradigm of the Fermi-Hubbard model. There, electrons can be perfectly localized to atomic lattice sites, resulting in a vanishing direct exchange energy and a dominant anti-ferromagnetic "super-exchange" interaction.

Consequently, the layer-decoupled double Hofstadter model should have *bilayer quantum Hall ferromagnets* as favorable ground states, namely

$$|\boldsymbol{n}_{\mathsf{T}}, \boldsymbol{n}_{\mathsf{B}}\rangle = \prod_{\mathbf{k}} \hat{\varphi}^{\dagger}_{\mathsf{T},\boldsymbol{n}_{\mathsf{T}}}(\mathbf{k})\hat{\varphi}^{\dagger}_{\mathsf{B},\boldsymbol{n}_{\mathsf{B}}}(\mathbf{k})\,|0\rangle\,. \tag{2.20}$$

Here, each layer is associated with an order parameter characterizing its spontaneous magnetization:

$$\boldsymbol{n}_{\ell} \in S^2 \simeq SU(2)/U(1), \tag{2.21}$$

and electronic states whose spins are aligned to this axis:

$$\hat{\varphi}^{\dagger}_{\ell,\boldsymbol{n}_{\ell}} = \cos(\theta_{\ell}/2)\hat{\varphi}^{\dagger}_{\ell,\uparrow} + e^{i\phi_{\ell}}\sin(\theta_{\ell}/2)\hat{\varphi}^{\dagger}_{\ell,\downarrow}, \tag{2.22}$$

where ϕ_{ℓ} and θ_{ℓ} are the azimuthal and polar angles of $\boldsymbol{n}_{\ell}$, respectively. We can place this intuition on rigorous analytical footing by recognizing that the term $\delta\hat{\rho}_{\mathbf{q}\ell}\delta\hat{\rho}_{-\mathbf{q}\ell}$ appearing in the strong-coupling interaction $\hat{\mathcal{V}}$ [Eq. (2.15)] is positive semi-definite for each $\mathbf{q}$. This implies that any state annihilated by every $\delta\hat{\rho}_{\mathbf{q}\ell}$ is an exact ground state of this interaction. In particular, this is true of the ferromagnetic trial states in Eq. (2.20):

$$\delta\hat{\rho}_{\mathbf{q}\ell}\,|\boldsymbol{n}_{\mathsf{T}}, \boldsymbol{n}_{\mathsf{B}}\rangle = 0, \quad \forall\, \boldsymbol{n}_{\mathsf{T/B}} \in S^2. \tag{2.23}$$

Analytically, this follows from the Pauli exclusion principle and the form factors $\Lambda_{\mathbf{q}\ell}(\mathbf{k})$ being layer-diagonal in the $g = 0$ limit, Eq. (2.19), that is itself a consequence of layer $U(1)$ symmetry. This shows that the trial states (2.20) are exact ground states of the strong-coupling Hamiltonian (2.15) and are therefore approximate ground states of the full Hamiltonian.

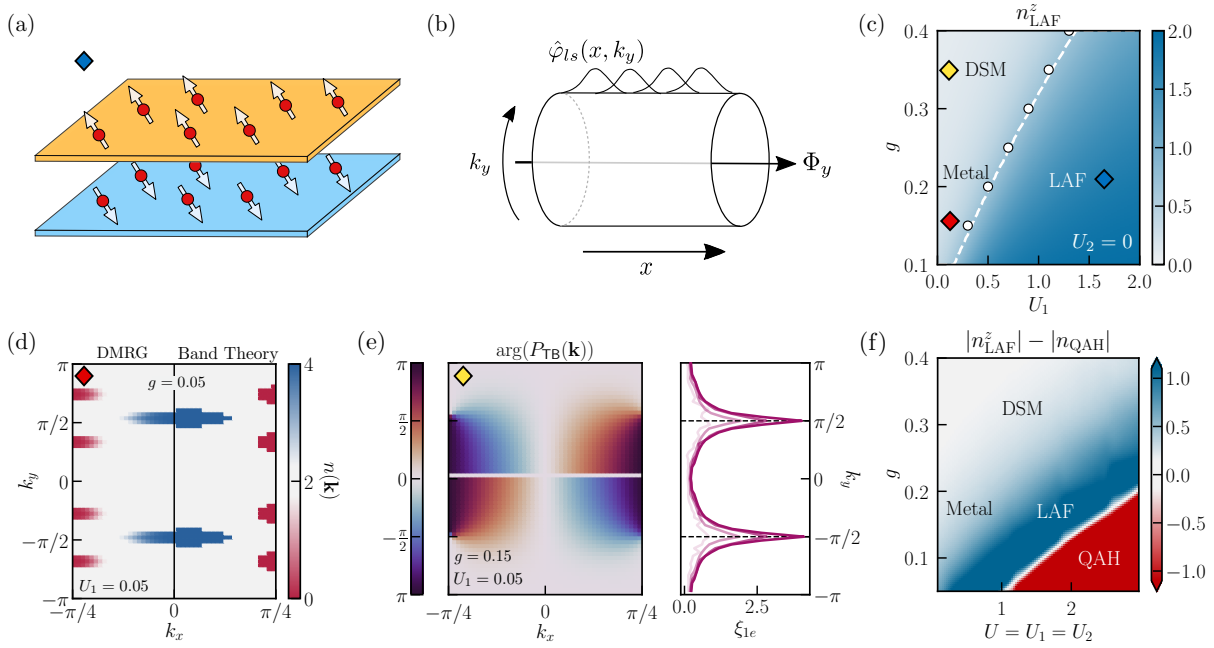

Figure 2.3: **The Layer Anti-Ferromagnet and Competing Phases.** (a) Schematic depiction of the LAF at $\nu = 2$, a quantum spin Hall insulator with opposite spin polarization in opposite layers. We will later argue that hole-doping this state gives rise to an unconventional superconductor. (b) We numerically evidence the LAF using cylinder iDMRG in a basis of hybrid Wannier orbitals indexed by unit cell x, momentum k_y, spin s, and (dressed) layer l. Threading flux Φ_y through the cylinder shifts the discrete k_y momenta by Φ_y/L_y, enabling continuous access of all momenta in the BZ. (c) In particular, working at $L_y = 5$, we evaluate the LAF polarization (2.29) as a function of g and U_1 (at fixed $\nu = 2$ and $U_2 = 0$), finding the LAF phase in the majority of the strong coupling regime. The approximate phase boundary to a weak-coupling metal and Dirac semi-metal (DSM) is marked with a dotted line (See Sec. 2.3 for details). (d) The metal is identified by examining the fermion occupations $n(\mathbf{k})$ across the BZ, where we find pockets of excess electrons or holes. We find near-quantitative agreement between the flux-threaded iDMRG data (left) and the occupations according to the non-interacting band structure (right). (e) In contrast, the DSM is characterized both by phase winding of $P_{\mathsf{TB}}(\mathbf{k})$ [defined in Eq. (2.31)] and a peak in the $1e$ correlation length at $k_y = \pm\pi/2$ that grows with χ. From light to dark: $\chi = 128,\ 512,\ 1536,\ 3096$. (f) The presence of inter-layer repulsion modifies the phase diagram by introducing a quantum anomalous Hall insulator that competes with the LAF.

Between-Layer Anti-Ferromagnetism

Upon including the inter-layer tunneling g, the above trial ground states, Eq. (2.20), are expressed in the layer-polarized basis. We then treat the residual single-particle terms perturbatively. Similar to the original microscopic basis, the $\mathcal{O}(g)$ terms shuttle electrons between the dressed layer orbitals, or quantitatively:

$$\delta\hat{h}_g = \sum_{\mathbf{k}} \hat{\varphi}^\dagger_{\mathbf{k}} \Big[h^x_g(\mathbf{k}) l^x + h^y_g(\mathbf{k}) l^y \Big] \hat{\varphi}_{\mathbf{k}} \approx \hat{\mathcal{P}} \hat{h}_g \hat{\mathcal{P}}. \tag{2.24}$$

Since the bilayer quantum Hall ferromagnets are insulators, these virtual tunneling processes hybridize them with gapped excitations, generically lowering their energy due to level repulsion. Since such tunneling processes are forbidden by Pauli exclusion when $\boldsymbol{n}_{\mathsf{T/B}}$ are aligned—as opposed to anti-aligned—the effect of g is to introduce an anti-ferromagnetic "super-exchange" interaction between the top and bottom layers. As a consequence of second-order perturbation theory in g, any trial state with $\boldsymbol{n}_{\mathsf{T}} = -\boldsymbol{n}_{\mathsf{B}}$ is reduced in energy by

$$J = \langle \mathrm{LAF} | \, \delta\hat{h}_g \hat{\mathcal{V}}^{-1} \delta\hat{h}_g \, | \mathrm{LAF} \rangle \sim \frac{g^2}{U_1}. \tag{2.25}$$

This energetic advantage selects out LAF states, i.e., bilayer quantum Hall ferromagnets that spontaneously break the $SU(2)_S$ spin rotation symmetry down to $U(1)$ by condensing the vector order parameter

$$\boldsymbol{n}_{\mathrm{LAF}} = \boldsymbol{n}_{\mathsf{T}} - \boldsymbol{n}_{\mathsf{B}}. \tag{2.26}$$

This establishes the LAF as a ground state of the full Hamiltonian in the limit of vanishingly-flat in-layer dispersion $\delta h_0(\mathbf{k})$ [Eq. (2.14)] and perturbatively small g. In the next section, we go beyond these limits via a large-scale numerical investigation.

Numerical Phase Diagram at $\nu = 2$

We now present the phase diagram of our model at the filling fraction $\nu = 2$, which we obtain using cylinder iDMRG methods that we describe below. Consistent with our analytical expectations, we find a robust LAF phase at large values of the in-layer interaction U_1. Furthermore, we numerically characterize competing quantum orders, finding evidence for weakly-interacting metallic phases inherited from the band structure and a layer-polarized quantum anomalous Hall insulating state at large U_2.

Cylinder iDMRG Numerical Method

Let us now describe the cylinder iDMRG numerical method that we will use to obtain the phase diagram at $\nu = 2$ and, upon doping, superconductivity. Since we are interested in the physics at partial filling of the isolated flat bands, we restrict to matrix product state (MPS) wave functions that live entirely within these bands, thereby reducing the number of degrees of freedom from all $4q$ bands to just 4, for layer and spin. Moreover, since the fragile

topology of the flat band subspace forbids an exponentially-localized basis that respects all the symmetries [23–27], we choose a computational basis of mixed position-momentum space states. Such states, commonly referred to as "hybrid" Wannier states [28, 179–182, 184], are exponentially-localized *along* the cylinder and are delocalized *around* the cylinder. A similar topological restriction arises in TBG [69, 76], where a line of work by some of us has established the use of such states in cylinder iDMRG [185–187].

This basis, which we encode into the MPS tensors, takes the following form:

$$\hat{\varphi}_{ls}(j, k_y) = \frac{1}{\sqrt{N_x}} \sum_{k_x=0}^{2\pi/q} e^{ik_x qj} \hat{\varphi}_{ls}(\mathbf{k}), \tag{2.27}$$

and is depicted graphically in Fig. 2.3(b). Here, j labels "rings" along the cylinder length, $k_y = (2\pi n + \Phi_y)/L_y$ labels discrete momentum cuts through the BZ that can be shifted by tuning the flux through the cylinder, $\Phi_y \in [0, 2\pi)$. The basis is chosen such that its Fourier transform $\hat{\varphi}_{ls}(\mathbf{k})$ is a layer-polarized basis (as described in Sec. 2.2), permitting $\hat{\varphi}_{ls}(j, k_y)$ to be labeled by dressed-layer and spin. Moreover, the phase of each $\hat{\varphi}_{ls}(\mathbf{k})$ is chosen such that $\hat{\varphi}_{ls}(j, k_y)$ are maximally localized in the $\hat{\mathbf{x}}$ direction [28, 188], giving hybrid Wannier states (see Appendix A for more details). Each ring of this computational cylinder, therefore, has a total of $2 \times 2 \times L_y$ tensors whose physical legs encode the occupations of fermions at a given dressed-layer, spin, and momentum. Our numerics explicitly conserve electric charge $U(1)_Q$, spin $U(1)_S \subset SU(2)_S$, and $\mathbb{Z}/L_y\mathbb{Z}$ momentum around the cylinder.

Carrying out iDMRG on this model requires "MPO compression" [170]. When the Hamiltonian is resolved in the basis (2.27), both the dispersion and interaction become long-ranged. A naive matrix product operator (MPO) representation of this Hamiltonian has bond dimension $D \approx 10^6$, far beyond what is computationally feasible. We therefore apply an MPO compression technique [170, 185] to create a faithful MPO representation of our Hamiltonian with bond dimension $D \approx 300$ and operator norm errors of $\delta < 10^{-3}t$ or better. We consider cylinder circumferences $L_y = 5, 6, 7$. Since the the MPS bond dimension required to accurately describe ground states increases exponentially with L_y, we employ parallelized iDMRG simulations to reach MPS bond dimensions as large as $\chi = 12288$ using the open source `tenpy` library [189].

The LAF at Strong In-Layer Interactions

We now numerically verify the presence of LAF order at $\nu = 2$ in the regime of large in-layer repulsive interactions $U_1 \gg t$. First, however, we must address a subtlety associated with the cylinder geometry used for iDMRG. Since the underlying infinite cylinder is quasi-1D and the candidate LAF state spontaneously breaks continuous spin rotational symmetry, Hohenberg-Mermin-Wagner (HMW) considerations imply that it must disorder due to quantum fluctuations [190–192]. The resulting quasi-1D state is symmetric with a spin gap that decays exponentially in the cylinder circumference [193]. Moreover, its LAF polarization, though finite at finite bond dimension, decays to zero as $\chi \to \infty$. To estimate the extent of

the LAF phase in the 2D limit, we take an approach analogous to a susceptibility experiment. In particular, we add a weak Zeeman field to the Hamiltonian:

$$\hat{H} \to \hat{H} + B_z \sum_{\mathbf{r}\in\mathbb{Z}^2} \hat{\psi}^\dagger_{\mathbf{r}} \ell^z s^z \hat{\psi}_{\mathbf{r}}, \tag{2.28}$$

and take $B_z = 10^{-2}$, which is much smaller than all other microscopic scales in the problem. Such a Zeeman field explicitly breaks $SU(2)_S$ spin symmetry down to $U(1)_S$ but leaves all other symmetries unbroken.[4] We then approximately identify the phase extent of the LAF in the 2D limit by evaluating

$$n^z_{\mathrm{LAF}}(\mathbf{r}) = \langle \hat{\psi}^\dagger_{\mathbf{r}} \ell^z s^z \hat{\psi}_{\mathbf{r}} \rangle \tag{2.29}$$

in iDMRG, which effectively measures the susceptibility to LAF ordering. Fig. 2.3(c) shows n^z_{LAF} as a function of g and U_1 at fixed $U_2 = 0$, with a heuristic phase boundary identified where $\partial n^z_{\mathrm{LAF}}/\partial U_1$ has the largest slope. In Appendix A, we numerically verify that the LAF region of the phase diagram is insulating by computing the charge-1e correlation length, ξ_{1e}, and demonstrating that it converges to a finite value as $\chi \to \infty$. In summary, we have numerically identified the presence of a LAF insulating state at $\nu = 2$ that inhabits a broad portion of the strong-coupling regime, confirming our analytical expectations.

Competing Phases at Weak Interactions

Next, we explore the weakly-interacting regime. We first remark that the non-interacting band structure at $\nu = 2$ exhibits two distinct phases as a function of g. The first occurs at $g \ll 1$, where the nearly-degenerate, weakly-hybridized Hofstadter bands give rise to a metal with a one-dimensional Fermi surface. In contrast, sufficiently large g gaps out these bands except at the two Dirac cones protected by $\mathcal{I}$ and $SU(2)_S$ (see Sec. 2.2), yielding a Dirac semimetal (DSM).

Using iDMRG, we confirm that these phases persist in the presence of weak interactions. We diagnose the metallic phase by plotting the fermionic occupations

$$n(\mathbf{k}) = \sum_{l,s} \langle \hat{\varphi}^\dagger_{ls}(\mathbf{k}) \hat{\varphi}_{ls}(\mathbf{k}) \rangle \,. \tag{2.30}$$

Since we work at finite cylinder circumference, we access only a finite number of cuts through the BZ. Nonetheless, we can gain continuous momentum resolution by threading flux through our cylinder [194], as depicted in Fig. 2.3(b). The results of this are shown in Fig. 2.3(d) for $g = 0.15$ and $U_1 = 0.05$. We find that the occupancies obtained using iDMRG quantitatively match the band structure occupancies of the non-interacting limit.

[4] In the presence of such a field, the LAF is no longer a symmetry-breaking phase but remains a topologically non-trivial quantum spin Hall insulator.

Next, we confirm the DSM by two independent means.[5] A defining characteristic of this state is that it possesses two Dirac cones that wind in the same direction within each spin sector. This can be detected via the winding of $\arg P_{\mathsf{TB}}(\mathbf{k})$, where P is the correlation matrix [185]:

$$P_{ll'}(\mathbf{k}) = \sum_s \langle \hat{\varphi}^\dagger_{l's}(\mathbf{k}) \hat{\varphi}_{ls}(\mathbf{k}) \rangle \,. \tag{2.31}$$

Fig. 2.3(c) plots $\arg P_{\mathsf{TB}}(\mathbf{k})$ over the flux-threaded BZ at $g = 0.05$ with finite interactions $U_1 = 0.05$. We find that it indeed has the same winding around the points $\mathbf{k}_\pm = (\pi/4, \pm\pi/2)$. That these points are Dirac cones—even at finite interaction strength—can be confirmed by computing the maximum charge-1e correlation length $\xi_{1e}(k_y)$ as a function of the momentum k_y around the cylinder, made continuous by threading flux. In a weakly-interacting system, this quantity parameterizes the decay of correlations of the form $\langle \hat{\varphi}^\dagger_{x,k_y} \hat{\varphi}_{0,k_y} \rangle \sim e^{-x/\xi_{1e}(k_y)}$. As such, when charge-1$e$ excitations are gapless, ξ_{1e} should diverge. Indeed, we find that it strongly peaks and grows rapidly with bond dimension precisely when k_y passes through the isolated values $\pm\pi/2$, indicative of a semi-metallic gap closure [see Fig. 2.3(e)].

Robustness of LAF to Interlayer Interactions

We further confirm the robustness of the LAF phase by re-introducing the inter-layer repulsion U_2. Even at $U \equiv U_2 = U_1$ (a regime more relevant to the experimental realizations in Sec. 2.6 below), we find that the LAF continues to occupy a sizable phase space, but is accompanied by a layer-polarized correlated insulator at smaller values of g [See Fig. 2.3(f)]. In this phase, $\hat{\psi}^\dagger_{\mathbf{r}} \ell^z \hat{\psi}_{\mathbf{r}}$ acquires a non-zero expectation value, thereby breaking both C_{2x} and $C_{2z}\mathcal{I}$ spontaneously. Since the dressed-layer index is locked to Chern (Sec. 2.2), then it also has a quantized Hall conductance of $\sigma_{xy} = 2 \times e^2/h$, making it a quantum anomalous Hall (QAH) phase. We detect the presence of both the LAF and QAH phase simultaneously by plotting

$$|n_{\mathrm{LAF}}(\mathbf{r})| - |n_{\mathrm{QAH}}(\mathbf{r})| = |\langle \hat{\psi}^\dagger_{\mathbf{r}} \ell^z s^z \hat{\psi}_{\mathbf{r}} \rangle| - |\langle \hat{\psi}^\dagger_{\mathbf{r}} \ell^z \hat{\psi}_{\mathbf{r}} \rangle| \tag{2.32}$$

as a function of g and U, which is positive in the LAF phase and negative in the QAH phase. In Fig. 2.3(f), we observe a first-order phase transition between the LAF and the QAH phase at large U.

2.4 Numerical Evidence for Superconductivity

In this section, we use large-scale cylinder iDMRG to argue that hole-doping the LAF gives rise to a robust finite-circumference superconducting phase, which pairs holes with opposite

[5] Note that in the presence of B_z, the Dirac cones are generically gapped out, as explicitly breaking $SU(2)_S$ removes their topological protection. Nevertheless, since B_z is weak compared to the single-particle energy scales, the DSM can still be identified using the present diagnostics.

spin and between opposite layers. In particular, in Subsection 2.4, we undertake a careful double scaling analysis of the superconducting correlations in both bond dimension and cylinder circumference at a particular point in parameter space. We find strong evidence for a superconducting state at $L_y = 5$ as well as indications, though ultimately inconclusive, that this behavior persists at larger circumference. Subsequently, in Sec. 2.4, we work at fixed circumference $L_y = 5$ and demonstrate that this superconducting ground state belongs to a robust and stable superconducting phase. In particular, we find that superconductivity is present across various parameter regimes and always coexists with LAF order, suggesting that the broad LAF phase at $\nu = 2$ is the "parent state" of the putative superconductor. Finally, we find that this $L_y = 5$ superconducting order is stable to sizable inter-layer repulsive interactions and a finite spatial interaction range, both of which add additional repulsive interactions to the channels in which we find superconductivity.

Existence of Superconducting Order

In 2D systems, superconductivity typically manifests as a charge-$2e$ operator $\hat{\Delta}(\mathbf{r})$ having long-range order:

$$\lim_{\mathbf{r}\to\infty} |\langle \hat{\Delta}^\dagger(\mathbf{r})\hat{\Delta}(0)\rangle| \to \text{constant}, \quad \text{(2D)} \tag{2.33}$$

thereby spontaneously breaking $U(1)_Q$ symmetry down to $\mathbb{Z}_2$. However, to diagnose a superconducting state with iDMRG, two important subtleties arise due to the finite circumference and bond dimension of the simulations. This subsection gives a brief technical discussion of some of these subtleties and presents numerical evidence for the existence of a superconductor in the double Hofstadter model. Readers more interested in the phenomenological properties of the purported superconducting phase may skip to the next section.

Superconductivity in Cylinder iDMRG

Let us discuss how superconductivity manifests in general in cylinder iDMRG (see also [168, 195]). First, since iDMRG uses a quasi-1D cylinder geometry with finite circumference L_y, we must understand how to diagnose the quasi-1D analog of the superconductor—the *Luther-Emery liquid*—and characterize its approach to a superconductor as $L_y \to \infty$. The Luther-Emery liquid is characterized by the presence of fractionalized excitations—namely gapless "chargeons" and gapped "spinons"— that independently carry the electron's charge and spin (see e.g. [196]). As a consequence, charge-$2e$ excitations (with vanishing total $\hat{S}^z$) have correlations that exhibit algebraic long-range order:

$$|\langle \hat{\Delta}^\dagger(\mathbf{r})\hat{\Delta}(0)\rangle| \sim |\mathbf{r}|^{-\eta(L_y)} \quad (L_y\text{-cylinder}). \tag{2.34}$$

As the cylinder circumference is increased, the realization of true long-range superconducting order in 2D is tied to the behavior $\eta(L_y) \to 0$ as $L_y \to \infty$. In the Luther-Emery liquid, furthermore, correlation functions of electrons (gapped states comprised of both the chargeon

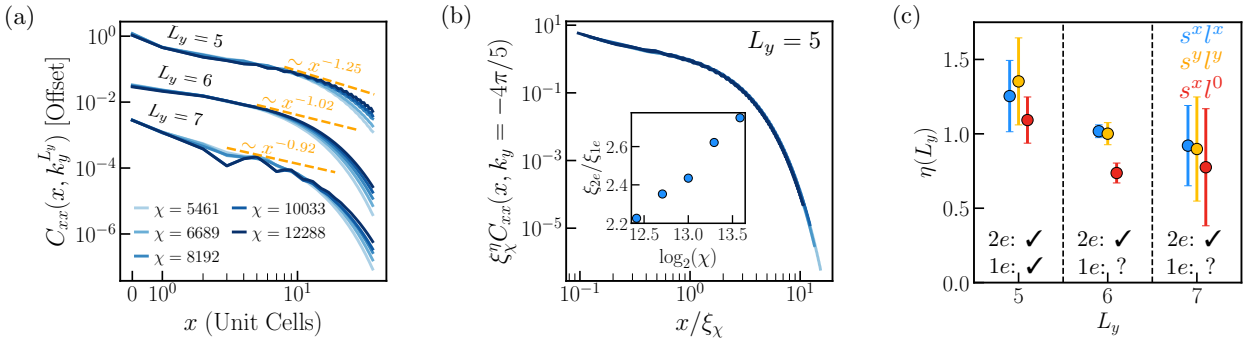

Figure 2.4: **Evidence for Superconductivity.** Working at fixed parameters $(g, U_1, U_2) = (0.15, 1.5, 0)$ and doping $\nu = 2 - 1/L_y$, we provide our numerical evidence for the existence of a superconducting state at $L_y = 5$ and algebraically-decaying pair correlations at all three circumferences. In (a), we examine the superconducting correlation function [Eq. (2.38)] as a function of bond dimension χ for each circumference, finding that they each approach a power law as $\chi \to \infty$. The power law obtained via a scaling collapse [see panel (b)] is shown with an orange dashed line. For ease of viewing, the correlations for $L_y = 6, 7$ are offset vertically by an arbitrary amount. (b) Power law behavior is quantitatively demonstrated by performing a scaling collapse [Eq. (2.39)], shown here for $L_y = 5$. To differentiate this power law behavior from that of a gapless metallic state, in the inset we show that the ratio ξ_{2e}/ξ_{1e} increases as a function of bond dimension, a hallmark of a superconducting state [See Sec. 2.4]. (c) Power-law exponents of the superconducting correlations for all three channels as a function of cylinder circumference L_y. The powers $\eta(L_y)$ decrease as L_y increases, consistent with the survival of superconductivity in the 2D limit. At the bottom of the panel, we summarize our confidence in the requisite gaplessness of $2e$ excitations and gap to $1e$ excitations at each circumference (See Sec. 2.4 for more details).

and spinon) exhibit exponential decay:

$$\langle \hat{\varphi}^\dagger(\mathbf{r}) \hat{\varphi}(0) \rangle_{\text{LE}} \sim e^{-|\mathbf{r}|/\xi_{1e}}. \tag{2.35}$$

At finite circumference, this behavior crucially distinguishes the Luther-Emery liquid from the Luttinger liquid, where such correlations are algebraic.

A second important subtlety concerns the finite bond dimension of the MPS, which only permits the expression of exponentially-decaying (connected) correlations, and introduces a length scale ξ_χ associated to the largest non-trivial eigenvalue of the MPS transfer matrix. As a consequence, power law correlations of any charge-Q operator are cut off at a distance $\xi_{Q,\chi} \leq \xi_\chi$ that scales with bond dimension according to [197–199]:

$$\log(\xi_{Q,\chi}) \propto \log(\chi). \tag{2.36}$$

However, in practice, this scaling behavior can also be found in *gapped* systems when the true correlation length ξ, which dictates the exponential decay and is inversely related to

the energy gap, greatly exceeds ξ_χ. This makes it difficult to distinguish the Luttinger and Luther-Emery liquids discussed above, especially in scenarios where the latter has a very small spinon gap, as both may appear to show algebraic scaling of $\xi_{1e,\chi}$. Nevertheless, even in such cases, the two could be distinguished by making use of standard arguments in the finite entanglement scaling theory of matrix product states [197–199]. In particular, when the MPS is attempting to capture a fully gapless state like the Luttinger liquid, ξ_χ is the only length scale present in the correlations of the state. As such, we expect correlation functions of charge Q operators will decay with a correlation length $\xi_{Q,\chi} = a_Q \xi_\chi$, where a_Q (at asymptotically large χ) is a constant of proportionality that does not depend on bond dimension. For the Luttinger liquid, this leads to the sharp prediction that ξ_{2e}/ξ_{1e} approaches a constant as $\chi \to \infty$. This contrasts with the Luther-Emery liquid, in which ξ_{2e}/ξ_{1e} is expected to diverge.

In summary, to demonstrate the existence of superconductivity in cylinder iDMRG, one must in principle perform a double scaling analysis. At each fixed circumference, the state must approach a Luther-Emery liquid, characterized by algebraic correlations of charge-$2e$ operators and the divergence of ξ_{2e}/ξ_{1e} with bond dimension. In addition, in principle, one must show that the exponent of algebraic decay for charge-$2e$ operators goes as $\eta(L_y) \to 0$ as $L_y \to \infty$. However, since increasing the cylinder circumference results in exponential scaling of the simulation complexity, cylinder iDMRG studies can typically only demonstrate convergence to a Luther-Emery liquid for a few, relatively small circumferences [200–204].

Bond Dimension Scaling

We begin by providing strong numerical evidence for Luther-Emery liquid physics at $L_y = 5$ by performing a careful scaling in the bond dimension. We work at fixed hole doping $\nu = 2-1/5$ and at parameters $(g, U_1) = (0.15, 1.5)$, choosing for the moment to set $U_2 = 0$, though we emphasize that our results are robust to the inclusion of further repulsive interactions (as we illustrate in Subsection 2.4). As discussed above, we must demonstrate that the ground state exhibits algebraically-decaying correlation functions of charge-$2e$ operators. To this end, we work in the computational basis of fermions defined in Eq. (2.27) and introduce the following set of zero y-momentum charge-$2e$ operators:

$$\hat{\Delta}^\dagger_{\alpha\beta}(x; \delta x, k_y) = \hat{\varphi}^T\Big(x + \frac{\delta x}{2}, k_y\Big) s^\alpha l^\beta \hat{\varphi}\Big(x - \frac{\delta x}{2}, -k_y\Big), \tag{2.37}$$

where x is the center of mass position of the holes, δx is their relative position,[6] and $\alpha, \beta \in \{0, x, y, z\}$. We then consider correlation functions of such operators:

$$C_{\alpha\beta}(x, k_y) = N_{2h}^{-1} \langle \hat{\Delta}^\dagger_{\alpha\beta}(x; 0, k_y) \hat{\Delta}_{\alpha\beta}(0; 0, k_y) \rangle, \tag{2.38}$$

which we choose to normalize by the average number of available hole pairs $N_{2h} = |2 - \nu|/2$. This correlation function is shown in Fig. 2.4(a) for $k_y^{L_y=5} = 4\pi/5$ and $\alpha\beta = xx$. As the

[6] Here, δx is implicitly assumed to be even. For odd δx, we instead take the holes to be at $x + (\delta x + 1)/2$ and $x - (\delta x - 1)/2$ (see Appendix A).

bond dimension increases, the correlation length increases and C_{xx} approaches a power law (the dashed straight line on the log-log scale), signaling the onset of algebraic order. To gain further quantitative confirmation, we perform a scaling collapse of the form

$$C^{(\chi)}_{xx}(x, k_y) = \xi^{-\eta}_{2e,\chi}\, g_{xx}(x/\xi_{2e,\chi}, k_y), \tag{2.39}$$

where $C^{(\chi)}_{xx}$ is the correlation function Eq. (2.38) at bond dimension χ and $\xi_{2e,\chi}$ is its correlation length. This scaling collapse, shown in Fig. 2.4(b), is achieved with a power law exponent $\eta(L_y = 5) = 1.3 \pm 0.2$. This data confirms the existence of algebraic long-range order in $2e$ pair correlations at fixed L_y.

In addition, we demonstrate that the behavior of the $1e$ correlations is consistent with a Luther-Emery liquid and not a Luttinger liquid (see Sec. 2.4 for the distinction). To do so, we investigate the ratio $\xi_{2e,\chi}/\xi_{1e,\chi}$ as a function of bond dimension, which we plot in the inset of Fig. 2.4(b). We find that the ratio increases rapidly with bond dimension which, per the discussion of Sec. 2.4, is inconsistent with the behavior of a Luttinger liquid and suggests a gap in the $1e$ sector. In fact, employing the recently developed methods of Refs. [199, 205], we obtain an extrapolated, and clearly finite, value $\xi^{-1}_{1e,\infty} = 0.11$ in units of inverse $4a$, the length of the unit cell. In contrast, $|\xi^{-1}_{2e,\infty}| < 0.003$ is nearly zero, consistent with our above evidence for algebraic order in this charge sector. This demonstrates that the ground state at $L_y = 5$ is a Luther-Emery liquid, the quasi-1D analog of the superconducting phase.

We conclude with some important phenomenological observations about the superconducting correlations. In particular, algebraic long-range order is most dominantly seen in the following pairing channels:

$$s^x l^x,\ s^y l^y, \tag{2.40}$$

appearing with nearly equal strength, as well as the $s^x l^0$ channel, which is notably of much weaker strength. As such, the pairing is between opposite spins and predominantly between opposite layers. The approximately equal strength of the $s^x l^x$ and $s^y l^y$ correlations are a consequence of an approximate $U(1)$ symmetry generated by $s^z l^z$. This symmetry also explains the dominance of inter-layer pairing over $s^x l^0$, which we henceforth ignore. In summary, the dominant condensing pairing channels imply that the superconducting order is due to the condensation of inter-spin, inter-layer hole pairs. We return to this point in Sec. 2.5 in our analysis of the superconducting pairing symmetry.

Circumference Scaling

Having established the presence of a Luther-Emery liquid state at finite circumference $L_y = 5$, we now investigate whether such a state tends to a *bona fide* superconductor in the 2D limit by investigating it at larger circumferences. This investigation is challenging for three distinct reasons. First, as with all DMRG studies, the computational resources required increase *exponentially* with the $2 \times 2 \times L_y$ tensors that wrap around the cylinder. To partially compensate for this scaling, we use parallelized iDMRG for circumferences $L_y = 6, 7$ with bond

dimensions up to $\chi = 12288$. As a remark, compared to the Fermi-Hubbard model at the same L_y, our projected four-flavor model has twice as many degrees of freedom, making it vastly more expensive to simulate. Second, since the electronic filling must be commensurate with the periodicity of the MPS, we are limited to the circumference-dependent densities $\nu = 2 - 1/L_y$.[7] This makes it difficult to directly compare the physics at each circumference. Finally, we will later show in Sec. 2.5 that the superconductor pairs holes at an emergent Fermi surface (or more accurately Fermi points at finite circumference). Crucially, the number and location of Fermi points vary significantly for small and accessible L_y and, unlike in the Hubbard model, are non-monotonic in cylinder circumference (see Appendix A). This makes studying the approach to the 2D limit particularly challenging in our model. Nevertheless, in what follows we analyze the superconducting correlations for each accessible circumference, ensuring that the MPS truncation error is 3×10^{-5} or better at each bond dimension. Ultimately, we find signatures of large pair correlations at $L_y = 6, 7$ but are unable to rule out the possibility of a Luttinger liquid at these circumferences.

We first determine whether the states we find are gapless in the charge-$2e$ sector by examining correlation functions of the form Eq. (2.38). These are plotted in Fig. 2.4(a) at all three circumferences in the $\alpha\beta = xx$ channel, with the larger two L_y vertically offset for display, and taken at $k_y^{L_y=6} = -2\pi/3$ and $k_y^{L_y=7} = -2\pi/7$. Evidently, at each circumference, these correlations become algebraically long-ranged with increasing bond dimension. The exponents of algebraic decay are then extracted by collapsing under a scaling hypothesis analogous to Eq. (2.39) and are shown in Fig. 2.4(c) for each circumference and for each of the dominant superconducting channels. We find a quantitative decrease in $\eta(L_y)$ as L_y increases for the xx and yy channels, consistent with the superconducting expectation that $\eta(L_y) \to 0$ as $L_y \to \infty$. For the $x0$ channels, the superconducting correlations at $L_y = 6$ are found to have a quantitatively different exponent and behavior as compare with the other; we comment in Appendix A that this coincides with it having a different pairing symmetry in the $x0$ channel at $L_y = 6$.

Next, we investigate the behavior of the $1e$-correlations, which we find to be more subtle and ultimately inconclusive. We provide the core results here and give further details in Appendix A. Recall that our previous analysis of $L_y = 5$ found that these charge-$1e$ correlations remained exponentially decaying even as $\chi \to \infty$. This was evidenced by the growth of ξ_{2e}/ξ_{1e} and by performing a systematic extrapolation [199, 205] to infinite bond dimension that revealed a non-zero inverse correlation length $\xi^{-1}_{1e,\infty}(L_y = 5) \approx 0.11$. The charge-$2e$ and $1e$ correlations therefore both matched the expectations for a Luther-Emery liquid, Eqs. (2.34, 2.35), at $L_y = 5$. This conclusively identified the $L_y = 5$ ground state as a quasi-1D superconductor.

At larger circumferences, however, the situation is less clear. At $L_y = 6$, we find that the behavior of the $1e$-correlations does not conclusively point to either a Luttinger liquid or a Luther-Emery liquid. On the one hand, we find that the magnitude of ξ_{2e} is nearly

[7] Since $L_y = 5, 6, 7$ are coprime, prohibitively large unit cells would be required to have equal fillings at each circumference.

2.5 times larger than ξ_{1e} at $\chi = 12288$, indicating large superconducting pair correlations in the state. This is suggestive of a Luther-Emery liquid. On the other hand, we find that ξ_{2e}/ξ_{1e} is roughly constant with bond dimension, which fails to exclude a Luttinger liquid. Generally, at this circumference, we conclude that the finite-bond dimension state is too far from a 'scaling limit' to properly differentiate the two possibilities. This is evidenced by extrapolating $\xi^{-1}_{1e/2e,\infty}(L_y = 6)$ using the method detailed in Ref. [205] and finding that we are too far from convergence to obtain sensible (e.g. non-negative) values of these quantities.

We conclude by discussing the case of $L_y = 7$. Here, unlike the previous two cases, we find that ξ_{2e} is only slightly larger than ξ_{1e} with a ratio ξ_{2e}/ξ_{1e} that remains relatively constant across the largest bond dimensions we can access. As such, at this circumference, both correlation lengths appear to diverge as a function of bond dimension, though much larger bond dimension would be required for a more definitive determination. Hence, there is little evidence in direct support of a Luther-Emery liquid over a Luttinger liquid. Indeed, the two may exhibit similar behavior when the finite-χ correlation length is too small to resolve the charge gap (see Sec. 2.4). Altogether, this highly circumference-dependent behavior prevents us from drawing firm conclusions about the 2D phase.

Robustness of the Superconducting Phase

Restricting to $L_y = 5$, where our detailed bond-dimension-scaling analysis conclusively demonstrated the existence of a superconductor, we now evaluate the extent and robustness of the finite-circumference superconducting phase. To do so, we use a heuristic, but nonetheless principled, diagnostic of superconductivity that enables detailed investigation of the double Hofstadter phase diagram with the available computation resources. We find that the superconductor appears exclusively upon doping the LAF insulating state at $\nu = 2$ and that it is nearly maximally LAF polarized, leading us to posit that the LAF insulator is the parent state of the superconductor. Moreover, the superconducting phase is found to exist across a broad range of hole densities $\nu < 2$ and is, rather surprisingly, substantially resilient to additional repulsive interactions, namely those between the layers and at a longer range.

Our diagnostic consists of examining the scaling of ξ_{2e}/ξ_{1e} as a function of bond dimension. In particular, following the discussion of Section 2.4, the bond dimension scaling of this quantity can be used to distinguish a Luther-Emery liquid from a Luttinger liquid or any fully gapped quasi-1D phase. In our numerics, we label portions of the phase diagrams "superconducting" if the ratio ξ_{2e}/ξ_{1e} is both increasing as a function of bond dimension and, in particular, if it has exceeded unity at the largest bond dimension available.

The Superconducting Phase: LAF Coexistence

We now chart the portions of parameter space that host superconductivity at $L_y = 5$. We begin by studying the (g, U_1) plane at a fixed electronic density $\nu = 1.8$ and in the absence of inter-layer interactions. Using the diagnostic described above, superconductivity is found to occupy a broad portion of the strong-coupling regime that hosts the LAF insulator at integer

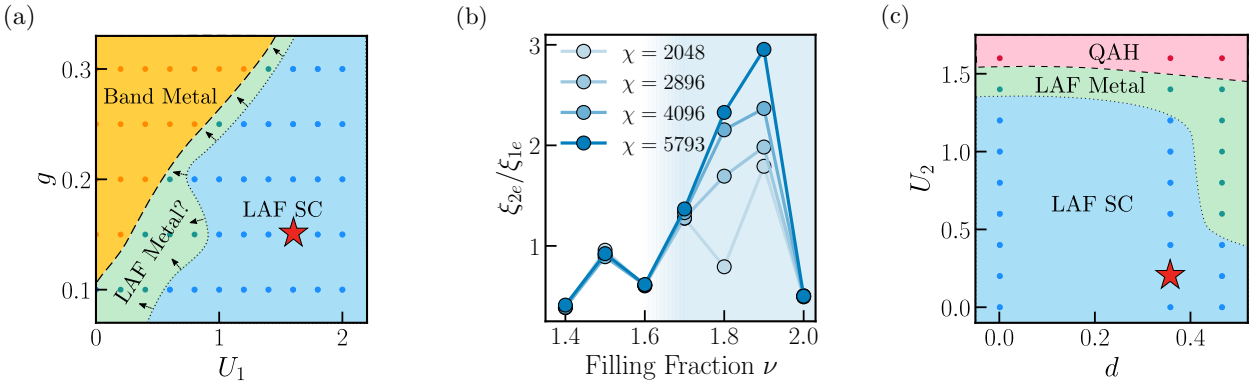

Figure 2.5: **Robustness of the $L_y = 5$ Superconductor.** We investigate the extent of the $L_y = 5$ superconducting phase by examining the ratio ξ_{2e}/ξ_{1e} (see Sec. 2.4 for more details). In panel (a), we depict the phase diagram at $\nu = 1.8$ in the absence of inter-layer repulsion. A robust LAF-polarized superconducting region appears where the LAF order was found at integer filling, suggesting the LAF may be the parent state for the superconductor. We mark, with a star, the point at which the scaling analysis of Sec. 2.4 was performed and remark that the phase competes with a band metal and LAF-polarized metal, the latter of which retreats with increasing bond dimension (see Section 2.4). In panel (b), we fix $g = 0.1$ and $U_1 = 1.8$ and depict our heuristic diagnostic, the growth of the ratio ξ_{2e}/ξ_{1e} vs. χ, as a function of the electronic density $\nu \in [1.4, 2]$. Superconductivity is found across the span $1.7 \lesssim \nu < 2$, with metallic LAF behavior beginning at $\nu = 1.6$. In Appendix A, we show that the system remains LAF-polarized throughout this range, further cementing the LAF as the superconducting parent state. In panel (c), we examine the robustness of our superconductor to additional repulsive interactions. In particular, fixing $(g, U_1) = (0.1, 1.4)$, we chart the phase diagram as a function of inter-layer repulsion U_2 and interaction range d [See Eq. (2.41)]. We find the superconductor is remarkably robust, giving way initially to a LAF metallic phase when U_2 is sufficiently large, and then to a layer-polarized metallic phase when U_2 exceeds U_1. In Appendix A, we performed a scaling analysis similar to that detailed in Sec 2.4 for the point marked with a red star.

filling [see Fig. 2.5(a)]. Intriguingly, the superconductor itself is always found to have sizable coexistent LAF polarization. Moreover, its correlations are most long-ranged in the channels Eq. (2.40), suggesting a consistent pairing symmetry throughout the superconducting phase. On the other hand, in the weak-coupling regime with small U_1, we identify a metallic state with nearly-vanishing LAF polarization, i.e. a band metal. In between these two phases, we observe a metallic state with significant LAF polarization.

Similar to our identification of the LAF phase boundary at $\nu = 2$, we demarcate the transition between the weak-coupling and LAF metallic phases by a dotted boundary corresponding to the largest slope $\partial n^z_{\mathrm{LAF}}/\partial U_1$. In contrast, the boundary between the LAF metallic and superconducting phases is more sensitive to bond dimension, even at the sizable value $\chi = 5793$. This exemplifies a pattern that is pervasive in our numerical data: LAF metallic states commonly undergo a finite-χ transition into the LAF superconducting phase at a bond dimension that depends sensitively on parameters, whereas the reverse is exceedingly rare. As a result, we expect that the set of points that meet the criteria for superconductivity will continue to grow with bond dimension, and that the LAF metallic phase may purely be an artifact of the finite accuracy of our simulations.

The intrinsic coexistence between superconductivity and LAF polarization is further elucidated by tuning the electronic density in the range $\nu \in [1.4, 2]$. To access density increments of 1/10 of a band, we quadruple the MPS unit cell. In Fig. 2.5(b), we plot our diagnostic for the superconducting order—the ratio ξ_{2e}/ξ_{1e} as a function of bond dimension—and find it that indicates the persistence of superconductivity in the range $1.7 \lesssim \nu < 2$. Moreover, in Appendix A, we demonstrate that the system remains substantially LAF-polarized across this parameter regime, with n^z_{LAF} decreasing only linearly in the hole doping. At the remaining parameter points $1.4 \leq \nu \leq 1.6$, we find evidence of metallic correlations and possible translation symmetry-breaking along the x direction, though we caution that a careful circumference scaling analysis would be required to identify the precise nature of this nearby phase. Across the entire range of fillings, and in particular across the superconducting region, we find a persistent LAF polarization that nearly saturates the maximal value ν, i.e., the total density of electrons. This ubiquitous coexistence with LAF order leads us to hypothesize that the LAF insulator is the "parent state" of the superconducting state. We further corroborate this claim in Sec. 2.5 where we identify the superconductor as a weak-pairing instability of holes at the LAF's mean-field Fermi surface.

Stability to Further Repulsive Perturbations

We now show that the superconductor is robust to both large inter-layer repulsion and a finite interaction range. To this end, we replace the microscopic on-site interactions with a longer-range Gaussian, parameterized as:

$$\hat{V} = \sum_{\mathbf{r}} e^{-\frac{|\mathbf{r}-\mathbf{r}'|^2}{2d^2}} : \left[\frac{U_1}{2}(\hat{n}^2_{\mathbf{r}\mathsf{T}} + \hat{n}^2_{\mathbf{r}\mathsf{B}}) + U_2 \hat{n}_{\mathbf{r}\mathsf{T}}\hat{n}_{\mathbf{r}\mathsf{B}}\right] : \tag{2.41}$$

where d specifies the interaction range. In Fig. 2.5(c), we show the extent of the superconducting phase in the (d, U_2) plane at the fixed parameters $(g, U_1) = (0.1, 1.4)$. Remarkably, in spite of the pairing being predominantly inter-layer (see Subsection 2.4), we find the superconductor survives in the presence of substantial inter-layer repulsion $U_2 \sim \mathcal{O}(U_1)$ and is further resilient to simultaneously increasing the range of the interactions. While the superconducting phase is globally identified by using the heuristic diagnostic introduced at the beginning of Sec. 2.4, we cement its existence at $L_y = 5$ in the presence of additional inter-layer repulsion by performing a detailed scaling analysis of the superconducting correlations, analogous to the one performed in Sec. 2.4. We also see indications, via a slow but monotic increase in the ratio ξ_{2e}/ξ_{1e}, that this behavior may persist at $L_y = 6$. These analyses are detailed fully in Appendix A and are performed at the parameter point $(d, U_2) = (0.358, 0.2)$ [marked with a star on Fig. 2.5(c)].

Despite the resilience of the superconducting phase, we find that when d is increased sufficiently, the superconductor gives way to a translation-invariant, LAF-polarized metallic state. Moreover, we remark that increasing U_2 in excess of U_1 induces a transition out of the LAF phase into a layer-polarized, translation-invariant metal that originates from the $\nu = 2$ QAH insulator.

Stability to Changing the Zeeman Field

We conclude by remarking briefly on the influence of the Zeeman field B_z [Eq. (2.28)]. Recall that this weak pinning field is necessary in order to stabilize LAF polarization, which otherwise disorders due to the quasi-1D cylinder geometry (see Section 2.3). Though the bulk of our calculations are performed at the fixed value $B_z = 10^{-2}$, a scan of the Zeeman field reveals superconductivity at values as small as $B_z = 10^{-3}$. For comparison, the bandwidth, the inter-layer tunneling and average interaction energy per electron are of order 10^{-1}. At some larger values of B_z, we encounter numerical errors in the limit of only in-layer Hubbard interactions, i.e., $U_2 = d = 0$, though we find that enlarging the MPS unit cell greatly improves convergence and favors a translation-invariant LAF metallic state. On the other hand, no convergence issues are encountered at the finite values $(U_2, d) = (0.2, 0.466)$, at which superconductivity appears to persist up to $B_z = 0.1$. Additional details and numerical data are provided in Appendix A.

2.5 Emergent Weak-Pairing Description of the Superconductor

We now turn to characterizing the superconducting order reported in the previous section. We do so by examining the so-called *pair wavefunction* [121]:

$$\Delta_{\alpha\beta}(\mathbf{k}) = \langle \hat{\varphi}^T(\mathbf{k}) s^\alpha l^\beta \hat{\varphi}(-\mathbf{k}) \rangle \equiv \langle \hat{\Delta}^\dagger_{\alpha\beta}(\mathbf{k}) \rangle, \tag{2.42}$$

where we refer to the two-hole operator, colloquially, as the *Cooper pair* operator. In Sec. 2.5, we introduce a novel technique to probe this quantity in iDMRG numerics, which may be applied to a variety of 2D systems. By examining $\Delta(\mathbf{k})$ across the Brillouin zone in Sec. 2.5, we find that it peaks at specific locations that coincide with the Fermi surface of non-interacting holes above the LAF insulator predicted within self-consistent Hartree-Fock. This phenomenology is characteristic of a (BCS-like) superconducting state formed from the pairing of holes near this LAF Fermi surface. We emphasize that this weak-pairing phenomenology emerges in a context where the interaction scale is the largest energy scale present and is found via non-perturbative iDMRG numerics that do not presuppose a mean-field description of the state.

Moreover, the emergent mean-field description enables us to characterize other phenomenological features of the superconductor. In particular, in Sec. 2.5, we use the pair wave function (2.42) to uniquely characterize the pairing symmetry of the superconductor and find that, among other symmetry indices, it is p-wave. Finally, in Sec. 2.5 we leverage results from BCS theory to heuristically estimate the transition temperature of the superconducting state.

Numerically Probing the Superconducting Pair Wavefunction

The definition of the pair wavefunction (2.42) implicitly assumes that the ground state wavefunction is a superconducting condensate in which the number of Cooper pairs in the ground state wavefunction is uncertain. This presents an obstacle to extracting this quantity in our iDMRG calculations, as $U(1)$ particle number conservation causes $\Delta(\mathbf{k})$ to vanish uniformly. Here, we provide an account of how to circumvent this difficulty. Broadly, we do so by introducing a *proxy* pair wavefunction $\widetilde{\Delta}_{\alpha\beta}(\mathbf{k})$ that can be extracted within iDMRG and is proportional to $\Delta_{\alpha\beta}(\mathbf{k})$. Readers more interested in our physical results may skip to the next subsection where this quantity is used to probe the structure and pairing symmetry of the superconductor.

In the $L_y \to \infty$ limit, the definite $U(1)_Q$ charge of the iDMRG ground state implies that it will fail to satisfy cluster decomposition, defined as [206]:

$$\lim_{|\mathbf{r}|\to\infty} \Big(\langle \hat{\Delta}^\dagger(\mathbf{r}) \hat{\Delta}(0) \rangle - \langle \hat{\Delta}^\dagger(\mathbf{r}) \rangle \langle \hat{\Delta}(0) \rangle \Big) = 0 \tag{2.43}$$

As a result, long-range superconducting order [defined in Eq. (2.33)], does not imply a finite expectation value of the Cooper pair operator. Nevertheless, let us assume that there exist cluster decomposition-satisfying ground states $|\varphi\rangle$ of the 2D superconducting manifold for which

$$\lim_{|\mathbf{r}|\to\infty} \lim_{L_y\to\infty} \Big(\langle \hat{\Delta}^\dagger(\mathbf{r}) \hat{\Delta}(0) \rangle_{\psi(L_y)} - \langle \hat{\Delta}^\dagger(\mathbf{r}) \rangle_{\varphi} \langle \hat{\Delta}(0) \rangle_{\varphi} \Big) = 0, \tag{2.44}$$

where $\langle \cdots \rangle_a = \langle a | \cdots | a \rangle$ and $|\psi(L_y)\rangle$ is the iDMRG ground state at circumference L_y.

The pair wavefunction can then be extracted numerically as follows. First, we define the *proxy* pair wavefunction by the following correlation function:

$$\widetilde{\Delta}_{\alpha\beta,x,p_y}(\mathbf{k}) = \langle \hat{\Delta}^\dagger_{\alpha\beta}(0;\mathbf{k})\hat{\Delta}_{\alpha\beta}(x;0,p_y)\rangle_{\psi(L_y)}. \tag{2.45}$$

Here $\hat{\Delta}_{\alpha\beta}(x;0,p_y)$ is as defined in Eq. (2.37), while the $\hat{\Delta}^\dagger$ term is defined by a Fourier transform in the relative position coordinate:

$$\hat{\Delta}^\dagger_{\alpha\beta}(x;\mathbf{k}) = \sum_{\delta x} \hat{\Delta}^\dagger_{\alpha\beta}(x;\delta x,k_y)e^{ik_x\delta x}, \tag{2.46}$$

which, when averaged over the center of mass x, is equal to the Cooper pair operator defined in Eq. (2.42).

The proxy pair wavefunction—which need not vanish in $U(1)$-conserving iDMRG since it involves the expectation value of a charge-neutral operator—should be thought of as a function of $\mathbf{k}$ (with fixed parameters x and p_y). Provided that we consider translationally-invariant states and take x to be larger than both the characteristic size of the Cooper pair (the "coherence length") ξ_{SC} and the connected correlation length ξ, then for sufficiently large L_y we expect that:

$$\widetilde{\Delta}_{\alpha\beta,x,p_y}(\mathbf{k}) = C^{\alpha\beta}_{x,p_y}\langle \hat{\Delta}^\dagger_{\alpha\beta}(\mathbf{k})\rangle_\varphi + \mathcal{O}\left(e^{-|x-\xi_{\mathrm{SC}}|/\xi}\right), \tag{2.47}$$

where the prefactor is a $\mathbf{k}$-independent constant and $|\varphi\rangle$ is a cluster decomposition-satisfying superconducting ground state of the 2D system. As such, by examining the proxy pair wavefunction $\widetilde{\Delta}(\mathbf{k})$ as a function of momentum, we gain direct insight into the structure of the true pair wavefunction $\Delta(\mathbf{k})$.

Emergent Weak Pairing at the LAF Fermi Surface

In this section, we demonstrate that our superconductor arises from the momentum space "BCS" pairing of holes above the LAF insulator. To be explicit, we will provide evidence that this emergent weak-pairing picture occurs as a two-step process. First, strong interactions select LAF-polarized ground states, even in the presence of hole doping. Such "normal" states are well-described by a LAF bandstructure that strongly renormalizes the four non-interacting bands into two valence bands and two conduction bands. Second, holes—initially occupying a normal LAF metallic state—pair at the renormalized Fermi surface, triggering a superconducting instability. Before continuing, we emphasize once again that this weak-pairing picture emerges in a setting where repulsive interactions are the dominant energy scale.

As preliminary evidence for this picture, we plot the density of electrons in the superconducting state as a function of momentum [see Fig. 2.6(a)], finding that the density is depleted in localized "pockets" of momentum space but is otherwise uniform. To understand the origin of these disconnected Fermi surfaces, we examine the mean-field band structure of the

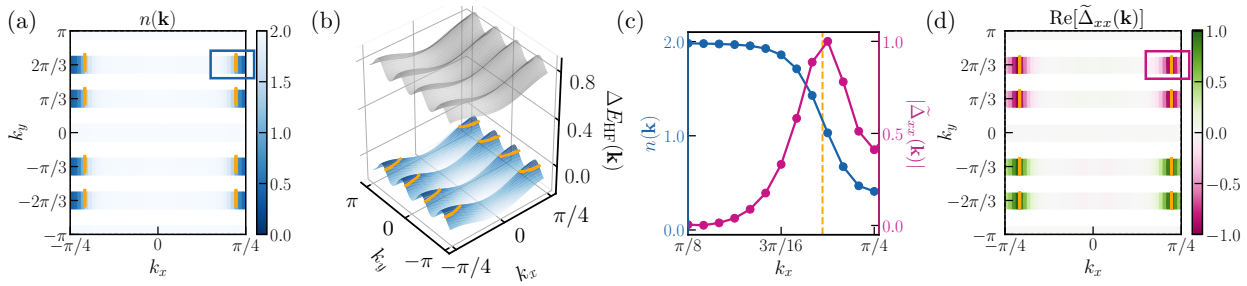

Figure 2.6: **Evidence for Weak Pairing at the LAF Fermi Surface.** (a) The electronic density of the putative superconducting iDMRG groundstate for the $L_y = 6$ cylinder, shown here at $\chi = 12288$ and $(g, U_1, \nu) = (0.15, 1.5, 2 - 1/6)$, is uniform in the majority of the Brillouin zone but sharply depleted in isolated regions. The locations of these drops in the density match the mean-field Fermi surface of non-interacting holes above the LAF insulating state, marked in orange (in all subplots) and obtained using self-consistent Hartree-Fock (SCHF). In (b), we plot the SCHF band structure computed at $\nu = 2$ on 48×48 unit cells. The energy ΔE_{HF} of the two-fold degenerate valence band is shaded in blue and defined relative to the valence band edge. For small hole-doping away from $\nu = 2$, the Fermi surface (shown in orange) consists of four disconnected pockets. As SCHF enforces electronic $U(1)$ (disallowing pairing), this strongly-interacting effective bandstructure is a metallic "parent state" for superconductivity. In (c), we zoom into one particular pocket—specified by blue and magenta boxes in (a) and (d), respectively—and plot both the electronic density (left axis) and the proxy pair wavefunction Eq. (2.45) (right axis) obtained from iDMRG. The former drops off rapidly, while the latter sharply peaks, precisely at the location of the SCHF Fermi surface, strongly suggesting that the superconductor arises from a weak-pairing instability upon hole-doping the $\nu = 2$ insulating LAF state. Panel (d) gives a global view of the proxy pair wavefunction, whose real part is orders of magnitude larger than its imaginary part. From its sign structure, we deduce the unconventional pairing symmetry of the superconductor, namely that it is p-wave and is phenomenologically consistent with a Bogoliubov gap function $\delta(\mathbf{k}) \sim \sin(k_y)(s^+ l^+ + s^- l^-)$.

LAF insulator computed using standard (see e.g. [31]) self-consistent Hartree-Fock (SCHF). We show these bands in Fig. 2.6(b), with the lower two degenerate bands corresponding to the occupied electronic states of the LAF insulator and the upper two degenerate bands corresponding to the spectrum of gapped single-electron excitations above the LAF. At lowest order in g, these two sets of bands are merely the bare Hofstadter bands, but massively split by the interaction scale. In Fig. 2.6(a,b), we mark the Hartree-Fock Fermi energy at filling $\nu = 1.8$ with orange lines, finding that their locations coincide closely with drops in the iDMRG electronic density.

To further corroborate the BCS picture described above, we examine the structure of the pair wavefunction, Eq. (2.42). We first lay out our expectations. If BCS theory was applicable, we would expect the pair wavefunction to be related to the Bogoliubov gap $\delta_{\alpha\beta}(\mathbf{k})$ by

$$\Delta_{\alpha\beta}(\mathbf{k}) = \frac{\delta_{\alpha\beta}(\mathbf{k})}{2\sqrt{(E_{\mathrm{HF}}(\mathbf{k}) - E_F)^2 + \delta^2_{\alpha\beta}(\mathbf{k})}}, \tag{2.48}$$

where $E_{\mathrm{HF}}(\mathbf{k})$ is the dispersion of holes above the normal LAF state—corresponding to the Koopman spectrum of hole excitations in self-consistent Hartree-Fock—and E_F is the Fermi level. Generally, we expect the superconducting gap $\delta_{\alpha\beta}$ to be smaller than the characteristic scale of the dispersion, namely the bandwidth. Within the validity of BCS mean field theory, we would therefore expect Eq. (2.48) to vanish sufficiently far from the Fermi surface. On the other hand, the pair wavefunction would peak at the Fermi surface, at which it would be proportional to the phase of the gap function: $\Delta_{\alpha\beta}(\mathbf{k}) = \delta_{\alpha\beta}(\mathbf{k})/2|\delta_{\alpha\beta}(\mathbf{k})|$.

These expectations are borne out in our iDMRG numerics. In particular, in Fig. 2.6(c,d) we plot the proxy pair wavefunction (2.45) and find that it peaks precisely at the Fermi surface and decays quickly away from it. In Fig. 2.6(c), we zoom into one Fermi pocket and observe excellent agreement between the Fermi surface predicted from Hartree-Fock, the location at which the charge density drops off in iDMRG, and the peak in the proxy pair wavefunction. In Fig. 2.6(d), we plot the latter over the Brillouin zone and find that its magnitude is maximal at each of the four disconnected Hartree-Fock Fermi surfaces, providing further evidence that the superconductor arises as an instability of the LAF Fermi surface. We leave the analysis and interpretation of the relative complex phase of $\Delta_{\alpha\beta}(\mathbf{k})$ to the next subsection.

Pairing Symmetry

In what follows, we characterize the pairing symmetry of the superconducting state by using the proxy pair wavefunction $\widetilde{\Delta}(\mathbf{k})$. To be precise, the pairing symmetry corresponds to the irreducible co-representation—the generalization of a representation to incorporate anti-unitary symmetries—of the magnetic space group under which the pair wavefunction transforms [121, 124, 207]. In our case, since the Cooper pairs that condense to form the superconductor carry zero total momentum, we need only specify the transformation properties under the discrete rotations C_{2z} and C_{2x}, the non-trivial magnetic translation m_x,

and the anti-unitary spacetime inversion symmetry $\mathcal{I}$ (see Appendix A). Since these operators each square to the identity and mutually commute in the zero-momentum sector, these generators act on Cooper pairs as the group $(\mathbb{Z}_2)^3 \times \mathbb{Z}_2^{\mathsf{K}}$ with anti-unitary $\mathbb{Z}_2^{\mathsf{K}}$. Given that the co-representations of $\mathbb{Z}_2^{\mathsf{K}}$ are trivial, specifying the irreducible representation amounts to identifying three $\mathbb{Z}_2$ characters for each condensed superconducting channel $s^\alpha l^\beta$.

Let $\hat{g}$ be the unitary operator corresponding to a symmetry $g \in \{C_{2x}, C_{2z}, m_x\}$. We define the corresponding characters $\nu_g^{\alpha\beta}$ by [121, 124]:

$$\langle \hat{g}^\dagger \hat{\Delta}_{\alpha\beta}^\dagger(\mathbf{k}) \hat{g} \rangle = \nu_g^{\alpha\beta} \Delta_{\alpha\beta}(\mathbf{k}), \tag{2.49}$$

where $\nu_g^{\alpha\beta} = \pm 1$ and $\alpha\beta$ (no implicit summation) correspond specifically to the dominant condensed channels specified in Eq. (2.40). Intuitively, the characters capture how the pair wavefunction transforms under the application of symmetries on the ground state. More generally, the role of these characters is played by matrices $\boldsymbol{\nu}_g$ that form a co-representation of the magnetic space group (see Appendix A for a more formal and general treatment).

As an illustrative example, we compute the index for $g = C_{2z}$. Its action on our Cooper pairs is given by:

$$\hat{C}_{2z} \hat{\Delta}_{\alpha\beta}^\dagger(\mathbf{k}) \hat{C}_{2z}^{-1} = \hat{\Delta}_{\alpha\beta}^\dagger(-\mathbf{k}). \tag{2.50}$$

In the case $\alpha\beta = xx$, whose proxy pair wavefunction we have plotted in Fig. 2.6(d), we readily observe that $\widetilde{\Delta}_{xx}(-\mathbf{k}) = -\widetilde{\Delta}_{xx}(\mathbf{k})$. From this and Eq. (2.49), we immediately find that:

$$\nu_{C_{2z}}^{xx} = -1 \qquad (p\text{-wave symmetry}). \tag{2.51}$$

We also find that that $\nu_g^{yy} = \nu_g^{x0} = -1$, indicating that all condensed channels are p-wave in nature.

A similar analysis can be performed for the other symmetries. In particular, inspection of the proxy pair wavefunction likewise leads to the conclusion

$$\nu_{C_{2x}}^{\alpha\beta} = \nu_{m_x}^{\alpha\beta} = -1, \tag{2.52}$$

for both dominant pairing channels $\alpha\beta = xx, yy$. Finally, for the anti-unitary symmetry $\mathcal{I}$, our choice of layer-polarized basis guarantees that $\hat{\mathcal{I}} \hat{\Delta}_{\alpha\beta}^\dagger(\mathbf{k}) \hat{\mathcal{I}}^{-1} = \hat{\Delta}_{\alpha\beta}^\dagger(\mathbf{k})$. This implies that the pair wavefunction has a constant phase, assuming that $\mathcal{I}$ remains unbroken in the ground state. Indeed, our numerically-obtained proxy pair wavefunction is found to be purely real.

We conclude by remarking that our numerical observations are consistent with a superconductor whose Bogoliubov gap function $\delta_{\alpha\beta}(\mathbf{k})$ has the same symmetry properties as $\sin(k_y)$ for $\alpha\beta = xx, yy$. Moreover, in Appendix A, we provide numerical evidence that the pair wavefunction in the $\alpha\beta = xx$ channel appears with a relative minus sign compared to the $\alpha\beta = yy$ channel. As such, the symmetry properties of a putative gap function can be summarized as:

$$\delta(\mathbf{k}) \sim \sin(k_y)(s^+ l^+ + s^- l^-). \tag{2.53}$$

Consistent with a parent LAF state, the gap function corresponds to non-unitary pairing with $\delta^\dagger(\mathbf{k})\delta(\mathbf{k}) \propto (1 + s^z l^z)/2 = P_{\mathrm{LAF}}$, the LAF projector. Furthermore, while this form

of the gap function typically implies the presence of symmetry-enforced nodes along the lines $k_y = 0, \pm\pi$, our superconductor instead remains gapped. This is because the Fermi surface at which pairing occurs is disconnected and does not intersect either of these lines in momentum space (see Fig. 2.6).

Estimate of Transition Temperature

The weak-pairing picture for the superconducting state, advocated for above, provides a heuristic framework for estimating the superconducting transition temperature. To this end, we recall that the finite temperature transition out of a $(2+1)d$ superconductor occurs either due to: (i) the loss of phase coherence and algebraically-long-ranged phase correlations, or (ii) the unbinding of Cooper pairs. The former is described by a Berezinskii–Kosterlitz–Thouless (BKT) transition corresponding to the proliferation of vortices in the superconductor and has a transition temperature that is typically upper bounded by the ground state superfluid stiffness ρ_s as [121, 124]:

$$T_c^{\mathrm{BKT}} \lesssim \pi\rho_s/2. \tag{2.54}$$

In contrast, the Cooper pair unbinding transition occurs at a temperature scale set by the maximum Bogoliubov gap δ_{SC} at the Fermi surface [121, 124]:

$$T_c^p \sim \delta_{\mathrm{SC}}. \tag{2.55}$$

With input from self-consistent Hartree-Fock, we can estimate both scales.

In a BCS-like superconductor, the superfluid stiffness at $T = 0$ is set by the density of paired dopants divided by their effective mass, which in two dimensions scales as the Fermi energy [208]. As such,

$$T_c^{\mathrm{BKT}} \lesssim \pi\rho_s/2 \sim \pi E_F/2 \approx 0.03\,t. \tag{2.56}$$

On the other hand, the approximate magnitude of the Bogoliubov gap δ_{SC} can be extracted from the pair wavefunction $\Delta_{\alpha\beta}(\mathbf{k})$. In particular, for momenta around the Fermi surface $\mathbf{k} \approx \mathbf{k}_F$, Eq. (2.48) implies that

$$4\Delta^2_{\alpha\beta}(\mathbf{k}) \approx \frac{\delta^2_{\alpha\beta}(\mathbf{k}_F)}{\delta^2_{\alpha\beta}(\mathbf{k}_F) + v_F^2(\mathbf{k}-\mathbf{k}_F)^2}. \tag{2.57}$$

Here, we made the linear approximation $E_{\mathrm{HF}}(\mathbf{k}) - E_F \approx v_F(\mathbf{k}-\mathbf{k}_F)$, with v_F being the Fermi velocity, and took $\delta_{\alpha\beta}(\mathbf{k}) \approx \delta_{\alpha\beta}(\mathbf{k}_F)$. As such, around the Fermi surface, $4\Delta^2_{\alpha\beta}(\mathbf{k})$ is predicted to have a Lorentzian profile whose half-width-half-maximum is equal to $\delta_{\alpha\beta}(\mathbf{k}_F)/v_F$. Maximizing over the dominant channels $\alpha\beta = xx, yy$ and taking $v_F = 0.17$ obtained from self-consistent Hartree-Fock at $L_y = 5$, we obtain the following estimate for the Bogoliubov gap:

$$T_c^p \sim \delta_{\mathrm{SC}} \approx 0.01\,t. \tag{2.58}$$

In particular, we find that the pair-breaking temperature T_c^p is comparable to or less than the BKT temperature. Though we expect the superconducting transition temperature to therefore be set by the energy scale δ_{SC}, we carefully note the possibility of a BKT-type thermal transition out of the superconducting phase. This is because of a reduction in the condensate fraction (equivalently, the Cooper pair density) at finite temperature due to thermal fluctuations, which can significantly decrease the superfluid stiffness ρ_s as we approach the pair-breaking scale. Consequently, as $T \to T_c^p$, the small value of ρ_s can decrease the cost of vortices and cause them to proliferate, triggering a BKT transition that preempts T_c^p.

2.6 Relation to Chiral Twisted Bilayer Graphene

Thus far, this chapter has focused on theoretically and numerically analyzing the double Hofstadter model: explicating its symmetries and topology, detailing its undoped phase diagram, and arguing for the emergence of a p-wave superconducting state at non-integer filling. Here we elucidate a relationship to moiré materials via a "dictionary" between the degrees of freedom and symmetries of the double Hofstadter model and models of magic-angle TBG.

Recall that we formulated the double Hofstadter model in an effort to explore, in a minimal setting, the interplay between a set of ingredients commonly found in moiré materials. Nevertheless, the presence of both correlated insulating states and unconventional superconductivity in this model, both appearing independently in experimental and theoretical studies of moiré graphene platforms, invites us to make precise the connection to such systems. In this section, we reveal a close structural correspondence with the chiral model of magic-angle twisted bilayer graphene[8] [31, 74, 75, 209].

At the level of their band structures, the similarities between the two models are already striking. In chiral TBG, the low-energy single-particle subspace also consists of energetically narrow bands with $w_2 = 1$ fragile topology in each flavor sector (i.e., valley and spin) and, consequently, hosts two Dirac cones of the same chirality per flavor [24, 68–73]. Furthermore, just as the low-energy bands of the double Hofstadter model are naturally expressed in a Chern basis (2.11) of layer-polarized orbitals, the flat bands of chiral TBG are conveniently described by a basis of graphene sublattice-polarized Chern bands [31].

Going beyond single-particle physics, we will construct an explicit dictionary between the interacting models. To do so, let us first recall some details of the strong-coupling theory of TBG. The narrow bands of TBG are modeled by electrons carrying electronic spin s and valley pseudospin τ, with each electron occupying one of two narrow sublattice-polarized bands labeled by σ, for a total of eight flavors. At the magic angle, these sublattice-polarized bands are exactly flat and the chiral model has a large $U(4) \times U(4)$ symmetry generated by independent spin and valley rotations in each Chern sector [31, 75]. In Fig. 2.7 (Top), we depict the division of the eight flat bands into two $U(4)$-symmetric subspaces with opposite

[8] For a pedagogical review of chiral TBG, we refer the reader to Ref. [32].

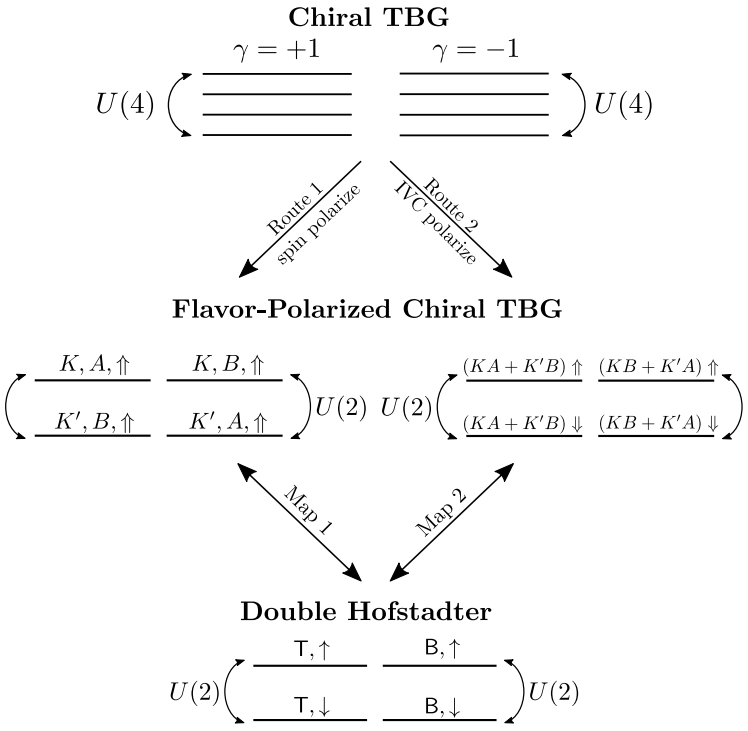

Figure 2.7: **Connection to Chiral Models of TBG.** (Top) Chiral TBG at its magic angle is typically described by a $U(4) \times U(4)$-symmetric model with eight internal states per momentum. These states can be partitioned into two $U(4)$-symmetric four-dimensional subspaces whose wavefunctions carry Chern number $\gamma = \pm 1$. (Middle) Upon flavor-polarizing, this model reduces to a four-band $U(2) \times U(2)$ symmetric model; the $U(2)$'s correspond to independent pseudo-spin rotations in opposite Chern sectors. (Middle, Left) When the flavor that is polarized is the electronic spin, this pseudo-spin roughly corresponds to the valley [See Eq. (2.59)]. (Middle, Right) In contrast, when the electrons polarize into particular intervalley-coherent orbitals, this pseudospin corresponds to the electronic spin [See Eq. (2.60)]. (Bottom) Both $U(2) \times U(2)$ symmetric models can be mapped to the strong-coupling double Hofstadter model [see Eq. (2.15)].

Chern numbers. Since experiments on TBG suggest some degree of flavor polarization in the vicinity of the superconductor (see e.g. [80, 81, 210]), many theoretical works reduce the eight degrees of freedom of the $U(4) \times U(4)$ model to four active flavors. The result is a model with a $U(2) \times U(2)$ continuous symmetry (corresponding to charge conservation and independent rotations of a pseudospin) within each Chern sector $\gamma^z = \sigma^z\tau^z$ [31, 211]. These flavor-polarized models can be mapped explicitly to the double Hofstadter model.

Here, we consider two particular routes to flavor polarization studied in the literature [See Fig. 2.7 (Middle)]. In the first route, the electronic spin is assumed to be fully polarized, and the resulting pseudospin $\boldsymbol{\eta}$ is related to the valley. Each $U(2)$ symmetry is then generated by the electric charge, along with a pseudospin [32]

$$\boldsymbol{\eta} = (\sigma^x\tau^x, \sigma^x\tau^y, \tau^z). \tag{2.59}$$

In the second route, recently posited in Ref. [211], electron-phonon coupling causes the electrons to polarize into particular intervalley-coherent orbitals [See Fig. 2.7 (Middle, Right)]. The resulting pseudospin is then just the electronic spin

$$\widetilde{\boldsymbol{\eta}} = (s^x, s^y, s^z), \tag{2.60}$$

whose components, along with electric charge, similarly serve as generators for each $U(2)$ symmetry.

To map these two flavor-polarized models to the double Hofstadter model, we recall from Sec. 2.2 that the latter has an enhanced $U(2) \times U(2)$ continuous symmetry in the decoupled ($g = 0$) limit. We may then identify the Chern index and pseudospin of the chiral models with the layer and electronic spin of the decoupled double Hofstadter model, respectively:

$$l^z \longleftrightarrow \gamma^z, \qquad \boldsymbol{s} \longleftrightarrow \begin{cases} \boldsymbol{\eta} & \text{(Map 1)} \\ \widetilde{\boldsymbol{\eta}} & \text{(Map 2)} \end{cases}. \tag{2.61}$$

Map 1 and Map 2, summarized in Fig. 2.7 (Bottom), are bijections of both the degrees of freedom and continuous symmetries between the double Hofstadter model and flavor-polarized models of chiral TBG.

This identification extends to the Hamiltonian level. Since the dispersion vanishes at the magic angle in the chiral limit, the projected Hamiltonian $\hat{H}^{\text{TBG}} = \sum_{\mathbf{q}} V_{\mathbf{q}} : \hat{\rho}_{\mathbf{q}}\hat{\rho}_{-\mathbf{q}} :$ with $\hat{\rho}_{\mathbf{q}} = \sum_{\mathbf{k}} \hat{c}^\dagger_{\mathbf{k}}\Lambda^{\text{TBG}}_{\mathbf{q}}(\mathbf{k})\hat{c}_{\mathbf{k}+\mathbf{q}}$ is entirely specified by the form factors Λ^{TBG} [*c.f.* Eq. (2.16)]. Symmetries constrain their matrix structure to be $\Lambda^{\text{TBG}}_{\mathbf{q}}(\mathbf{k}) = F_{\mathbf{q}}(\mathbf{k})e^{i\Phi_{\mathbf{q}}(\mathbf{k})\gamma^z}$ [32]. For the double Hofstader model, the form factors (2.19) in the decoupled limit are $\Lambda_{\mathbf{q}}(\mathbf{k}) = F^S_{\mathbf{q}}(\mathbf{k})e^{i\Phi^S_{\mathbf{q}}(\mathbf{k})l^z}$, which therefore have exactly the same structure. Moreover, departure from the magic angle in chiral TBG introduces a non-zero dispersion $h\gamma^{x/y}$ that hybridizes the two Chern sectors (see Fig. 2.7) [31, 32, 79]. Such a term maps directly onto the inter-layer tunneling $gl^{x/y}$ of the double Hofstadter model.[9] Maps 1 & 2 therefore give an almost term-by-term correspondence in matrix structure between the Hamiltonians.

[9] In the double Hofstadter model, finite inter-layer tunneling g also introduces an $\mathcal{O}(g)$ interaction term from F^A in Eq. (2.19).

The similarities between the Hamiltonians suggest that their ground states may also be analogous. To check this, we apply the above mappings to the LAF ground state at $\nu = 2$. Recall that the LAF state occupies the layer-polarized bands in the pattern:

$$|\text{LAF}\rangle = \quad \begin{matrix} & \mathcal{C}=+1 & \mathcal{C}=-1 \\ |\uparrow\rangle & \bullet\!-\!\bullet\!-\!\bullet\!-\!\bullet & \text{———} \\ |\downarrow\rangle & \text{———} & \bullet\!-\!\bullet\!-\!\bullet\!-\!\bullet \end{matrix} \tag{2.62}$$

Under Map 1, the LAF becomes either the Valley Hall (VH) state or the Kramer's Intervalley Coherent State (KIVC) (which are symmetry-equivalent in chiral TBG). Strikingly, these are the ground states of the strong coupling model of chiral TBG at $|\nu| = 2$ [31, 75]. Under Map 2, the LAF instead corresponds to the "TIVC-QSH" state, which has intervalley coherence and forms a spontaneous quantum spin Hall insulator in the microscopic electronic spin. Studies of TBG where electron-phonon terms favor the relevant flavor polarization of Route 2 indeed find a TIVC-QSH ground state [211]. The LAF therefore maps to ground states of flavor polarized models of TBG. This is remarkable. Indeed, this suggests that the double Hofstadter model—which minimally incorporates the ingredients introduced in Sec. 2.1—may yield valuable conceptual insight into the interacting phenomena present in chiral TBG.

We conclude this section by highlighting notable differences between chiral TBG and the double Hofstadter model. Manifestly, the unit cells are quite different: hexagonal with C_{6z} symmetry for unstrained TBG, versus rectangular in the double Hofstadter model.Chiral TBG also has an exact particle-hole symmetry [32], whereas particle-hole is only approximately satisfied in the lowest-band-projected double Hofstadter model, becoming exact only in the $q \to \infty$ limit. Another obvious difference lies in the interactions, which are local in the double Hofstadter model but longer ranged (screened Coulomb) in models of TBG. While the range of interactions is expected to affect the energetics of excitations above the aforementioned insulating ground state [57], the relevance of the different discrete symmetries is less obvious and requires further investigation.

However, the key difference between the two models lies in the gauge-invariant properties of the Bloch wavefunctions [212]. These include the Berry curvature, or more generally the "quantum geometry" (reviewed in [32, 89]), and determine numerous physical quantities like the interaction-generated (Hartree-Fock) dispersion [31]. A key feature of TBG is that all these quantities are sharply concentrated near the Γ point, which is known to strongly affect the ground state phenomenology (see e.g. [213–216]). In the double Hofstader model, by contrast, these quantities are distributed almost uniformly across the Brillouin zone, and the quantum geometry is much closer to an ideal "vortexable" limit [217] (comparable to TBG at a chiral ratio $w_0/w_1 \sim 0.3$; details in Appendix A). Incorporating such an inhomogeneity into the double Hofstadter model could help gain a "bottom-up" view of the phenomenology of TBG and is an interesting direction for future research. Nevertheless, given that experiments in magic-angle TBG [218] and its multi-layer generalizations [141] point towards nodal pairing [219], the emergence of p-wave unconventional superconductivity

in the related double Hofstadter model makes it a valuable departure point to explore pairing in more realistic moiré models.

2.7 Discussion

In this chapter, we introduced the double Hofstadter model, a simple lattice model featuring strong repulsive interactions, narrow topological bands, and time-reversal symmetry. By using state-of-the-art cylinder iDMRG, we investigated the ground state phase diagram of this model. We found strong numerical evidence for the existence of a robust p-wave superconductor at circumference $L_y = 5$ upon hole-doping a quantum spin Hall (QSH) insulator appearing at half-filling of the flat band subspace. This correlated insulator, which we termed the Layer Anti-Ferromagnet (LAF), has opposite spin polarization in opposite, time-reversal-related Hofstadter layers. Using a novel technique for probing the gap function of the superconducting condensate, we deduced both its pairing symmetry and characterized it as a "BCS"-like superconductor comprised of Cooper pairs near the mean-field LAF Fermi surface. We also presented an experimental blueprint for implementing the double Hofstadter model in near-term optical lattice setups and elucidated a close correspondence to chiral models of twisted bilayer graphene (TBG).

Before discussing our work in a broader context, we comment on the extent of our evidence for superconductivity and routes toward a more definitive verification. Recall that our results were enabled by exploiting recent developments in the compression of matrix product operators [170], extensive parallelization, and working at the largest accessible bond dimensions. Although this enabled us to find definitive superconducting signatures at $L_y = 5$, the story at the larger circumferences, though promising, remains unclear. Indeed, this is a consequence of a fundamental limitation of the cylinder iDMRG method, namely the exponential complexity of scaling the circumference. An important and interesting direction for future work is to more conclusively demonstrate superconductivity in the 2D limit, either by developing new numerical methods to enable larger scale exploration *within* cylinder iDMRG, or by developing and utilizing *intrinsically* 2D numerical methods [220].

Caveats aside, one of the most intriguing features of this superconducting state is the persistence of superconductivity down to a very small LAF Zeeman pinning field, Eq. (2.28). While we introduced this as a numerical convenience—namely for stabilizing the LAF phase—its numerical value in this study is smaller than all other microscopic energy scales. It is therefore likely that superconductivity is stabilized in the absence of any Zeeman field. In this limit, the LAF is a *spontaneous* symmetry-breaking state whose various low-energy fluctuations may play an essential role in the pairing mechanism.

This phenomenological feature of the model suggests intriguing connections to previous literature on superconductivity in doped, spontaneous QSH systems [221, 222] and important qualitative difference from prior numerical studies of superconductivity in models where the spin rotational symmetry is broken explicitly by strong spin-orbit coupling, e.g., interacting Kane-Mele systems [223–226]. In the former case, superconductivity arises from the conden-

sation of low-lying charge-2e skyrmions of the QSH order parameter. A recent microscopic treatment of this mechanism demonstrated pairing within a purely repulsive model, which was proposed as a theory for superconductivity in TBG [79, 168, 227]. The skyrmion mechanism was studied numerically both in coupled opposite-field Landau levels using iDMRG [168] and in models with effective local interactions amenable to QMC simulation [228, 229], as well as within effective field theory approaches [169].

An interesting future direction would be to study the relationship between a skyrmion superconductor and that which we have presented here. In particular, while we have argued that our superconductor is "BCS"-like and is phenomenologically consistent with the weak pairing of holes at a Fermi surface, a skyrmion superconductor is, in its simplest manifestation, formed from tightly-bound, bosonic skyrmion "molecules." Interpolating between these limits, for instance through spin polarons or baby skyrmions, is an active area of research [230, 231]. In the case where both superconductors have p-wave pairing symmetry, such a transition could constitute a novel realization of the p-wave BCS-BEC phase transition [232, 233].

Given that topology plays an essential role in a skyrmion superconductor by imbuing individual skyrmion textures with electric charge, it is important to understand the extent to which the weak-pairing superconductor presented here depends on the topology of its parent state. For instance, one can imagine modifying the single-particle problem so that the low-energy bands are exponentially Wannierizable but the spread of these Wannier functions is sufficiently broad to favor a spontaneous—but topologically trivial—LAF insulating state [183]. One could determine whether superconductivity still manifests in this context and whether it is similarly robust.

Finally, we further remark on routes to experimentally realizing the double Hofstadter model, both in solid-state and cold-atom settings. In the main text, we highlighted a precise mapping to the degrees of freedom of chiral TBG, but also commented on how these systems may differ energetically. Given these differences, an interesting direction of future research would be to identify solid-state materials that realize double Hofstadter systems more faithfully, for instance in the family of moiré TMDs. While our study primarily sought to understand zero-temperature behaviors, directly accessing ground state physics in cold atom quantum simulators remains an outstanding challenge. Namely, experiments typically either remove entropy by coupling to finite-temperature thermodynamic reservoirs [154, 234] or indirectly probe the ground state through quasi-adiabatic state preparation [157]. These obstacles motivate a systematic exploration of both the finite-temperature equilibrium phenomenology of the double Hofstadter model (e.g., applying the insights developed in Ref. [235]), as well as non-equilibrium dynamical state preparation in this system, which has the potential to drastically influence the observed order [236].

Chapter 3

Chiral Spin Liquid and Quantum Phase Transition in the Triangular Lattice Hofstadter-Hubbard Model

The Kalmeyer-Laughlin chiral spin liquid (CSL) is one of the earliest and most important examples of a topologically-ordered quantum state [37, 38, 111] and has been extensively studied in the context of spin models [82, 117, 237, 238]. Recently, considerable effort has been devoted to identifying electronic settings in which the CSL may emerge [107, 108, 110, 118, 119, 239–245]. These studies set the stage for the investigation of charge fluctuation-driven transitions out of the CSL phase into other phases such as metals [107], superconductors [246], exotic charge-density waves [247], and quantum Hall states [118, 248].

The triangular Hofstadter-Hubbard model is thought to host both conventional and CSL electronic phases in the regime of strong orbital magnetic flux [104–106, 109, 116, 117, 249, 250]. It is parameterized by an on-site interaction U and single-particle hoppings of magnitude t and phases consistent with a magnetic flux of $\Phi_\triangle$ per triangular plaquette (see Fig. 3.1a). When $\Phi_\triangle = \pi/2$, this system realizes a spin-singlet integer quantum Hall (IQH) insulator at small U and density of one electron per site, with $\sigma_{xy} = 2e^2/h$. At very large U, the state is a non-topological Mott insulator with a large charge gap, 120° antiferromagnetic (AF) order, and gapless spin excitations described by a nearest-neighbor Heisenberg exchange coupling of magnitude $\sim t^2/U$.

A qualitative argument for the existence of an intermediate CSL phase is that the leading correction to the large-U Heisenberg spin Hamiltonian is a chiral term $S\cdot S\times S$ with coefficient $J_\triangle \sim t^3 \sin\Phi_\triangle/U^2$, which explicitly breaks both time-reversal and parity symmetry and favors a CSL state [104–106, 116, 117, 250, 251]. Very recently, Kuhlenkamp *et al.* presented cylinder iDMRG evidence of this intermediate CSL phase starting from $U \gtrsim 8.5t$ at flux $\Phi_\triangle = \pi/3$ and $U \gtrsim 10.5t$ at $\Phi_\triangle = \pi/2$ [118].

The nature of the IQH-CSL transition, however, is not well understood. Parton mean field theories have been proposed for square lattice and honeycomb systems [248, 252]. Beyond this, there has been very little direct investigation into the nature of the putative critical

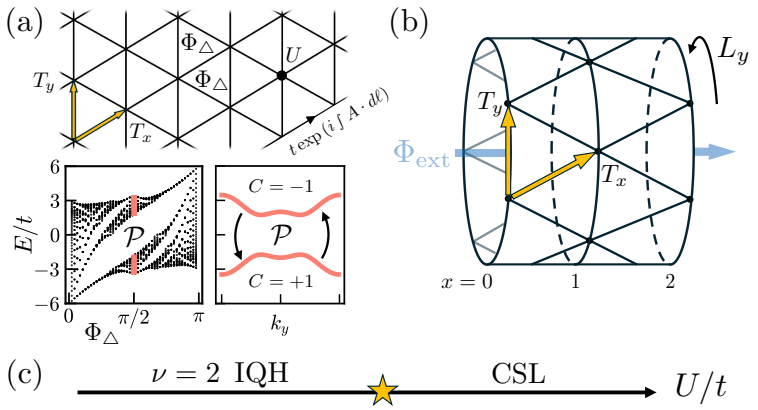

Figure 3.1: (a) Upper panel: The triangular Hofstadter-Hubbard model, with magnetic translations $T_{x,y}$, Hubbard interactions U, and flux per triangle $\Phi_\triangle$ indicated. Lower left panel: "butterfly" representation of non-interacting spectrum in the plane of $\Phi_\triangle$ and energy E. The band structure at $\Phi_\triangle = \pi/2$ enjoys a doubled "magnetic" unit cell and particle-hole symmetry $\mathcal{P}$ relating opposite $C = \pm 1$ bands [lower right panel]. (b) A finite segment of the circumference-L_y cylinder, threaded by $\Phi_{\rm ext}$ external flux. With the chosen "YC-L_y" cylindrical geometry, T_y is orthogonal to the cylinder axis and $x \in \mathbb{Z}$ indexes rings. (c) Expected 2+1D phase diagram at a density of $n = 1$ electron per site as a function of U/t showing the integer quantum Hall (IQH) and chiral spin liquid (CSL) phases, with their transition marked by a star.

point from either theory or numerics. In particular, the iDMRG investigation of Ref. [118] unearthed the IQH-CSL transition only as a crossover indicated by a weak maximum in a correlation length.

In this chapter, we use a compactification to infinite-length, finite-circumference cylinders (see Fig. 3.1b) in combination with a symmetry analysis and large-scale iDMRG simulations [34–36] to characterize the IQH and CSL states, as well as the transition between them. We show that a combination of particle-hole interchange and translation is spontaneously broken on odd-circumference cylinders in the CSL phase and present evidence that the IQH-CSL transition is in fact continuous in these geometries, with no intervening phase. We argue that the critical fluctuations are spin-singlet, with both spin and electron correlation functions decaying exponentially with distance. Considering also even-circumference cylinders, we argue that in 2+1D, the IQH and CSL phases are separated by a continuous quantum phase transition that hosts critical current fluctuations.

3.1 Model, Particle-Hole Symmetry and Compactification

We study the Hofstadter-Hubbard model on the triangular lattice, defined pictorially in Fig. 3.1(a). In this model, electrons hop between nearest-neighboring sites and experience an Aharonov-Bohm phase of $\Phi_\triangle$ upon orbiting a triangular plaquette (see App. A1 for details). We focus on the consequences of the orbital motion, setting the Zeeman coupling to zero [118, 119]. We fix $\Phi_\triangle = \pi/2$, which endows the Hamiltonian with a unitary particle-hole (PH) symmetry $\mathcal{P}$ chosen to act as

$$\mathcal{P} c^\dagger_{x,y} \mathcal{P}^{-1} = (-1)^{x+y} (i\sigma_y) c_{x,y}, \quad \mathcal{P} i \mathcal{P}^{-1} = +i, \tag{3.1}$$

(the spin rotation $i\sigma_y$ is included in $\mathcal{P}$ so it leaves the spin operator $\boldsymbol{S} = \frac{1}{2} c^\dagger \boldsymbol{\sigma} c$ invariant; see App. C). Denoting translation along the two non-parallel directions shown in Fig. 3.1 as $T_{x,y}$, which we represent in a gauge where

$$T_x c^\dagger_{x,y} T_x^{-1} = (-1)^y c^\dagger_{x+1,y}, \quad T_y c^\dagger_{x,y} T_y^{-1} = c^\dagger_{x,y+1}, \tag{3.2}$$

we obtain the required magnetic translation algebra $T_x T_y = -T_y T_x$. The commuting translations $(T_x)^2, T_y$ define a larger "magnetic" unit cell with two sub-bands with Chern numbers $C = \pm 1$ related to each other by $\mathcal{P}$ (Fig. 3.1a). We fix the filling to $n = 1$ electron per lattice site, corresponding to full filling of the lowest spin-degenerate magnetic sub-band.

Dimensional reduction can break the T_x symmetry. Consider the closed "tin can" shaped surface specified by a pair of adjacent lattice rings at x and $x+1$. Applying Gauss's law on this surface [120, 253], with Φ_x denoting the external flux through the cylinder ring at x, we have $\Phi_{x+1} + 2L_y \Phi_\Delta \equiv \Phi_x$ modulo 2π. The ring fluxes are therefore uniform when L_y is even, but staggered when L_y is odd. In the latter case, T_x is explicitly broken.

Consider the odd circumference case and fix the ring fluxes to alternate between 0 and π. Though T_x is broken, the combined translation-like operation $\mathcal{P}T_x$ ("glide-PH") commutes with the Hamiltonian. The IQH state, being adiabatically connected to the unique ground state of the non-interacting Hamiltonian, respects $\mathcal{P}T_x$. However, the odd-L_y CSL phase breaks $\mathcal{P}T_x$ spontaneously. To see this, note that in the CSL phase the charge fluctuations are gapped; when U is large, the low energy degrees of freedom are described by an effective spin model [117]. Since $\mathcal{P}\boldsymbol{S}\mathcal{P}^{-1} = \boldsymbol{S}$, this spin model has a pure translation symmetry t_x. Since each ring contains an odd number of spin-1/2 moments, the Lieb-Schulz-Mattis theorem requires that any gapped ground state be at least twofold degenerate [254], *e.g.*, by breaking t_x spontaneously. The same conclusion can be drawn from the anyon content of the CSL: the presence of one semion per unit cell [253, 255–257] causes t_x to permute the two minimally-entangled ground states [258–260].

We can also interpret the CSL symmetry breaking in terms of the parton decomposition of the electron into a bosonic chargon b carrying the charge and a fermionic spinon f carrying the spin, $c_\sigma = b f_\sigma$ [149, 261, 262]. This requires introducing an *internal* gauge field a. In

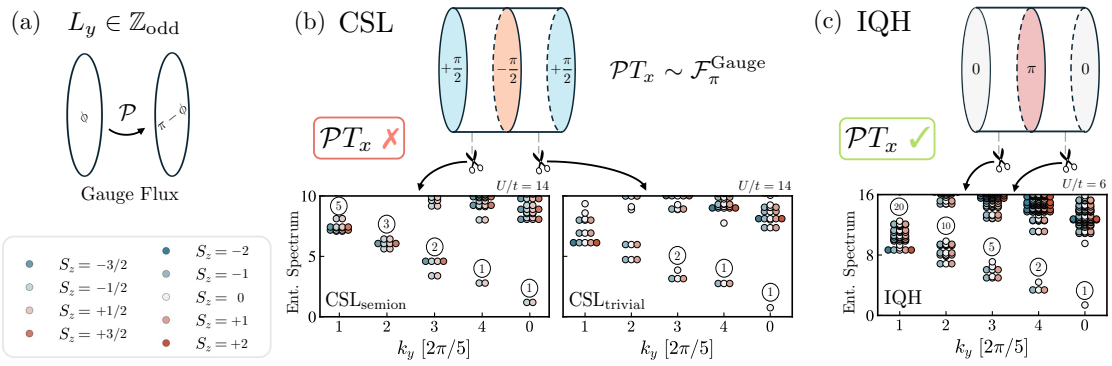

Figure 3.2: CSL symmetry breaking at odd circumference. (a) The particle-hole operation $\mathcal{P}$ transforms the internal gauge flux through an odd-L_y cylinder ring from ϕ to $\pi-\phi$. (b) Upper panel: In an odd-L_y CSL ground state, the alternating pattern of these internal fluxes at strong coupling $(\pi/2, -\pi/2, \dots)$ spontaneously breaks $\mathcal{P}T_x$ symmetry, whose action is then equivalent to threading π internal flux. Lower panel: the low-lying entanglement eigenvalues at cuts between adjacent pairs of rings, which not only exhibit the approximate degeneracy expected for the CSL at each S_z [circled numerals], but also signal spontaneous breaking of $\mathcal{P}T_x$. (c) The internal flux configuration [upper panel] and entanglement spectrum [lower panel] of the IQH.

both the CSL and IQH phases, the saddle point configuration of the internal gauge field yields an internal flux through the triangular surface plaquettes that matches the external flux, $\phi_\triangle = \pi/2$ [82, 117, 246]. Moreover, assuming T_x^2 is unbroken and L_y is odd, the internal flux through adjacent cylinder *rings* may be written as $(\phi, \phi+\pi)$, again differing by π due to Gauss's law. Since the CSL ground states are adiabatically connected to the Mott limit where $\mathcal{P}$ acts as the identity operator, at strong coupling their internal ring fluxes will energetically lock to $(\pi/2, -\pi/2)$ or $(-\pi/2, \pi/2)$, which are both insensitive to the action of $\mathcal{P}$, namely $\phi \to \pi - \phi$ (Fig. 3.2a). These two configurations are related by $\mathcal{P}T_x \simeq t_x$, indicating spontaneous symmetry breaking (SSB) in these odd-L_y geometries (Fig. 3.2b). In the IQH phase where the chargon is condensed, the Higgs mechanism instead pins together the internal and external gauge fields [263–265]. The resulting internal ring flux pattern $(0, \pi)$ respects $\mathcal{P}T_x$, consistent with a unique, gapped ground state (Fig. 3.2c, top).

3.2 Numerical Observation of Phase Transition

We have used the iDMRG algorithm to determine the ground state on cylinders of circumference $L_y = 3, 4, 5, 6$. For the numerically studied range $U \leq 14$, we find no sign of the strong-coupling 120° AF, so we focus on the IQH and CSL phases. We study the entanglement spectrum (ES) [266, 267] at a bipartition of the system into left and right semi-infinite

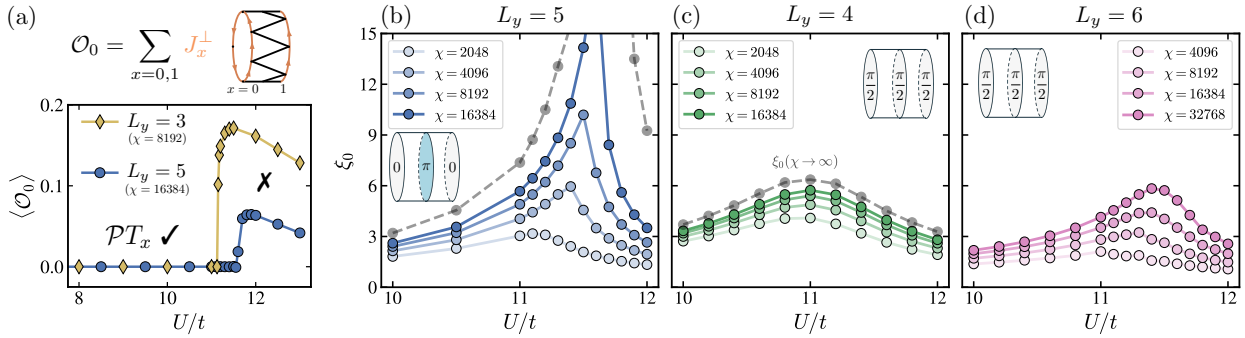

Figure 3.3: Evidence for the IQH-CSL continuous phase transition. (a) Upper panel: Sketch of two cylinder rings, illustrating the $\mathbb{Z}_2$ order parameter $\mathcal{O}_0$ defined as the total circumferential current operator [orange arrows]. Lower panel: $\langle \mathcal{O}_0 \rangle$ versus U/t for the two odd-circumference cylinders, with $\langle \mathcal{O}_0 \rangle \neq 0$ implying $\mathcal{P}T_x$ is spontaneously broken. (b-d) Correlation length in the $(Q, S_z, k_y) = 0$ charge sector for a range of MPS bond dimensions [increasing light to dark] and extrapolated to infinite bond dimension for $L_y = 4, 5$ [gray points]; the insets specify the external magnetic flux through the cylinder rings.

cylinders [107, 118]. According to the Li-Haldane proposal [267], the low-energy part of the ES corresponds to the conformal field theory (CFT) of the physical edge and exhibits degeneracies characteristic of the CFT [268–275]. We see (Fig. 3.2b,c) that the CSL phase has degeneracy $(1, 1, 2, 3, 5, \dots)$, corresponding to the free boson CFT [276], while the IQH phase has $(1, 2, 5, 10, 20 \dots)$, corresponding to two copies of the free boson CFT. Consistent with the above expectations, the CSL phase spontaneously breaks $\mathcal{P}T_x$ symmetry on odd-L_y cylinders as seen from the different entanglement spectra observed on adjacent cuts (Fig. 3.2b, bottom), whereas the ES of the IQH is fully invariant under $\mathcal{P}T_x$ (Fig. 3.2c, bottom).

We also construct a $\mathbb{Z}_2$ order parameter for $\mathcal{P}T_x$, $\mathcal{O} = \sum_{x \in \mathbb{Z}} J_x^\perp$ where $J_x^\perp$ is the average current along the circumferential bonds on ring x. In the chosen gauge:

$$J_x^\perp = (-1)^x L_y^{-1} \sum_y i(c_{x,y}^\dagger c_{x,y+1} - \text{h.c.}) \tag{3.3}$$

It can be verified that $(\mathcal{P}T_x) J_x^\perp (\mathcal{P}T_x)^\dagger = -J_{x+1}^\perp$, so that $\mathcal{O}$ is charged under $\mathcal{P}T_x$. Since all the ground states are invariant under $(\mathcal{P}T_x)^2$ so that $\langle J_x^\perp \rangle = \langle J_{x+2}^\perp \rangle$, then it suffices to examine the condensation of $\mathcal{O}_0 = J_0^\perp + J_1^\perp$. In the CSL phase, $\langle \mathcal{O}_0 \rangle \neq 0$ (see Fig. 3.3a), signaling SSB. Near the transition at odd L_y, the transfer matrix spectrum [277] contains a *diverging* correlation length in the $(Q, S_z, k_y) = 0$ charge sector (see Fig. 3.3(b) for $L_y = 5$ and Appendix B for $L_y = 3$) consistent with the order parameter $\mathcal{O}$. Threading $\Phi_{\text{ext}} = \pi/2$ external flux through each odd-L_y cylinder reduces the transition to a crossover since glide-PH symmetry is explicitly broken unless $\Phi_{\text{ext}} \in \pi\mathbb{Z}$.

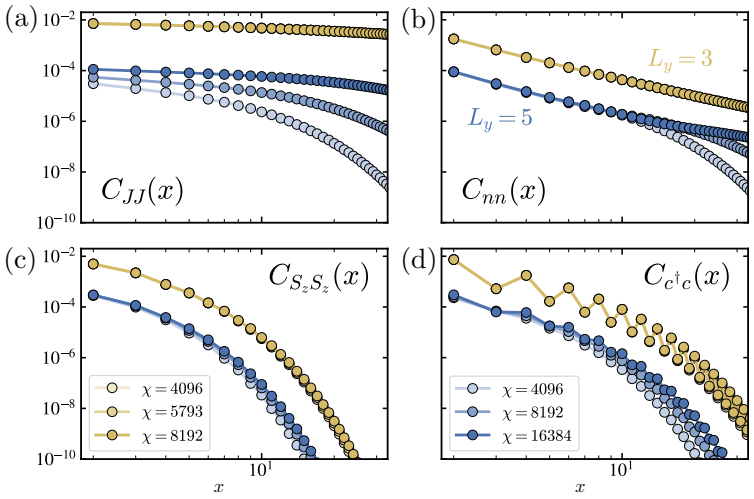

Figure 3.4: Connected correlations for the odd-circumference cylinders at their critical point, $U_c(L_y = 3) = 11.1$ [yellow] and $U_c(L_y = 5) = 11.6$ [blue]. The $L_y = 5$ correlation functions are scaled down by 10 for ease of viewing. (a-b) Current-current and density-density correlations, approaching quasi-long range order as a function of MPS bond dimension χ [increasing light to dark]. (c-d) Spin-spin and electron-hole correlations decay exponentially, demonstrating a spin gap and gap to charge-1e excitations.

On the even-circumference geometries $L_y = 4, 6$ we reproduce the weak crossover, with a correlation length of $\lesssim 1.5$ lattice sites, found by Kuhlenkamp *et al.* for $L_y = 6$ and $\Phi_{\text{ext}} = 0$ [118] (App. E1). Remarkably, upon threading $\Phi_{\text{ext}} = \pi/2$, the correlation length in the range $10 < U < 12$ increases dramatically, notably in the same charge-neutral sector in which our odd-circumference correlation lengths diverge [see Fig. 3.3(c,d)]. At $L_y = 4$, extrapolation to infinite bond dimension following Ref. [205] predicts a maximal extrapolated value of $\xi_{L_y=4}^{\chi\to\infty} = 6.6$ in units of cylinder rings (see App. E2). While at $L_y = 6$, we obtain $\xi = 5.8$ at the largest bond dimension $\chi = 32768$, the correlation length is still growing rapidly with χ. This hampers the precise extrapolation of $\xi_{L_y=6}^{\chi\to\infty}$ but also indicates it substantially exceeds $\xi_{L_y=4}^{\chi\to\infty}$. This suggests that the larger even-L_y geometries will exhibit a sequence of increasingly-sharp crossovers toward 2+1D criticality.

We now discuss the behavior of correlation functions. The connected current correlator $C_{JJ}(x) = \langle J_0^\perp J_x^\perp \rangle_c$ exhibits power-law decay at the approximate transition points $U_c(L_y = 3) = 11.1$ and $U_c(L_y = 5) = 11.6$ (Fig. 3.4a), *i.e.*, U at which the correlation length is largest at the largest available χ. The critical fluctuations also manifest in the charge density: the connected correlations $C_{nn}(x) = \langle n_0 n_x \rangle_c$ (with n_x averaged over ring x) decay algebraically (Fig. 3.4b), but fall off much more rapidly than the current correlations. While there is no SSB for $L_y = 4, 6$ we still observe an enhanced correlation length and slow decay of the current and density correlations (App. H).

On the other hand, the connected spin correlations $C_{S^zS^z}(x) = |\langle S^z_0 S^z_x \rangle_c|$ (with S^z_x averaged over ring x) exhibit clear exponential decay at the odd-L_y critical points, with no apparent enhancement from $L_y = 3$ to $L_y = 5$ (Fig. 3.4c). The electron correlators $C_{c^\dagger c}(x) = L_y^{-2} \sum_{k_y} |\langle c^\dagger(0, k_y) c(x, k_y)\rangle|$ likewise decay exponentially (Fig. 3.4d), so that both spin and electronic excitations remain gapped at the transition. Should these behaviors persist in the thermodynamic limit, they imply that the 2+1D critical point is continuous and hosts gapless, charge-neutral spin-singlet excitations, particularly of the charge current.

We comment briefly on the nature of the odd-L_y quasi-$(1+1)$D critical points. As the $1e$ and $2e$ correlators remain gapped (App. F1), the data are incompatible with Luttinger and Luther-Emery liquid criticality. The spontaneous breaking of a $\mathbb{Z}_2$ symmetry suggests the transition is in the 2D Ising universality class. In fact, we note that a 1+1D Mott transition of the Ising type has been proposed in the "ionic" Hubbard chain [278–280], which shares symmetries and behavior with our odd-L_y model [281–284] (App. F2). Further investigation into this transition, particularly how it evolves to the 2+1D transition and which operators remain critical and with what exponents, is needed. The prominence of the current-current correlations, namely their slow fall-off at both short and long distances, strongly suggests they will remain prominent at the 2+1D critical point.

3.3 Discussion

Our numerical data on both even and odd-circumference cylinder geometries provides confirming evidence of a CSL phase and indicates that the CSL-IQH transition is in fact continuous in the Hofstadter-Hubbard model at $\pi/2$ flux per triangle. The single-electron and spin gaps remain nonzero across the transition, but the current-current correlation function exhibits prominent power-law behavior at the critical point, implying a neutral excitation becomes gapless at criticality. This raises the possibility of further experimental and numerical investigation of this transition. In particular, methods such as quantum Monte Carlo or fermionic PEPS may be able to access wider systems, yielding confirming evidence of a quantum critical point, estimates of critical exponents and conformal invariance, and spectral signatures of spin-charge separation within the CSL phase [285–287].

A broader message of this chapter is that the ability to extrapolate 2+1D physics from dimensionally-reduced data is greatly enhanced by analyzing how symmetries, candidate ground states and their phase transitions respond to spatial compactification and flux threading. In particular, the properties of transitions into topologically-ordered phases may generally be illuminated by studying compactifications in which topological ground state degeneracy is encoded as symmetry breaking at finite cylinder width. Leveraging such techniques systematically, it would be valuable to characterize the contexts in which UV features of Mott phases, namely spin liquids, offer improved understanding of their charge fluctuation-driven quantum phase transitions.

Chapter 4

Anyon Superconductivity from Topological Criticality

The search for electron pairing mechanisms that go beyond the well-established BCS/"pairing glue" paradigm, exemplified by the electron-phonon mechanism [122, 288, 289], has a long history. A popular theoretical route has been to consider situations where charge is associated with topological excitations [55, 79, 85, 221, 222, 227, 290–295]. The best known of these proposals are the resonating valence bond (RVB) [294, 296–298] and anyon superconductivity scenarios [39, 40, 111–113, 299–303], where doping a quantum spin liquid with fractionalized charge excitations leads to superconductivity. In the anyon superconductivity approach proposed soon after the discovery of high-T_c superconductivity in the layered cuprates, the starting point is the chiral spin liquid (CSL) phase introduced by Kalmeyer and Laughlin [37]. Although interest in the anyon superconductivity mechanism in the context of high-T_c cuprates has waned, it remains a remarkable theoretical example of superconductivity emerging from a chiral insulator.

Spin liquids have proven elusive, and even where they are proposed to appear, superconductivity need not arise upon doping. The triangular lattice Hubbard model with time reversal symmetry has been reported to host a CSL ground state at intermediate coupling [107, 108, 285, 304]. However, various magnetic orders and other spin liquid phases are so close in energy to the CSL [104–106, 109] that its existence in this model, and in related time reversal-symmetric extended Heisenberg models [100, 106, 109, 305, 306], is not definitively established [307, 308]. Further, the existence of superconductivity at small hole doping in the intermediate-coupling regime [309, 310] relevant to the putative CSL has not been clearly demonstrated. Indeed, a density matrix renormalization group (DMRG) analysis reports a metal rather than a superconductor [204]. In addition, there is no spin liquid in the weak-coupling regime where superconductivity has also been proposed [146, 311, 312].

In this chapter, we show that superconductivity emerges naturally in the vicinity of *topological criticality* arising from a continuous transition between two topologically-distinct insulators, with time reversal symmetry explicitly broken by a magnetic field. The crucial point is that a change in topology requires closing and reopening a gap at the transition,

in this case a charge gap associated with a bosonic charge-2e mode. Near the topological critical point, these bosonic modes are the lowest-energy local charge excitations, while unpaired electronic states appear only at higher energies. Modest doping then introduces paired carriers, which can superconduct.

We illustrate the potential of this idea through explicit calculations in a microscopic Hofstadter-Hubbard model argued to host an integer quantum Hall (IQH) phase at weak coupling with charge and spin edge modes, and a CSL phase with only a spin edge mode, arising upon increasing electron correlations via repulsive Hubbard interactions [114, 118]. These insulators appear at a density of one electron per lattice site, henceforth referred to as "half filling," with superconductivity emerging upon doping electrons or holes. In Fig. 4.1(a), we present a schematic phase diagram in the plane of chemical potential μ and Hubbard U.

Our study goes beyond previous proposals for superconductivity in the Hofstadter flux regime, which considered only attractive [313–319] and perturbatively weak repulsive interactions [161]. The investigation of the present strongly-repulsive model is motivated by its potential realization in transition metal dichalcogenide (TMD) moiré materials [118, 119], whose advent has opened new avenues for realizing exotic quantum phases and enabled the controlled variation of their doping [6, 8, 11]. The large unit cells of these materials make the Hofstadter flux regime experimentally accessible, while the Zeeman coupling can be quenched [118].

We present general arguments supported by a parton treatment and effective field theory that reveal low-energy Cooper pairs near the putative IQH-CSL critical point. Furthermore, we contend that doping in its vicinity leads to superconductivity. On the CSL side, the superconductor is shown to arise via the *anyon superconductivity* mechanism. Pairing is then examined numerically with exact diagonalization (ED) and DMRG, which reveal that charge-2e excitations are indeed the lowest-energy local charge excitations, per unit charge, over a broad range of parameters, a compelling precursor to superconductivity upon doping. Strikingly, the pairing extends beyond the CSL, well into the IQH side of the phase diagram where anyons cannot be invoked, consistent with the softening of the 2e gap by topological criticality.

Importantly, this mechanism does not rely on strict quantum criticality. Superconductivity emerges in a non-infinitesimal neighborhood of the topological critical point and will therefore persist even if the transition is weakly-first-order or one of the phases is proximal but avoided. Its precursor, electron pairing, appears even in the finite systems accessible in our numerics. Altogether, our results suggest that superconductivity can arise in a regime with both strong repulsive interactions and broken time reversal symmetry, a combination that normally disfavors superconductivity.

The remainder of this chapter is organized as follows. In Sec. 4.1, we introduce the Hofstadter-Hubbard model as well as its continuous and magnetic space group symmetries. In Sec. 4.2, we provide a parton description of the putative topological critical point and the mechanism for obtaining superconductivity upon doping each side of the transition. In Sec. 4.3, we provide numerical evidence for electron pairing using both ED and DMRG. Sec. 4.4 is a summary and conclusion suggesting avenues for future research. Appendix C

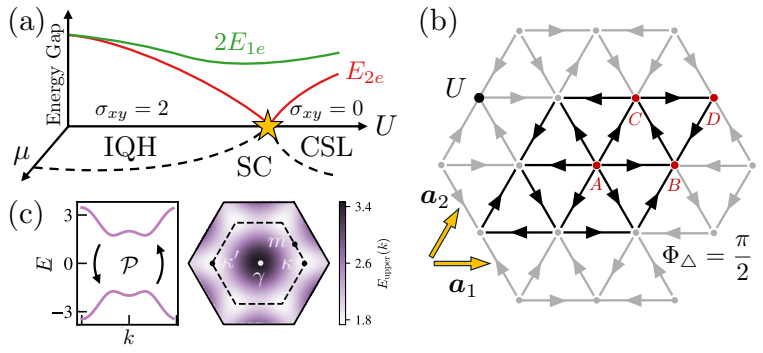

Figure 4.1: (a) Schematic depiction of the predicted energy gap to $2e$ excitations (red) and twice the energy of $1e$ excitations (green) at half filling of the Hofstadter-Hubbard model with $\Phi_\triangle = \pi/2$ flux per triangle as a function of interaction strength U in the 2D limit. Proposed phase diagram in the plane of U and chemical potential μ. The star indicates a topological quantum phase transition from an integer quantum Hall (IQH) insulator to chiral spin liquid (CSL) at half filling. The dashed lines show the chemical potential required to add carriers and produce a chiral superconductor (SC) with topologically-protected edge modes. (b) Finite region of the two-dimensional model with $\Phi_\triangle = \pi/2$ flux per triangle, repulsive on-site interactions U, and Bravais vectors $\boldsymbol{a}_{1,2}$ indicated. The hoppings may be chosen to be C_6-invariant and imaginary (each arrow indicates an amplitude $-it$), with a four-site unit cell (sublattices A-D in red). (c) Left: band structure at $\Phi_\triangle = \pi/2$ consisting of two bands related by particle-hole symmetry $\mathcal{P}$. Right: two-dimensional color map of energy as a function of momentum for the upper energy band over the Brillouin zone of the 2×2 unit cell (note the bands are two-fold degenerate at every momentum).

gives details of calculations described in the main text and supporting data.

4.1 Model and Symmetries

The Hofstadter-Hubbard model (see Fig. 4.1b), with hoppings t_{ij} from site j to i and on-site interaction H_I, is given by $H_{\text{HH}} = -\sum_{ij} t_{ij} c_i^\dagger c_j + H_I$. The hopping amplitudes t_{ij} are complex numbers with phases encoding the orbital magnetic flux [96]. In this chapter, we specialize to the triangular lattice with $\Phi_\triangle = \pi/2$ flux per triangle [114, 118] for which the hopping amplitudes can be chosen to be purely imaginary, so that the single-particle term in the Hamiltonian may be written as:

$$H_0 = i \sum_{\langle ij \rangle} \tau_{ij} \left(c_{i\sigma}^\dagger c_{j\sigma} - c_{j\sigma}^\dagger c_{i\sigma} \right). \tag{4.1}$$

The arrows on bonds in Fig. 4.1(b) indicate our sign convention that the hopping from site j to i along an arrow has $\tau_{ij} = -t < 0$, while hopping opposite an arrow has the opposite

sign. We report energies in units of t.

The symmetries of H_0 are most clearly exposed by mapping to Majorana fermions, $c_{j\uparrow} = \frac{1}{2}(\chi_1^j + i\chi_2^j)$ and $c_{j\downarrow} = \frac{1}{2}(\chi_3^j + i\chi_4^j)$, where $\{\chi_a^i,\, \chi_b^j\} = 2\delta_{ab}\delta_{ij}$ so that H_0 takes the form [320]:

$$H_0 = \frac{i}{2} \sum_{1\le a\le 4} \sum_{\langle ij\rangle} \tau_{ij} \chi_a^i \chi_a^j, \tag{4.2}$$

which is seen to have an O(4) symmetry, corresponding to proper/improper rotations of the Majorana four-component vector. The Hubbard interaction

$$H_I = U \sum_i (n_{i,\uparrow} - 1/2)(n_{i,\downarrow} - 1/2) \tag{4.3}$$

can be written in the Majorana representation as $H_I = -(U/4)\sum_i \chi_1^i \chi_2^i \chi_3^i \chi_4^i$. Note that the interaction breaks the O(4) symmetry of the hopping model down to SO(4). The operators in the determinant -1 sector, corresponding to improper rotations, are related to particle-hole transformations that flip the sign of U (*e.g.*, conjugating only the spin-up electrons) and are therefore not symmetries of the interacting theory. The particle-hole operation which *preserves* the sign of U is a symmetry, identified in Ref. [114].

Contained in SO(4) are the spin $\mathrm{SU}(2)_s$ and pseudospin $\mathrm{SU}(2)_c$ symmetry subgroups identified by Yang and Zhang [321–323], and by Affleck [320]. While the pseudospin symmetry is typically associated with bipartite lattice Hubbard models [324], we highlight that it is more generally present whenever there exists a gauge in which the hoppings are purely imaginary [82], and that $\mathrm{SU}(2)_c$ reduces to the usual charge $\mathrm{U}(1)_c$ for generic long-range interactions. The $\mathrm{SU}(2)_c$ pseudospin symmetry will play an important role in our study of the topological phase transition in Sec. 4.2.

The model is additionally symmetric under operations in the magnetic space group generated by the rotation C_6 and translation T_1 along the nearest-neighbor direction $\boldsymbol{a}_1$ (see Fig. 4.1b). Their explicit form, which we provide in Appendix Sec. 1B, depends on the choice of gauge for the electron operators. However, they satisfy certain gauge-invariant generating relations which will prove important for interpreting the pairing symmetry in Sec. 4.3. Because the magnetic space group is a $\mathrm{U}(1)_c$ extension [325], the overall $\mathrm{U}(1)_c$ phase of each spatial symmetry is ambiguous. We make the following convenient choices: we fix $(C_6)^6 = 1$, choose T_1 to satisfy $C_2 T_1 C_2^\dagger = T_1^\dagger$ which constrains it modulo a sign, and define rotated nearest-neighbor translations by $T_{j+1} = C_6^j T_1 C_6^{-j}$. Moreover, due to the $\pi/2$ flux per triangle, one may verify the following gauge-invariant relations:

$$T_2 T_1 = (-1)^{N_F} T_1 T_2, \quad T_5 T_3 T_1 = (\pm i)^{N_F}, \tag{4.4}$$

where N_F is the fermion number. The sign ambiguity in the second relation arises because our conventions do not fix the sign of T_1; we remedy this by choosing $+i$. When acting on charge-$2e$ *pairs*, with $N_F = 2$, the first relation is trivial but the second is not. This is the origin of the unorthodox pairing symmetry we uncover in Sec. 4.3.

4.2 Parton Theory

Topological Criticality at Half Filling

We introduce a parton construction that captures the effects of on-site U, in effect performing a Gutzwiller projection on the IQH wavefunction to obtain the CSL [248, 252]. This formalism reproduces the phase diagram of the half-filled model obtained numerically in Refs. [114, 118] and allows us to study the effects of doping. While it is possible to proceed by retaining the $\mathrm{SU}(2)_c$ pseudospin symmetry [324], we relegate this treatment to Appendix Sec. 6 and, for ease of presentation, derive here a slave-rotor theory retaining only $\mathrm{U}(1)_c$ along with $\mathrm{SU}(2)_s$. We begin by introducing a U(1) rotor variable $e^{i\theta}$ and its conjugate integer-valued "angular momentum" L at each site [326]. We write the electron operator as $c^\dagger_{i,\sigma} = f^\dagger_{i,\sigma} e^{i\theta_i}$ where f is a fermionic "spinon" carrying the electronic spin. The redundancy introduced by the rotors is alleviated by imposing the following constraint at each site:

$$L_i = f^\dagger_{i,\uparrow} f_{i,\uparrow} + f^\dagger_{i,\downarrow} f_{i,\downarrow} - 1. \tag{4.5}$$

Note that a singly-filled site is represented by $L_i = 0$, while the doublon/empty sites correspond to $L_i = \pm 1$. The Hubbard model can then be rewritten as [326]:

$$H = -\sum_{\langle ij\rangle,\sigma} t_{ij} e^{i(\theta_i - \theta_j)} f^\dagger_{i,\sigma} f_{j,\sigma} + \text{h.c.} + \frac{U}{2}\sum_i L_i^2. \tag{4.6}$$

To make progress, we adopt a mean field approach, replacing operator bilinears by their mean field values:

$$\begin{aligned} H_{\mathrm{MF}} &= H_f + H_\theta \\ H_f &= -\sum_{\langle ij\rangle,\sigma} \tilde{t}_{ij} f^\dagger_{i,\sigma} f_{j,\sigma} + \text{h.c.} \\ H_\theta &= -\sum_{\langle ij\rangle,\sigma} Q_{ij} e^{i(\theta_i-\theta_j)} + \text{h.c.} + \frac{U}{2}\sum_i L_i^2, \end{aligned} \tag{4.7}$$

where $Q_{ij} = t_{ij}\langle f^\dagger_{i,\sigma} f_{j,\sigma}\rangle$ and $\tilde{t}_{ij} = t_{ij}\langle e^{i(\theta_i-\theta_j)}\rangle$. Let us summarize the main results, leaving the detailed analysis of this mean field theory to Appendix Sec. 2. Consistency with the numerical results of Ref. [114], namely a spin gap throughout the transition, requires that the spinons f be gapped. The most natural possibility, consistent with the projective construction of the CSL in the Mott limit [82], is that the spinons see $\Phi_\triangle = \pi/2$ net flux per plaquette, like the microscopic electrons, and enter a spin-singlet Chern insulator with total Chern number $C = 2$. Since the rotor bosons then see no net flux,[1] H_θ displays a superfluid-Mott transition on increasing U, corresponding to the electronic IQH-CSL transition. A mean field treatment of H_θ locates this critical point (see Appendix Sec. 2) at $U^*/t \approx 9.6$, close to the transition point $U^*/t \approx 12$ estimated by iDMRG [114, 118].

[1] This contrasts with the scenario of electrons at zero magnetic field [246, 247], where the two parton species experience opposite, non-zero net flux.

Using (4.7), we show that the universal response properties of the spinon-rotor mean field solutions are consistent with that of the IQH and CSL. We introduce a gauge field on bonds to account for gauge fluctuations about the mean field solution [327], giving $Q_{ij} \to Qe^{-ia_{ij}}$ and $\tilde{t}_{ij} \to \tilde{t}_{ij}e^{+ia_{ij}}$. Further, we introduce a gauge field A (A_s) coupled minimally to the rotors (spinons) to probe the charge (spin) response. Restricting to energies below the spin gap, we may integrate out the spinons; the unit Chern number for each spin species yields the following Chern-Simons terms [328–330]:

$$\mathcal{L}_{\text{CSL}} = \frac{2}{4\pi}(a \wedge da + A_s \wedge dA_s). \tag{4.8}$$

We employ the notation $a \wedge da = \epsilon_{\mu\nu\lambda} a^\mu \partial^\nu a^\lambda$, where summation over Greek spacetime indices is implicit and ϵ is the three-dimensional antisymmetric tensor.

We now turn to the rotor charge excitations. Since we are interested here in long wavelength properties, it is convenient to pass to the continuum limit and utilize a coarse-grained "soft-spin" description [331], replacing $\psi \sim e^{i\theta}$ and introducing a potential $V(\psi) = m^2|\psi|^2 + \lambda|\psi|^4$. Note that there is only a single bosonic field ψ, corresponding to a single minimum in the rotor dispersion, a consequence of the vanishing average flux experienced by the rotors. Tuning the sign of m^2 from positive to negative induces condensation of ψ, as we describe below. The resulting effective field theory is:[2]

$$\mathcal{L} = |\mathcal{D}_{A-a}\psi|^2 - V(\psi) + \frac{2}{4\pi} a \wedge d\, a + \frac{2}{4\pi} A_s \wedge d\, A_s, \tag{4.9}$$

where $\mathcal{D}_b^\mu = \partial^\mu - ib^\mu$, and we have performed field rescaling to bring it into this form. The time component a_0 is introduced to enforce the on-site constraint, Eq. (4.5). We now consider the two phases and their transition.

Phase I: $m^2 < 0$, $\langle\psi\rangle \neq 0$

In the small-U limit we expect the rotor variables to "condense," which introduces a Higgs mass term for $a - A$. Integrating over a yields the response theory $\mathcal{L}_{\text{I}}[A, A_s] = \frac{2}{4\pi} A \wedge dA + \frac{2}{4\pi} A_s \wedge dA_s$. Thus we have an insulator without intrinsic topological order, with precisely the charge and spin quantum Hall conductance of the spin-singlet integer quantum Hall state, namely $\sigma_{xy} = 2 \cdot e^2/h$ and $\sigma^s_{xy} = 2 \cdot \hbar/8\pi$. The latter describes the quantized response of spin to a Zeeman gradient, termed the spin quantum Hall effect [334], and is distinct from the quantum spin Hall effect [335, 336].

Phase II: $m^2 > 0$, $\langle\psi\rangle = 0$

In the larger-U regime, the rotor condensate disappears and the ψ field is gapped. The low-energy effective action in this phase is then $\mathcal{L}_{\text{II}}[a, A, A_s] = \frac{2}{4\pi} a \wedge da + \frac{2}{4\pi} A_s \wedge dA_s = \mathcal{L}_{\text{CSL}}$.

[2] While resembling the Zhang-Hansson-Kivelson composite boson description of the FQHE [332, 333], Eq. (4.9) differs in its Lorentz-invariance, particle-hole symmetry $(\psi, a) \to (\psi^*, -a)$ absent the probe gauge fields, and integer-level dynamical Chern-Simons term.

While the quantized spin response is the same as in Phase I (guaranteed by the spin gap being maintained throughout), the charge Hall conductivity vanishes. Semion topological order now arises from the dynamical $U(1)_2$ Chern-Simons term. These are the characteristic properties of the CSL phase [82]. Moreover, the change of σ_{xy} across the IQH-CSL transition implies that the charge gap *must* close if the transition is continuous.

Critical Point

In the mean field approximation, the critical point corresponds to setting $m^2 = 0$ in (4.9), so that the ψ field becomes gapless. Intuition for this field is gained by recognizing that the fractionalized spin-1/2 semion excitation in the CSL phase combines with the electron to give a semionic charge-e spin-0 excitation, represented by the non-local ψ field. At mean field level, the microscopic particle-hole symmetry ensures that the IQH-CSL transition is continuous and belongs to the 3D XY universality class [331].

To characterize the critical point beyond the mean field approximation, and assess whether the transition remains continuous, we consider gauge field fluctuations and the dynamical Chern-Simons term in (4.9). This full theory cannot be solved exactly, and the Chern-Simons term introduces a sign problem that would hamper large-scale quantum Monte Carlo simulations [337]. Alternatively, one can study the microscopic Hamiltonian of Sec. 4.1 using tensor network methods. Indeed, the cylinder DMRG studies of Refs. [114, 118] provide direct evidence that the transition is continuous and that electron excitations are gapped across the transition. This points to spin-singlet Cooper pairs being the cheapest local charge excitations near the critical point, which we demonstrate numerically in Sec. 4.3.

In addition, we can study deformations of the parton critical theory that *can* be characterized analytically and are known to exhibit a continuous transition. Specifically, consider (4.9) but with Chern-Simons term $\frac{N}{4\pi} a \wedge da$, while retaining the single bosonic scalar field ψ. While we are interested in the case $N = 2$, observe that $N = 1$ and $N = 0$ both correspond to continuous transitions: under fermion-boson duality [338], the former describes the free-fermion Dirac critical point separating two insulators with Chern numbers $C = 0 \to 1$, while the latter describes the 2+1D superconductor-insulator transition [339, 340]. Furthermore, in the $N = \infty$ limit, the theory reduces to the 3D XY transition since gauge field fluctuations are suppressed. The existence of a continuous transition in the $N = 0, 1, \infty$ deformed theories suggests that the $N = 2$ transition can also be continuous.

We shed further light on the IQH-CSL transition by mapping it to an *equivalent*, better-studied bosonic transition between a trivial insulator and $\nu = -1/2$ Laughlin state of charge-$2e$ Cooper pairs [341–344]. The equivalence can be seen by "stacking" an invertible $\nu = -2$ IQH phase above Phases I and II [247]. This trivializes both the spin and charge response of the IQH and maps the CSL to a phase with Hall conductance $\sigma_{xy} = -\frac{1}{2}\frac{(2e)^2}{h}$ but no spin response, namely a Laughlin liquid of Cooper pairs. The transition can thus be viewed as a plateau transition of Cooper pairs, rationalizing there being gapless Cooper pairs at the critical point.

This bosonic transition is argued to be continuous, with critical exponents and universal conductivity computed perturbatively, in several works [341, 342, 345]. In contrast, Ref. [346] proposes a first-order transition scenario, while acknowledging that a continuous transition remains possible elsewhere on the phase boundary. More recently, DMRG studies of models of hardcore bosons support a continuous transition [347, 348], though they do not estimate critical exponents or check for signatures of conformal invariance.

In Ref. [344], the bosonic trivial-to-Laughlin transition theory is expressed both in a form equivalent to (4.9) and as its fermionic dual, a QED_3-Chern-Simons theory [343]. Due to a conjectured "level-rank" duality [349], the theory is believed to possess an emergent SO(3) symmetry [344, 350], rotating between the boson density, creation, and annihilation operators, which go gapless at criticality. Should this critical point be described by a conformal field theory, the putative SO(3) symmetry imposes an important constraint: since the conserved density has protected scaling dimension 2, the Cooper pair insertion operator should have the same scaling dimension [344]. Remarkably, our lattice model provides a microscopic realization of this transition in which the pseudospin $\mathrm{SU}(2)_c$ symmetry introduced in Sec. 4.1 explicitly implements this conjectured SO(3) symmetry. In fact, we exploit the pseudospin symmetry within the non-abelian slave-rotor formalism [324] to derive a bosonic $\mathrm{SU}(2)_1$ Chern-Simons theory dual to (4.9) (see Appendix Sec. 6 for details). The conserved current of this theory manifestly transforms as an SO(3) vector under pseudospin rotations, in striking agreement with the predictions presented above [344].

Non-zero Doping

In this section, we turn to non-zero doping and discuss the different regions of the phase diagram of Fig. 4.1(a). In particular, we describe how both insulating phases considered above naturally give rise to superconductivity upon doping, with proximity to topological criticality playing the crucial role of relegating electron excitations to high energies.[3] On the IQH side, we argue this occurs via the condensation of low-lying charge-$2e$ modes, while on the CSL side we show how superconductivity arises within a parton description of the low-lying fractionalized charge carriers.

Starting from the IQH (or Phase I), the persistence of the spin gap and reduction of the charge-$2e$ gap by topological criticality implies that doped charges enter as spin-singlet Cooper pair excitations, *i.e.*, bound states of electrons. This can be seen from the effective theory (Eq. 4.9) in the phase where ψ is condensed. Shifting variables $a \to a + A$ yields the coupling $2\frac{A_0}{2\pi}\nabla \times \boldsymbol{a}$, where $\nabla \times \boldsymbol{a} = \partial_x a_y - \partial_y a_x$, which implies that charges enter as vortices of the ψ condensate. In particular, by flux quantization $\int \nabla \times \boldsymbol{a} \in 2\pi\mathbb{Z}$, they are forced to enter as charge-$2e$ objects, or Cooper pairs.

Per unit cell of the triangular lattice, these pairs experience 2π external flux, twice that of their constituent electrons. Thus, magnetic translations do *not* enforce degenerate minima

[3] This distinguishes our mechanism from those invoking proximity to a critical point in a *metal* [351], where a fluctuating order parameter is commonly proposed to induce electron pairing [352].

in the energy landscape of Cooper pair excitations, unlike at generic flux fractions where the Cooper pair effective mass would also be suppressed by a narrower bosonic Hofstadter bandwidth.[4] In fact, in Sec. 4.3 we provide numerical evidence that there is a dispersive, non-degenerate $2e$ bound state. At $U/t = 6$ on the 4×4 torus, in subsection 4.3 we estimate its effective mass to be $m_{\text{Cooper}} \approx 1.3\,\hbar^2/ta^2$. While this provides an order-of-magnitude estimate of the Cooper pair effective mass deep in the IQH phase, the parton theory dictates that the effective mass vanishes on approaching the critical point, with the dispersion approaching $\omega \propto |k|$. Moreover, we expect the low-lying Cooper pairs to have a characteristic size ℓ_c controlled by the spin gap.

We now consider doping the IQH insulator. At sufficiently low dopant density compared to ℓ_c^{-2} and ξ^{-2}, where ξ is the charge-$2e$ correlation length (see Appendix Sec. 4), we have a dilute gas of Cooper pairs with short-range repulsive interactions and small effective mass. These are expected to enter a superfluid phase, where the superfluid density increases continuously from zero as μ is tuned across the IQH-superconductor transition, as in the Bose-Hubbard model away from integer filling [331, 356]. At higher densities, it would be valuable to explore in detail whether longer-range bosonic interactions mediated by critical fluctuations can lead to crystallization [357] or phase separation [358].

The charge and spin response of the spin-singlet IQH insulator are $\sigma_{xy} = 2 \cdot e^2/h$ and $\sigma^s_{xy} = 2 \cdot \hbar/8\pi$, respectively, with edge chiral central charge $c_- = 2$. On condensing spin-singlet Cooper pairs, the spin quantum Hall response is unaffected since the spin sector remains gapped. However, including their superfluid response removes the quantization of charge Hall conductance, while the chiral central charge is unchanged [86]. This predicts edge states usually associated with the weak-pairing "$d + id$" superconductors [334, 359]. However, as later shown in Sec. 4.3, we are far from the weak-pairing limit, so that the symmetry of the Cooper pair wavefunction is unrelated to the topological properties and edge states of the superconductor [360]. Moreover, as we later discuss in Sec. 4.3, the terminology regarding pairing symmetry must be adapted to the present scenario of magnetic space group symmetries [161, 207].

Starting from the CSL (or Phase II), we now have fractionalized elementary excitations and must appeal to the parton description. Our analysis elucidates a remarkable connection to the mechanism of anyon superconductivity, and also the possible microscopic realization of higher-charge superconductivity in related models. We consider doping a finite charge density of $0 < y \ll 1$ *holes* per site, which requires that the rotor density be $\langle L_i \rangle = -y$. The constraint (4.5) correspondingly demands a depletion of spinons relative to integer filling: $\langle n^f_{i\uparrow} + n^f_{i\downarrow} \rangle = 1 - y$, which seemingly poses a problem since we expect the spin gap, and hence the spinon gap, to remain open upon light doping. Fortunately, since the spinons occupy bands with Chern number $C_\uparrow = C_\downarrow = 1$, their density can be tuned by introducing additional gauge flux $n_\phi \equiv (\nabla \times \boldsymbol{a})/2\pi = -y/2$.

To evaluate the resulting physical behavior and elucidate the possibility of supercon-

[4] The condensation of interacting Hofstadter bosons has been established even at smaller flux fractions [353–355].

ductivity, let us concentrate on hole doping and replace our rotor with a hardcore bosonic "holon" b on each site, with $n_b = b^\dagger b \in \{0, 1\}$, and write $c^\dagger_\sigma = b f^\dagger_\sigma$. The Hilbert space on each site is restricted to empty and single-electron states, which both satisfy the *slave-boson* constraint $n_b = 1 - n_f$ [246]. Following our previous analysis but with the canonical boson b rather than the rotor, integrating out f leaves:

$$\begin{aligned}\mathcal{L}_{\text{doped}} = b^* \left(i\partial_t + a_0 - A_0\right) b - |\vec{D}_{a-A} b|^2 - V(b) \\ + \frac{2}{4\pi} a \wedge da + \frac{2}{4\pi} A_s \wedge dA_s.\end{aligned} \tag{4.10}$$

This theory incorporates the feature that the density of holons is constrained to be $n_b = -2n_\phi$, seen from the equation of motion for a_0. While there are a variety of possible phases of bosons at the filling $\nu_{\text{holon}} = -2$, a very natural one is the bosonic integer quantum Hall (bIQH) state with *even* integer Hall conductivity [361, 362], a symmetry protected topological (SPT) phase [363] (where the protecting U(1) symmetry is taken to be the gauge "symmetry"). The bIQH phase hosts symmetry-protected counter-propagating edge states and has no intrinsic topological order. Thus it is entirely captured by its effective response [361], probed here by the gauge field combination $a - A$, namely $\Delta\mathcal{L}_{\text{holon}} = -\frac{2}{4\pi}(a - A) \wedge d(a - A)$. Adding this to the effective theory for Phase II we obtain the finite-doping theory in which, importantly, the dynamical Chern-Simons term cancels out:

$$\mathcal{L}_{\text{doped}} = \frac{2}{2\pi} A \wedge da - \frac{2}{4\pi} A \wedge dA + \frac{2}{4\pi} A_s \wedge dA_s. \tag{4.11}$$

Regarding A as a classical field, this phase therefore lacks intrinsic topological order. When $A = 0$, it has a single bulk gapless mode due to the Maxwell dynamics of a, representing the Goldstone mode of the broken $\text{U}(1)_c$ symmetry. From the Ioffe-Larkin rule for adding spinon and holon resistivity tensors, $\rho = \rho_{\text{spinon}} + \rho_{\text{holon}}$ [127, 364–366], we also conclude that the fluid has vanishing resistivity [246]. This is because the partons have opposite Hall responses with respect to a:

$$\rho_{\text{spinon}} = -\rho_{\text{holon}} = \frac{1}{2}\begin{pmatrix} 0 & -1 \\ 1 & 0 \end{pmatrix}. \tag{4.12}$$

Furthermore, we see from the first term in (4.11) that a fundamental flux $\int \nabla \times \boldsymbol{a} = 2\pi$ couples minimally to A and binds $2e$ charge. This is therefore a superconductor of Cooper pairs, and the monopole operator that inserts unit flux of a is their creation operator. In fact, (4.11) (with Maxwell terms for a and A) can be mapped to a Ginzburg–Landau Lagrangian for a 2D superconductor [303, 367].

The Chern-Simons term for A_s in (4.11) indicates a spin quantum Hall response of $\sigma^s_{xy} = 2 \cdot \hbar/8\pi$. Moreover, the edge chiral central charge is $c_- = 2$ (see Appendix Sec. 3). We conclude that this superconductor has precisely the same topological and response properties as the one originating from the IQH. This motivates the minimal phase diagram shown in Fig. 4.1(a), where a single superconducting phase emanates from the IQH and CSL phases upon doping.

Relation to Anyon Superconductivity

The discussion above has a close correspondence to anyon (or more precisely *semion*) superconductivity, proposed in Refs. [39, 40, 111–113, 299–302]. These works argued that a gas of charge-e semions, obtained for instance by doping a CSL, can realize a superconducting state. This problem can be mapped to that of bosons b' attached to π statistical flux, which transmutes their statistics to those of the original semions [368]. In this description, the boson and flux densities are therefore related by $n_{b'} = -2n_\phi$, exactly the relation satisfied by the slave bosons in (4.10). The analysis following that equation provides a direct link between our long-wavelength theory of the doped CSL, derived for the Hubbard-Hofstadter model, and the effective theory of semion superconductivity, most transparently its bosonic formulation developed in Ref. [368]. Our analysis provides an alternative characterization of the semion superconductor, namely as a bIQH phase of the b' bosons [246].

We emphasize that a key advantage of our setup is that proximity to topological criticality in the CSL phase renders doped semions (carrying charge e and no spin) energetically favorable compared to electrons. It also provides renewed motivation for studying the CSL-superconductor transition, which, to our knowledge, has not been characterized in detail in the anyon superconductivity literature. We hope that the bosonic SPT perspective presented above will offer new tools and insights for advancing its understanding [369, 370].

The bIQH characterization presented above also offers insight into the possible microscopic realization of charge-Ne superconductivity with $N \in 2\mathbb{Z}$. Consider electrons in the fundamental representation of a flavor SU(N) symmetry and apply a background flux of $2\pi/N$ per unit cell. At a density of one electron per site, the non-interacting phase is an IQH insulator with $\sigma_{xy} = Ne^2/h$ where the lowest Hofstadter band is filled by all N flavors. On increasing U, we expect to realize a CSL with $\mathrm{SU}(N)_1$ (or equivalently $\mathrm{U}(1)_N$) topological order and chiral central charge $c_- = N - 1$ [252]. A possible critical theory is then the SU(N) analogue of (4.9) above, represented as a complex scalar field χ coupled to a U(1) gauge field with a level-N Chern-Simons term:

$$\mathcal{L} = |\mathcal{D}_{A-a}\chi|^2 - V(\chi) + \frac{N}{4\pi} a \wedge d\, a. \tag{4.13}$$

The IQH and CSL again correspond to the condensed and gapped phases for χ, respectively. Upon doping, superconductivity can arise if the excess bosons enter a bIQH phase, yielding a Hall contribution $\frac{M}{4\pi} a \wedge da$ where M is necessarily even [361]. Therefore, the Chern-Simons term in (4.13) may be canceled out, and a conventional superconductor can arise [303], for *even* integer N. Furthermore, these correspond to a condensate of charge-Ne electron composites which are singlets under the SU(N) and clearly can only condense for *even* N. Note that the charge-e anyons in this scenario have statistical angle $\theta = \pi/N$, distinct from $\pi(1 - 1/N)$ in the classic anyon superconductivity scenario [113]. They only agree for the special case of $N = 2$, *i.e.*, semion superconductivity, considered in this chapter.

At $N = 2$, it is tempting to view anyon superconductivity as arising from the *binding* of pairs of charge-e semions into bosons, that then condense. We remark however that

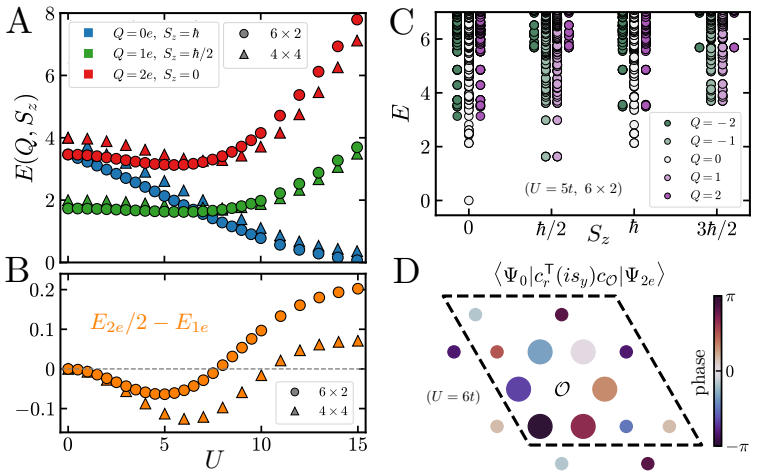

Figure 4.2: (a) Exact diagonalization (ED) energies of the lowest-lying states in three charge sectors (indicated in legend) for both the 4×4 site (triangular markers) and 6×2 site systems (circles). (b) Plot of $E_{2e}/2 - E_{1e}$ vs. U, whose negative value indicates electron pairing. (c) ED energy spectrum on the 6×2 site torus at $U/t = 5$. The energies are arranged by total spin S_z and electric charge Q (indicated in legend); they organize into multiplets of the spin and pseudospin SU(2) symmetries. (d) Overlap of the spin-singlet pairing operator $c_{\boldsymbol{r}}^\mathsf{T}(is_y)c_\mathcal{O}$ between the half-filled ground state and two-electron excitation for all sites $\boldsymbol{r}$ on a 4×4 site torus at $U/t = 6$, with origin indicated by $\mathcal{O}$. Its magnitude and phase are specified by marker area and color, respectively.

this route would leave the remaining semionic excitations deconfined, resulting in a very different fractionalized superconductor "SC*" [371] that retains semionic excitations. Due to the absence of a Chern-Simons term for a in (4.11), the anyon superconductor mechanism evidently yields a superconductor of the more conventional variety [113, 368].

4.3 Numerical Evidence for Cooper Pairing

In the preceding section, we presented field-theoretic arguments for the nature of the putative critical theory and its excitations, as well as the intriguing possibility of topological superconductivity upon doping near this critical point. Here, we provide explicit numerical evidence for an important precursor to superconductivity, electron pairing above the half-filled ground states.

Exact Diagonalization

We first investigate the system using exact diagonalization (ED). We focus on 6×2 and 4×4-site systems, the latter being the largest we can access. We diagonalize the Hamiltonian at

the particle-hole-symmetric point $\mu = 0$, and organize the spectrum by the charge Q and spin S_z quantum numbers, taking the convention where the half-filled ground state has $Q = S_z = 0$ and zero energy. To construct the 6×2 torus, we identify points separated by the vectors $6\boldsymbol{a}_1$ and by $2\boldsymbol{a}_2 - 4\boldsymbol{a}_1$. On the 4×4 system, we identify points related by $4\boldsymbol{a}_1$ and $4\boldsymbol{a}_2$ (see Fig. 4.1(b) for the definition of the lattice vectors $\boldsymbol{a}_{1,2}$).

In Fig. 4.2(a), we plot the energies of the lowest-lying excited states in the charge sectors (Q, S_z) specified by $\{(0e, \hbar), (1e, \hbar/2), (2e, 0)\}$, for both the 6×2 and 4×4 systems. While we focus on the electron-doped side, adding holes is energetically equivalent under particle-hole symmetry. The lowest $0e$ excitation energy decreases monotonically as a function of U. On the other hand, both $1e$ and $2e$ exhibit minima at intermediate coupling: for the 6×2 system, these occur at $U_{1e}^{\min}/t \simeq 6.0$ and $U_{2e}^{\min}/t \simeq 5.5$, whereas on the 4×4 torus these values increase to $U_{1e}^{\min}/t \simeq 8$ and $U_{2e}^{\min}/t \simeq 7$.

The ED calculation convincingly demonstrates that the lowest-lying charge excitations are paired over a remarkably broad range of interaction strengths U. Specifically, the energy E_{2e} of the lowest-lying charge-$2e$ state is less than that of two individual electronic excitations, *i.e.*, $E_{2e} - 2E_{1e} < 0$. We plot this quantity in Fig. 4.2(b), which we find to be negative in the range $0 < U/t \leq 7.5$ for the 6×2 system and over an even broader range $0 < U/t \leq 10$ for the larger 4×4 system. The maximum magnitude of the pairing energy increases from $0.06t$ to $0.13t$ between the two systems, constituting 4% and 7% of the corresponding $1e$ energies, respectively. The location of this maximum is $U_{\max}/t \simeq 5$ for the 6×2 system, increasing to $U_{\max}/t \simeq 6$ on the larger 4×4 torus. Though these features occur at smaller interaction strength than the expected IQH-CSL transition point $U/t \approx 12$ reported by previous cylinder iDMRG studies [114, 118], we anticipate that $U_{\max}$ will continue to increase with increasing system size.

The numerical observation of pairing is important confirming evidence for topological criticality and the associated softening of charge-$2e$ modes. Moreover, as argued in Sec. 4.2, the existence of pairing in the IQH phase is a direct precursor to superconductivity and is likewise expected in the CSL near criticality. To estimate the Cooper pair effective mass, crucial to phase stiffness, we thread small external flux φ through the torus and compute the change in the charge-$2e$ energy E_{2e}. For concreteness, we fix $U/t = 6$ on the 4×4 torus, where pairing is maximal, though on larger systems we expect this point to reside deep in the IQH phase (see Refs. [114, 118]). At small φ, we obtain a quadratic fit $E_{2e}(\varphi)/t \approx 5.01(\varphi/2\pi)^2$. Threading 2π flux shifts the total *two*-electron momentum $\boldsymbol{q}$ by $2/L$ times a primitive reciprocal vector of magnitude $4\pi/a\sqrt{3}$, where $L = 4$ is the length of the torus. Matching the dispersion to $\hbar^2 q^2/2m_{\text{Cooper}}$ with $\varphi/2\pi = qa\sqrt{3}/2\pi$, we estimate $m_{\text{Cooper}} \approx 1.3\,\hbar^2/ta^2$ at the chosen system size and interaction strength, providing an order-of-magnitude estimate for the pair effective mass in the IQH phase.

We note that the pairing energy $E_{2e}/2 - E_{1e}$ cannot be positive in the thermodynamic limit because it is always possible to create a well-separated pair of $1e$ excitations with energy equal to that of independent electrons. Its taking positive values for $U/t > 7.5$ and $U/t > 10$ on the 6×2 and 4×4 systems, respectively, is therefore a finite size effect. Given that the interactions are repulsive, the observed (negative) electron pairing energy at smaller U

has no similarly-compelling finite-size explanation, thus pointing to topological criticality as its origin. Furthermore, the fact that pairing extends down to seemingly arbitrarily-small values (probed down to $U/t = 10^{-3}$) suggests a weak-coupling origin complementary to pairing induced strictly by proximity to criticality.

Each of the systems under consideration possesses the SO(4) symmetry explicated in Sec. 4.1. Accordingly, we observe that the ED spectrum organizes into multiplets of the spin and pseudospin SU(2) symmetries. This is displayed in Fig. 4.2(c) for the 6×2 torus at $U/t = 5$, in which eigenstates with fixed spin S_z but different total charge Q populate multiplets of the pseudospin $\mathrm{SU}(2)_c$. For both system sizes, the $(Q, S_z) = (0e, \hbar)$ state in Fig. 4.2(a) belongs to a pseudospin-singlet spin-triplet irreducible representation, while the $(Q, S_z) = (2e, 0)$ branch is a pseudospin-triplet spin-singlet.

We remark that pairing was not observed on the smaller 4×2 torus, nor on the 6×2 system with the identification $\boldsymbol{r} \sim \boldsymbol{r} + 2\boldsymbol{a}_2 \sim \boldsymbol{r} + 6\boldsymbol{a}_1$, though we recall that pairing was observed at 6×2 under the boundary identification specified earlier. Nonetheless, it is suggestive that pairing is present on the largest accessible system, the 4×4 torus studied above. Verifying pairing at larger system sizes, employing approximate methods beyond ED, is an important task for future work. In the next section, we take one step forward by establishing electron pairing in a cylindrical geometry of finite width but *infinite* length using tensor network methods.

Segment DMRG

Here we employ the "infinite boundary condition" technique [277, 372–374], referred to henceforth as the "segment" DMRG method [168, 189, 373], to obtain excited states and their energies. Starting from an infinite MPS approximation to the ground state at half-filling, we allow the tensors of the excited state MPS to differ on a segment spanning N_r cylinder rings. DMRG is then used within this variational class to minimize the excitation energy for fixed quantum numbers Q, S_z, and circumferential momentum k_y relative to the ground state.

For the XC4 cylinder considered here and shown schematically in Fig. 4.3(a), we identify points separated by $4\boldsymbol{a}_2 - 2\boldsymbol{a}_1 \propto \hat{y}$ around the circumferential direction (with circumference $2\sqrt{3}a$), but take the cylinder to have infinite length, with $\boldsymbol{a}_1$ parallel to the cylinder axis. Each cylinder ring consists of two spinful lattice sites. As in Ref. [114], we employ a gauge in which the magnetic unit cell consists of two sites, with magnetic Bravais vectors given by $\boldsymbol{a}_1$ and $2\boldsymbol{a}_2 - \boldsymbol{a}_1$. This results in two distinct momenta k_y, corresponding to the eigenvalues of the circumferential translation $(T_2)^2 T_1^\dagger$. To obtain the parent half-filled states, we use the iDMRG algorithm [34–36], and conserve the charges (Q, S_z, k_y) for both the ground state and the segment excitation calculations.

Accurate results require converging in three separate parameters: the bond dimension χ_{undoped} of the half-filled ground state, the bond dimension of tensors within the variational segment—which we parameterize by the maximum magnitude Λ of the discarded singular values—and the number of cylinder rings N_r in the segment. In Fig. 4.3(b), we plot the

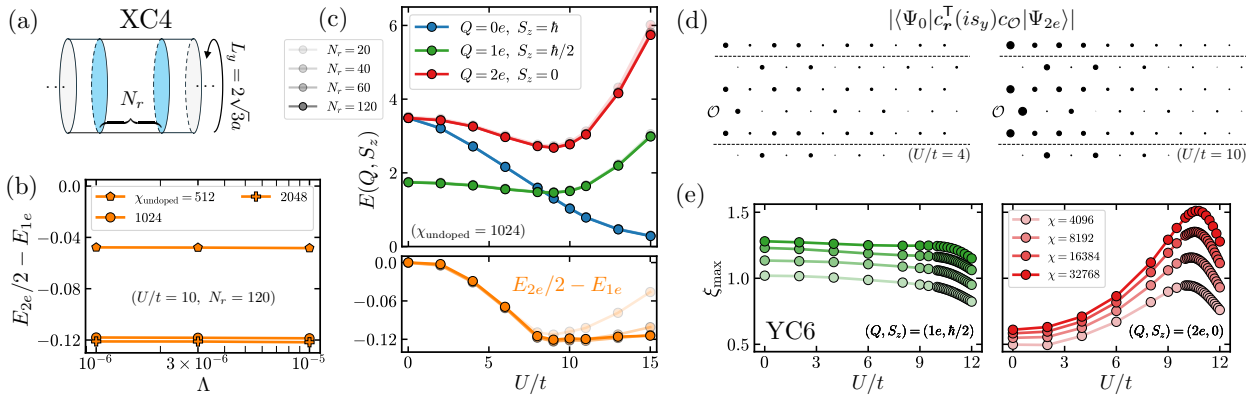

Figure 4.3: (a) Illustration of the infinite-length XC4 cylinder with circumference $L_y = 2\sqrt{3}a$, where a is the lattice spacing. The "segment" DMRG method consists of optimizing a finite number of tensors (describing N_r cylinder rings) sandwiched between two semi-infinite MPS environments derived from a reference (half-filled) ground state with bond dimension χ_{undoped}. (b) Electron pairing energy $E_{2e}/2 - E_{1e}$ vs. maximum magnitude Λ of discarded singular values in the finite segment, with legend indicating χ_{undoped}. (c) Upper panel: energies of excitations with charges (Q, S_z) (indicated in legend) vs. Hubbard U, with fixed $\chi_{\text{undoped}} = 1024$ and $\Lambda = 10^{-5}$. The legend indicates N_r (increasing light to dark). Lower panel: electron pairing energy vs. U. (d) Magnitude of the pair wavefunction at both $U/t = 4$ and $U/t = 10$, computed from respective iDMRG ground states with $\chi_{\text{undoped}} = 1024$ and segment excitations with $N_r = 120$. The two dotted lines are related under the cylinder identification; outside points are periodic images. (e) Correlation lengths of the half-filled YC6 ground state in the $1e$ (left panel) and $2e$ (right) sectors, in units of cylinder rings, as a function of bond dimension (increasing light to dark) and U.

pairing energy (for $U/t = 10$ and $N_r = 120$ rings) as a function of Λ and parent state bond dimension. The energy is found to depend more strongly on the latter, but shows little quantitative difference between $\chi_{\text{undoped}} = 1024$ and 2048, permitting us to choose the less expensive option at other interactions U. We focus on the XC4 cylinder because it is the largest system on which we can obtain $\lesssim 0.01t$ error in the energy using available resources, and because the smaller YC3 cylinder does not exhibit pairing, presumably due to insufficient cylinder width.

In Fig. 4.3(c), we plot the excitation energies in the charge sectors (Q, S_z) given by $\{(0e, \hbar), (1e, \hbar/2), (2e, 0)\}$ as a function of Hubbard interaction U and the segment length N_r (increasing with shading, light to dark), fixing $\chi_{\text{undoped}} = 1024$. For each (Q, S_z), we initialize in each momentum sector k_y and take the minimum energy. We remark that the energy curves bear strong resemblance to those obtained from ED in Fig. 4.2(a). For the DMRG, we observe that the smaller-U simulations exhibit more rapid energetic convergence in N_r. Both the $1e$ and $2e$ energies monotonically decrease from $U/t = 0$ to a minimum at

$U/t \approx 9$ and increase rapidly thereafter. Consistent with ED, their energies indicate electron pairing $E_{2e}/2 - E_{1e} < 0$ over a broad range of interaction strengths, from $U = 0$ to at least $U/t = 15$. The maximum pairing strength of $0.12t$ occurs at $U/t = 9$, near the putative critical point discussed in Sec. 4.2, constituting 8.3% of the corresponding $1e$ energy, though the data in fact exhibits a plateau in the pairing energy beginning at this U.

The behavior of the charge-neutral $S_z = \hbar$ excitation branch (see Fig. 4.3c) strongly resembles the corresponding energy curve in ED, where we identified it as belonging to a spin-triplet, pseudospin-singlet representation. In the segment DMRG data, this excitation energy decreases gradually from its expected value of $2\sqrt{3}t$ at $U = 0$ to zero at $U/t > 15$. This agrees with the results from ED for both the 6×2 and 4×4-site systems, shown in Fig. 4.2(a), where this gap similarly closes at $U/t > 15$. Agreement between these three geometries suggests this feature persists in the thermodynamic limit, where it may be associated with a transition to the 120° antiferromagnetic phase, setting an upper-bound on the extent of the putative CSL phase.

Though our explicit DMRG pairing calculations are limited to the XC4 cylinder, indirect evidence for the persistence and possible enhancement of pairing on wider cylinders is provided by the behavior of the transfer matrix spectrum associated with the translation-invariant half-filled parent state [114, 118]. The dominant transfer matrix eigenvalues, resolved by charge sector (Q, S_z, k_y), relate to ground state connected correlation lengths of operators carrying those charges [375, 376]. In the YC-L_y cylinder sequence [107], the correlation length associated with spin-singlet $2e$ excitations becomes more pronounced as L_y increases from $L_y = 3$ to 6 (see Appendix Sec. 4). In Fig. 4.3(e), we showcase the $2e$ and $1e$ correlation lengths on the YC6 cylinder, where the pronounced peak of ξ_{2e} and its prominence over ξ_{1e} suggests the persistence of electron pairing on this wider cylinder. The same pattern holds when comparing the XC4 and XC6 cylinders. In all cases, by threading flux if necessary, we ensure that the fluxes penetrating the cylinder rings are consistent with the particle-hole SO(4) symmetry of Sec. 4.1.

Pairing Symmetry

In this section, we discuss the symmetry of the charge-$2e$ paired states obtained in ED and DMRG. We argue that these low-energy excitations are spin-singlet and energetically non-degenerate, carrying odd angular momentum under site-centered rotations and even angular momentum under bond-centered rotations.

On the 4×4 system studied in ED, the uniqueness of the lowest-energy charge-$2e$ excited state for all U implies that it is spin-singlet and transforms in a one-dimensional irreducible representation of the magnetic space group generated by T_1, C_6. We find the pair carries momentum $T_j|\Psi_{2e}\rangle = -|\Psi_{2e}\rangle$ for all nearest-neighbour translations T_j. Counterintuitively, this is in fact the unique momentum which is rotation-symmetric: invariance under C_6 requires each T_j to have the same eigenvalue, while (4.4) requires $T_5 T_3 T_1 = -1$ when acting on a pair, which together imply $T_j = -1$. Moreover, we find that $C_2|\Psi_{2e}\rangle = -|\Psi_{2e}\rangle$, so that the state has odd angular momentum with respect to site-centered rotations. However, for

each *bond*-centered rotation $C_2^{\text{bond}} = T_j C_2$, we therefore have $C_2^{\text{bond}}|\Psi_{2e}\rangle = +|\Psi_{2e}\rangle$, which has invariant meaning since $(C_2^{\text{bond}})^2 = 1$ in every fermion number sector. Thus, the pair has even angular momentum with respect to all bond-centered rotations.[5]

By anti-symmetry of the wavefunction, spin-singlet pairing should therefore be allowed between sites related by C_2^{bond} but disallowed when they are related by a site-centered rotation C_2^{site}. This is exactly borne out in the 4×4 ED numerical data. In Fig. 4.2(d), we plot the spin-singlet "pair wavefunction" $\langle \Psi_0 | c_{\boldsymbol{r}}^{\mathsf{T}} (i s_y) c_{\mathcal{O}} | \Psi_{2e} \rangle$ at $U/t = 6$, where Ψ_0 is the ground state, $\mathcal{O}$ is the origin, and c^{T} denotes the transpose of the column vector of electron annihilation operators. We observe that the wavefunction vanishes when $\boldsymbol{r}$ is related to $\mathcal{O}$ by some C_2^{site}, in agreement with the above arguments. Moreover, the pair is well-localized, with nearest-neighbour pairing having much larger magnitude than next-nearest-neighbour pairing. Though the phase winding in Fig. 4.2(d) suggests the pairing symmetry is "$p+ip$", we caution that the C_3 eigenvalue of the charge-$2e$ excited state does not have obvious invariant meaning as it can be modified by the redefinition $C_3 \to (e^{2\pi i/3})^{N_F} C_3$. Nonetheless, on the 4×4 torus, we have unambiguously confirmed spin-singlet pairing, carrying odd (even) angular momentum under site-centered (bond-centered) rotations.

On the XC4 cylinder, three-fold rotation symmetry is explicitly broken. Nonetheless, the segment DMRG pair excitations exhibit the same pairing symmetry as above. We verify this explicitly by computing the pair wavefunction, choosing $\mathcal{O}$ at the center of the segment.[6] We find it is odd under $\boldsymbol{r} \to C_2 \boldsymbol{r}$ and that the spin-triplet overlap is several orders of magnitude smaller than spin-singlet. Moreover, as shown in Fig. 4.3(d) for $U/t = 4$ and 10, we find that the pair wavefunction vanishes approximately (error is induced by finite N_r) when $\boldsymbol{r}$ and $\mathcal{O}$ are related by some C_2^{site}, which indicates $C_2^{\text{site}}|\Psi_{2e}\rangle = -|\Psi_{2e}\rangle$. Similarly, we conclude that $C_2^{\text{bond}}|\Psi_{2e}\rangle = +|\Psi_{2e}\rangle$. These plots also show that the size of the excitation decreases with U. Finally, since we conserve momentum around the cylinder, our excited states are labeled by their eigenvalue under the circumferential translation $T = (T_2)^2 T_1^\dagger$. For all U, the paired eigenstate satisfies $T|\Psi_{2e}\rangle = -|\Psi_{2e}\rangle$, consistent with our expectation $T_1 = T_2 = -1$.

We anticipate that our pairing symmetry results will help guide future numerical investigations of pairing and superconductivity in this model, especially those employing techniques that operate within a fixed charge sector, such as the ED and DMRG performed in this chapter.

4.4 Discussion

A central message of this chapter is that topological superconductivity can emerge in a regime with both strong repulsive interactions and broken time reversal symmetry. Electron pairing was investigated and was clearly observed in our numerical calculations in the present Hofstadter-Hubbard model. It is strongest in the regime of intermediate interaction strength

[5] All other bond-centered two-fold rotations are related by the square of some translation operator and thus have the same eigenvalue.

[6] The inversion center $\mathcal{O}$ is approximate since the segment contains a finite, even number of rings.

close to the putative IQH-CSL critical point [114, 118] and remarkably remains non-zero down to perturbatively-weak interactions. The pairs are spin-singlet, with odd (even) angular momentum under site-centered (bond-centered) rotations.

These numerical observations support the principal idea that proximity to topological quantum criticality can offer a robust route to superconductivity, even in remarkably simple settings. The crucial ingredient here is that the topological transition is associated with the closing of the charge gap, while the spin gap remains open. From the IQH-CSL critical theory formulated for the present Hofstadter-Hubbard model, we argued that doping naturally leads to a topological superconductor. On the CSL side of the phase diagram, this relates to the storied mechanism of semion superconductivity. However, given the broad extent around criticality where superconductivity is anticipated, it is not strictly necessary for this mechanism that the topological critical point or the CSL be accessed in a given model. For instance, superconductivity could emerge upon doping the IQH well away from criticality, even in a scenario where the CSL is entirely subsumed by a conventional magnetically-ordered phase, or if the transition exists but is weakly first-order. Likewise, we do not expect C_2 breaking or deviation from particle-hole symmetry to play a significant role away from the weak-coupling regime.

We now list key areas for future exploration. A more complete characterization of the quantum critical point and its associated conformal field theory would further elucidate the likely-universal nature of superconducting onset upon doping the IQH, CSL, and the critical point itself. It may also shed light on potential competition with conventional [357] and fractionalized [377, 378] crystalline phases at non-zero doping. Another immediate next step is numerically verifying the existence of the superconducting ground state in this model, for instance with cylinder DMRG [120, 184, 379] or other suitable methods. Furthermore, to distinguish features unique to our model from those of the general theoretical scenario near criticality, it will be necessary to compare with a broader class of models that relax various symmetries. Such results should also be compared to existing numerical observations of superconductivity in related models on the triangular lattice [380], most notably chiral t-J models with real hoppings [201, 380–382], where charge fluctuations integral to topological criticality are absent at half filling.

Next, we highlight promising experimental realizations in moiré materials. Triangular lattices formed by TMD sheets with a moiré potential offer both valley and layer "pseudospin" degrees of freedom [233, 383–387]. As proposed in Refs. [118, 119], the Hofstadter-Hubbard model considered here could be realized by applying a perpendicular magnetic field to such a system with a tens-of-nanometer moiré lattice constant. The field would conveniently polarize the valley (*i.e.*, true spin) degree of freedom due to the Zeeman effect, yielding the effective model of Sec. 4.1, with layer pseudospin playing the role of spin. Further numerical studies of this model and its deformations would help guide the experimental exploration of criticality and superconductivity in these moiré platforms.

Finally, the recent observation of the fractional quantum anomalous Hall effect in twisted bilayer $MoTe_2$ [90–92, 388] and rhombohedral multilayer graphene [93], as well as fractional Chern insulators in both magic-angle graphene at weak magnetic field [33] and in the field-

induced Chern bands of Bernal bilayer graphene aligned with hexagonal boron nitride [13], motivate exploring the behavior of charged anyons subject to substantial lattice effects, as we have in this chapter. Further, a recent experiment on quadrilayer rhombohedral graphene demonstrates that chiral superconductivity is possible even at strong magnetic fields [389], a hopeful sign for the class of mechanisms proposed here, motivating the study of routes to pairing and superconductivity in the strong time-reversal-breaking regime.

Bibliography

[1] R. Bistritzer and A. H. MacDonald, "Moiré bands in twisted double-layer graphene," *Proceedings of the National Academy of Science*, vol. 108, no. 30, pp. 12 233–12 237, Jul. 2011. DOI: 10.1073/pnas.1108174108.

[2] Y. Cao, V. Fatemi, S. Fang, *et al.*, "Unconventional superconductivity in magic-angle graphene superlattices,", vol. 556, no. 7699, pp. 43–50, Apr. 2018. DOI: 10.1038/nature26160.

[3] Y. Cao, V. Fatemi, A. Demir, *et al.*, "Correlated insulator behaviour at half-filling in magic-angle graphene superlattices,", vol. 556, no. 7699, pp. 80–84, Apr. 2018. DOI: 10.1038/nature26154.

[4] D. M. Kennes, M. Claassen, L. Xian, *et al.*, "Moiré heterostructures as a condensed-matter quantum simulator," *Nature Physics*, vol. 17, no. 2, pp. 155–163, Feb. 2021. DOI: 10.1038/s41567-020-01154-3.

[5] D. Huang, J. Choi, C.-K. Shih, and X. Li, "Excitons in semiconductor moiré superlattices," *Nature Nanotechnology*, vol. 17, no. 3, pp. 227–238, Mar. 2022. DOI: 10.1038/s41565-021-01068-y.

[6] K. P. Nuckolls and A. Yazdani, "A microscopic perspective on moiré materials," *Nature Reviews Materials*, vol. 9, no. 7, pp. 460–480, Jul. 2024. DOI: 10.1038/s41578-024-00682-1.

[7] E. Y. Andrei and A. H. MacDonald, "Graphene bilayers with a twist," *Nature Materials*, vol. 19, no. 12, pp. 1265–1275, Dec. 2020. DOI: 10.1038/s41563-020-00840-0.

[8] K. F. Mak and J. Shan, "Semiconductor moiré materials," *Nature Nanotechnology*, vol. 17, no. 7, pp. 686–695, Jul. 2022. DOI: 10.1038/s41565-022-01165-6.

[9] L. Ju, A. H. MacDonald, K. F. Mak, J. Shan, and X. Xu, "The fractional quantum anomalous Hall effect," *Nature Reviews Materials*, vol. 9, no. 7, pp. 455–459, Jul. 2024. DOI: 10.1038/s41578-024-00694-x.

[10] E. Barré, M. Dandu, S. Kundu, A. Sood, F. H. da Jornada, and A. Raja, "Engineering interlayer hybridization in van der Waals bilayers," *Nature Reviews Materials*, vol. 9, no. 7, pp. 499–508, Jul. 2024. DOI: 10.1038/s41578-024-00666-1.

[11] L. Balents, C. R. Dean, D. K. Efetov, and A. F. Young, "Superconductivity and strong correlations in moiré flat bands," *Nature Physics*, vol. 16, no. 7, pp. 725–733, Jul. 2020. DOI: 10.1038/s41567-020-0906-9.

[12] P. C. Adak, S. Sinha, A. Agarwal, and M. M. Deshmukh, "Tunable moiré materials for probing Berry physics and topology," *Nature Reviews Materials*, vol. 9, no. 7, pp. 481–498, Jul. 2024. DOI: 10.1038/s41578-024-00671-4.

[13] E. M. Spanton, A. A. Zibrov, H. Zhou, *et al.*, "Observation of fractional Chern insulators in a van der Waals heterostructure," *Science*, vol. 360, no. 6384, pp. 62–66, Apr. 2018. DOI: 10.1126/science.aan8458.

[14] P. G. Harper, "Single band motion of conduction electrons in a uniform magnetic field," *Proceedings of the Physical Society. Section A*, vol. 68, no. 10, p. 874, Oct. 1955. DOI: 10.1088/0370-1298/68/10/304.

[15] L. Landau, "Diamagnetismus der Metalle," *Zeitschrift fur Physik*, vol. 64, no. 9-10, pp. 629–637, Sep. 1930. DOI: 10.1007/BF01397213.

[16] D. R. Hofstadter, "Energy levels and wave functions of bloch electrons in rational and irrational magnetic fields," *Phys. Rev. B*, vol. 14, pp. 2239–2249, 6 Sep. 1976. DOI: 10.1103/PhysRevB.14.2239.

[17] A. L. Sharpe, E. J. Fox, A. W. Barnard, *et al.*, "Emergent ferromagnetism near three-quarters filling in twisted bilayer graphene," *Science*, vol. 365, no. 6453, pp. 605–608, Aug. 2019. DOI: 10.1126/science.aaw3780.

[18] M. Serlin, C. L. Tschirhart, H. Polshyn, *et al.*, "Intrinsic quantized anomalous Hall effect in a moiré heterostructure," *Science*, vol. 367, no. 6480, pp. 900–903, Feb. 2020. DOI: 10.1126/science.aay5533.

[19] T. Li, S. Jiang, B. Shen, *et al.*, "Quantum anomalous Hall effect from intertwined moiré bands,", vol. 600, no. 7890, pp. 641–646, Dec. 2021. DOI: 10.1038/s41586-021-04171-1.

[20] D. J. Thouless, M. Kohmoto, M. P. Nightingale, and M. den Nijs, "Quantized hall conductance in a two-dimensional periodic potential," *Phys. Rev. Lett.*, vol. 49, pp. 405–408, 6 Aug. 1982. DOI: 10.1103/PhysRevLett.49.405.

[21] J. E. Avron, R. Seiler, and B. Simon, "Homotopy and quantization in condensed matter physics," *Phys. Rev. Lett.*, vol. 51, pp. 51–53, 1 Jul. 1983. DOI: 10.1103/PhysRevLett.51.51.

[22] M. Kohmoto, "Topological invariant and the quantization of the Hall conductance," *Annals of Physics*, vol. 160, no. 2, pp. 343–354, Apr. 1985. DOI: 10.1016/0003-4916(85)90148-4.

[23] H. C. Po, H. Watanabe, and A. Vishwanath, "Fragile topology and wannier obstructions," *Phys. Rev. Lett.*, vol. 121, p. 126 402, 12 Sep. 2018. DOI: 10.1103/PhysRevLett.121.126402.

[24] J. Ahn, S. Park, and B.-J. Yang, "Failure of nielsen-ninomiya theorem and fragile topology in two-dimensional systems with space-time inversion symmetry: Application to twisted bilayer graphene at magic angle," *Phys. Rev. X*, vol. 9, p. 021 013, 2 Apr. 2019. DOI: 10.1103/PhysRevX.9.021013.

[25] A. Bouhon, A. M. Black-Schaffer, and R.-J. Slager, "Wilson loop approach to fragile topology of split elementary band representations and topological crystalline insulators with time-reversal symmetry," *Phys. Rev. B*, vol. 100, p. 195 135, 19 Nov. 2019. DOI: 10.1103/PhysRevB.100.195135.

[26] D. V. Else, H. C. Po, and H. Watanabe, "Fragile topological phases in interacting systems," *Phys. Rev. B*, vol. 99, p. 125 122, 12 Mar. 2019. DOI: 10.1103/PhysRevB.99.125122.

[27] B. Bradlyn, Z. Wang, J. Cano, and B. A. Bernevig, "Disconnected elementary band representations, fragile topology, and wilson loops as topological indices: An example on the triangular lattice," *Phys. Rev. B*, vol. 99, p. 045 140, 4 Jan. 2019. DOI: 10.1103/PhysRevB.99.045140.

[28] N. Marzari and D. Vanderbilt, "Maximally localized generalized wannier functions for composite energy bands," *Phys. Rev. B*, vol. 56, pp. 12 847–12 865, 20 Nov. 1997. DOI: 10.1103/PhysRevB.56.12847.

[29] A. Altland and B. Simons, *Condensed matter field theory*. 2023. DOI: 10.1017/9781108781244.

[30] N. Bultinck, S. Chatterjee, and M. P. Zaletel, "Mechanism for anomalous hall ferromagnetism in twisted bilayer graphene," *Phys. Rev. Lett.*, vol. 124, p. 166 601, 16 Apr. 2020. DOI: 10.1103/PhysRevLett.124.166601.

[31] N. Bultinck, E. Khalaf, S. Liu, S. Chatterjee, A. Vishwanath, and M. P. Zaletel, "Ground state and hidden symmetry of magic-angle graphene at even integer filling," *Phys. Rev. X*, vol. 10, p. 031 034, 3 Aug. 2020. DOI: 10.1103/PhysRevX.10.031034.

[32] P. J. Ledwith, E. Khalaf, and A. Vishwanath, "Strong coupling theory of magic-angle graphene: A pedagogical introduction," *Annals of Physics*, vol. 435, p. 168 646, 2021, Special issue on Philip W. Anderson, ISSN: 0003-4916. DOI: https://doi.org/10.1016/j.aop.2021.168646.

[33] Y. Xie, A. T. Pierce, J. M. Park, *et al.*, "Fractional Chern insulators in magic-angle twisted bilayer graphene," *Nature*, vol. 600, no. 7889, pp. 439–443, Dec. 2021. DOI: 10.1038/s41586-021-04002-3.

[34] S. R. White, "Density matrix formulation for quantum renormalization groups," *Phys. Rev. Lett.*, vol. 69, pp. 2863–2866, 19 Nov. 1992. DOI: 10.1103/PhysRevLett.69.2863.

[35] S. R. White, "Density-matrix algorithms for quantum renormalization groups," *Phys. Rev. B*, vol. 48, pp. 10 345–10 356, 14 Oct. 1993. DOI: 10.1103/PhysRevB.48.10345.

[36] I. P. McCulloch, "Infinite size density matrix renormalization group, revisited," *arXiv e-prints*, arXiv:0804.2509, Apr. 2008. DOI: 10.48550/arXiv.0804.2509.

[37] V. Kalmeyer and R. B. Laughlin, "Equivalence of the resonating-valence-bond and fractional quantum hall states," *Phys. Rev. Lett.*, vol. 59, pp. 2095–2098, 18 Nov. 1987. DOI: 10.1103/PhysRevLett.59.2095.

[38] V. Kalmeyer and R. B. Laughlin, "Theory of the spin liquid state of the heisenberg antiferromagnet," *Phys. Rev. B*, vol. 39, pp. 11 879–11 899, 16 Jun. 1989. DOI: 10.1103/PhysRevB.39.11879.

[39] R. B. Laughlin, "Superconducting Ground State of Noninteracting Particles Obeying Fractional Statistics," *Physical Review Letters*, vol. 60, no. 25, pp. 2677–2680, Jun. 1988, Publisher: American Physical Society. DOI: 10.1103/PhysRevLett.60.2677.

[40] R. B. Laughlin, "The Relationship Between High-Temperature Superconductivity and the Fractional Quantum Hall Effect," *Science*, vol. 242, no. 4878, pp. 525–533, Oct. 1988, Publisher: American Association for the Advancement of Science. DOI: 10.1126/science.242.4878.525.

[41] R. B. Laughlin, "Nobel Lecture: Fractional quantization," *Reviews of Modern Physics*, vol. 71, no. 4, pp. 863–874, Jul. 1999. DOI: 10.1103/RevModPhys.71.863.

[42] K. v. Klitzing, G. Dorda, and M. Pepper, "New method for high-accuracy determination of the fine-structure constant based on quantized hall resistance," *Phys. Rev. Lett.*, vol. 45, pp. 494–497, 6 Aug. 1980. DOI: 10.1103/PhysRevLett.45.494.

[43] S. M. Girvin, "Course 2: The Quantum Hall Effect: Novel Excitations and Broken Symmetries," in *Topological Aspects of Low Dimensional Systems*, A. Comtet, T. Jolicoeur, S. Ouvry, and F. David, Eds., vol. 69, Jan. 1999, p. 53. DOI: 10.48550/arXiv.cond-mat/9907002.

[44] R. B. Laughlin, "Quantized hall conductivity in two dimensions," *Phys. Rev. B*, vol. 23, pp. 5632–5633, 10 May 1981. DOI: 10.1103/PhysRevB.23.5632.

[45] B. I. Halperin, "Quantized hall conductance, current-carrying edge states, and the existence of extended states in a two-dimensional disordered potential," *Phys. Rev. B*, vol. 25, pp. 2185–2190, 4 Feb. 1982. DOI: 10.1103/PhysRevB.25.2185.

[46] Q. Niu and D. J. Thouless, "Quantised adiabatic charge transport in the presence of substrate disorder and many-body interaction," *Journal of Physics A Mathematical General*, vol. 17, no. 12, pp. 2453–2462, Aug. 1984. DOI: 10.1088/0305-4470/17/12/016.

[47] L. A. Ponomarenko, R. V. Gorbachev, G. L. Yu, *et al.*, "Cloning of Dirac fermions in graphene superlattices,", vol. 497, no. 7451, pp. 594–597, May 2013. DOI: 10.1038/nature12187.

[48] C. R. Dean, L. Wang, P. Maher, *et al.*, "Hofstadter's butterfly and the fractal quantum Hall effect in moiré superlattices,", vol. 497, no. 7451, pp. 598–602, May 2013. DOI: 10.1038/nature12186.

[49] B. Hunt, J. D. Sanchez-Yamagishi, A. F. Young, *et al.*, "Massive Dirac Fermions and Hofstadter Butterfly in a van der Waals Heterostructure," *Science*, vol. 340, no. 6139, pp. 1427–1430, Jun. 2013. DOI: 10.1126/science.1237240.

[50] C.-Z. Chang, C.-X. Liu, and A. H. MacDonald, "Colloquium: Quantum anomalous hall effect," *Rev. Mod. Phys.*, vol. 95, p. 011 002, 1 Jan. 2023. DOI: 10.1103/RevModPhys.95.011002.

[51] F. D. M. Haldane, "Model for a quantum hall effect without landau levels: Condensed-matter realization of the "parity anomaly"," *Phys. Rev. Lett.*, vol. 61, pp. 2015–2018, 18 Oct. 1988. DOI: 10.1103/PhysRevLett.61.2015.

[52] C.-Z. Chang, J. Zhang, X. Feng, *et al.*, "Experimental Observation of the Quantum Anomalous Hall Effect in a Magnetic Topological Insulator," *Science*, vol. 340, no. 6129, pp. 167–170, Apr. 2013. DOI: 10.1126/science.1234414.

[53] C.-X. Liu, S.-C. Zhang, and X.-L. Qi, "The Quantum Anomalous Hall Effect: Theory and Experiment," *Annual Review of Condensed Matter Physics*, vol. 7, pp. 301–321, Mar. 2016. DOI: 10.1146/annurev-conmatphys-031115-011417.

[54] G. Chen, A. L. Sharpe, E. J. Fox, *et al.*, "Tunable correlated Chern insulator and ferromagnetism in a moiré superlattice,", vol. 579, no. 7797, pp. 56–61, Mar. 2020. DOI: 10.1038/s41586-020-2049-7.

[55] S. L. Sondhi, A. Karlhede, S. A. Kivelson, and E. H. Rezayi, "Skyrmions and the crossover from the integer to fractional quantum hall effect at small zeeman energies," *Phys. Rev. B*, vol. 47, pp. 16 419–16 426, 24 Jun. 1993. DOI: 10.1103/PhysRevB.47.16419.

[56] K. Moon, H. Mori, K. Yang, *et al.*, "Spontaneous interlayer coherence in double-layer quantum hall systems: Charged vortices and kosterlitz-thouless phase transitions," *Phys. Rev. B*, vol. 51, pp. 5138–5170, 8 Feb. 1995. DOI: 10.1103/PhysRevB.51.5138.

[57] A. H. MacDonald, H. A. Fertig, and L. Brey, "Skyrmions without sigma models in quantum hall ferromagnets," *Phys. Rev. Lett.*, vol. 76, pp. 2153–2156, 12 Mar. 1996. DOI: 10.1103/PhysRevLett.76.2153.

[58] J. P. Eisenstein, "Exciton Condensation in Bilayer Quantum Hall Systems," *Annual Review of Condensed Matter Physics*, vol. 5, pp. 159–181, Mar. 2014. DOI: 10.1146/annurev-conmatphys-031113-133832.

[59] E. Tutuc, M. Shayegan, and D. A. Huse, "Counterflow measurements in strongly correlated gaas hole bilayers: Evidence for electron-hole pairing," *Phys. Rev. Lett.*, vol. 93, p. 036 802, 3 Jul. 2004. DOI: 10.1103/PhysRevLett.93.036802.

[60] K. Nomura and A. H. MacDonald, "Quantum hall ferromagnetism in graphene," *Phys. Rev. Lett.*, vol. 96, p. 256 602, 25 Jun. 2006. DOI: 10.1103/PhysRevLett.96.256602.

[61] A. F. Young, C. R. Dean, L. Wang, *et al.*, "Spin and valley quantum Hall ferromagnetism in graphene," *Nature Physics*, vol. 8, no. 7, pp. 550–556, Jul. 2012. DOI: 10.1038/nphys2307.

[62] Y. Barlas, K. Yang, and A. H. MacDonald, "Quantum Hall effects in graphene-based two-dimensional electron systems," *Nanotechnology*, vol. 23, no. 5, 052001, p. 052 001, Feb. 2012. DOI: 10.1088/0957-4484/23/5/052001.

[63] J. Kang and O. Vafek, "Strong coupling phases of partially filled twisted bilayer graphene narrow bands," *Phys. Rev. Lett.*, vol. 122, p. 246 401, 24 Jun. 2019. DOI: 10.1103/PhysRevLett.122.246401.

[64] A. H. Castro Neto, F. Guinea, N. M. R. Peres, K. S. Novoselov, and A. K. Geim, "The electronic properties of graphene," *Rev. Mod. Phys.*, vol. 81, pp. 109–162, 1 Jan. 2009. DOI: 10.1103/RevModPhys.81.109.

[65] M. I. B. Utama, R. J. Koch, K. Lee, *et al.*, "Visualization of the flat electronic band in twisted bilayer graphene near the magic angle twist," *Nature Physics*, vol. 17, no. 2, pp. 184–188, Feb. 2021. DOI: 10.1038/s41567-020-0974-x.

[66] Q. Li, H. Zhang, Y. Wang, *et al.*, "Evolution of the flat band and the role of lattice relaxations in twisted bilayer graphene," *Nature Materials*, vol. 23, no. 8, pp. 1070–1076, Aug. 2024, ISSN: 1476-4660. DOI: 10.1038/s41563-024-01858-4.

[67] J. Xiao, A. Inbar, J. Birkbeck, *et al.*, "The Interacting Energy Bands of Magic Angle Twisted Bilayer Graphene Revealed by the Quantum Twisting Microscope," *arXiv e-prints*, arXiv:2506.20738, arXiv:2506.20738, Jun. 2025. DOI: 10.48550/arXiv.2506.20738.

[68] H. C. Po, L. Zou, A. Vishwanath, and T. Senthil, "Origin of mott insulating behavior and superconductivity in twisted bilayer graphene," *Phys. Rev. X*, vol. 8, p. 031 089, 3 Sep. 2018. DOI: 10.1103/PhysRevX.8.031089.

[69] H. C. Po, L. Zou, T. Senthil, and A. Vishwanath, "Faithful tight-binding models and fragile topology of magic-angle bilayer graphene," *Phys. Rev. B*, vol. 99, p. 195 455, 19 May 2019. DOI: 10.1103/PhysRevB.99.195455.

[70] L. Zou, H. C. Po, A. Vishwanath, and T. Senthil, "Band structure of twisted bilayer graphene: Emergent symmetries, commensurate approximants, and wannier obstructions," *Phys. Rev. B*, vol. 98, p. 085 435, 8 Aug. 2018. DOI: 10.1103/PhysRevB.98.085435.

[71] Z. Song, Z. Wang, W. Shi, G. Li, C. Fang, and B. A. Bernevig, "All magic angles in twisted bilayer graphene are topological," *Phys. Rev. Lett.*, vol. 123, p. 036 401, 3 Jul. 2019. DOI: 10.1103/PhysRevLett.123.036401.

[72] K. Hejazi, C. Liu, H. Shapourian, X. Chen, and L. Balents, "Multiple topological transitions in twisted bilayer graphene near the first magic angle," *Phys. Rev. B*, vol. 99, p. 035 111, 3 Jan. 2019. DOI: 10.1103/PhysRevB.99.035111.

[73] J. Liu, J. Liu, and X. Dai, "Pseudo landau level representation of twisted bilayer graphene: Band topology and implications on the correlated insulating phase," *Phys. Rev. B*, vol. 99, p. 155 415, 15 Apr. 2019. DOI: 10.1103/PhysRevB.99.155415.

[74] G. Tarnopolsky, A. J. Kruchkov, and A. Vishwanath, "Origin of magic angles in twisted bilayer graphene," *Phys. Rev. Lett.*, vol. 122, p. 106 405, 10 Mar. 2019. DOI: 10.1103/PhysRevLett.122.106405.

[75] B. Lian, Z.-D. Song, N. Regnault, D. K. Efetov, A. Yazdani, and B. A. Bernevig, "Twisted bilayer graphene. iv. exact insulator ground states and phase diagram," *Phys. Rev. B*, vol. 103, p. 205 414, 20 May 2021. DOI: 10.1103/PhysRevB.103.205414.

[76] M. Koshino, N. F. Q. Yuan, T. Koretsune, M. Ochi, K. Kuroki, and L. Fu, "Maximally localized wannier orbitals and the extended hubbard model for twisted bilayer graphene," *Phys. Rev. X*, vol. 8, p. 031 087, 3 Sep. 2018. DOI: 10.1103/PhysRevX.8.031087.

[77] N. N. T. Nam and M. Koshino, "Lattice relaxation and energy band modulation in twisted bilayer graphene," *Phys. Rev. B*, vol. 96, p. 075 311, 7 Aug. 2017. DOI: 10.1103/PhysRevB.96.075311.

[78] S. Carr, S. Fang, Z. Zhu, and E. Kaxiras, "Exact continuum model for low-energy electronic states of twisted bilayer graphene," *Phys. Rev. Res.*, vol. 1, p. 013 001, 1 Aug. 2019. DOI: 10.1103/PhysRevResearch.1.013001.

[79] E. Khalaf, S. Chatterjee, N. Bultinck, M. P. Zaletel, and A. Vishwanath, "Charged skyrmions and topological origin of superconductivity in magic-angle graphene," *Science Advances*, vol. 7, no. 19, May 2021, ISSN: 2375-2548. DOI: 10.1126/sciadv.abf5299.

[80] D. Wong, K. P. Nuckolls, M. Oh, *et al.*, "Cascade of electronic transitions in magic-angle twisted bilayer graphene,", vol. 582, no. 7811, pp. 198–202, Jun. 2020. DOI: 10.1038/s41586-020-2339-0.

[81] U. Zondiner, A. Rozen, D. Rodan-Legrain, *et al.*, "Cascade of phase transitions and Dirac revivals in magic-angle graphene,", vol. 582, no. 7811, pp. 203–208, Jun. 2020. DOI: 10.1038/s41586-020-2373-y.

[82] X.-G. Wen, *Quantum Field Theory of Many-Body Systems: From the Origin of Sound to an Origin of Light and Electrons*. Oxford University Press, Sep. 2007, ISBN: 9 780199 227259. DOI: 10.1093/acprof:oso/9780199227259.001.0001.

[83] D. C. Tsui, H. L. Stormer, and A. C. Gossard, "Two-dimensional magnetotransport in the extreme quantum limit," *Phys. Rev. Lett.*, vol. 48, pp. 1559–1562, 22 May 1982. DOI: 10.1103/PhysRevLett.48.1559.

[84] T. H. Hansson, M. Hermanns, S. H. Simon, and S. F. Viefers, "Quantum hall physics: Hierarchies and conformal field theory techniques," *Rev. Mod. Phys.*, vol. 89, p. 025 005, 2 May 2017. DOI: 10.1103/RevModPhys.89.025005.

[85] R. B. Laughlin, "Anomalous quantum hall effect: An incompressible quantum fluid with fractionally charged excitations," *Phys. Rev. Lett.*, vol. 50, pp. 1395–1398, 18 May 1983. DOI: 10.1103/PhysRevLett.50.1395.

[86] A. Kitaev, "Anyons in an exactly solved model and beyond," *Annals of Physics*, vol. 321, no. 1, pp. 2–111, 2006, January Special Issue, ISSN: 0003-4916. DOI: https://doi.org/10.1016/j.aop.2005.10.005.

[87] B. I. Halperin, "Statistics of quasiparticles and the hierarchy of fractional quantized hall states," *Phys. Rev. Lett.*, vol. 52, pp. 1583–1586, 18 Apr. 1984. DOI: 10.1103/PhysRevLett.52.1583.

[88] X. G. Wen and Q. Niu, "Ground-state degeneracy of the fractional quantum hall states in the presence of a random potential and on high-genus riemann surfaces," *Phys. Rev. B*, vol. 41, pp. 9377–9396, 13 May 1990. DOI: 10.1103/PhysRevB.41.9377.

[89] Z. Liu and E. J. Bergholtz, "Recent developments in fractional Chern insulators," in *Encyclopedia of Condensed Matter Physics (Second Edition)*, T. Chakraborty, Ed., Second Edition, Oxford: Academic Press, 2024, pp. 515–538, ISBN: 978-0-323-91408-6. DOI: https://doi.org/10.1016/B978-0-323-90800-9.00136-0.

[90] J. Cai, E. Anderson, C. Wang, *et al.*, "Signatures of fractional quantum anomalous Hall states in twisted $MoTe_2$," *Nature*, vol. 622, no. 7981, pp. 63–68, Oct. 2023. DOI: 10.1038/s41586-023-06289-w.

[91] Y. Zeng, Z. Xia, K. Kang, *et al.*, "Thermodynamic evidence of fractional chern insulator in moiré mote2," *Nature*, vol. 622, no. 7981, pp. 69–73, Jul. 2023, ISSN: 1476-4687. DOI: 10.1038/s41586-023-06452-3.

[92] H. Park, J. Cai, E. Anderson, *et al.*, "Observation of fractionally quantized anomalous Hall effect," *Nature*, vol. 622, no. 7981, pp. 74–79, Oct. 2023. DOI: 10.1038/s41586-023-06536-0.

[93] Z. Lu, T. Han, Y. Yao, *et al.*, "Fractional quantum anomalous Hall effect in multilayer graphene," *Nature*, vol. 626, no. 8000, pp. 759–764, Feb. 2024. DOI: 10.1038/s41586-023-07010-7.

[94] A. Auerbach, *Interacting electrons and quantum magnetism*. Springer Science & Business Media, 1998.

[95] R. Masaoka, T. Soejima, and H. Watanabe, "Quadratic dispersion relations in gapless frustration-free systems," *Phys. Rev. B*, vol. 110, p. 195 140, 19 Nov. 2024. DOI: 10.1103/PhysRevB.110.195140.

[96] R. Peierls, "Zur Theorie des Diamagnetismus von Leitungselektronen," *Zeitschrift fur Physik*, vol. 80, no. 11-12, pp. 763–791, Nov. 1933. DOI: 10.1007/BF01342591.

[97] F. D. M. Haldane and E. H. Rezayi, "Periodic laughlin-jastrow wave functions for the fractional quantized hall effect," *Phys. Rev. B*, vol. 31, pp. 2529–2531, 4 Feb. 1985. DOI: 10.1103/PhysRevB.31.2529.

[98] X.-G. Wen, "Topological Orders and Chern-Simons Theory in Strongly Correlated Quantum Liquid," *International Journal of Modern Physics B*, vol. 5, no. 10, pp. 1641–1648, Jan. 1991. DOI: 10.1142/S0217979291001541.

[99] L. Cincio and G. Vidal, "Characterizing topological order by studying the ground states on an infinite cylinder," *Phys. Rev. Lett.*, vol. 110, p. 067 208, 6 Feb. 2013. DOI: 10.1103/PhysRevLett.110.067208.

[100] Z. Zhu and S. R. White, "Spin liquid phase of the $S = \frac{1}{2}$ $J_1 - J_2$ heisenberg model on the triangular lattice," *Phys. Rev. B*, vol. 92, p. 041 105, 4 Jul. 2015. DOI: 10.1103/PhysRevB.92.041105.

[101] R. B. Laughlin, "Spin hamiltonian for which quantum hall wavefunction is exact," *Annals of Physics*, vol. 191, no. 1, pp. 163–202, Apr. 1989. DOI: 10.1016/0003-4916(89)90339-4.

[102] R. Thomale, E. Kapit, D. F. Schroeter, and M. Greiter, "Parent hamiltonian for the chiral spin liquid," *Phys. Rev. B*, vol. 80, p. 104 406, 10 Sep. 2009. DOI: 10.1103/PhysRevB.80.104406.

[103] A. E. B. Nielsen, J. I. Cirac, and G. Sierra, "Laughlin spin-liquid states on lattices obtained from conformal field theory," *Phys. Rev. Lett.*, vol. 108, p. 257 206, 25 Jun. 2012. DOI: 10.1103/PhysRevLett.108.257206.

[104] S.-S. Gong, W. Zhu, J.-X. Zhu, D. N. Sheng, and K. Yang, "Global phase diagram and quantum spin liquids in a spin-$\frac{1}{2}$ triangular antiferromagnet," *Phys. Rev. B*, vol. 96, p. 075 116, 7 Aug. 2017. DOI: 10.1103/PhysRevB.96.075116.

[105] A. Wietek and A. M. Läuchli, "Chiral spin liquid and quantum criticality in extended S =1/2 Heisenberg models on the triangular lattice,", vol. 95, no. 3, 035141, p. 035 141, Jan. 2017. DOI: 10.1103/PhysRevB.95.035141.

[106] S. N. Saadatmand and I. P. McCulloch, "Detection and characterization of symmetry-broken long-range orders in the spin-$\frac{1}{2}$ triangular heisenberg model," *Phys. Rev. B*, vol. 96, p. 075 117, 7 Aug. 2017. DOI: 10.1103/PhysRevB.96.075117.

[107] A. Szasz, J. Motruk, M. P. Zaletel, and J. E. Moore, "Chiral spin liquid phase of the triangular lattice hubbard model: A density matrix renormalization group study," *Phys. Rev. X*, vol. 10, p. 021 042, 2 May 2020. DOI: 10.1103/PhysRevX.10.021042.

[108] A. Szasz and J. Motruk, "Phase diagram of the anisotropic triangular lattice hubbard model," *Phys. Rev. B*, vol. 103, p. 235 132, 23 Jun. 2021. DOI: 10.1103/PhysRevB.103.235132.

[109] T. Cookmeyer, J. Motruk, and J. E. Moore, "Four-spin terms and the origin of the chiral spin liquid in mott insulators on the triangular lattice," *Phys. Rev. Lett.*, vol. 127, p. 087 201, 8 Aug. 2021. DOI: 10.1103/PhysRevLett.127.087201.

[110] Z. Zou and R. Laughlin, "Charged excitations of the chiral spin liquid," *Physical Review B*, vol. 42, no. 7, p. 4073, 1990.

[111] X. G. Wen, F. Wilczek, and A. Zee, "Chiral spin states and superconductivity," *Phys. Rev. B*, vol. 39, pp. 11 413–11 423, 16 Jun. 1989. DOI: 10.1103/PhysRevB.39.11413.

[112] A. L. Fetter, C. B. Hanna, and R. B. Laughlin, "Random-phase approximation in the fractional-statistics gas," *Physical Review B*, vol. 39, no. 13, pp. 9679–9681, May 1989, Publisher: American Physical Society. DOI: 10.1103/PhysRevB.39.9679.

[113] Y.-H. Chen, F. Wilczek, E. Witten, and B. I. Halperin, "On Anyon Superconductivity," *International Journal of Modern Physics B*, vol. 3, no. 7, pp. 1001–1067, Jan. 1989. DOI: 10.1142/S0217979289000725.

[114] S. Divic, T. Soejima, V. Crépel, M. P. Zaletel, and A. Millis, "Chiral Spin Liquid and Quantum Phase Transition in the Triangular Lattice Hofstadter-Hubbard Model," *arXiv e-prints*, arXiv:2406.15348, Jun. 2024. DOI: 10.48550/arXiv.2406.15348.

[115] S. Divic, V. Crépel, T. Soejima, *et al.*, "Anyon superconductivity from topological criticality in a hofstadter hubbard model," *Proceedings of the National Academy of Sciences*, vol. 122, no. 33, e2426680122, 2025. DOI: 10.1073/pnas.2426680122.

[116] D. Sen and R. Chitra, "Large-u limit of a hubbard model in a magnetic field: Chiral spin interactions and paramagnetism," *Phys. Rev. B*, vol. 51, pp. 1922–1925, 3 Jan. 1995. DOI: 10.1103/PhysRevB.51.1922.

[117] O. I. Motrunich, "Orbital magnetic field effects in spin liquid with spinon fermi sea: Possible application to $\kappa-(ET)_2Cu_2(CN)_3$," *Phys. Rev. B*, vol. 73, p. 155 115, 15 Apr. 2006. DOI: 10.1103/PhysRevB.73.155115.

[118] C. Kuhlenkamp, W. Kadow, A. Imamoglu, and M. Knap, "Chiral pseudospin liquids in moiré heterostructures," *Phys. Rev. X*, vol. 14, p. 021 013, 2 Apr. 2024. DOI: 10.1103/PhysRevX.14.021013.

[119] Y.-H. Zhang, D. N. Sheng, and A. Vishwanath, "Su(4) chiral spin liquid, exciton supersolid, and electric detection in moiré bilayers," *Phys. Rev. Lett.*, vol. 127, p. 247 701, 24 Dec. 2021. DOI: 10.1103/PhysRevLett.127.247701.

[120] R. Sahay, S. Divic, D. E. Parker, *et al.*, "Superconductivity in a topological lattice model with strong repulsion," *Phys. Rev. B*, vol. 110, p. 195 126, 19 Nov. 2024. DOI: 10.1103/PhysRevB.110.195126.

[121] V. P. Mineev, K. Samokhin, and L. Landau, *Introduction to unconventional superconductivity*. CRC Press, 1999.

[122] J. Bardeen, L. N. Cooper, and J. R. Schrieffer, "Theory of superconductivity," *Phys. Rev.*, vol. 108, pp. 1175–1204, 5 Dec. 1957. DOI: 10.1103/PhysRev.108.1175.

[123] W. Kohn and J. M. Luttinger, "New mechanism for superconductivity," *Phys. Rev. Lett.*, vol. 15, pp. 524–526, 12 Sep. 1965. DOI: 10.1103/PhysRevLett.15.524.

[124] M. Sigrist and K. Ueda, "Phenomenological theory of unconventional superconductivity," *Rev. Mod. Phys.*, vol. 63, pp. 239–311, 2 Apr. 1991. DOI: 10.1103/RevModPhys.63.239.

[125] K. M. Shen and J. S. Davis, "Cuprate high-tc superconductors," *Materials today*, vol. 11, no. 9, pp. 14–21, 2008.

[126] P. W. ANDERSON, *The Theory of Superconductivity in the High-T"c" Cuprate Superconductors*. Princeton University Press, 1997.

[127] P. A. Lee, N. Nagaosa, and X.-G. Wen, "Doping a mott insulator: Physics of high-temperature superconductivity," *Rev. Mod. Phys.*, vol. 78, pp. 17–85, 1 Jan. 2006. DOI: 10.1103/RevModPhys.78.17.

[128] S. Sachdev, "Colloquium: Order and quantum phase transitions in the cuprate superconductors," *Rev. Mod. Phys.*, vol. 75, pp. 913–932, 3 Jul. 2003. DOI: 10.1103/RevModPhys.75.913.

[129] B. Keimer, S. A. Kivelson, M. R. Norman, S. Uchida, and J. Zaanen, "High Temperature Superconductivity in the Cuprates," *arXiv e-prints*, arXiv:1409.4673, Sep. 2014. DOI: 10.48550/arXiv.1409.4673.

[130] H.-H. Wen and S. Li, "Materials and Novel Superconductivity in Iron Pnictide Superconductors," *Annual Review of Condensed Matter Physics*, vol. 2, pp. 121–140, Mar. 2011. DOI: 10.1146/annurev-conmatphys-062910-140518.

[131] Q. Si, R. Yu, and E. Abrahams, "High-temperature superconductivity in iron pnictides and chalcogenides," *Nature Reviews Materials*, vol. 1, no. 4, p. 16 017, Apr. 2016. DOI: 10.1038/natrevmats.2016.17.

[132] R. M. Fernandes, A. I. Coldea, H. Ding, I. R. Fisher, P. J. Hirschfeld, and G. Kotliar, "Iron pnictides and chalcogenides: a new paradigm for superconductivity,", vol. 601, no. 7891, pp. 35–44, Jan. 2022. DOI: 10.1038/s41586-021-04073-2.

[133] M. Yankowitz, S. Chen, H. Polshyn, *et al.*, "Tuning superconductivity in twisted bilayer graphene," *Science*, vol. 363, no. 6431, pp. 1059–1064, Mar. 2019. DOI: 10.1126/science.aav1910.

[134] X. Lu, P. Stepanov, W. Yang, *et al.*, "Superconductors, orbital magnets and correlated states in magic-angle bilayer graphene,", vol. 574, no. 7780, pp. 653–657, Oct. 2019. DOI: 10.1038/s41586-019-1695-0.

[135] E. Codecido, Q. Wang, R. Koester, *et al.*, "Correlated insulating and superconducting states in twisted bilayer graphene below the magic angle," *Science Advances*, vol. 5, no. 9, eaaw9770, 2019. DOI: 10.1126/sciadv.aaw9770.

[136] H. S. Arora, R. Polski, Y. Zhang, *et al.*, "Superconductivity in metallic twisted bilayer graphene stabilized by WSe_2,", vol. 583, no. 7816, pp. 379–384, Jul. 2020. DOI: 10.1038/s41586-020-2473-8.

[137] K. P. Nuckolls, R. L. Lee, M. Oh, *et al.*, "Quantum textures of the many-body wavefunctions in magic-angle graphene,", vol. 620, no. 7974, pp. 525–532, Aug. 2023. DOI: 10.1038/s41586-023-06226-x.

[138] Y. Zhang, R. Polski, C. Lewandowski, *et al.*, "Promotion of superconductivity in magic-angle graphene multilayers," *Science*, vol. 377, no. 6614, pp. 1538–1543, Sep. 2022. DOI: 10.1126/science.abn8585.

[139] J. M. Park, Y. Cao, K. Watanabe, T. Taniguchi, and P. Jarillo-Herrero, "Tunable strongly coupled superconductivity in magic-angle twisted trilayer graphene,", vol. 590, no. 7845, pp. 249–255, Feb. 2021. DOI: 10.1038/s41586-021-03192-0.

[140] Z. Hao, A. M. Zimmerman, P. Ledwith, *et al.*, "Electric field–tunable superconductivity in alternating-twist magic-angle trilayer graphene," *Science*, vol. 371, no. 6534, pp. 1133–1138, Mar. 2021. DOI: 10.1126/science.abg0399.

[141] H. Kim, Y. Choi, C. Lewandowski, *et al.*, "Evidence for unconventional superconductivity in twisted trilayer graphene,", vol. 606, no. 7914, pp. 494–500, Jun. 2022. DOI: 10.1038/s41586-022-04715-z.

[142] J. M. Park, Y. Cao, L.-Q. Xia, *et al.*, "Robust superconductivity in magic-angle multilayer graphene family," *Nature Materials*, vol. 21, no. 8, pp. 877–883, Jul. 2022. DOI: 10.1038/s41563-022-01287-1.

[143] H. Zhou, T. Xie, T. Taniguchi, K. Watanabe, and A. F. Young, "Superconductivity in rhombohedral trilayer graphene,", vol. 598, no. 7881, pp. 434–438, Sep. 2021. DOI: 10.1038/s41586-021-03926-0.

[144] Y. Zhang, R. Polski, A. Thomson, *et al.*, "Enhanced superconductivity in spin-orbit proximitized bi-layer graphene,", vol. 613, no. 7943, pp. 268–273, Jan. 2023. DOI: 10.1038/s41586-022-05446-x.

[145] J. Hubbard, "Electron Correlations in Narrow Energy Bands," *Proceedings of the Royal Society of London Series A*, vol. 276, no. 1365, pp. 238–257, Nov. 1963. DOI: 10.1098/rspa.1963.0204.

[146] D. P. Arovas, E. Berg, S. A. Kivelson, and S. Raghu, "The Hubbard Model," *Annual Review of Condensed Matter Physics*, vol. 13, pp. 239–274, Mar. 2022. DOI: 10.1146/annurev-conmatphys-031620-102024.

[147] H. Tasaki, "The Hubbard Model: Introduction and Selected Rigorous Results," *arXiv e-prints*, cond-mat/9512169, cond–mat/9512169, Dec. 1995. DOI: 10.48550/arXiv.cond-mat/9512169.

[148] M. Dine, T. Banks, and S. Sachdev. WORLD SCIENTIFIC, 2011, pp. 559–620. DOI: 10.1142/8153.

[149] S.-S. Lee and P. A. Lee, "U(1) gauge theory of the hubbard model: Spin liquid states and possible application to $\kappa-(\mathrm{BEDT-TTF})_2\mathrm{Cu}_2(\mathrm{CN})_3$," *Phys. Rev. Lett.*, vol. 95, p. 036 403, 3 Jul. 2005. DOI: 10.1103/PhysRevLett.95.036403.

[150] W. Wu, M. S. Scheurer, S. Chatterjee, S. Sachdev, A. Georges, and M. Ferrero, "Pseudogap and fermi-surface topology in the two-dimensional hubbard model," *Phys. Rev. X*, vol. 8, p. 021 048, 2 May 2018. DOI: 10.1103/PhysRevX.8.021048.

[151] M. S. Scheurer, S. Chatterjee, W. Wu, M. Ferrero, A. Georges, and S. Sachdev, "Topological order in the pseudogap metal," *Proceedings of the National Academy of Science*, vol. 115, no. 16, E3665–E3672, Apr. 2018. DOI: 10.1073/pnas.1720580115.

[152] S. Sachdev, "Topological order, emergent gauge fields, and Fermi surface reconstruction," *Reports on Progress in Physics*, vol. 82, no. 1, 014001, p. 014 001, Jan. 2019. DOI: 10.1088/1361-6633/aae110.

[153] C. S. Chiu, G. Ji, A. Mazurenko, D. Greif, and M. Greiner, "Quantum state engineering of a hubbard system with ultracold fermions," *Phys. Rev. Lett.*, vol. 120, p. 243 201, 24 Jun. 2018. DOI: 10.1103/PhysRevLett.120.243201.

[154] A. Mazurenko, C. S. Chiu, G. Ji, *et al.*, "A cold-atom Fermi-Hubbard antiferromagnet,", vol. 545, no. 7655, pp. 462–466, May 2017. DOI: 10.1038/nature22362.

[155] D. Mitra, P. T. Brown, E. Guardado-Sanchez, *et al.*, "Quantum gas microscopy of an attractive Fermi-Hubbard system," *Nature Physics*, vol. 14, no. 2, pp. 173–177, Feb. 2018. DOI: 10.1038/nphys4297.

[156] S. Scherg, T. Kohlert, P. Sala, *et al.*, "Observing non-ergodicity due to kinetic constraints in tilted Fermi-Hubbard chains," *Nature Communications*, vol. 12, 4490, p. 4490, Jul. 2021. DOI: 10.1038/s41467-021-24726-0.

[157] A. Bohrdt, L. Homeier, C. Reinmoser, E. Demler, and F. Grusdt, "Exploration of doped quantum magnets with ultracold atoms," *Annals of Physics*, vol. 435, p. 168 651, 2021, Special issue on Philip W. Anderson, ISSN: 0003-4916. DOI: https://doi.org/10.1016/j.aop.2021.168651.

[158] B. M. Spar, E. Guardado-Sanchez, S. Chi, Z. Z. Yan, and W. S. Bakr, "Realization of a fermi-hubbard optical tweezer array," *Phys. Rev. Lett.*, vol. 128, p. 223 202, 22 Jun. 2022. DOI: 10.1103/PhysRevLett.128.223202.

[159] T. Hartke, B. Oreg, C. Turnbaugh, N. Jia, and M. Zwierlein, "Direct observation of nonlocal fermion pairing in an attractive Fermi-Hubbard gas," *Science*, vol. 381, no. 6653, pp. 82–86, Jul. 2023. DOI: 10.1126/science.ade4245.

[160] P. T. Brown, D. Mitra, E. Guardado-Sanchez, *et al.*, "Bad metallic transport in a cold atom Fermi-Hubbard system," *Science*, vol. 363, no. 6425, pp. 379–382, Jan. 2019. DOI: 10.1126/science.aat4134.

[161] D. Shaffer, J. Wang, and L. H. Santos, "Unconventional self-similar Hofstadter superconductivity from repulsive interactions," *Nature Communications*, vol. 13, 7785, p. 7785, Dec. 2022. DOI: 10.1038/s41467-022-35316-z.

[162] W.-L. Tu, F. Schindler, T. Neupert, and D. Poilblanc, "Competing orders in the hofstadter t-J model," *Phys. Rev. B*, vol. 97, p. 035 154, 3 Jan. 2018. DOI: 10.1103/PhysRevB.97.035154.

[163] M. M. Ma śka and M. Mierzejewski, "Upper critical field for anisotropic superconductivity: A tight-binding approach," *Phys. Rev. B*, vol. 64, p. 064 501, 6 Jul. 2001. DOI: 10.1103/PhysRevB.64.064501.

[164] R. O. Umucal ılar and M. Iskin, "Bcs theory of time-reversal-symmetric hofstadter-hubbard model," *Phys. Rev. Lett.*, vol. 119, p. 085 301, 8 Aug. 2017. DOI: 10.1103/PhysRevLett.119.085301.

[165] M. Iskin, "Hofstadter-hubbard model with opposite magnetic fields: Bardeen-cooper-schrieffer pairing and superfluidity in the nearly flat butterfly bands," *Phys. Rev. A*, vol. 96, p. 043 628, 4 Oct. 2017. DOI: 10.1103/PhysRevA.96.043628.

[166] V. Kozii, M. P. Zaletel, and N. Bultinck, "Spin-triplet superconductivity from intervalley goldstone modes in magic-angle graphene," *Phys. Rev. B*, vol. 106, p. 235 157, 23 Dec. 2022. DOI: 10.1103/PhysRevB.106.235157.

[167] J. Wen, M. Kargarian, A. Vaezi, and G. A. Fiete, "Doping the kane-mele-hubbard model: A slave-boson approach," *Phys. Rev. B*, vol. 84, p. 235 149, 23 Dec. 2011. DOI: 10.1103/PhysRevB.84.235149.

[168] S. Chatterjee, M. Ippoliti, and M. P. Zaletel, "Skyrmion superconductivity: Dmrg evidence for a topological route to superconductivity," *Phys. Rev. B*, vol. 106, p. 035 421, 3 Jul. 2022. DOI: 10.1103/PhysRevB.106.035421.

[169] M. Christos, S. Sachdev, and M. S. Scheurer, "Superconductivity, correlated insulators, and wess–zumino–witten terms in twisted bilayer graphene," *Proceedings of the National Academy of Sciences*, vol. 117, no. 47, pp. 29 543–29 554, Nov. 2020. DOI: 10.1073/pnas.2014691117.

[170] D. E. Parker, X. Cao, and M. P. Zaletel, "Local matrix product operators: Canonical form, compression, and control theory," *Phys. Rev. B*, vol. 102, p. 035 147, 3 Jul. 2020. DOI: 10.1103/PhysRevB.102.035147.

[171] O. Vafek and J. Kang, "Renormalization group study of hidden symmetry in twisted bilayer graphene with coulomb interactions," *Phys. Rev. Lett.*, vol. 125, p. 257 602, 25 Dec. 2020. DOI: 10.1103/PhysRevLett.125.257602.

[172] N. Goldman, I. Satija, P. Nikolic, *et al.*, "Realistic time-reversal invariant topological insulators with neutral atoms," *Phys. Rev. Lett.*, vol. 105, p. 255 302, 25 Dec. 2010. DOI: 10.1103/PhysRevLett.105.255302.

[173] M. Aidelsburger, M. Atala, M. Lohse, J. T. Barreiro, B. Paredes, and I. Bloch, "Realization of the Hofstadter Hamiltonian with Ultracold Atoms in Optical Lattices," *Physical Review Letters*, vol. 111, no. 18, p. 185 301, Oct. 2013. DOI: 10.1103/PhysRevLett.111.185301.

[174] C. J. Kennedy, G. A. Siviloglou, H. Miyake, W. C. Burton, and W. Ketterle, "Spin-orbit coupling and quantum spin hall effect for neutral atoms without spin flips," *Phys. Rev. Lett.*, vol. 111, p. 225 301, 22 Nov. 2013. DOI: 10.1103/PhysRevLett.111.225301.

[175] S. Zhang, C. Lv, and Q. Zhou, "Synthetic tensor gauge fields," *Physical Review Research*, vol. 7, no. 1, 013013, p. 013 013, Jan. 2025. DOI: 10.1103/PhysRevResearch.7.013013.

[176] F. Harper, S. H. Simon, and R. Roy, "Perturbative approach to flat chern bands in the hofstadter model," *Phys. Rev. B*, vol. 90, p. 075 104, 7 Aug. 2014. DOI: 10.1103/PhysRevB.90.075104.

[177] D. Bauer, T. S. Jackson, and R. Roy, "Quantum geometry and stability of the fractional quantum hall effect in the hofstadter model," *Phys. Rev. B*, vol. 93, p. 235 133, 23 Jun. 2016. DOI: 10.1103/PhysRevB.93.235133.

[178] V. Melik-Alaverdian and N. E. Bonesteel, "Composite fermions and landau-level mixing in the fractional quantum hall effect," *Phys. Rev. B*, vol. 52, R17032–R17035, 24 Dec. 1995. DOI: 10.1103/PhysRevB.52.R17032.

[179] X.-L. Qi, "Generic wave-function description of fractional quantum anomalous hall states and fractional topological insulators," *Phys. Rev. Lett.*, vol. 107, p. 126 803, 12 Sep. 2011. DOI: 10.1103/PhysRevLett.107.126803.

[180] C. Sgiarovello, M. Peressi, and R. Resta, "Electron localization in the insulating state: Application to crystalline semiconductors," *Phys. Rev. B*, vol. 64, p. 115 202, 11 Aug. 2001. DOI: 10.1103/PhysRevB.64.115202.

[181] A. A. Soluyanov and D. Vanderbilt, "Wannier representation of Z_2 topological insulators," *Phys. Rev. B*, vol. 83, p. 035 108, 3 Jan. 2011. DOI: 10.1103/PhysRevB.83.035108.

[182] A. A. Soluyanov and D. Vanderbilt, "Computing topological invariants without inversion symmetry," *Phys. Rev. B*, vol. 83, p. 235 401, 23 Jun. 2011. DOI: 10.1103/PhysRevB.83.235401.

[183] C. Repellin, Z. Dong, Y.-H. Zhang, and T. Senthil, "Ferromagnetism in narrow bands of moiré superlattices," *Phys. Rev. Lett.*, vol. 124, p. 187 601, 18 May 2020. DOI: 10.1103/PhysRevLett.124.187601.

[184] J. Motruk, M. P. Zaletel, R. S. K. Mong, and F. Pollmann, "Density matrix renormalization group on a cylinder in mixed real and momentum space," *Phys. Rev. B*, vol. 93, p. 155 139, 15 Apr. 2016. DOI: 10.1103/PhysRevB.93.155139.

[185] T. Soejima, D. E. Parker, N. Bultinck, J. Hauschild, and M. P. Zaletel, "Efficient simulation of moiré materials using the density matrix renormalization group," *Phys. Rev. B*, vol. 102, p. 205 111, 20 Nov. 2020. DOI: 10.1103/PhysRevB.102.205111.

[186] T. Wang, D. E. Parker, T. Soejima, *et al.*, "Ground-state order in magic-angle graphene at filling $\nu = -3$: A full-scale density matrix renormalization group study," *Phys. Rev. B*, vol. 108, p. 235 128, 23 Dec. 2023. DOI: 10.1103/PhysRevB.108.235128.

[187] D. E. Parker, T. Soejima, J. Hauschild, M. P. Zaletel, and N. Bultinck, "Strain-induced quantum phase transitions in magic-angle graphene," *Phys. Rev. Lett.*, vol. 127, p. 027 601, 2 Jul. 2021. DOI: 10.1103/PhysRevLett.127.027601.

[188] D. Vanderbilt, *Berry Phases in Electronic Structure Theory: Electric Polarization, Orbital Magnetization and Topological Insulators*. 2018. DOI: 10.1017/9781316662205.

[189] J. Hauschild and F. Pollmann, "Efficient numerical simulations with Tensor Networks: Tensor Network Python (TeNPy)," *SciPost Phys. Lect. Notes*, p. 5, 2018. DOI: 10.21468/SciPostPhysLectNotes.5.

[190] P. C. Hohenberg, "Existence of long-range order in one and two dimensions," *Phys. Rev.*, vol. 158, pp. 383–386, 2 Jun. 1967. DOI: 10.1103/PhysRev.158.383.

[191] N. D. Mermin and H. Wagner, "Absence of ferromagnetism or antiferromagnetism in one- or two-dimensional isotropic heisenberg models," *Phys. Rev. Lett.*, vol. 17, pp. 1133–1136, 22 Nov. 1966. DOI: 10.1103/PhysRevLett.17.1133.

[192] B. I. Halperin, "On the Hohenberg-Mermin-Wagner Theorem and Its Limitations," *Journal of Statistical Physics*, vol. 175, no. 3-4, pp. 521–529, May 2019. DOI: 10.1007/s10955-018-2202-y.

[193] I. Affleck, "Quantum spin chains and the haldane gap," *Journal of Physics: Condensed Matter*, vol. 1, no. 19, p. 3047, May 1989. DOI: 10.1088/0953-8984/1/19/001.

[194] Y.-C. He, M. P. Zaletel, M. Oshikawa, and F. Pollmann, "Signatures of dirac cones in a dmrg study of the kagome heisenberg model," *Phys. Rev. X*, vol. 7, p. 031 020, 3 Jul. 2017. DOI: 10.1103/PhysRevX.7.031020.

[195] Y. Gannot and S. A. Kivelson, "How quantum phases on cylinders approach the two-dimensional limit," *Phys. Rev. B*, vol. 107, p. 075 127, 7 Feb. 2023. DOI: 10.1103/PhysRevB.107.075127.

[196] A. Seidel and D.-H. Lee, "The luther-emery liquid: Spin gap and anomalous flux period," *Phys. Rev. B*, vol. 71, p. 045 113, 4 Jan. 2005. DOI: 10.1103/PhysRevB.71.045113.

[197] L. Tagliacozzo, T. R. de Oliveira, S. Iblisdir, and J. I. Latorre, "Scaling of entanglement support for matrix product states," *Phys. Rev. B*, vol. 78, p. 024 410, 2 Jul. 2008. DOI: 10.1103/PhysRevB.78.024410.

[198] F. Pollmann, S. Mukerjee, A. M. Turner, and J. E. Moore, "Theory of finite entanglement scaling at one-dimensional quantum critical points," *Phys. Rev. Lett.*, vol. 102, p. 255 701, 25 Jun. 2009. DOI: 10.1103/PhysRevLett.102.255701.

[199] B. Vanhecke, J. Haegeman, K. Van Acoleyen, L. Vanderstraeten, and F. Verstraete, "Scaling hypothesis for matrix product states," *Phys. Rev. Lett.*, vol. 123, p. 250 604, 25 Dec. 2019. DOI: 10.1103/PhysRevLett.123.250604.

[200] H.-C. Jiang and T. P. Devereaux, "Superconductivity in the doped Hubbard model and its interplay with next-nearest hopping t," *Science*, vol. 365, no. 6460, pp. 1424–1428, Sep. 2019. DOI: 10.1126/science.aal5304.

[201] Y.-F. Jiang and H.-C. Jiang, "Topological superconductivity in the doped chiral spin liquid on the triangular lattice," *Phys. Rev. Lett.*, vol. 125, p. 157 002, 15 Oct. 2020. DOI: 10.1103/PhysRevLett.125.157002.

[202] Y.-F. Jiang, J. Zaanen, T. P. Devereaux, and H.-C. Jiang, "Ground state phase diagram of the doped hubbard model on the four-leg cylinder," *Phys. Rev. Res.*, vol. 2, p. 033 073, 3 Jul. 2020. DOI: 10.1103/PhysRevResearch.2.033073.

[203] C.-M. Chung, M. Qin, S. Zhang, U. Schollwöck, and S. R. White, "Plaquette versus ordinary d-wave pairing in the t'-hubbard model on a width-4 cylinder," *Phys. Rev. B*, vol. 102, p. 041 106, 4 Jul. 2020. DOI: 10.1103/PhysRevB.102.041106.

[204] Z. Zhu, D. N. Sheng, and A. Vishwanath, "Doped mott insulators in the triangular-lattice hubbard model," *Phys. Rev. B*, vol. 105, p. 205 110, 20 May 2022. DOI: 10.1103/PhysRevB.105.205110.

[205] M. M. Rams, P. Czarnik, and L. Cincio, "Precise extrapolation of the correlation function asymptotics in uniform tensor network states with application to the bose-hubbard and xxz models," *Phys. Rev. X*, vol. 8, p. 041 033, 4 Nov. 2018. DOI: 10.1103/PhysRevX.8.041033.

[206] S. Weinberg, *The quantum theory of fields*. Cambridge university press, 1995, vol. 2.

[207] D. Shaffer, J. Wang, and L. H. Santos, "Theory of hofstadter superconductors," *Phys. Rev. B*, vol. 104, p. 184 501, 18 Nov. 2021. DOI: 10.1103/PhysRevB.104.184501.

[208] P. Coleman, *Introduction to many-body physics*. Cambridge University Press, 2015.

[209] Y. H. Kwan, G. Wagner, T. Soejima, *et al.*, "Kekulé spiral order at all nonzero integer fillings in twisted bilayer graphene," *Phys. Rev. X*, vol. 11, p. 041 063, 4 Dec. 2021. DOI: 10.1103/PhysRevX.11.041063.

[210] J. Yu, B. A. Foutty, Z. Han, *et al.*, "Correlated Hofstadter spectrum and flavour phase diagram in magic-angle twisted bilayer graphene," *Nature Physics*, vol. 18, no. 7, pp. 825–831, Apr. 2022. DOI: 10.1038/s41567-022-01589-w.

[211] Y. H. Kwan, G. Wagner, N. Bultinck, S. H. Simon, E. Berg, and S. A. Parameswaran, "Electron-phonon coupling and competing kekulé orders in twisted bilayer graphene," *Phys. Rev. B*, vol. 110, p. 085 160, 8 Aug. 2024. DOI: 10.1103/PhysRevB.110.085160.

[212] E. Blount, "Formalisms of band theory," in *Solid state physics*, vol. 13, Elsevier, 1962, pp. 305–373.

[213] S. Liu, E. Khalaf, J. Y. Lee, and A. Vishwanath, "Nematic topological semimetal and insulator in magic-angle bilayer graphene at charge neutrality," *Phys. Rev. Res.*, vol. 3, p. 013 033, 1 Jan. 2021. DOI: 10.1103/PhysRevResearch.3.013033.

[214] D. Parker, P. Ledwith, E. Khalaf, *et al.*, "Field-tuned and zero-field fractional Chern insulators in magic angle graphene," *arXiv e-prints*, arXiv:2112.13837, Dec. 2021. DOI: 10.48550/arXiv.2112.13837.

[215] X. Wang and O. Vafek, "Narrow bands in magnetic field and strong-coupling hofstadter spectra," *Phys. Rev. B*, vol. 106, p. L121111, 12 Sep. 2022. DOI: 10.1103/PhysRevB.106.L121111.

[216] Z.-D. Song and B. A. Bernevig, "Magic-angle twisted bilayer graphene as a topological heavy fermion problem," *Phys. Rev. Lett.*, vol. 129, p. 047 601, 4 Jul. 2022. DOI: 10.1103/PhysRevLett.129.047601.

[217] P. J. Ledwith, A. Vishwanath, and D. E. Parker, "Vortexability: A unifying criterion for ideal fractional chern insulators," *Phys. Rev. B*, vol. 108, p. 205 144, 20 Nov. 2023. DOI: 10.1103/PhysRevB.108.205144.

[218] M. Oh, K. P. Nuckolls, D. Wong, *et al.*, "Evidence for unconventional superconductivity in twisted bilayer graphene,", vol. 600, no. 7888, pp. 240–245, Dec. 2021. DOI: 10.1038/s41586-021-04121-x.

[219] E. Lake, A. S. Patri, and T. Senthil, "Pairing symmetry of twisted bilayer graphene: A phenomenological synthesis," *Phys. Rev. B*, vol. 106, p. 104 506, 10 Sep. 2022. DOI: 10.1103/PhysRevB.106.104506.

[220] Z. Dai, Y. Wu, T. Wang, and M. P. Zaletel, "Fermionic Isometric Tensor Network States in Two Dimensions," *arXiv e-prints*, arXiv:2211.00043, Oct. 2022. DOI: 10.48550/arXiv.2211.00043.

[221] T. Grover and T. Senthil, "Topological spin hall states, charged skyrmions, and superconductivity in two dimensions," *Phys. Rev. Lett.*, vol. 100, p. 156 804, 15 Apr. 2008. DOI: 10.1103/PhysRevLett.100.156804.

[222] A. G. Abanov and P. B. Wiegmann, "Chiral nonlinear σ models as models for topological superconductivity," *Phys. Rev. Lett.*, vol. 86, pp. 1319–1322, 7 Feb. 2001. DOI: 10.1103/PhysRevLett.86.1319.

[223] C. L. Kane and E. J. Mele, "Z_2 topological order and the quantum spin hall effect," *Phys. Rev. Lett.*, vol. 95, p. 146 802, 14 Sep. 2005. DOI: 10.1103/PhysRevLett.95.146802.

[224] J. Yuan, J.-H. Gao, W.-Q. Chen, F. Ye, Y. Zhou, and F.-C. Zhang, "Edge superconducting correlation in the attractive-U kane-mele-hubbard model," *Phys. Rev. B*, vol. 86, p. 104 505, 10 Sep. 2012. DOI: 10.1103/PhysRevB.86.104505.

[225] T. Ma, H.-Q. Lin, and J. E. Gubernatis, "Triplet p + ip pairing correlations in the doped Kane-Mele-Hubbard model: A quantum Monte Carlo study," *EPL (Europhysics Letters)*, vol. 111, no. 4, 47003, p. 47 003, Aug. 2015. DOI: 10.1209/0295-5075/111/47003.

[226] K. Lee, T. Hazra, M. Randeria, and N. Trivedi, "Topological superconductivity in dirac honeycomb systems," *Phys. Rev. B*, vol. 99, p. 184 514, 18 May 2019. DOI: 10.1103/PhysRevB.99.184514.

[227] S. Chatterjee, N. Bultinck, and M. P. Zaletel, "Symmetry breaking and skyrmionic transport in twisted bilayer graphene," *Phys. Rev. B*, vol. 101, p. 165 141, 16 Apr. 2020. DOI: 10.1103/PhysRevB.101.165141.

[228] Y. Liu, Z. Wang, T. Sato, *et al.*, "Superconductivity from the condensation of topological defects in a quantum spin-Hall insulator," *Nature Communications*, vol. 10, 2658, p. 2658, Jun. 2019. DOI: 10.1038/s41467-019-10372-0.

[229] Z. Wang, Y. Liu, T. Sato, *et al.*, "Doping-induced quantum spin hall insulator to superconductor transition," *Phys. Rev. Lett.*, vol. 126, p. 205 701, 20 May 2021. DOI: 10.1103/PhysRevLett.126.205701.

[230] E. Khalaf and A. Vishwanath, "Baby skyrmions in Chern ferromagnets and topological mechanism for spin-polaron formation in twisted bilayer graphene," *Nature Communications*, vol. 13, 6245, p. 6245, Oct. 2022. DOI: 10.1038/s41467-022-33673-3.

[231] F. Schindler, O. Vafek, and B. A. Bernevig, "Trions in twisted bilayer graphene," *Phys. Rev. B*, vol. 105, p. 155 135, 15 Apr. 2022. DOI: 10.1103/PhysRevB.105.155135.

[232] V. Gurarie, L. Radzihovsky, and A. V. Andreev, "Quantum phase transitions across a p-wave feshbach resonance," *Phys. Rev. Lett.*, vol. 94, p. 230 403, 23 Jun. 2005. DOI: 10.1103/PhysRevLett.94.230403.

[233] V. Crépel, D. Guerci, J. Cano, J. H. Pixley, and A. Millis, "Topological Superconductivity in Doped Magnetic Moiré Semiconductors,", vol. 131, no. 5, 056001, p. 056 001, Aug. 2023. DOI: 10.1103/PhysRevLett.131.056001.

[234] B. Yang, H. Sun, C.-J. Huang, *et al.*, "Cooling and entangling ultracold atoms in optical lattices," *Science*, vol. 369, no. 6503, pp. 550–553, Jul. 2020. DOI: 10.1126/science.aaz6801.

[235] J. S. Hofmann, E. Khalaf, A. Vishwanath, E. Berg, and J. Y. Lee, "Fermionic monte carlo study of a realistic model of twisted bilayer graphene," *Phys. Rev. X*, vol. 12, p. 011 061, 1 Mar. 2022. DOI: 10.1103/PhysRevX.12.011061.

[236] R. Sahay, A. Vishwanath, and R. Verresen, "Quantum Spin Puddles and Lakes: NISQ-Era Spin Liquids from Non-Equilibrium Dynamics," *arXiv e-prints*, arXiv:2211.01381, Nov. 2022. DOI: 10.48550/arXiv.2211.01381.

[237] K. Yang, L. K. Warman, and S. M. Girvin, "Possible spin-liquid states on the triangular and kagomé lattices," *Phys. Rev. Lett.*, vol. 70, pp. 2641–2644, 17 Apr. 1993. DOI: 10.1103/PhysRevLett.70.2641.

[238] Y.-C. He, D. N. Sheng, and Y. Chen, "Chiral spin liquid in a frustrated anisotropic kagome heisenberg model," *Phys. Rev. Lett.*, vol. 112, p. 137 202, 13 Apr. 2014. DOI: 10.1103/PhysRevLett.112.137202.

[239] B. Bauer, L. Cincio, B. P. Keller, *et al.*, "Chiral spin liquid and emergent anyons in a Kagome lattice Mott insulator," *Nature Communications*, vol. 5, 5137, p. 5137, Oct. 2014. DOI: 10.1038/ncomms6137.

[240] Z. Zhu, "Chiral spin liquid versus Mott antiferromagnetism in the triangular-lattice Hubbard model,", vol. 110, no. 4, L041113, p. L041113, Jul. 2024. DOI: 10.1103/PhysRevB.110.L041113.

[241] C. Hickey, L. Cincio, Z. Papić, and A. Paramekanti, "Haldane-Hubbard Mott Insulator: From Tetrahedral Spin Crystal to Chiral Spin Liquid,", vol. 116, no. 13, 137202, p. 137 202, Apr. 2016. DOI: 10.1103/PhysRevLett.116.137202.

[242] A. G. Grushin and C. Repellin, "Amorphous and Polycrystalline Routes toward a Chiral Spin Liquid,", vol. 130, no. 18, 186702, p. 186 702, May 2023. DOI: 10.1103/PhysRevLett.130.186702.

[243] J. Zang, J. Wang, J. Cano, and A. J. Millis, "Hartree-fock study of the moiré hubbard model for twisted bilayer transition metal dichalcogenides," *Phys. Rev. B*, vol. 104, p. 075 150, 7 Aug. 2021. DOI: 10.1103/PhysRevB.104.075150.

[244] V. Crépel and A. Millis, "Spinon pairing induced by chiral in-plane exchange and the stabilization of odd-spin chern number spin liquid in twisted $MoTe_2$," *Phys. Rev. Lett.*, vol. 133, p. 146 503, 14 Oct. 2024. DOI: 10.1103/PhysRevLett.133.146503.

[245] A. Ghiotto, E.-M. Shih, G. S. S. G. Pereira, *et al.*, "Quantum criticality in twisted transition metal dichalcogenides,", vol. 597, no. 7876, pp. 345–349, Sep. 2021. DOI: 10.1038/s41586-021-03815-6.

[246] X.-Y. Song, A. Vishwanath, and Y.-H. Zhang, "Doping the chiral spin liquid: Topological superconductor or chiral metal," *Phys. Rev. B*, vol. 103, p. 165 138, 16 Apr. 2021. DOI: 10.1103/PhysRevB.103.165138.

[247] X.-Y. Song and Y.-H. Zhang, "Deconfined criticalities and dualities between chiral spin liquid, topological superconductor and charge density wave Chern insulator," *SciPost Phys.*, vol. 15, p. 215, 2023. DOI: 10.21468/SciPostPhys.15.5.215.

[248] J. He, S.-P. Kou, Y. Liang, and S. Feng, "Chiral spin liquid in a correlated topological insulator," *Phys. Rev. B*, vol. 83, p. 205 116, 20 May 2011. DOI: 10.1103/PhysRevB.83.205116.

[249] L. Balents, "Spin liquids in frustrated magnets,", vol. 464, no. 7286, pp. 199–208, Mar. 2010. DOI: 10.1038/nature08917.

[250] Y. Huang, D. N. Sheng, and J.-X. Zhu, "Magnetic field induced partially polarized chiral spin liquid in a transition metal dichalcogenide moiré system," *Phys. Rev. B*, vol. 109, p. 165 109, 16 Apr. 2024. DOI: 10.1103/PhysRevB.109.165109.

[251] W.-J. Hu, S.-S. Gong, and D. N. Sheng, "Variational monte carlo study of chiral spin liquid in quantum antiferromagnet on the triangular lattice," *Phys. Rev. B*, vol. 94, p. 075 131, 7 Aug. 2016. DOI: 10.1103/PhysRevB.94.075131.

[252] G. Chen, K. R. Hazzard, A. M. Rey, and M. Hermele, "Synthetic-gauge-field stabilization of the chiral-spin-liquid phase," *Physical Review A*, vol. 93, no. 6, p. 061 601, 2016.

[253] Y.-M. Lu, Y. Ran, and M. Oshikawa, "Filling-enforced constraint on the quantized Hall conductivity on a periodic lattice," *Annals of Physics*, vol. 413, 168060, p. 168 060, Feb. 2020. DOI: 10.1016/j.aop.2019.168060.

[254] E. Lieb, T. Schultz, and D. Mattis, "Two soluble models of an antiferromagnetic chain," *Annals of Physics*, vol. 16, no. 3, pp. 407–466, 1961, ISSN: 0003-4916. DOI: https://doi.org/10.1016/0003-4916(61)90115-4.

[255] X.-G. Wen, "Quantum orders and symmetric spin liquids," *Phys. Rev. B*, vol. 65, p. 165 113, 16 Apr. 2002. DOI: 10.1103/PhysRevB.65.165113.

[256] X.-G. Wen, "Quantum orders in an exact soluble model," *Phys. Rev. Lett.*, vol. 90, p. 016 803, 1 Jan. 2003. DOI: 10.1103/PhysRevLett.90.016803.

[257] A. M. Essin and M. Hermele, "Classifying fractionalization: Symmetry classification of gapped $\mathbb{Z}_2$ spin liquids in two dimensions," *Phys. Rev. B*, vol. 87, p. 104 406, 10 Mar. 2013. DOI: 10.1103/PhysRevB.87.104406.

[258] Y. Zhang, T. Grover, A. Turner, M. Oshikawa, and A. Vishwanath, "Quasiparticle statistics and braiding from ground-state entanglement,", vol. 85, no. 23, 235151, p. 235 151, Jun. 2012. DOI: 10.1103/PhysRevB.85.235151.

[259] M. P. Zaletel and A. Vishwanath, "Constraints on topological order in mott insulators," *Phys. Rev. Lett.*, vol. 114, p. 077 201, 7 Feb. 2015. DOI: 10.1103/PhysRevLett.114.077201.

[260] M. P. Zaletel, Y.-M. Lu, and A. Vishwanath, "Measuring space-group symmetry fractionalization in $\mathbb{Z}_2$ spin liquids," *Phys. Rev. B*, vol. 96, p. 195 164, 19 Nov. 2017. DOI: 10.1103/PhysRevB.96.195164.

[261] S. Florens and A. Georges, "Slave-rotor mean-field theories of strongly correlated systems and the mott transition in finite dimensions," *Phys. Rev. B*, vol. 70, p. 035 114, 3 Jul. 2004. DOI: 10.1103/PhysRevB.70.035114.

[262] T. Senthil, "Theory of a continuous mott transition in two dimensions," *Phys. Rev. B*, vol. 78, p. 045 109, 4 Jul. 2008. DOI: 10.1103/PhysRevB.78.045109.

[263] P. W. Anderson, "Plasmons, gauge invariance, and mass," *Phys. Rev.*, vol. 130, pp. 439–442, 1 Apr. 1963. DOI: 10.1103/PhysRev.130.439.

[264] P. W. Higgs, "Broken Symmetries and the Masses of Gauge Bosons,", vol. 13, no. 16, pp. 508–509, Oct. 1964. DOI: 10.1103/PhysRevLett.13.508.

[265] S. Sachdev, *Quantum Phases of Matter*, 1st ed. Cambridge University Press, Mar. 2023. DOI: 10.1017/9781009212717.

[266] P. Calabrese and A. Lefevre, "Entanglement spectrum in one-dimensional systems," *Phys. Rev. A*, vol. 78, p. 032 329, 3 Sep. 2008. DOI: 10.1103/PhysRevA.78.032329.

[267] H. Li and F. D. M. Haldane, "Entanglement spectrum as a generalization of entanglement entropy: Identification of topological order in non-abelian fractional quantum hall effect states," *Phys. Rev. Lett.*, vol. 101, p. 010 504, 1 Jul. 2008. DOI: 10.1103/PhysRevLett.101.010504.

[268] A. Kitaev and J. Preskill, "Topological entanglement entropy," *Phys. Rev. Lett.*, vol. 96, p. 110 404, 11 Mar. 2006. DOI: 10.1103/PhysRevLett.96.110404.

[269] L. Fidkowski, "Entanglement spectrum of topological insulators and superconductors," *Phys. Rev. Lett.*, vol. 104, p. 130 502, 13 Apr. 2010. DOI: 10.1103/PhysRevLett.104.130502.

[270] A. Chandran, M. Hermanns, N. Regnault, and B. A. Bernevig, "Bulk-edge correspondence in entanglement spectra," *Phys. Rev. B*, vol. 84, p. 205 136, 20 Nov. 2011. DOI: 10.1103/PhysRevB.84.205136.

[271] X.-L. Qi, H. Katsura, and A. W. W. Ludwig, "General relationship between the entanglement spectrum and the edge state spectrum of topological quantum states," *Phys. Rev. Lett.*, vol. 108, p. 196 402, 19 May 2012. DOI: 10.1103/PhysRevLett.108.196402.

[272] A. Sterdyniak, A. Chandran, N. Regnault, B. A. Bernevig, and P. Bonderson, "Real-space entanglement spectrum of quantum hall states," *Phys. Rev. B*, vol. 85, p. 125 308, 12 Mar. 2012. DOI: 10.1103/PhysRevB.85.125308.

[273] B. Swingle and T. Senthil, "Geometric proof of the equality between entanglement and edge spectra,", vol. 86, no. 4, 045117, p. 045 117, Jul. 2012. DOI: 10.1103/PhysRevB.86.045117.

[274] H.-H. Tu, Y. Zhang, and X.-L. Qi, "Momentum polarization: An entanglement measure of topological spin and chiral central charge," *Phys. Rev. B*, vol. 88, p. 195 412, 19 Nov. 2013. DOI: 10.1103/PhysRevB.88.195412.

[275] V. Crépel, B. Estienne, B. A. Bernevig, P. Lecheminant, and N. Regnault, "Matrix product state description of Halperin states,", vol. 97, no. 16, 165136, p. 165 136, Apr. 2018. DOI: 10.1103/PhysRevB.97.165136.

[276] X. G. Wen, "Gapless boundary excitations in the quantum hall states and in the chiral spin states," *Phys. Rev. B*, vol. 43, pp. 11 025–11 036, 13 May 1991. DOI: 10.1103/PhysRevB.43.11025.

[277] V. Zauner, M. Ganahl, H. G. Evertz, and T. Nishino, "Time evolution within a comoving window: scaling of signal fronts and magnetization plateaus after a local quench in quantum spin chains," *Journal of Physics Condensed Matter*, vol. 27, no. 42, 425602, p. 425 602, Oct. 2015. DOI: 10.1088/0953-8984/27/42/425602.

[278] N. Nagaosa and J.-i. Takimoto, "Theory of Neutral-Ionic Transition in Organic Crystals. I. Monte Carlo Simulation of Modified Hubbard Model," *Journal of the Physical Society of Japan*, vol. 55, no. 8, p. 2735, Aug. 1986. DOI: 10.1143/JPSJ.55.2735.

[279] N. Nagaosa, "Theory of Neutral-Ionic Transition in Organic Crystals. III. Effect of the Electron-Lattice Interaction," *Journal of the Physical Society of Japan*, vol. 55, no. 8, p. 2754, Aug. 1986. DOI: 10.1143/JPSJ.55.2754.

[280] T. Egami, S. Ishihara, and M. Tachiki, "Lattice effect of strong electron correlation - Implication for ferroelectricity and superconductivity," *Science*, vol. 261, no. 5126, pp. 1307–1310, Sep. 1993. DOI: 10.1126/science.261.5126.1307.

[281] M. Fabrizio, A. O. Gogolin, and A. A. Nersesyan, "From band insulator to mott insulator in one dimension," *Phys. Rev. Lett.*, vol. 83, pp. 2014–2017, 10 Sep. 1999. DOI: 10.1103/PhysRevLett.83.2014.

[282] M. Fabrizio, A. Gogolin, and A. Nersesyan, "Critical properties of the double-frequency sine-gordon model with applications," *Nuclear Physics B*, vol. 580, no. 3, pp. 647–687, 2000, ISSN: 0550-3213. DOI: https://doi.org/10.1016/S0550-3213(00)00247-9.

[283] L. Tincani, R. M. Noack, and D. Baeriswyl, "Critical properties of the band-insulator-to-mott-insulator transition in the strong-coupling limit of the ionic hubbard model," *Phys. Rev. B*, vol. 79, p. 165 109, 16 Apr. 2009. DOI: 10.1103/PhysRevB.79.165109.

[284] R. Verresen, J. Bibo, and F. Pollmann, "Quotient symmetry protected topological phenomena," *arXiv e-prints*, arXiv:2102.08967, Feb. 2021. DOI: 10.48550/arXiv.2102.08967.

[285] W. Kadow, L. Vanderstraeten, and M. Knap, "Hole spectral function of a chiral spin liquid in the triangular lattice hubbard model," *Phys. Rev. B*, vol. 106, p. 094 417, 9 Sep. 2022. DOI: 10.1103/PhysRevB.106.094417.

[286] N. Wagner, D. Guerci, A. J. Millis, and G. Sangiovanni, "Edge zeros and boundary spinons in topological mott insulators," *Phys. Rev. Lett.*, vol. 133, p. 126 504, 12 Sep. 2024. DOI: 10.1103/PhysRevLett.133.126504.

[287] S. Bollmann, C. Setty, U. F. P. Seifert, and E. J. König, "Topological green's function zeros in an exactly solved model and beyond," *Phys. Rev. Lett.*, vol. 133, p. 136 504, 13 Sep. 2024. DOI: 10.1103/PhysRevLett.133.136504.

[288] H. Fröhlich, "Theory of the superconducting state. i. the ground state at the absolute zero of temperature," *Phys. Rev.*, vol. 79, pp. 845–856, 5 Sep. 1950. DOI: 10.1103/PhysRev.79.845.

[289] J. Bardeen, "Zero-point vibrations and superconductivity," *Phys. Rev.*, vol. 79, pp. 167–168, 1 Jul. 1950. DOI: 10.1103/PhysRev.79.167.3.

[290] T. H. R. Skyrme, "Particle states of a quantized meson field," *Proc. Roy. Soc. Lond. A*, vol. 262, pp. 237–245, 1961. DOI: 10.1098/rspa.1961.0115.

[291] P. Anderson, "Resonating valence bonds: A new kind of insulator?" *Materials Research Bulletin*, vol. 8, no. 2, pp. 153–160, 1973, ISSN: 0025-5408. DOI: https://doi.org/10.1016/0025-5408(73)90167-0.

[292] P. Fazekas and P. W. Anderson, "On the ground state properties of the anisotropic triangular antiferromagnet," *The Philosophical Magazine: A Journal of Theoretical Experimental and Applied Physics*, vol. 30, no. 2, pp. 423–440, 1974. DOI: 10.1080/14786439808206568.

[293] W. P. Su, J. R. Schrieffer, and A. J. Heeger, "Solitons in polyacetylene," *Phys. Rev. Lett.*, vol. 42, pp. 1698–1701, 25 Jun. 1979. DOI: 10.1103/PhysRevLett.42.1698.

[294] S. A. Kivelson, D. S. Rokhsar, and J. P. Sethna, "Topology of the resonating valence-bond state: Solitons and high-T_c superconductivity," *Phys. Rev. B*, vol. 35, pp. 8865–8868, 16 Jun. 1987. DOI: 10.1103/PhysRevB.35.8865.

[295] D.-H. Lee and C. L. Kane, "Boson-vortex-skyrmion duality, spin-singlet fractional quantum hall effect, and spin-1/2 anyon superconductivity," *Phys. Rev. Lett.*, vol. 64, pp. 1313–1317, 12 Mar. 1990. DOI: 10.1103/PhysRevLett.64.1313.

[296] P. W. Anderson, "The resonating valence bond state in la¡sub¿2¡/sub¿cuo¡sub¿4¡/sub¿ and superconductivity," *Science*, vol. 235, no. 4793, pp. 1196–1198, 1987. DOI: 10.1126/science.235.4793.1196.

[297] G. Baskaran, Z. Zou, and P. Anderson, "The resonating valence bond state and high-tc superconductivity — a mean field theory," *Solid State Communications*, vol. 63, no. 11, pp. 973–976, 1987, ISSN: 0038-1098. DOI: https://doi.org/10.1016/0038-1098(87)90642-9.

[298] G. Kotliar and J. Liu, "Superexchange mechanism and d-wave superconductivity," *Phys. Rev. B*, vol. 38, pp. 5142–5145, 7 Sep. 1988. DOI: 10.1103/PhysRevB.38.5142.

[299] X. G. Wen and A. Zee, "Effective theory of the t- and p-breaking superconducting state," *Phys. Rev. Lett.*, vol. 62, pp. 2873–2876, 24 Jun. 1989. DOI: 10.1103/PhysRevLett.62.2873.

[300] X. G. Wen and A. Zee, "Compressibility and superfluidity in the fractional-statistics liquid," *Phys. Rev. B*, vol. 41, pp. 240–253, 1 Jan. 1990. DOI: 10.1103/PhysRevB.41.240.

[301] D.-H. Lee and M. P. A. Fisher, "Anyon superconductivity and the fractional quantum Hall effect," en, *Physical Review Letters*, vol. 63, no. 8, pp. 903–906, Aug. 1989, ISSN: 0031-9007. DOI: 10.1103/PhysRevLett.63.903.

[302] Y. Hosotani and S. Chakravarty, "Superconductivity in the anyon model," *Phys. Rev. B*, vol. 42, pp. 342–346, 1 Jul. 1990. DOI: 10.1103/PhysRevB.42.342.

[303] T. Banks and J. D. Lykken, "Landau-Ginzburg description of anyonic superconductors," *Nuclear Physics B*, vol. 336, no. 3, pp. 500–516, Jun. 1990. DOI: 10.1016/0550-3213(90)90439-K.

[304] B.-B. Chen, Z. Chen, S.-S. Gong, D. N. Sheng, W. Li, and A. Weichselbaum, "Quantum spin liquid with emergent chiral order in the triangular-lattice hubbard model," *Phys. Rev. B*, vol. 106, p. 094 420, 9 Sep. 2022. DOI: 10.1103/PhysRevB.106.094420.

[305] S.-S. Gong, W. Zheng, M. Lee, Y.-M. Lu, and D. N. Sheng, "Chiral spin liquid with spinon fermi surfaces in the spin-$\frac{1}{2}$ triangular heisenberg model," *Phys. Rev. B*, vol. 100, p. 241 111, 24 Dec. 2019. DOI: 10.1103/PhysRevB.100.241111.

[306] Y.-F. Jiang and H.-C. Jiang, "Nature of quantum spin liquids of the $S = \frac{1}{2}$ heisenberg antiferromagnet on the triangular lattice: A parallel dmrg study," *Phys. Rev. B*, vol. 107, p. L140411, 14 Apr. 2023. DOI: 10.1103/PhysRevB.107.L140411.

[307] T. Shirakawa, T. Tohyama, J. Kokalj, S. Sota, and S. Yunoki, "Ground-state phase diagram of the triangular lattice hubbard model by the density-matrix renormalization group method," *Phys. Rev. B*, vol. 96, p. 205 130, 20 Nov. 2017. DOI: 10.1103/PhysRevB.96.205130.

[308] A. Wietek, R. Rossi, F. Simkovic, *et al.*, "Mott Insulating States with Competing Orders in the Triangular Lattice Hubbard Model," *Physical Review X*, vol. 11, no. 4, 041013, p. 041 013, Oct. 2021. DOI: 10.1103/PhysRevX.11.041013.

[309] K. S. Chen, Z. Y. Meng, U. Yu, S. Yang, M. Jarrell, and J. Moreno, "Unconventional superconductivity on the triangular lattice hubbard model," *Phys. Rev. B*, vol. 88, p. 041 103, 4 Jul. 2013. DOI: 10.1103/PhysRevB.88.041103.

[310] V. Zampronio and T. Macrı, "Chiral superconductivity in the doped triangular-lattice Fermi-Hubbard model in two dimensions," *Quantum*, vol. 7, p. 1061, Jul. 2023. DOI: 10.22331/q-2023-07-20-1061.

[311] S. Raghu, S. A. Kivelson, and D. J. Scalapino, "Superconductivity in the repulsive hubbard model: An asymptotically exact weak-coupling solution," *Phys. Rev. B*, vol. 81, p. 224 505, 22 Jun. 2010. DOI: 10.1103/PhysRevB.81.224505.

[312] Y. Gannot, Y.-F. Jiang, and S. A. Kivelson, "Hubbard ladders at small U revisited," *Phys. Rev. B*, vol. 102, p. 115 136, 11 Sep. 2020. DOI: 10.1103/PhysRevB.102.115136.

[313] M. M. Maśka, "Reentrant superconductivity in a strong applied field within the tight-binding model," en, *Physical Review B*, vol. 66, no. 5, p. 054 533, Aug. 2002, ISSN: 0163-1829, 1095-3795. DOI: 10.1103/PhysRevB.66.054533.

[314] S. Mo and A. Sudbø, "Fermion-pairing on a square lattice in extreme magnetic fields," en, *Physica C: Superconductivity*, vol. 383, no. 3, pp. 279–286, Dec. 2002, ISSN: 09214534. DOI: 10.1016/S0921-4534(02)01345-X.

[315] H. Zhai, R. O. Umucalılar, and M. O. Oktel, "Pairing and Vortex Lattices for Interacting Fermions in Optical Lattices with a Large Magnetic Field," en, *Physical Review Letters*, vol. 104, no. 14, p. 145 301, Apr. 2010, ISSN: 0031-9007, 1079-7114. DOI: 10.1103/PhysRevLett.104.145301.

[316] M. Iskin, "Stripe-ordered superfluid and supersolid phases in the attractive Hofstadter-Hubbard model," en, *Physical Review A*, vol. 91, no. 1, p. 011 601, Jan. 2015, ISSN: 1050-2947, 1094-1622. DOI: 10.1103/PhysRevA.91.011601.

[317] G. S. Jeon, J. K. Jain, and C.-X. Liu, "Topological superconductivity in Landau levels," en, *Physical Review B*, vol. 99, no. 9, p. 094 509, Mar. 2019, ISSN: 2469-9950, 2469-9969. DOI: 10.1103/PhysRevB.99.094509.

[318] R. Sohal and E. Fradkin, "Intertwined order in fractional Chern insulators from finite-momentum pairing of composite fermions," en, *Physical Review B*, vol. 101, no. 24, p. 245 154, Jun. 2020, ISSN: 2469-9950, 2469-9969. DOI: 10.1103/PhysRevB.101.245154.

[319] J. Schirmer, C. .-. Liu, and J. K. Jain, "Phase diagram of superconductivity in the integer quantum Hall regime," *Proceedings of the National Academy of Science*, vol. 119, no. 28, e2202948119, e2202948119, Jul. 2022. DOI: 10.1073/pnas.2202948119.

[320] I. Affleck, "Field theory methods and strongly correlated electrons," in *Physics, Geometry and Topology*, H. C. Lee, Ed. Boston, MA: Springer US, 1990, pp. 1–13, ISBN: 978-1-4615-3802-8. DOI: 10.1007/978-1-4615-3802-8_1.

[321] C. N. Yang, "η pairing and off-diagonal long-range order in a hubbard model," *Phys. Rev. Lett.*, vol. 63, pp. 2144–2147, 19 Nov. 1989. DOI: 10.1103/PhysRevLett.63.2144.

[322] C. N. Yang and S. C. Zhang, "SO_4 Symmetry in a Hubbard Model," *Modern Physics Letters B*, vol. 4, no. 11, pp. 759–766, Jan. 1990. DOI: 10.1142/S0217984990000933.

[323] C. N. Yang, "Remarks and generalizations about SU $_2\times$SU $_2$ symmetry of Hubbard models," *Physics Letters A*, vol. 161, no. 3, pp. 292–294, Dec. 1991. DOI: 10.1016/0375-9601(91)90020-9.

[324] M. Hermele, "Su(2) gauge theory of the hubbard model and application to the honeycomb lattice," *Phys. Rev. B*, vol. 76, p. 035 125, 3 Jul. 2007. DOI: 10.1103/PhysRevB.76.035125.

[325] W. Florek, "Magnetic translation groups as group extensions," *Reports on Mathematical Physics*, vol. 34, no. 1, pp. 81–95, 1994, ISSN: 0034-4877. DOI: https://doi.org/10.1016/0034-4877(94)90019-1.

[326] S. Florens and A. Georges, "Quantum impurity solvers using a slave rotor representation," *Phys. Rev. B*, vol. 66, p. 165 111, 16 Oct. 2002. DOI: 10.1103/PhysRevB.66.165111.

[327] J. B. Marston and I. Affleck, "Large-n limit of the hubbard-heisenberg model," *Phys. Rev. B*, vol. 39, pp. 11 538–11 558, 16 Jun. 1989. DOI: 10.1103/PhysRevB.39.11538.

[328] L. Alvarez-Gaumé and E. Witten, "Gravitational anomalies," *Nuclear Physics B*, vol. 234, no. 2, pp. 269–330, Apr. 1984. DOI: 10.1016/0550-3213(84)90066-X.

[329] A. N. Redlich, "Parity violation and gauge noninvariance of the effective gauge field action in three dimensions," *Phys. Rev. D*, vol. 29, pp. 2366–2374, 10 May 1984. DOI: 10.1103/PhysRevD.29.2366.

[330] X.-L. Qi, T. L. Hughes, and S.-C. Zhang, "Topological field theory of time-reversal invariant insulators," *Phys. Rev. B*, vol. 78, p. 195 424, 19 Nov. 2008. DOI: 10.1103/PhysRevB.78.195424.

[331] M. P. A. Fisher, P. B. Weichman, G. Grinstein, and D. S. Fisher, "Boson localization and the superfluid-insulator transition," *Phys. Rev. B*, vol. 40, pp. 546–570, 1 Jul. 1989. DOI: 10.1103/PhysRevB.40.546.

[332] S. C. Zhang, T. H. Hansson, and S. Kivelson, "Effective-field-theory model for the fractional quantum hall effect," *Phys. Rev. Lett.*, vol. 62, pp. 82–85, 1 Jan. 1989. DOI: 10.1103/PhysRevLett.62.82.

[333] S. C. Zhang, "The Chern-Simons Theory of the Fractional Quantum Hall Effect," *International Journal of Modern Physics B*, vol. 6, no. 1, pp. 25–58, Jan. 1992. DOI: 10.1142/S0217979292000037.

[334] T. Senthil, J. B. Marston, and M. P. A. Fisher, "Spin quantum hall effect in unconventional superconductors," *Phys. Rev. B*, vol. 60, pp. 4245–4254, 6 Aug. 1999. DOI: 10.1103/PhysRevB.60.4245.

[335] C. L. Kane and E. J. Mele, "Quantum spin hall effect in graphene," *Phys. Rev. Lett.*, vol. 95, p. 226 801, 22 Nov. 2005. DOI: 10.1103/PhysRevLett.95.226801.

[336] B. A. Bernevig and S.-C. Zhang, "Quantum spin hall effect," *Phys. Rev. Lett.*, vol. 96, p. 106 802, 10 Mar. 2006. DOI: 10.1103/PhysRevLett.96.106802.

[337] O. Golan, A. Smith, and Z. Ringel, "Intrinsic sign problem in fermionic and bosonic chiral topological matter," *Phys. Rev. Res.*, vol. 2, p. 043 032, 4 Oct. 2020. DOI: 10.1103/PhysRevResearch.2.043032.

[338] N. Seiberg, T. Senthil, C. Wang, and E. Witten, "A duality web in 2 + 1 dimensions and condensed matter physics," *Annals of Physics*, vol. 374, pp. 395–433, Nov. 2016. DOI: 10.1016/j.aop.2016.08.007.

[339] M. E. Peskin, "Mandelstam-'t hooft duality in abelian lattice models," *Annals of Physics*, vol. 113, no. 1, pp. 122–152, 1978, ISSN: 0003-4916. DOI: https://doi.org/10.1016/0003-4916(78)90252-X.

[340] C. Dasgupta and B. I. Halperin, "Phase transition in a lattice model of superconductivity," *Phys. Rev. Lett.*, vol. 47, pp. 1556–1560, 21 Nov. 1981. DOI: 10.1103/PhysRevLett.47.1556.

[341] X.-G. Wen and Y.-S. Wu, "Transitions between the quantum hall states and insulators induced by periodic potentials," *Physical review letters*, vol. 70, no. 10, p. 1501, 1993.

[342] W. Chen, M. P. A. Fisher, and Y.-S. Wu, "Mott transition in an anyon gas," *Phys. Rev. B*, vol. 48, pp. 13 749–13 761, 18 Nov. 1993. DOI: 10.1103/PhysRevB.48.13749.

[343] M. Barkeshli and J. McGreevy, "Continuous transition between fractional quantum hall and superfluid states," *Phys. Rev. B*, vol. 89, p. 235 116, 23 Jun. 2014. DOI: 10.1103/PhysRevB.89.235116.

[344] J. Y. Lee, C. Wang, M. P. Zaletel, A. Vishwanath, and Y.-C. He, "Emergent multi-flavor qed$_3$ at the plateau transition between fractional chern insulators: Applications to graphene heterostructures," *Phys. Rev. X*, vol. 8, p. 031 015, 3 Jul. 2018. DOI: 10.1103/PhysRevX.8.031015.

[345] J. Ye and S. Sachdev, "Coulomb interactions at quantum hall critical points of systems in a periodic potential," *Phys. Rev. Lett.*, vol. 80, pp. 5409–5412, 24 Jun. 1998. DOI: 10.1103/PhysRevLett.80.5409.

[346] L. Pryadko and S.-C. Zhang, "Fluctuation-induced first order transition between the quantum hall liquid and insulator," *Phys. Rev. Lett.*, vol. 73, pp. 3282–3285, 24 Dec. 1994. DOI: 10.1103/PhysRevLett.73.3282.

[347] J. Motruk and F. Pollmann, "Phase transitions and adiabatic preparation of a fractional chern insulator in a boson cold-atom model," *Phys. Rev. B*, vol. 96, p. 165 107, 16 Oct. 2017. DOI: 10.1103/PhysRevB.96.165107.

[348] T.-S. Zeng, "Phase transitions of bosonic fractional quantum hall effect in topological flat bands," *Phys. Rev. B*, vol. 103, p. 085 122, 8 Feb. 2021. DOI: 10.1103/PhysRevB.103.085122.

[349] P.-S. Hsin and N. Seiberg, "Level/rank duality and Chern-Simons-matter theories," *Journal of High Energy Physics*, vol. 2016, no. 9, 95, p. 95, Sep. 2016. DOI: 10.1007/JHEP09(2016)095.

[350] F. Benini, P.-S. Hsin, and N. Seiberg, "Comments on global symmetries, anomalies, and duality in (2 + 1) d," *Journal of High Energy Physics*, vol. 2017, no. 4, 135, p. 135, Apr. 2017. DOI: 10.1007/JHEP04(2017)135.

[351] E. Berg, S. Lederer, Y. Schattner, and S. Trebst, "Monte Carlo Studies of Quantum Critical Metals," *Annual Review of Condensed Matter Physics*, vol. 10, pp. 63–84, Mar. 2019. DOI: 10.1146/annurev-conmatphys-031218-013339.

[352] T. Shibauchi, A. Carrington, and Y. Matsuda, "A Quantum Critical Point Lying Beneath the Superconducting Dome in Iron Pnictides," *Annual Review of Condensed Matter Physics*, vol. 5, pp. 113–135, Mar. 2014. DOI: 10.1146/annurev-conmatphys-031113-133921.

[353] M. Ö. Oktel, M. Ni ţ ă, and B. Tanatar, "Mean-field theory for bose-hubbard model under a magnetic field," *Phys. Rev. B*, vol. 75, p. 045 133, 4 Jan. 2007. DOI: 10.1103/PhysRevB.75.045133.

[354] S. Powell, R. Barnett, R. Sensarma, and S. Das Sarma, "Bogoliubov theory of interacting bosons on a lattice in a synthetic magnetic field," *Phys. Rev. A*, vol. 83, p. 013 612, 1 Jan. 2011. DOI: 10.1103/PhysRevA.83.013612.

[355] C. J. Kennedy, W. C. Burton, W. C. Chung, and W. Ketterle, "Observation of Bose-Einstein condensation in a strong synthetic magnetic field," *Nature Physics*, vol. 11, no. 10, pp. 859–864, Oct. 2015. DOI: 10.1038/nphys3421.

[356] D. S. Fisher and P. C. Hohenberg, "Dilute bose gas in two dimensions," *Phys. Rev. B*, vol. 37, pp. 4936–4943, 10 Apr. 1988. DOI: 10.1103/PhysRevB.37.4936.

[357] B. J. Alder and D. S. Peters, "Superfluid Region for a Bose-Coulomb Gas with Hard Cores," en, *Europhysics Letters (EPL)*, vol. 10, no. 1, pp. 1–6, Sep. 1989, ISSN: 0295-5075, 1286-4854. DOI: 10.1209/0295-5075/10/1/001.

[358] P. Nozieres and D. Pines, *Theory of Quantum Liquids: Superfluid Bose Liquids* (Advanced Books Classics v.2). Boulder: Chapman and Hall/CRC, 2018, ISBN: 9 780429 492679.

[359] S. Moroz, A. Prem, V. Gurarie, and L. Radzihovsky, "Topological order, symmetry, and hall response of two-dimensional spin-singlet superconductors," *Phys. Rev. B*, vol. 95, p. 014 508, 1 Jan. 2017. DOI: 10.1103/PhysRevB.95.014508.

[360] N. Read and D. Green, "Paired states of fermions in two dimensions with breaking of parity and time-reversal symmetries and the fractional quantum hall effect," *Phys. Rev. B*, vol. 61, pp. 10 267–10 297, 15 Apr. 2000. DOI: 10.1103/PhysRevB.61.10267.

[361] Y.-M. Lu and A. Vishwanath, "Theory and classification of interacting integer topological phases in two dimensions: A chern-simons approach," *Phys. Rev. B*, vol. 86, p. 125 119, 12 Sep. 2012. DOI: 10.1103/PhysRevB.86.125119.

[362] T. Senthil and M. Levin, "Integer quantum hall effect for bosons," *Physical Review Letters*, vol. 110, no. 4, Jan. 2013, ISSN: 1079-7114. DOI: 10.1103/physrevlett.110.046801.

[363] X. Chen, Z.-C. Gu, Z.-X. Liu, and X.-G. Wen, "Symmetry protected topological orders and the group cohomology of their symmetry group," *Phys. Rev. B*, vol. 87, p. 155 114, 15 Apr. 2013. DOI: 10.1103/PhysRevB.87.155114.

[364] L. B. Ioffe and A. I. Larkin, "Gapless fermions and gauge fields in dielectrics," *Phys. Rev. B*, vol. 39, pp. 8988–8999, 13 May 1989. DOI: 10.1103/PhysRevB.39.8988.

[365] N. Nagaosa and P. A. Lee, "Normal-state properties of the uniform resonating-valence-bond state," *Phys. Rev. Lett.*, vol. 64, pp. 2450–2453, 20 May 1990. DOI: 10.1103/PhysRevLett.64.2450.

[366] L. B. Ioffe and G. Kotliar, "Transport phenomena near the mott transition," *Phys. Rev. B*, vol. 42, pp. 10 348–10 359, 16 Dec. 1990. DOI: 10.1103/PhysRevB.42.10348.

[367] J. D. Lykken, J. Sonnenschien, and N. Weiss, "The theory of anyonic superconductivity; a review," *International Journal of Modern Physics A; (United States)*, vol. 6:29, Dec. 1991, ISSN: ISSN 0217-751X. DOI: 10.1142/S0217751X91002434.

[368] D.-H. Lee and M. P. A. Fisher, "Anyon Superconductivity and Charge-Vortex Duality," *International Journal of Modern Physics B*, vol. 5, no. 16-17, pp. 2675–2699, Jan. 1991. DOI: 10.1142/S0217979291001061.

[369] T. Grover and A. Vishwanath, "Quantum phase transition between integer quantum hall states of bosons," *Phys. Rev. B*, vol. 87, p. 045 129, 4 Jan. 2013. DOI: 10.1103/PhysRevB.87.045129.

[370] Y.-M. Lu and D.-H. Lee, "Quantum phase transitions between bosonic symmetry-protected topological phases in two dimensions: Emergent QED_3 and anyon superfluid," *Phys. Rev. B*, vol. 89, p. 195 143, 19 May 2014. DOI: 10.1103/PhysRevB.89.195143.

[371] T. Senthil and M. P. A. Fisher, "Z_2 gauge theory of electron fractionalization in strongly correlated systems," *Phys. Rev. B*, vol. 62, pp. 7850–7881, 12 Sep. 2000. DOI: 10.1103/PhysRevB.62.7850.

[372] H. N. Phien, G. Vidal, and I. P. McCulloch, "Infinite boundary conditions for matrix product state calculations," *Phys. Rev. B*, vol. 86, p. 245 107, 24 Dec. 2012. DOI: 10.1103/PhysRevB.86.245107.

[373] M. P. Zaletel, R. S. K. Mong, and F. Pollmann, "Topological characterization of fractional quantum hall ground states from microscopic hamiltonians," *Phys. Rev. Lett.*, vol. 110, p. 236 801, 23 Jun. 2013. DOI: 10.1103/PhysRevLett.110.236801.

[374] H. N. Phien, G. Vidal, and I. P. McCulloch, "Dynamical windows for real-time evolution with matrix product states," *Phys. Rev. B*, vol. 88, p. 035 103, 3 Jul. 2013. DOI: 10.1103/PhysRevB.88.035103.

[375] V. Zauner, D. Draxler, L. Vanderstraeten, *et al.*, "Transfer matrices and excitations with matrix product states," *New Journal of Physics*, vol. 17, no. 5, 053002, p. 053 002, May 2015. DOI: 10.1088/1367-2630/17/5/053002.

[376] U. Schollwöck, "The density-matrix renormalization group in the age of matrix product states," *Annals of physics*, vol. 326, no. 1, pp. 96–192, 2011.

[377] H.-C. Jiang, T. Devereaux, and S. Kivelson, "Holon Wigner Crystal in a Lightly Doped Kagome Quantum Spin Liquid," en, *Physical Review Letters*, vol. 119, no. 6, p. 067 002, Aug. 2017, ISSN: 0031-9007, 1079-7114. DOI: 10.1103/PhysRevLett.119.067002.

[378] Y.-F. Jiang, T. P. Devereaux, and H.-C. Jiang, "Ground-state phase diagram and superconductivity of the doped hubbard model on six-leg square cylinders," *Phys. Rev. B*, vol. 109, p. 085 121, 8 Feb. 2024. DOI: 10.1103/PhysRevB.109.085121.

[379] M. Qin, C.-M. Chung, H. Shi, *et al.*, "Absence of superconductivity in the pure two-dimensional hubbard model," *Phys. Rev. X*, vol. 10, p. 031 016, 3 Jul. 2020. DOI: 10.1103/PhysRevX.10.031016.

[380] Z. Zhu and Q. Chen, "Superconductivity in doped triangular mott insulators: The roles of parent spin backgrounds and charge kinetic energy," *Phys. Rev. B*, vol. 107, p. L220502, 22 Jun. 2023. DOI: 10.1103/PhysRevB.107.L220502.

[381] Y. Huang and D. N. Sheng, "Topological chiral and nematic superconductivity by doping mott insulators on triangular lattice," *Phys. Rev. X*, vol. 12, p. 031 009, 3 Jul. 2022. DOI: 10.1103/PhysRevX.12.031009.

[382] Y. Huang, S.-S. Gong, and D. N. Sheng, "Quantum phase diagram and spontaneously emergent topological chiral superconductivity in doped triangular-lattice mott insulators," *Phys. Rev. Lett.*, vol. 130, p. 136 003, 13 Mar. 2023. DOI: 10.1103/PhysRevLett.130.136003.

[383] F. Wu, T. Lovorn, E. Tutuc, I. Martin, and A. H. MacDonald, "Topological Insulators in Twisted Transition Metal Dichalcogenide Homobilayers,", vol. 122, no. 8, 086402, p. 086 402, Mar. 2019. DOI: 10.1103/PhysRevLett.122.086402.

[384] Y. Zhang, T. Liu, and L. Fu, "Electronic structures, charge transfer, and charge order in twisted transition metal dichalcogenide bilayers,", vol. 103, no. 15, 155142, p. 155 142, Apr. 2021. DOI: 10.1103/PhysRevB.103.155142.

[385] H. Zheng, B. Wu, S. Li, *et al.*, "Localization-enhanced moiré exciton in twisted transition metal dichalcogenide heterotrilayer superlattices," *Light: Science & Applications*, vol. 12, no. 1, 117, p. 117, Dec. 2023. DOI: 10.1038/s41377-023-01171-w.

[386] S. Zhang, B. Zhou, and Y.-H. Zhang, "Approximate SU(4) spin models on triangular and honeycomb lattices in twisted AB-Stacked WSe_2 homo-bilayer," *arXiv e-prints*, arXiv:2302.07750, arXiv:2302.07750, Feb. 2023. DOI: 10.48550/arXiv.2302.07750.

[387] V. Crépel and N. Regnault, "Attractive Haldane bilayers for trapping non-Abelian anyons,", vol. 110, no. 11, 115109, p. 115 109, Sep. 2024. DOI: 10.1103/PhysRevB.110.115109.

[388] F. Xu, Z. Sun, T. Jia, *et al.*, "Observation of integer and fractional quantum anomalous hall effects in twisted bilayer $MoTe_2$," *Phys. Rev. X*, vol. 13, p. 031 037, 3 Sep. 2023. DOI: 10.1103/PhysRevX.13.031037.

[389] T. Han, Z. Lu, Z. Hadjri, *et al.*, "Signatures of chiral superconductivity in rhombohedral graphene," *Nature*, May 2025, ISSN: 1476-4687. DOI: 10.1038/s41586-025-09169-7.

[390] A. Abouelkomsan, K. Yang, and E. J. Bergholtz, "Quantum metric induced phases in moiré materials," *Phys. Rev. Res.*, vol. 5, p. L012015, 1 Feb. 2023. DOI: 10.1103/PhysRevResearch.5.L012015.

[391] R. Roy, "Band geometry of fractional topological insulators," *Phys. Rev. B*, vol. 90, p. 165 139, 16 Oct. 2014. DOI: 10.1103/PhysRevB.90.165139.

[392] P. J. Ledwith, G. Tarnopolsky, E. Khalaf, and A. Vishwanath, "Fractional chern insulator states in twisted bilayer graphene: An analytical approach," *Phys. Rev. Res.*, vol. 2, p. 023 237, 2 May 2020. DOI: 10.1103/PhysRevResearch.2.023237.

[393] J. Wang, J. Cano, A. J. Millis, Z. Liu, and B. Yang, "Exact landau level description of geometry and interaction in a flatband," *Phys. Rev. Lett.*, vol. 127, p. 246 403, 24 Dec. 2021. DOI: 10.1103/PhysRevLett.127.246403.

[394] C. Bradley and A. Cracknell, *The mathematical theory of symmetry in solids: representation theory for point groups and space groups*. Oxford University Press, 2010.

[395] J. Herzog-Arbeitman, Z.-D. Song, N. Regnault, and B. A. Bernevig, "Hofstadter topology: Noncrystalline topological materials at high flux," *Phys. Rev. Lett.*, vol. 125, p. 236 804, 23 Dec. 2020. DOI: 10.1103/PhysRevLett.125.236804.

[396] A. P. Kampf, M. Sekania, G. I. Japaridze, and P. Brune, "Nature of the insulating phases in the half-filled ionic Hubbard model," *Journal of Physics Condensed Matter*, vol. 15, no. 34, pp. 5895–5907, Sep. 2003. DOI: 10.1088/0953-8984/15/34/319.

[397] S. R. Manmana, V. Meden, R. M. Noack, and K. Schönhammer, "Quantum critical behavior of the one-dimensional ionic hubbard model," *Phys. Rev. B*, vol. 70, p. 155 115, 15 Oct. 2004. DOI: 10.1103/PhysRevB.70.155115.

[398] M. Tsuchiizu and A. Furusaki, "Ground-state phase diagram of the one-dimensional half-filled extended hubbard model," *Phys. Rev. B*, vol. 69, p. 035 103, 3 Jan. 2004. DOI: 10.1103/PhysRevB.69.035103.

[399] Z. Song, U. F. P. Seifert, Z.-X. Luo, and L. Balents, "Mott insulators in moiré transition metal dichalcogenides at fractional fillings: Slave-rotor mean-field theory," *Phys. Rev. B*, vol. 108, p. 155 109, 15 Oct. 2023. DOI: 10.1103/PhysRevB.108.155109.

[400] X. G. Wen and A. Zee, "Classification of abelian quantum hall states and matrix formulation of topological fluids," *Phys. Rev. B*, vol. 46, pp. 2290–2301, 4 Jul. 1992. DOI: 10.1103/PhysRevB.46.2290.

[401] N. Seiberg and E. Witten, "Gapped boundary phases of topological insulators via weak coupling," *Progress of Theoretical and Experimental Physics*, vol. 2016, no. 12, 12C101, p. 12C101, Dec. 2016. DOI: 10.1093/ptep/ptw083.

[402] Y.-M. Lu and A. Vishwanath, "Classification and properties of symmetry-enriched topological phases: Chern-simons approach with applications to Z_2 spin liquids," *Phys. Rev. B*, vol. 93, p. 155 121, 15 Apr. 2016. DOI: 10.1103/PhysRevB.93.155121.

[403] T. Hansson, V. Oganesyan, and S. Sondhi, "Superconductors are topologically ordered," *Annals of Physics*, vol. 313, no. 2, pp. 497–538, 2004, ISSN: 0003-4916. DOI: https://doi.org/10.1016/j.aop.2004.05.006.

[404] M. Shiroishi, H. Ujino, and M. Wadati, "(4) symmetry of the transfer matrix for the one-dimensional hubbard model," *Journal of Physics A: Mathematical and General*, vol. 31, no. 10, p. 2341, Mar. 1998. DOI: 10.1088/0305-4470/31/10/010.

[405] X. G. Wen, "Non-abelian statistics in the fractional quantum hall states," *Phys. Rev. Lett.*, vol. 66, pp. 802–805, 6 Feb. 1991. DOI: 10.1103/PhysRevLett.66.802.

[406] E. Witten, "Quantum field theory and the Jones polynomial," *Communications in Mathematical Physics*, vol. 121, no. 3, pp. 351–399, 1989.

Appendix A

Appendix to Chapter 2

Organization

Below, we provide a detailed report of the numerical evidence and analytics underlying the claims and methods used in the main text. The appendices are organized in a similar order to the main text. In particular, Appendix A.1 expounds upon details of the double Hofstadter model, which was introduced in Sec. II of the main text. Subsequently, Appendix A.2 and A.3 provides additional details regarding the results of Sec. III. The former details the strong coupling theory of the double Hofstadter model, which we used to analytically argue for the presence of the LAF, and the latter provides numerical data supplementing that in the main text. Following this, we provide additional numerical data for how we characterize the superconductor (Appendix A.4), as well as further theoretical details on the pairing symmetry (Appendix A.5). Finally, we provide a detailed exposition of the mapping to models of chiral twisted bilayer graphene (Appendix A.6).

A.1 Additional Details on the Double Hofstadter Model

In the main text, we extensively studied the double Hofstadter model, namely its symmetries, non-interacting band structure, and ground states. Here, we provide some additional details regarding the model's single-particle physics. To set notation, let us recall the definition of the double Hofstadter model and then discuss the symmetries, band structure, and layer-polarized basis of the projected model.

Recall that the flux through the top/bottom layer is $\pm\Phi = \pm\Phi_0/q$ per square plaquette, where we fix $q = 4$. Our model has direct lattice vectors $\mathbf{a}_x = (qa, 0)$ and $\mathbf{a}_y = (0, a)$, a basis for a rectangular lattice $\mathbb{L}$. Consider a *square* grid of sites $\widetilde{\mathbb{L}}$ with separation a so that each unit cell $\mathbf{u} = m_1\mathbf{a}_x + m_2\mathbf{a}_y$ contains q sites at sublattice positions

$$\mathbf{r} = \mathbf{u} + \sigma = \mathbf{u} + (\sigma a, 0) \tag{A.1}$$

for $0 \leq \sigma < q$. At each site, we consider a row-vector of microscopic fermion creation operators

$$\hat{\psi}^\dagger_{\sigma,\ell s}(\mathbf{u}) = \left(\hat{\psi}^\dagger_{\sigma,\mathsf{T}\uparrow}(\mathbf{u}), \hat{\psi}^\dagger_{\sigma,\mathsf{B}\uparrow}(\mathbf{u}), \hat{\psi}^\dagger_{\sigma,\mathsf{T}\downarrow}(\mathbf{u}), \hat{\psi}^\dagger_{\sigma,\mathsf{B}\downarrow}(\mathbf{u})\right)_{\ell s}, \tag{A.2}$$

where layer $\ell \in \{\mathsf{T},\mathsf{B}\} = \{+1,-1\}$ and spin $s \in \{\uparrow,\downarrow\} = \{+1,-1\}$ are on-site degrees of freedom, for a total of four flavors per site. We often also use $\hat{\psi}^\dagger_{\mathbf{r}\ell s}$ as a short-hand for the operator $\hat{\psi}^\dagger_{\sigma,\ell s}(\mathbf{u})$ at the square lattice site $\mathbf{r} = \mathbf{u} + \boldsymbol{\sigma}$. Crucially, the layers are vertically separated, with a magnetic flux of $+\Phi_0$ per unit cell for the top layer and $-\Phi_0$ per unit cell in the bottom layer. Adopting a Landau gauge and setting $a = 1$ henceforth, the Hamiltonian for the double Hofstadter model is

$$\hat{H} = \hat{h} + \hat{V} \tag{A.3}$$

$$\hat{h} = -t \sum_{\mathbf{r}\in\widetilde{\mathbb{L}}} \left(\hat{\psi}^\dagger_{\mathbf{r}+\hat{y}} e^{\frac{2\pi i x}{qa}\ell^z} \hat{\psi}_{\mathbf{r}} + \hat{\psi}^\dagger_{\mathbf{r}+\hat{x}} \hat{\psi}_{\mathbf{r}} + \text{h.c.}\right) - g\hat{\psi}^\dagger_{\mathbf{r}} \ell^x \hat{\psi}_{\mathbf{r}} \tag{A.4}$$

$$\hat{V} = \frac{U_1}{2} \sum_{\mathbf{r}\in\widetilde{\mathbb{L}}} : \hat{n}^2_{\mathbf{r}\mathsf{T}} + \hat{n}^2_{\mathbf{r}\mathsf{B}} : + U_2 \sum_{\mathbf{r}\in\widetilde{\mathbb{L}}} : \hat{n}_{\mathbf{r}\mathsf{T}} \hat{n}_{\mathbf{r}\mathsf{B}} : \tag{A.5}$$

where $\hat{n}_{\mathbf{r}\ell} := \sum_s \hat{\psi}^\dagger_{\mathbf{r}\ell s}\hat{\psi}_{\mathbf{r}\ell s}$ and colons denotes normal ordering relative to the electronic vacuum. Each layer consists of a Harper-Hofstadter model with kinetic energy t, coupled by inter-layer tunneling g. Moreover, the model is manifestly charge conserving and independent of spin and hence has continuous $U(1)_Q$ charge and $SU(2)$ spin symmetries. We consider separate in-layer repulsion $U_1 > 0$ and between-layer repulsion $U_2 > 0$. We underscore that $\hat{H}$ is a purely repulsive model.

We remark that, in the main text, we find it convenient numerically to add a small field B_z to the Hamiltonian:

$$\hat{H} \to \hat{H} - B_z \sum_{\mathbf{r}\in\widetilde{\mathbb{L}}} \hat{\psi}^\dagger_{\mathbf{r}} s^z \ell^z \hat{\psi}_{\mathbf{r}}. \tag{A.6}$$

Such a term breaks the $SU(2)$ symmetry down to $U(1)_S$ and is called a Zeeman term as it Zeeman shifts the electronic spin of the top (bottom) layer with $\pm B_z$ consistent with the physical picture of the double Hofstadter model (with opposite magnetic fields in opposite layers).

Space Group Representation in Momentum Space

The following characterization of the symmetries of the double Hofstadter model holds for any even integer q, where $\Phi = \ell\Phi_0/q$ is the flux per plaquette in layer ℓ. In particular, this analysis applies to the case $q = 4$ considered in the main text. The full space group is generated by the operations

$$\hat{m}_x,\ \hat{m}_y,\ \hat{C}_{2x},\ \hat{C}_{2z},\ \hat{\mathcal{I}} \tag{A.7}$$

defined in the main text. In particular, $\hat{T}_1 = \hat{m}_x^2$ and $\hat{T}_2 = \hat{m}_y$, that correspond to translations by $qa\hat{x}$ and $a\hat{y}$, generate an abelian translation group. On the other hand, the full group of magnetic translations is non-abelian since $\hat{m}_y$ anti-commutes with $\hat{m}_y$ We therefore take $\hat{T}_1$ and $\hat{T}_2$ to define the minimal unit cell. The corresponding primitive reciprocal lattice vectors are:

$$\mathbf{G}_1 = \frac{2\pi}{qa}\hat{x}, \qquad \mathbf{G}_2 = \frac{2\pi}{a}\hat{y}. \tag{A.8}$$

Placing the system on a torus of size $qN_x \times N_y$ lattice sites, we define Fourier-transformed fermion operators by:

$$\hat{\psi}^\dagger_{\sigma,\ell s}(\mathbf{k}) = \frac{1}{\sqrt{N}} \sum_{\mathbf{u}\in\mathbb{L}} e^{i\mathbf{k}\cdot(\mathbf{u}+\sigma\hat{\mathbf{x}})} \hat{\psi}^\dagger_{\sigma,\ell s}(\mathbf{u}), \tag{A.9}$$

where $\boldsymbol{\sigma} = \sigma\hat{\mathbf{x}}$. Here, $N = N_1N_2$ is the total number of unit cells on the torus and $\mathbf{k}$ takes values in the magnetic Brillouin zone. The actions of the symmetries Eq. (A.7) on the Fourier-transformed fermion operators are as follows:

$$\mathrm{Ad}_{\mathcal{I}}\hat{\psi}^\dagger(\mathbf{k}) = \hat{\mathcal{I}}\hat{\psi}^\dagger(\mathbf{k})\hat{\mathcal{I}}^{-1} \quad = \hat{\psi}^\dagger(\mathbf{k})R\ell^x s^x \qquad \text{(anti-unitary)} \tag{A.10}$$

$$\mathrm{Ad}_{C_{2z}}\hat{\psi}^\dagger(\mathbf{k}) = \hat{C}_{2z}\hat{\psi}^\dagger(\mathbf{k})\hat{C}_{2z}^{-1} = \hat{\psi}^\dagger(-\mathbf{k})R \qquad \text{(unitary)} \tag{A.11}$$

$$\mathrm{Ad}_{C_{2x}}\hat{\psi}^\dagger(\mathbf{k}) = \hat{C}_{2x}\hat{\psi}^\dagger(\mathbf{k})\hat{C}_{2x}^{-1} = \hat{\psi}^\dagger(C_{2x}\mathbf{k})\ell^x s^x \qquad \text{(unitary)} \tag{A.12}$$

$$\mathrm{Ad}_{m_x}\hat{\psi}^\dagger(\mathbf{k}) = \hat{m}_x\hat{\psi}^\dagger(\mathbf{k})\hat{m}_x^{-1} = \hat{\psi}^\dagger(\mathbf{k}+\pi\hat{y})Se^{-ik_xq/2} \qquad \text{(unitary)} \tag{A.13}$$

$$\mathrm{Ad}_{m_y}\hat{\psi}^\dagger(\mathbf{k}) = \hat{m}_y\hat{\psi}^\dagger(\mathbf{k})\hat{m}_y^{-1} = \hat{\psi}^\dagger(\mathbf{k})e^{-ik_y} \qquad \text{(unitary)}, \tag{A.14}$$

where for each symmetry g, we have defined an adjoint superoperator $\mathrm{Ad}_g\hat{\mathcal{O}} = \hat{g}\hat{\mathcal{O}}\hat{g}^{-1}$ that performs the action of conjugation. Moreover, R is a $q\times q$ permutation matrix that describes how the sublattice degree of freedom transforms under a rotation about an atom at sublattice $\sigma = 0$:

$$[R]_{\sigma'\sigma} = \delta_{(-\sigma' \bmod q),\sigma}. \tag{A.15}$$

Note that R leaves the $\sigma = 0$ sublattice equivalence class invariant and satisfies $R = R^{-1}$. Similarly, S is a $q \times q$ permutation matrix that shifts the sublattices by $q/2$ sites in the $\hat{x}$ direction, i.e. by half the unit cell:

$$[S]_{\sigma'\sigma} = \delta_{(\sigma'+q/2 \bmod q),\sigma}, \tag{A.16}$$

and likewise satisfies $S = S^{-1}$. These sublattice matrices commute: $[S, R] = 0$.

Let us now comment on the algebraic relationships between the symmetry generators. Of relevance are the commutators of the adjoint superoperators, which we show in Table A.1. In particular, the entry of row g and column h is the action of the commutator $[\mathrm{Ad}_g, \mathrm{Ad}_h] = \mathrm{Ad}_g^{-1} \circ \mathrm{Ad}_h^{-1} \circ \mathrm{Ad}_g \circ \mathrm{Ad}_h$ on the vector space of one fermion operators, which is spanned by

		h				
		$\mathcal{I}$	C_{2z}	C_{2x}	m_x	m_y
g	$\mathcal{I}$	1	1	1	$e^{-ik_x q}$	e^{-2ik_y}
	C_{2z}	1	1	1	$e^{-ik_x q}$	e^{-2ik_y}
	C_{2x}	1	1	1	1	e^{-2ik_y}
	m_x	$e^{ik_x q}$	$e^{ik_x q}$	1	1	$e^{i\pi}$
	m_y	e^{2ik_y}	e^{2ik_y}	e^{2ik_y}	$e^{-i\pi}$	1

Table A.1: The action of the commutator $[\mathrm{Ad}_g, \mathrm{Ad}_h] = \mathrm{Ad}_g^{-1} \circ \mathrm{Ad}_h^{-1} \circ \mathrm{Ad}_g \circ \mathrm{Ad}_h$ on the vector space of one fermion (i.e. charge-e) operators spanned by the microscopic operators $\psi^\dagger(\mathbf{k})$. Here, g and h run over the generators of the magnetic symmetry group. We remark that the adjoint superoperators corresponding to these generators commute up to a momentum-dependent phase.

the microscopic operators $\psi^\dagger(\mathbf{k})$. Note that the diagonal of the table is the identity and that entries above the diagonal are related to those below via the identity

$$[\mathrm{Ad}_h, \mathrm{Ad}_g] = \mathrm{Ad}_h^{-1} \circ \mathrm{Ad}_g^{-1} \circ \mathrm{Ad}_h \circ \mathrm{Ad}_g = \left(\mathrm{Ad}_g^{-1} \circ \mathrm{Ad}_h^{-1} \circ \mathrm{Ad}_g \circ \mathrm{Ad}_h\right)^{-1} = [\mathrm{Ad}_g, \mathrm{Ad}_h]^{-1}, \tag{A.17}$$

which holds whether g and h are linear or anti-linear. Also note that each commutator $[\mathrm{Ad}_g, \mathrm{Ad}_h]$ is always a linear superoperator. Computing the commutators explicitly, we find that all the adjoint superoperators commute up to a momentum-dependent phase. In particular, these phases are such that they instead exactly *commute* when acting on the vector space of charge-$2e$ operators, which is constructed in the usual way from the generators $\psi^\dagger(\mathbf{k})$ of the charge-e fermionic Hilbert space space. Moreover, all the symmetry superoperators square to the identity on this same vector space of charge-$2e$ operators.

Band Structure of the Double Hofstadter Model

At a flux fraction of $\Phi = \Phi_0/q$ per square plaquette, the band structure of the double Hofstadter model features $2q$ bands per spin species. Moreover, since the model is spin rotationally-symmetric (in the $B_z = 0$ limit), each of these bands is additionally two-fold degenerate in spin. In this work, we focus on the lowest four bands, i.e. two bands times two spins. For small values of the inter-layer tunneling g, these bands are narrow and energetically well-isolated from the rest of the spectrum, as shown in Fig. A.1(b). In this same figure, we observe that these low-energy bands host two Dirac cones of the same chirality in each spin sector. To clarify the situation, Fig. A.1(e) shows the detailed view of the vicinity of the Dirac cones with Fermi levels at half occupancy marked by a dashed red line. At large $g = 0.35$, this exactly intersects the Dirac cones, so bandstruture describes a Dirac semimetal. At smaller values of the inter-layer tunneling [Fig. A.1(d)], the Dirac cones are

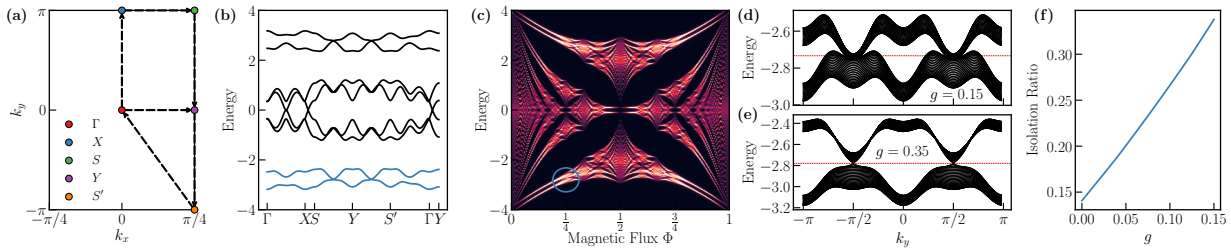

Figure A.1: **Band Structure of the Double Hofstadter Model.** (a) The Brillouin zone of the double Hofstadter model for $q = 4$. Dashed lines show a high-symmetry path. (b) The spectrum of the double Hofstadter model for $t = 1, g = 0.35, q = 4$ along the high-symmetry path. Each band is doubly-degenerate due to spin. We project down to the lower bands (blue). Note the presence of two Dirac cones between the two lowest bands at $\mathbf{k} = (\pi/4, \pm\pi/2)$. (c) The "double Hofstadter butterfly" spectrum for $t = 1, g = 0.1$ for $0 \leq \Phi = p/q \leq 1$. (Although we have taken $p = 1$ in the discussion in the main text, one can use the standard generalization to rational fractions p/q without changing the shape of the Brillouin zone.) Notice that the two lowest bands at $\Phi = 1/4$ (blue circle) are continuously connected to the two lowest Landau levels in the limit $q \to \infty$. (d) Constant k_x cuts of the bandstructure at $g = 0.15$. Note that the Fermi level at half-filling (dashed red line) is above the Dirac point, yielding both electron and hole pockets. (e) Constant k_x cuts at $g = 0.35$. The Fermi level now intersects the Dirac point, giving a Dirac semimetal. (f) Plot of the "isolation ratio" (defined as the ratio of the bandwidth of the low-energy manifold to the gap above it) vs. the interlayer tunneling g, for the range $0 \leq g \leq 0.15$ considered in the superconducting analysis presented in the main text.

buried below the Fermi level, indicating a band metal with both electron and hole-like Fermi pockets. This is consistent with the behavior at $g = 0$, where the bands are degenerate at each momentum and not entirely flat.

We now further comment on the structure and protection of the Dirac cones, assuming g is large enough that the half-filled state is semi-metallic. Whenever two Dirac cones are present in the spectrum, then symmetries are responsible for their topological protection and locations. Specifically, C_{2z} introduces an energetic degeneracy between $\mathbf{k}$ and $-\mathbf{k}$, whereas C_{2x} relates $\mathbf{k}$ to $C_{2x}\mathbf{k}$, and the magnetic translation m_x likewise makes $\mathbf{k}$ and $\mathbf{k}+\pi\hat{y}$ degenerate (assuming q is even so that these momenta are both allowed). This constrains the two Dirac cones to sit at only a finite number of isolated points in the Brillouin zone, namely $(k_x, k_y) \in \{0, \pm\pi/4, \pm\pi/2\} \times \{0, \pm\pi\}$. For energetic reasons, the Dirac cones of the double Hofstadter model incidentally reside at the particular locations $\mathbf{k} = (-\pi/4, \pm\pi/2)$. Provided that these Dirac cones exist, their topological protection can be guaranteed by the spacetime inversion symmetry $\mathcal{I}$ and spin $SU(2)$. To see this, it is convenient to think in the layer-polarized basis that was introduced in the main text and will be expounded

upon in more detail in Section A.1 of the supplemental material. First, note that the spin $SU(2)$ of our model constrains the single particle Hamiltonian of the two lowest bands to be $h(\mathbf{k}) = \sum_{\alpha\in\{0,x,y,z\}} h_\alpha(\mathbf{k})l^\alpha$. Moreover, in an appropriate gauge, spacetime inversion acts by $h(\mathbf{k}) = l^x h^*(\mathbf{k})l^x$, which precludes l^z from the single-particle Hamiltonian. Note that the gap between the two bands is only set by the $l^{x,y}$ components of h. Since the Hamiltonian looks like $h(\mathbf{k}) = h_0(\mathbf{k})l^0 + k_x l^x + k_y l^y + \mathcal{O}(\mathbf{k}^2)$ in the vicinity of each Dirac cone, we conclude that symmetric single-particle perturbations may be able to move the Dirac cones below the Fermi energy but cannot get rid of these gap closings. We conclude by noting that since our model is symmetric under spacetime inversion $\mathcal{I}$ and consists of two low-energy bands, the winding of polarization (as shown in Fig. A.2d) implies $w_2 = +1$ fragile topology [24].

We now brief comment on the energetic isolation of the lowest pair of bands. In this work, we focus on the case $q = 4$ since it is the smallest q for which the low-energy bands are well-isolated from the rest of the single-particle spectrum. In particular, as we show in Fig. A.1(f), the ratio of bandwidth to bandgap ratio (or "isolation ratio") at $q = 4$ and $g = 0.0$ is $0.22/1.53 \approx 0.15 \ll 1$. Moreover, it remains relatively small for the values $g \leq 0.15$ considered in our superconducting analysis. In contrast, in the case of $q = 3$ and $g = 0.0$, this ratio is $0.73/1.27 \approx 0.57$, which is a factor of four larger. Since our projection to the lowest-two bands (per spin sector) is best justified when the isolation ratio is small, we restrict to $q = 4$ to ensure our DMRG numerics are representative of the ground state of the full microscopic model.

Layer-Polarized Hybrid Wannier Computational Basis

In the single-particle subspace of the low-lying, narrow bands, it is desirable to construct a basis in which the Chern number is manifest. Inspired by the $g = 0$ limit, in which the Chern number is equivalent to the layer index $\mathcal{C} = \pm\ell$, we achieve this by constructing a "layer-polarized" basis whose single-particle states are maximally-polarized to one of the layers. Crucially, we use the gauge freedom within the low-energy bands to construct a "hybrid Wannier" basis of orbitals that are maximally exponentially-localized in the x direction but delocalized (namely, plane waves with momentum k_y) around the circumference of the cylinder.

To achieve a basis with the aforementioned properties, we perform 1D Wannier localization on each set of Bloch states on each wire k_y.[1] In doing so, we obtain the polarizations $P_x(k_y) \in [0, 1)$ of the 1D exponentially-localized orbitals. Within the Modern Theory of Polarization, these polarizations are related to the eigenvalues of the Wilson loop along each wire k_y. In addition, we demand that the basis transforms in a prescribed way under the anti-unitary symmetry $\mathcal{I}$, namely the following purely off-diagonal form:

$$O_{\mathcal{I}}(\mathbf{k}) = \langle v(\mathbf{k})|\hat{\mathcal{I}}|v(\mathbf{k})\rangle = e^{-2\pi i(P^+(k_y)+P^-(k_y))k_x/N_x} s^x\sigma^x, \tag{A.18}$$

[1]Due to the finite circumference L_y of the cylinder, k_y takes L_y-many quantized values. We therefore refer to each constant-k_y slice as a "wire," along which k_x is effectively continuous.

where s^x and σ^x are the usual Pauli matrix (in the spin and Wannier label), and the 1D Hybrid Wannier states are given by

$$|v_{ls}(\mathbf{k})\rangle = \hat{\varphi}^\dagger_{ls}(\mathbf{k})|0\rangle = \sum_{\sigma,\ell} \hat{\psi}^\dagger_{\sigma\ell s}(\mathbf{k})|0\rangle\, v_{\sigma\ell,l}(\mathbf{k}). \tag{A.19}$$

Since $\mathcal{I}$ anti-commutes with the position operator $\hat{\mathcal{I}}\hat{\mathbf{r}} = -\hat{\mathbf{r}}\hat{\mathcal{I}}$, then the two polarizations are opposite (modulo unity), which implies that $P^+(k_y) + P^-(k_y)$ takes an integer value on each wire.

Having chosen the above off-diagonal action of $\mathcal{I}$, we guarantee that our basis has several important and convenient properties. Most crucially, the basis is a *layer-polarized* basis. As defined in the main text, such a basis (i) diagonalizes the action of the (projected) layer operator

$$O_{\ell^z}(\mathbf{k}) = \langle v(\mathbf{k})|\hat{\ell}^z|v(\mathbf{k})\rangle = v^\dagger(\mathbf{k})\ell^z v(\mathbf{k}), \tag{A.20}$$

with (ii) eigenvalues $\lambda_l(\mathbf{k})$ that take a constant sign across the Brillouin zone. To see this, we recall that $\hat{\mathcal{I}}\hat{\psi}^\dagger(\mathbf{k})\hat{\mathcal{I}} = \hat{\psi}^\dagger(\mathbf{k})\ell^x s^x$, and remark that Eq. (A.18) is then equivalent to the constraint

$$v^\dagger(\mathbf{k})\ell^x v^*(\mathbf{k}) = e^{i\gamma(\mathbf{k})}\sigma^x, \tag{A.21}$$

where the coefficient is the complex phase:

$$e^{i\gamma(\mathbf{k})} = e^{-2\pi i(P^+(k_y)+P^-(k_y))k_x/N_x}. \tag{A.22}$$

Invoking the constraint Eq. (A.21), it is then straightforward to show that

$$\sigma^x O^*_{\ell^z}(\mathbf{k})\sigma^x = -O_{\ell^z}(\mathbf{k}). \tag{A.23}$$

Since $O_{\ell^z}(\mathbf{k})$ is a 2×2 Hermitian matrix, this expression implies that it is traceless and diagonal. Numerically, it takes the form $O_{\ell^z}(\mathbf{k}) = \lambda(\mathbf{k})\sigma^z$ with $0.9 < \lambda(\mathbf{k}) < 1$, for all parameters $g \in [0, 0.3]$ considered, so that the matrix is never singular. This concludes the proof that the states $|v_{ls}(\mathbf{k})\rangle$ constitute a layer-polarized basis, justifying the use of the symbol l (referred to in the main text as the "dressed layer" index) to label these states. Henceforth, we use l^a rather than σ^a to denote the Pauli matrices acting in the space of layer-polarized states.

Next, we derive the constraints imposed on the projected inter-layer tunneling in the layer-polarized basis. The matrix structure of $\hat{\mathcal{P}}\hat{h}_g\hat{\mathcal{P}}$ is related to the overlap $O_{\ell^x}(\mathbf{k})$, whose form is likewise constrained by Eq. (A.21) as follows:

$$l^x O^*_{\ell^x}(\mathbf{k})l^x = O_{\ell^x}(\mathbf{k}). \tag{A.24}$$

Since $O_{\ell^x}(\mathbf{k})$ is a 2×2 Hermitian matrix, this expression guarantees that it has no l^z matrix component. Though it may generally possess an identity component (i.e. a finite trace), we remark that this contribution is generally very small, namely of order $\mathcal{O}(g^2)$. In contrast,

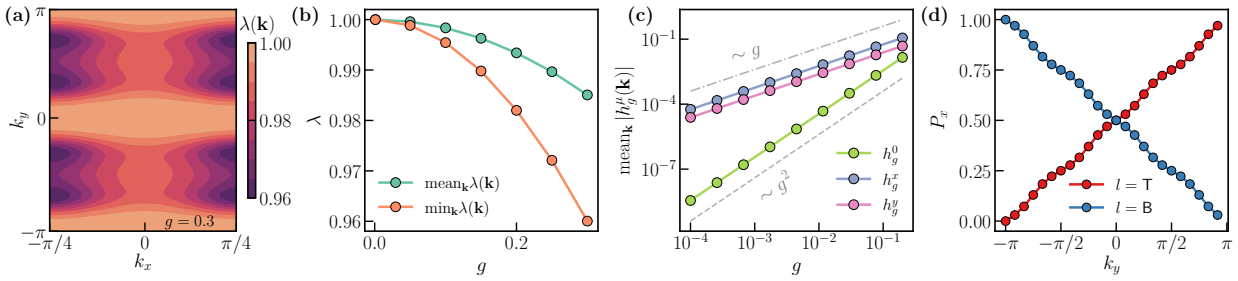

Figure A.2: **Layer Polarized Basis of the Double Hofstadter Model.** (a) The positive eigenvalue $\lambda(\mathbf{k})$ of the projected layer operator in the layer-polarized basis at $g = 0.3$. (b) The mean and minimum of this quantity, evaluated over the BZ, for a broad range of values $0 < g \leq 0.3$ of the inter-layer tunneling. Across this interval, λ is bounded below by $0.96 \sim 1$, indicating near-maximal layer polarization. (c) The BZ-average of the components of the projected inter-layer tunneling operator $\hat{\mathcal{P}}\hat{h}_g\hat{\mathcal{P}}$ expressed in the layer-polarized basis. The dominant components $\mu = x, y$ scale linearly in g, whereas the $\mu = 0$ component is quadratic and the $\mu = z$ component is made to vanish identically. (d) Polarizations $P^{\mathsf{T/B}}(k_y)$ on cuts of constant k_y at $g = 0.3$. The Chern number of a band obeys $C = \int P(k_y)dk_y$. Here the two bands wind oppositely, with crossings at $k_y = -\pi, 0$. This demonstrates the Chern number of the layer-polarized bands are $C = \pm 1$ for the top/bottom bands, and that these low-energy bands have a non-trivial fragile topological invariant [24], $w_2 = +1$.

the off-diagonal $l^{x,y}$ components go as $\mathcal{O}(g)$ (see Fig. A.2(c)). Altogether, the projected tunneling operator takes the following form:

$$\hat{\mathcal{P}}\hat{h}_g\hat{\mathcal{P}} \approx \sum_{\mathbf{k}} \hat{\varphi}^\dagger_{\mathbf{k}} \Big[h^x_g(\mathbf{k}) l^x + h^y_g(\mathbf{k}) l^y \Big] \hat{\varphi}_{\mathbf{k}}. \tag{A.25}$$

Applying similar arguments, it can be shown that the hybrid Wannier orbitals transform as:

$$\mathrm{Ad}_{\mathcal{I}}\hat{\varphi}^\dagger(\mathbf{k}) = \hat{\mathcal{I}}\hat{\varphi}^\dagger(\mathbf{k})\hat{\mathcal{I}}^{-1} = \hat{\varphi}^\dagger(\mathbf{k}) s^x l^x e^{i\gamma(\mathbf{k})} \quad \text{(anti-unitary)} \tag{A.26}$$

$$\mathrm{Ad}_{C_{2z}}\hat{\varphi}^\dagger(\mathbf{k}) = \hat{C}_{2z}\hat{\varphi}^\dagger(\mathbf{k})\hat{C}^{-1}_{2z} = \hat{\varphi}^\dagger(-\mathbf{k}) e^{i\gamma(\mathbf{k})} s(k_y) \quad \text{(unitary)} \tag{A.27}$$

$$\mathrm{Ad}_{C_{2x}}\hat{\varphi}^\dagger(\mathbf{k}) = \hat{C}_{2x}\hat{\varphi}^\dagger(\mathbf{k})\hat{C}^{-1}_{2x} = \hat{\varphi}^\dagger(C_{2x}\mathbf{k}) s^x l^x s(k_y) \quad \text{(unitary)} \tag{A.28}$$

$$\mathrm{Ad}_{m_x}\hat{\varphi}^\dagger(\mathbf{k}) = \hat{m}_x\hat{\varphi}^\dagger(\mathbf{k})\hat{m}^{-1}_x = \hat{\varphi}^\dagger_l(k_x, k_y + \pi) e^{-ik_x q/2} e^{i\mu_l(\mathbf{k})} \quad \text{(unitary)} \tag{A.29}$$

$$\mathrm{Ad}_{m_y}\hat{\varphi}^\dagger(\mathbf{k}) = \hat{m}_y\hat{\varphi}^\dagger(\mathbf{k})\hat{m}^{-1}_y = \hat{\varphi}^\dagger(\mathbf{k}) e^{-ik_y} \quad \text{(unitary)}, \tag{A.30}$$

where $s(k_y) = \pm 1$ is some wire-dependent sign factor and $e^{i\mu_l(\mathbf{k})}$ is some complex phase. For our particular numerical implementation, we additionally have that

$$e^{i\gamma(-\mathbf{k})} = e^{-i\gamma(\mathbf{k})}, \qquad s(-k_y) = s(k_y), \tag{A.31}$$

for all wires k_y. Moreover,

$$e^{i\mu_l(-\mathbf{k})} = e^{i\mu_l(\mathbf{k})} \qquad \text{and} \qquad e^{i\mu_{+1}(\mathbf{k})}e^{i\mu_{-1}(\mathbf{k})} = 1, \tag{A.32}$$

so long as $k_y \notin \{0, \pi\}$. These identities are indispensable for our analysis of the superconducting pairing symmetry in Appendix A.5. Finally, we remark that we assume our layer-polarized basis is periodic in the Brillouin zone:

$$\hat{\varphi}^\dagger_{ls}(\mathbf{k}+\mathbf{G}) = \hat{\varphi}^\dagger_{ls}(\mathbf{k}), \tag{A.33}$$

or equivalently that

$$v_{\sigma\ell,l}(\mathbf{k}+\mathbf{G}) = e^{-i\mathbf{G}\cdot\sigma}v_{\sigma\ell,l}(\mathbf{k}). \tag{A.34}$$

Quantum Geometry

To conclude our discussion of the single-particle aspects of the double Hofstadter model, we comment briefly on its quantum geometry. Quantum geometry studies the position operator projected into a few (often flat) bands. A key motivation for its study was determining when lattice systems were "close enough" to the lowest Landau level that one should expect fractional quantum Hall physics to appear, but also appears in numerous other contexts including optics and studies of flat band superconductivity. Here we use it to be able to make basis-independent comparisons to other systems, notably the lowest Landau level and to the Bistritzer-MacDonald model.

Consider a well-isolated band or set of bands whose Bloch periodic wavefunctions are $u_{\mathbf{k}n}(\mathbf{r}) = e^{-i\mathbf{k}\cdot\mathbf{r}}\psi_{\mathbf{k}n}(\mathbf{r})$ with associated projector $P_\mathbf{k} = \sum_n |u_{\mathbf{k}n}\rangle\langle u_{\mathbf{k}n}|$. Momentum space band geometry focuses on the Berry curvature $\mathcal{F}(\mathbf{k})$ and the Fubini-Study metric $g_{\mathrm{FS}}(\mathbf{k})$. These are defined by

$$g^{\mu\nu}_{\mathrm{FS}}(\mathbf{k}) = \mathrm{Re}[\eta^{\mu\nu}(\mathbf{k})], \quad \mathcal{F}^{\mu\nu}(\mathbf{k}) = -\frac{1}{2}\mathrm{Im}[\eta^{\mu\nu}(\mathbf{k})], \tag{A.35}$$

where

$$\eta^{\mu\nu}(\mathbf{k}) = \mathrm{Tr}[P_\mathbf{k}\hat{r}^\mu Q_\mathbf{k}\hat{r}^\nu P_\mathbf{k}] = \sum_n \langle\partial^{k_\mu}u_{\mathbf{k}n}|Q_\mathbf{k}|\partial^{k_\nu}u_{\mathbf{k}n}\rangle \tag{A.36}$$

is the quantum geometry tensor and $Q_\mathbf{k} = I - P_\mathbf{k}$. The non-zero component of the curvature $\Omega = \mathcal{F}^{xy}$ integrates to the Chern number: $C = \frac{1}{2\pi}\int d\mathbf{k}\Omega$. These are plotted for the double Hofstadter model for the top layer polarized band in Fig. A.3. Both quantities are rather uniform, and both have the same peaks and troughs whose four-fold structure is due to the (weakly broken) magnetic translation symmetry in each layer. Since the metric is related to the interaction-induced Fock dispersion [390], the resemblance of these quantities to the LAF bandstructure (shown in the main text) is not accidental.

This data allows us to compare the double Hofstadter model to the lowest Landau level. To this end, we recall the *trace inequality*[2]

$$T = \int T(\mathbf{k})\, d^2\mathbf{k} = \int \mathrm{Tr} g_{\mathrm{FS}}(\mathbf{k}) - \Omega(\mathbf{k})\, d^2\mathbf{k} \geq 0. \tag{A.37}$$

The lowest Landau level is entirely specified by its band geometry, in the sense that any $|C| = 1$ Chern band where: (I) $T = 0$, and (II) $\Omega(\mathbf{k})$ is constant is equivalent to the lowest Landau level [391]. Fig. A.3(c) plots the $\mathbf{k}$-resolved trace inequality, showing that the top layer-polarized band of the double Hofstader model is extremely close to the lowest Landau level. Indeed, in the limit $q \to \infty$, both $T \to 0$ and the standard deviation of the Berry curvature $\sigma[\mathcal{F}] \to 0$ [Fig. A.3(d)]. The layer-polarized bands of the double Hofstadter model are therefore closely adiabatically connected to the lowest Landau levels. This can be seen visually in Fig. A.1 (c), where one can trace the adiabatic connection from $q = 4$ (blue circle) to $q \to \infty$. Notably, this closeness of the top layer polarized band to the LLL (and the bottom layer polarized band to the LLL in opposite magnetic field) evolves only weakly with g [see Fig. A.1 (e)]. Conceptually, one can therefore think of the physics of the double Hofstadter model as descending from that of pairs Landau levels in opposite magnetic fields. However, as we saw in the main text, the small deviations from uniformity across the Brillouin zone determine the locations of the Fermi surface and the character of any superconductivity.

Another system that can be thought of as two approximate Landau levels in opposite magnetic fields is twisted bilayer graphene [74, 392]. There, however, the deviations from the ideal [393] or vortexable limit [217] are concentrated near the Γ point — a time-reversal invariant momentum point — whereas in the double Hofstadter model the trace inequality $T(\mathbf{k})$ is largest at non-high-symmetry points. The double Hofstadter model at $q = 4, g = 0.1$ has comparable trace inequality violation to the sublattice-polarized flat band of the Bistritzer-MacDonald model at chiral ratio $w_0/w_1 \approx 0.3$ [392]. Given these quantitative comparisons to both Landau levels and twisted bilayer graphene, it is reasonable to expect phenomena from those systems to manifest in the double Hofstadter model.

A.2 Additional Details on the Strong-Coupling Theory of the LAF

This section provides a complete treatment of the strong-coupling theory presented in the main text, which gave analytical predictions for the ground state at $\nu = 2$ electrons per unit cell. This filling is equal to that of a band insulator occupying two of the four narrow bands. Our treatment hews closely to related calculations in magic angle graphene, whose notation and conventions we largely follow [31, 32, 79]. Provided that the interaction scale U is smaller than the gap to the "remote" bands, (which is about $\sim 2t$ for $q = 4$ at $g = 0.1$),

[2]Comparing to the formula for the Chern number, the characteristic size of this quantity is 2π. Hence we plot $T/2\pi$.

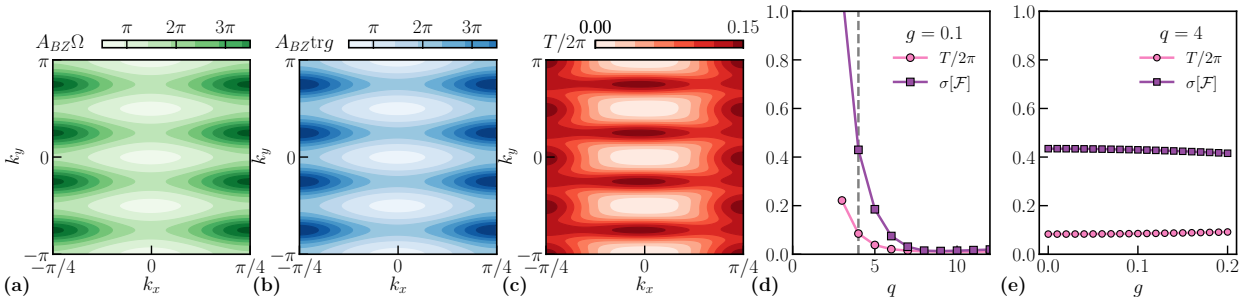

Figure A.3: **Quantum Geometry of the Double Hofstadter Model.** We work in the the top layer-polarized band at $q = 4, g = 0.1$ (unless otherwise noted). (a) Berry curvature $\Omega(\mathbf{k})$, normalized by the Brillouin zone area so that a uniform $C = 1$ band would have value 2π. (b) The trace of the Fubini-Study metric $g_{\mathrm{FS}}(\mathbf{k})$, defined in the text. (c) The violation of the trace inequality $T(\mathbf{k}) = \mathrm{Tr}g_{\mathrm{FS}}(\mathbf{k}) - \Omega(\mathbf{k})$ that vanishes for the lowest Landau level, or more generally for 'ideal' Chern bands. (d) The integrated trace violation $T/2\pi$ and standard deviation of the Berry curvature $\sigma[\mathcal{F}]$ as a function of flux q. These vanish as the band approaches the lowest Landau level limit at large q. (e) The same quantities evolve only weakly with g.

we expect the ground state at any filling $\nu \leq 4$ to be accurately captured by the flat-band projected Hamiltonian $\hat{\mathcal{P}}\hat{H}\hat{\mathcal{P}}$. Below we carefully define the projected interaction and dispersion and show, in the symmetric $g = 0$ limit, that the interaction selects out a manifold of Slater determinant ground states. We consider both the case $U_2 = 0$ where this manifold is comprised of bilayer quantum Hall ferromagnets (QHFMs) and the case $U_2 = U_1$ where these states compete with layer-polarized QAH states. Adding back $g > 0$ perturbatively, we will see that both the LAF — a particular family of anti-aligned bilayer QHFMs — and QAH insulators are selected as ground states. Our strong-coupling analysis is heavily inspired a formalism developed for twisted bilayer graphene, introduced in [31, 63, 75].

Flat Band-Projected Interaction

To make analytic progress on this Hamiltonian with strong-coupling theory, we must express the interaction in the appropriate form. We start from real space, transform to momentum space, then finally form an effective model for the flat band subspace. Consider a generic density-density interaction

$$\hat{V} = \sum_{\ell,\ell'} \sum_{\mathbf{r},\mathbf{r}'} V_{\ell\ell'}(\mathbf{r} - \mathbf{r}') : \hat{\rho}_{\mathbf{r}\ell}\hat{\rho}_{\mathbf{r}'\ell'} : , \qquad \hat{\rho}_{\mathbf{r}\ell} = \sum_{s} \hat{\psi}^{\dagger}_{\mathbf{r}\ell s}\hat{\psi}_{\mathbf{r}\ell s}, \tag{A.38}$$

where $V_{\mathsf{TB}} = V_{\mathsf{BT}} > 0$ is the inter-layer interaction and $V_{\mathsf{TT}} = V_{\mathsf{BB}} > 0$ is in-layer. Next, writing the lattice site as $\mathbf{r} = \mathbf{u} + \boldsymbol{\sigma}$ [see Eq. (A.1)], we consider the Fourier transformed

fermion operators

$$\hat{\psi}_{\sigma,\ell s}(\mathbf{u}) = \frac{1}{\sqrt{N}} \sum_b \sum_{\mathbf{k}\in \mathrm{BZ}} e^{i\mathbf{k}\cdot(\mathbf{u}+\sigma)} v_{\sigma\ell,b}(\mathbf{k}) \hat{\varphi}_{bs}(\mathbf{k}), \tag{A.39}$$

where BZ is the first Brillouin zone and b is a "generalized" band index. One can think of the v's as Bloch wavefunctions of the kinetic Hamiltonian defining a band basis. However, we use no specific properties of that basis; in fact, we will later specialize to the case where the v's define the layer-polarized basis. In any case, we additionally require a periodic gauge:

$$v_{\sigma\ell,b}(\mathbf{k}+\mathbf{G}) = e^{-i\mathbf{G}\cdot\sigma} v_{\sigma\ell,b}(\mathbf{k}). \tag{A.40}$$

This means the v's are specified entirely by their values on momenta within the first Brillouin zone. The Fourier transformed density is naturally written in terms of *layer-resolved form factors*, which are independent of spin:

$$[\Lambda_{\mathbf{q}\ell}(\mathbf{k})]_{bb'} = \left[v^\dagger(\mathbf{k}) P_\ell v(\mathbf{k}+\mathbf{q})\right]_{bb'} = \sum_\sigma v_{\sigma\ell,b}(\mathbf{k})^* v_{\sigma\ell,b'}(\mathbf{k}+\mathbf{q}). \tag{A.41}$$

Here $P_\ell = (\ell^0 + \ell\ell^z)/2$ is the projector onto the microscopic layer ℓ. We emphasize that the form factors are matrices that do not depend on spin; we therefore consider them as 2×2 matrices in the generalized band index b. Our choice of periodic gauge implies the following useful identities:

$$\Lambda_{-\mathbf{q}\ell}(\mathbf{k}+\mathbf{q}) = \Lambda_{\mathbf{q}\ell}(\mathbf{k})^\dagger, \quad \Lambda_{-\mathbf{G}\ell}(\mathbf{k}) = \Lambda_{\mathbf{G}\ell}(\mathbf{k})^\dagger, \quad \Lambda_{\mathbf{q}\ell}(\mathbf{k}+\mathbf{G}) = \Lambda_{\mathbf{q}\ell}(\mathbf{k}). \tag{A.42}$$

The Fourier transformed density operator may then be written as

$$\hat{\rho}_{\mathbf{q}\ell} = \frac{1}{\sqrt{qN}} \sum_{\mathbf{r}} e^{-i\mathbf{q}\cdot\mathbf{r}} \hat{\rho}_{\mathbf{r}\ell} = \frac{1}{\sqrt{qN}} \sum_{b,b',s} \sum_{\mathbf{k}} \hat{\varphi}^\dagger_{bs}(\mathbf{k}) [\Lambda_{\mathbf{q}\ell}(\mathbf{k})]_{bb'} \hat{\varphi}_{b's}(\mathbf{k}+\mathbf{q}), \tag{A.43}$$

where the second step follows from the Poisson summation formula and periodic gauge. Using the Fourier transformed potential $V_{\ell\ell'}(\mathbf{r}) = \frac{1}{qN}\sum_{\mathbf{q}\in\mathrm{EBZ}} e^{-i\mathbf{q}\cdot\mathbf{r}} V_{\ell\ell'}(\mathbf{q})$, the interaction then takes the form

$$\hat{V} = \sum_{\ell\ell'} \sum_{\mathbf{q}\in\mathrm{EBZ}} V_{\ell\ell'}(\mathbf{q}) : \hat{\rho}_{\mathbf{q}\ell} \hat{\rho}_{-\mathbf{q}\ell'} : \tag{A.44}$$

where colons denote normal ordering with respect to the vacuum. Here, EBZ denotes the "extended" Brillouin zone associated with the microscopic square lattice, to be distinguished from the BZ derived from the $q\times 1$ site unit cell.

Finally we make an effective model for the active bands. Since the active bands are energetically the lowest ones then, just as with the lowest Landau level, projecting into them amounts to restricting to a certain set of operators. Let $\mathcal{A}\cup\mathcal{R}$ be a partition of the generalized bands into "active" bands of the flat band subspace and all other "remote" bands. The associated many-body projector is $\hat{\mathcal{P}} = \prod_{\mathbf{k}\in\mathrm{BZ}} \prod_s \prod_{b\in\mathcal{R}} (1 - \hat{\varphi}^\dagger_{bs}(\mathbf{k})\hat{\varphi}_{bs}(\mathbf{k}))$. Crucially, since the interaction is normal-ordered with respect to the vacuum, and since the image of

$\hat{\mathcal{P}}$ contains no states that occupy the inactive bands $\mathcal{R}$, then $\hat{\mathcal{P}}\hat{V}\hat{\mathcal{P}}$ takes the same form as Eq. (A.44), except that the band indices in the expression for the density operator are *truncated* to $\mathcal{A}$. Therefore we have arrived at the flat band-projected interaction:

$$\hat{\mathcal{P}}\hat{V}\hat{\mathcal{P}} = \sum_{\ell\ell'} \sum_{\mathbf{q}\in \mathrm{EBZ}} V_{\ell\ell'}(\mathbf{q}) : \hat{\mathcal{P}}\hat{\rho}_{\mathbf{q}\ell}\hat{\mathcal{P}}\hat{\rho}_{-\mathbf{q}\ell}\hat{\mathcal{P}} : . \tag{A.45}$$

Strong-Coupling Form of the Hamiltonian

To apply strong-coupling theory, we must partition the full projected Hamiltonian into a *positive-definite* interaction $\hat{\mathcal{V}}$ plus residual terms that are perturbatively small or act trivially within the ground state manifold of $\hat{\mathcal{V}}$. In what follows, we discuss how this is performed in two distinct physical limits, namely $U_2 = 0$ and $U_2 = U_1$. In each case, strong-coupling theory requires that the interaction Hamiltonian be comprised of densities measured relative to a reference *background charge density* at $\nu = 2$, rather than the $\nu = 0$ vacuum. We first focus on the limit $g = 0$ where layer is a good quantum number, postponing a perturbative treatment of the inter-layer tunneling to the next section.

Case 1: Vanishing Inter-Layer Interactions

In the limit $U_2 = 0$ where the inter-layer interactions vanish, it is natural to posit that this background charge density evenly occupies each layer and is translationally-invariant. A family of states whose charge densities satisfy these properties is the manifold of bilayer QHFMs, defined as

$$|\mathbf{n}_\mathsf{T}, \mathbf{n}_\mathsf{B}\rangle = \prod_{\mathbf{k}} \hat{\varphi}^\dagger_{\mathsf{T},\boldsymbol{n}_\mathsf{T}}(\mathbf{k})\hat{\varphi}^\dagger_{\mathsf{B},\boldsymbol{n}_\mathsf{B}}(\mathbf{k})\,|0\rangle\,, \tag{A.46}$$

where the Fermion operators, whose spins are aligned to the axes

$$\mathbf{n}_l = (\cos\theta_l \sin\phi_l, \sin\theta_l \sin\phi_l, \cos\phi_l) \in S^2, \tag{A.47}$$

are defined in terms of the dressed layer orbitals (see Sec. A.1) by

$$\hat{\varphi}^\dagger_{l,\boldsymbol{n}_l} = \cos(\theta_l/2)\hat{\varphi}^\dagger_{l,\uparrow} + e^{i\phi_l}\sin(\theta_l/2)\hat{\varphi}^\dagger_{l,\downarrow}. \tag{A.48}$$

We now argue that the bilayer QHFMs Eq. (A.46) are exact eigenstates of the projected density operator Eq. (A.43) in the $g = 0$ limit, and use this fact to engineer a corresponding positive-definite "strong-coupling" interaction $\hat{\mathcal{V}}$ that exactly annihilates these states. This is pertinent to the original ground state problem because $\hat{\mathcal{V}}$ will be found to differ from the original projected interaction Eq. (A.45) by a single-particle term that approximates a *chemical potential*, up to perturbatively small momentum-dependent variations.

To show that the states $|\mathbf{n}_\mathsf{T}, \mathbf{n}_\mathsf{B}\rangle$ are exact zero modes of the projected density, we use the enhanced symmetry at $g = 0$. Note that the layer-projected form factors are greatly

restricted by $U(1)$ layer conservation. Namely, since layer is a good quantum number, the dressed layer index l is indistinguishable from the microscopic layer ℓ, and correspondingly:

$$[\Lambda_{\mathbf{q}\ell}(\mathbf{k})]_{ll'} \propto \delta_{l\ell}\delta_{l'\ell}. \tag{A.49}$$

The projected interactions therefore take the form

$$\hat{\mathcal{P}}\hat{\rho}_{\mathbf{q}\ell}\hat{\mathcal{P}}\left|\mathbf{n}_{\mathsf{T}},\mathbf{n}_{\mathsf{B}}\right\rangle = \frac{1}{\sqrt{qN}}\sum_{\mathbf{k}\in\mathrm{BZ}}\left[\Lambda_{\mathbf{q}\ell}(\mathbf{k})\right]_{\ell\ell}\sum_{s}\hat{\varphi}^{\dagger}_{\ell s}(\mathbf{k})\hat{\varphi}_{\ell s}(\mathbf{k}+\mathbf{q})\left|\mathbf{n}_{\mathsf{T}},\mathbf{n}_{\mathsf{B}}\right\rangle. \tag{A.50}$$

This expression vanishes due to Pauli exclusion unless $\mathbf{q}=\mathbf{G}$ is a reciprocal lattice vector, in which case $\hat{\varphi}(\mathbf{k}+\mathbf{G})=\hat{\varphi}(\mathbf{k})$ due to the periodic gauge convention Eq. (A.40). The Fermion bilinear then becomes a number density, and thus

$$\hat{\mathcal{P}}\hat{\rho}_{\mathbf{q}\ell}\hat{\mathcal{P}}\left|\mathbf{n}_{\mathsf{T}},\mathbf{n}_{\mathsf{B}}\right\rangle = \bar{\rho}_{\mathbf{q}\ell}\left|\mathbf{n}_{\mathsf{T}},\mathbf{n}_{\mathsf{B}}\right\rangle, \tag{A.51}$$

where

$$\bar{\rho}_{\mathbf{q}\ell} = \frac{1}{\sqrt{qN}}\sum_{\mathbf{k}\in\mathrm{BZ}}\sum_{\mathbf{G}}\delta_{\mathbf{q},\mathbf{G}}\,\mathrm{tr}\left[\Lambda_{\mathbf{G}\ell}(\mathbf{k})\right]. \tag{A.52}$$

Here tr denotes a trace over l, which is trivial in the $g=0$ limit, but provides a definition for $\bar{\rho}$ that will later prove useful in the case where g is perturbatively small. We have therefore demonstrated that the bilayer QHFM states are exact eigenstates of the density operator.

As forecasted above, this enables us to isolate a positive-definite portion of the projected interaction. As a preliminary step, define the *relative density operator* by

$$\delta\hat{\rho}_{\mathbf{q}\ell} = \hat{\mathcal{P}}\hat{\rho}_{\mathbf{q}\ell}\hat{\mathcal{P}} - \bar{\rho}_{\mathbf{q}\ell}\hat{I}. \tag{A.53}$$

By construction, this operator automatically annihilates each bilayer QHFM, defined above in Eq. (A.46). Applying standard identities (e.g., see Ref. [214]), one can then re-write the projected interaction in terms of these relative densities (without normal ordering) as

$$\hat{\mathcal{P}}\hat{V}\hat{\mathcal{P}} = \sum_{\ell\ell'}\sum_{\mathbf{q}\in\mathrm{EBZ}}V_{\ell\ell'}(\mathbf{q})\delta\hat{\rho}_{\mathbf{q}\ell}\delta\hat{\rho}_{-\mathbf{q}\ell'} + \hat{h}_{\mathrm{HF}}[I/2] + \text{constant}. \tag{A.54}$$

We remark that this identity holds even when $U_2 \geq 0$, in which case the off-diagonal layer components of $V(\mathbf{q})$ are non-zero. In the above, $\hat{h}_{\mathrm{HF}}$ is the Hartree-Fock Hamiltonian and I is the identity matrix in the spin and dressed layer indices. The Hartree-Fock Hamiltonian is a quadratic operator, defined relative to a correlation matrix $P(\mathbf{k})_{\alpha\beta} = \langle\hat{\varphi}^{\dagger}_{\mathbf{k}\beta}\hat{\varphi}_{\mathbf{k}\alpha}\rangle$, given by $\hat{h}_{\mathrm{HF}}[P] = \sum_{\mathbf{k},\alpha\beta}\hat{\varphi}^{\dagger}_{\mathbf{k}\alpha}\left(h_{\mathrm{H}}[P](\mathbf{k})_{\alpha\beta} + h_{\mathrm{F}}[P](\mathbf{k})_{\alpha\beta}\right)\hat{\varphi}_{\mathbf{k}\beta}$ with

$$h_{\mathrm{H}}[P](\mathbf{k}) = \frac{2s^0}{qN}\sum_{\ell\ell'}\sum_{\mathbf{G}}V_{\ell\ell'}(\mathbf{G})\Lambda_{\mathbf{G}\ell}(\mathbf{k})\,\mathrm{Tr}\left(\sum_{\mathbf{k}'\in\mathrm{BZ}}P(\mathbf{k}')\Lambda^{\dagger}_{\mathbf{G}\ell'}(\mathbf{k}')\right), \tag{A.55a}$$

$$h_{\mathrm{F}}[P](\mathbf{k}) = -\frac{2}{qN}\sum_{\ell\ell'}\sum_{\mathbf{q}\in\mathrm{EBZ}}V_{\ell\ell'}(\mathbf{q})\Lambda_{\mathbf{q}\ell}(\mathbf{k})P(\mathbf{k}+\mathbf{q})\Lambda_{\mathbf{q}\ell'}(\mathbf{k})^{\dagger}. \tag{A.55b}$$

Here, matrix multiplication is implicit, $\mathbf{G}$ is restricted to reciprocal lattice vectors that lie in the first extended Brillouin zone (EBZ), s^0 is the identity matrix in spin, and Tr denotes a trace over *both* bands and spin. The projection of the full Hamiltonian Eq. (A.3) may then be written in the "strong-coupling" form

$$\hat{\mathcal{P}}\hat{H}\hat{\mathcal{P}} = \delta\hat{h} + \hat{\mathcal{V}} = \left(\hat{\mathcal{P}}\hat{h}\hat{\mathcal{P}} + \hat{h}_{\mathrm{HF}}[I/2]\right) + \sum_{\ell\ell'}\sum_{\mathbf{q}\in\mathrm{EBZ}} V_{\ell\ell'}(\mathbf{q})\delta\hat{\rho}_{\mathbf{q}\ell}\delta\hat{\rho}_{-\mathbf{q}\ell'}, \tag{A.56}$$

up to an overall constant shift. Note that the last term is no longer normal ordered. Specializing again to the relevant case $U_2 = 0$, note that since $\delta\hat{\rho}_{-\mathbf{q}\ell} = \delta\hat{\rho}^\dagger_{\mathbf{q}\ell}$ and $V(\mathbf{q}) \geq 0$, then the strong-coupling interaction $\hat{\mathcal{V}}$ is positive semi-definite, which implies that any states it annihilates are necessarily also its ground states. We therefore conclude that the bilayer QHFMs [Eq. (A.46)] are all exact ground states of $\hat{\mathcal{V}}$.

In order to see that these states also constitute approximate ground states of the original projected Hamiltonian $\hat{\mathcal{P}}\hat{H}\hat{\mathcal{P}}$, it suffices to note that $\delta\hat{h}$, the quadratic term in the strong-coupling Hamiltonian, can be approximated by a chemical potential, which is constant at the fixed filling $\nu = 2$. Indeed, not only do we find that δh is proportional to the identity matrix $s^0 l^0$, but also that the momentum-dependent variations about its average are small. In particular, they are dominated by the bare Hofstadter bandwidth, which is $\sim 0.1\,t$ (at our standard value $q = 4$), as opposed to the contributions from $h_{\mathrm{HF}}[I/2]$. These bandwidth fluctuations, in turn, are much smaller than the energy scale U_1 responsible for the ferromagnetic alignment in each layer, and in fact vanish identically in the Landau level limit $\Phi_0/q \to 0$ (see Fig. A.1c).

Case 2: Equal In-Layer and Inter-Layer Interactions

We now formulate the strong-coupling Hamiltonian for the limit $U_2 = U_1$, which is relevant to the mapping to chiral TBG, and more closely approximates the parameter regimes accessible in near-term optical lattice implementations. Though the procedure will be almost identical to that above, we will discover that the family of approximate ground states is expanded, relative to the $U_2 = 0$ case, to include additional layer-polarized QAH insulating states.

As a first step, note that the interaction matrix takes a simple form in this limit:

$$V_{\ell\ell'}(\mathbf{q}) = V(\mathbf{q}) \begin{pmatrix} 1 & 1 \\ 1 & 1 \end{pmatrix}_{\ell\ell'}. \tag{A.57}$$

In other words, all its components are equal. As a result, in the interaction Hamiltonian itself, it is no longer necessary to resolve the fermionic density operator by its layer-projected components. Define the all-layer density by

$$\hat{\rho}_{\mathbf{q}} = \sum_{\ell} \hat{\rho}_{\mathbf{q}\ell} = \frac{1}{\sqrt{qN}} \sum_{l,l',s} \sum_{\mathbf{k}} \hat{\varphi}^\dagger_{ls}(\mathbf{k})[\Lambda_{\mathbf{q}}(\mathbf{k})]_{ll'}\hat{\varphi}_{l's}(\mathbf{k}+\mathbf{q}), \tag{A.58}$$

where $\Lambda_{\mathbf{q}}(\mathbf{k}) = \sum_\ell \Lambda_{\mathbf{q}\ell}(\mathbf{k})$ is the usual (layer-unresolved) form factor. This enables the projected interaction of Eq. (A.45) to be written in a simple form:

$$\hat{\mathcal{P}}\hat{V}\hat{\mathcal{P}} = \sum_{\mathbf{q}\in\mathrm{EBZ}} V(\mathbf{q}) : \hat{\mathcal{P}}\hat{\rho}_{\mathbf{q}}\hat{\mathcal{P}}\hat{\rho}_{-\mathbf{q}}\hat{\mathcal{P}} : . \tag{A.59}$$

Moreover, since the bilayer QHFM states Eq. (A.46) are eigenstates of the layer-resolved density operator [see Eq. (A.51)], then they are likewise eigenstates of the all-layer density operator:

$$\hat{\mathcal{P}}\hat{\rho}_{\mathbf{q}}\hat{\mathcal{P}}\,|\mathbf{n}_{\mathsf{T}}, \mathbf{n}_{\mathsf{B}}\rangle = \bar{\rho}_{\mathbf{q}}\,|\mathbf{n}_{\mathsf{T}}, \mathbf{n}_{\mathsf{B}}\rangle\,, \qquad \bar{\rho}_{\mathbf{q}} = \sum_\ell \bar{\rho}_{\mathbf{q}\ell} = \frac{1}{\sqrt{qN}} \sum_{\mathbf{k}\in\mathrm{BZ}} \sum_{\mathbf{G}} \delta_{\mathbf{q},\mathbf{G}}\,\mathrm{tr}\,[\Lambda_{\mathbf{G}}(\mathbf{k})]\,. \tag{A.60}$$

Setting $U_2 = U_1$ and summing over ℓ and ℓ', Eq. (A.56) assumes precisely the same form, with the strong-coupling interaction term given explicitly by:

$$\hat{\mathcal{V}} = \sum_{\mathbf{q}\in\mathrm{EBZ}} V(\mathbf{q})\delta\hat{\rho}_{\mathbf{q}}\delta\hat{\rho}_{-\mathbf{q}}. \tag{A.61}$$

The crucial difference compared to the $U_2 = 0$ case, however, is that this interaction admits a *broader* family of ground states beyond the bilayer QHFMs. In particular, $\hat{\mathcal{V}}$ is readily found to annihilate the layer-polarized QAH states, defined as

$$|\mathrm{QAH}, l\rangle = \prod_{\mathbf{k}} \hat{\varphi}^\dagger_{l,\uparrow}(\mathbf{k})\hat{\varphi}^\dagger_{l,\downarrow}(\mathbf{k})\,|0\rangle\,, \tag{A.62}$$

where $l = \mathsf{T}/\mathsf{B}$. Passing to the microscopic layer index ℓ, which is indistinguishable from l in the $g = 0$ limit, explicitly acting the density operator on this state gives

$$\hat{\rho}_{\mathbf{q}}|\mathrm{QAH}, \ell\rangle = \frac{1}{\sqrt{qN}} \sum_{l,l',s} \sum_{\mathbf{k}\in\mathrm{BZ}} \hat{\varphi}^\dagger_{ls}(\mathbf{k}) \sum_{\ell'} [\Lambda_{\mathbf{q}\ell'}(\mathbf{k})]_{ll'}\hat{\varphi}_{l's}(\mathbf{k}+\mathbf{q})|\mathrm{QAH}, \ell\rangle \tag{A.63}$$

$$= \frac{1}{\sqrt{qN}} \sum_{\mathbf{k}\in\mathrm{BZ}} [\Lambda_{\mathbf{q}\ell}(\mathbf{k})]_{\ell\ell} \sum_{s} \hat{\varphi}^\dagger_{\ell s}(\mathbf{k})\hat{\varphi}_{\ell s}(\mathbf{k}+\mathbf{q})|\mathrm{QAH}, \ell\rangle \tag{A.64}$$

$$= \frac{2}{\sqrt{qN}} \sum_{\mathbf{k}\in\mathrm{BZ}} \sum_{\mathbf{G}} \delta_{\mathbf{q},\mathbf{G}} [\Lambda_{\mathbf{G}\ell}(\mathbf{k})]_{\ell\ell}|\mathrm{QAH}, \ell\rangle. \tag{A.65}$$

To see that this eigenvalue is precisely $\bar{\rho}_{\mathbf{q}}$, we remark that the constraint of spacetime-inversion symmetry in our chosen periodic, layer-polarized gauge [see Eq. (A.21)] implies that the form factors must satisfy

$$\Lambda_{\mathbf{G}}(\mathbf{k}) = l^x \Lambda^*_{\mathbf{G}}(\mathbf{k}) l^x. \tag{A.66}$$

Since the form factors are layer-diagonal in the $g = 0$ limit, as clarified in Eq. (A.49), and the form factors at opposite reciprocal lattice vectors (which are both summed over) are related by $\Lambda_{\mathbf{G}}(\mathbf{k})^\dagger = \Lambda_{-\mathbf{G}}(\mathbf{k})$ as per Eq. (A.42), we then indeed have that

$$\delta\hat{\rho}_{\mathbf{q}}|\mathrm{QAH}, \ell\rangle = 0. \tag{A.67}$$

The QAH states and bilayer QHFMs are therefore both annihilated by the strong-coupling interaction Eq. (A.61) in the $U_2 = U_1$ limit. By arguments analogous to those presented in the $U_2 = 0$ subsection above, we reason that both of these families of states are approximate ground states of the full projected Hamiltonian.

Effects of Inter-Layer Tunneling

We now restore a small amount of inter-layer tunneling g and, working perturbatively within the ground state manifold of the strong-coupling interaction, find that both the LAF and QAH states are strong-coupling ground states in the $U_2 = U_1$ limit. The choice of a layer-polarized basis, discussed and constructed in Sec. A.1, is crucial to this analyis in the presence of finite g. In particular, before embarking on our perturbative analysis, we establish how the action of symmetries in a layer-polarized basis constrains the structure of the form factors.

The most significant constraint comes from the anti-unitary spacetime inversion symmetry $\mathcal{I}$. For the following analysis, it will be sufficient to work in the particular layer-polarized basis in which its action is as simple as possible. This is achieved by mapping the hybrid Wannier layer-polarized basis of Sec. A.1 to $\varphi^\dagger(\mathbf{k}) \to \varphi^\dagger(\mathbf{k})e^{i\gamma(\mathbf{k})/2}$, so that Eq. (A.26) becomes

$$\hat{\mathcal{I}}\hat{\varphi}^\dagger(\mathbf{k})\hat{\mathcal{I}}^{-1} = \hat{\varphi}^\dagger(\mathbf{k})s^x l^x. \tag{A.68}$$

Correspondingly, Eq. (A.21) becomes $v^\dagger(\mathbf{k})\ell^x v^*(\mathbf{k}) = \sigma^x$, which forgoes the exponential localization of the associated Wannier functions (or equivalently, smoothness of the gauge) while preserving the essential property of maximal layer polarization. This forces the form factor to obey the following simple constraint:

$$\Lambda_{\mathbf{q}}(\mathbf{k}) = l^x \Lambda^*_{\mathbf{q}}(\mathbf{k}) l^x. \tag{A.69}$$

Expanding the form factor as a linear combination of Pauli matrices,

$$\Lambda_{\mathbf{q}}(\mathbf{k}) = \sum_{\mu=0,x,y,z} \Lambda^\mu_{\mathbf{q}}(\mathbf{k}) l^\mu \tag{A.70}$$

then the above equation is equivalent to

$$\Lambda^0_{\mathbf{q}}(\mathbf{k}) = \Lambda^0_{\mathbf{q}}(\mathbf{k})^*, \quad \Lambda^x_{\mathbf{q}}(\mathbf{k}) = \Lambda^x_{\mathbf{q}}(\mathbf{k})^*, \quad \Lambda^y_{\mathbf{q}}(\mathbf{k}) = \Lambda^y_{\mathbf{q}}(\mathbf{k})^*, \quad \Lambda^z_{\mathbf{q}}(\mathbf{k}) = -\Lambda^z_{\mathbf{q}}(\mathbf{k})^*. \tag{A.71}$$

The form factor may therefore be written as the following sum of diagonal and off-diagonal terms, with $F^{S/A}_{\mathbf{q}}(\mathbf{k}), \Phi^{S/A}_{\mathbf{q}}(\mathbf{k}) \in \mathbb{R}$:

$$\Lambda_{\mathbf{q}}(\mathbf{k}) = F^S_{\mathbf{q}}(\mathbf{k}) e^{i\Phi^S_{\mathbf{q}}(\mathbf{k}) l^z} + F^A_{\mathbf{q}}(\mathbf{k}) l^x e^{i\Phi^A_{\mathbf{q}}(\mathbf{k}) l^z} = \Lambda^S_{\mathbf{q}}(\mathbf{k}) + \Lambda^A_{\mathbf{q}}(\mathbf{k}), \tag{A.72}$$

which commute and anti-commute with l^z, respectively. This expression for the form factor may be verified, by explicit calculation, to satisfy the constraint Eq. (A.69) above:

$$l^x \Lambda^*_{\mathbf{q}}(\mathbf{k}) l^x = F^S_{\mathbf{q}}(\mathbf{k}) l^x e^{-i\Phi^S_{\mathbf{q}}(\mathbf{k}) l^z} l^x + F^A_{\mathbf{q}}(\mathbf{k}) l^x l^x e^{-i\Phi^A_{\mathbf{q}}(\mathbf{k}) l^z} l^x = \Lambda_{\mathbf{q}}(\mathbf{k}). \tag{A.73}$$

Taking the limit $g = 0$ further constrains the form factors by restoring layer $U(1)$ symmetry, making them diagonal ($F^A = 0$). Otherwise, $F^A = \mathcal{O}(g)$ is of the same order as the inter-layer tunneling and must be treated with some care. We further remark the unitary discrete symmetries relate the form factors at symmetry-related momenta, which will not be relevant to our analysis.

These modifications to the form factors by the inter-layer tunneling — namely the acquisition of off-diagonal components — imprint themselves on both the strong-coupling Hamiltonian and its approximate ground states. This is fundamentally due to the fact finite g breaks layer $U(1)$ symmetry, thereby distinguishing the microscopic layer index ℓ from the dressed layer index l of our layer-polarized basis. The decomposition of the form factor in Eq. (A.72) yields a similar partitioning of both the projected density and the associated reference charge densities:

$$\hat{\rho}^{S/A}_{\mathbf{q}} = \frac{1}{\sqrt{qN}} \sum_{l,l',s} \sum_{\mathbf{k}} \hat{\varphi}^\dagger_{ls}(\mathbf{k}) [\Lambda^{S/A}_{\mathbf{q}}(\mathbf{k})]_{ll'} \hat{\varphi}_{l's}(\mathbf{k}+\mathbf{q}), \tag{A.74}$$

$$\bar{\rho}^{S/A}_{\mathbf{q}} = \frac{1}{\sqrt{qN}} \sum_{\mathbf{k}\in \mathrm{BZ}} \sum_{\mathbf{G}} \delta_{\mathbf{q},\mathbf{G}} \,\mathrm{tr}\left[\Lambda^{S/A}_{\mathbf{G}}(\mathbf{k})\right]. \tag{A.75}$$

In particular, since Λ^A is purely off-diagonal, then $\bar{\rho}^A$ vanishes identically. In terms of the relative densities $\delta\hat{\rho}^{S/A}_{\mathbf{q}} = \hat{\rho}^{S/A}_{\mathbf{q}} - \bar{\rho}^{S/A}_{\mathbf{q}}$, the strong-coupling interaction Eq. (A.61) therefore reads

$$\hat{\mathcal{V}} = \hat{\mathcal{V}}^S + \hat{\mathcal{V}}^A = \sum_{\mathbf{q}\in \mathrm{EBZ}} V(\mathbf{q}) \delta\hat{\rho}^S_{\mathbf{q}} \delta\hat{\rho}^S_{-\mathbf{q}} + \sum_{\mathbf{q}\in \mathrm{EBZ}} V(\mathbf{q}) \left(\delta\hat{\rho}^A_{\mathbf{q}} \delta\hat{\rho}^S_{-\mathbf{q}} + \delta\hat{\rho}^S_{\mathbf{q}} \delta\hat{\rho}^A_{-\mathbf{q}}\right), \tag{A.76}$$

where $\hat{\mathcal{V}}^A = \mathcal{O}(g)$ since it contains one factor Λ^A, and we dropped the AA term since it is $\mathcal{O}(g^2)$.

The bilayer QHFMs Eq. (A.46) and QAH states Eq. (A.62) are annihilated by $\delta\hat{\rho}^S_{\mathbf{q}}$ but not by $\delta\hat{\rho}^A_{\mathbf{q}}$. This motivates performing degenerate perturbation theory in the ground state manifold of $\hat{\mathcal{V}}^S$, which consists of precisely these states. The perturbations include not only the anti-symmetric term $\hat{\mathcal{V}}^A$, but also certain terms in the single-particle Hamiltonian $\delta\hat{h}$, which includes corrections from the re-organization of the interaction, analogous to Eq. (A.56). As in that case, the l^0 component of δh is small relative to the interaction scale and moreover acts diagonally in (and does not energetically distinguish) the states in the degenerate manifold. This leaves the off-diagonal components of the total single-particle Hamiltonian, which we collect altogether:

$$\delta\hat{h}_g = \sum_{\mathbf{k}} \hat{\varphi}^\dagger_{\mathbf{k}} \left[h^x_g(\mathbf{k}) l^x + h^y_g(\mathbf{k}) l^y\right] \hat{\varphi}_{\mathbf{k}} = \mathcal{O}(g). \tag{A.77}$$

Since both this term and $\delta\hat{\rho}^A_{\mathbf{q}}$ change the relative dressed-layer occupation of the degenerate ground states, they therefore do not modify their energies at first order. Nonetheless, they

do facilitate *second-order* virtual processes in which fermions hop between the two dressed layers and hop back. Since an $\mathcal{O}(U)$ energetic penalty is incurred in the virtual state, assuming it is not Pauli blocked, then some of the degenerate states will enjoy an $\mathcal{O}(g^2/U)$ energetic benefit and therefore be singled out as the preferred ground states in the presence of finite g. This intuition can be made more quantitatively precise by computing second-order perturbative energetic corrections using the Schrieffer-Wolff formalism [208], analogous to that detailed in Refs. [31, 32] in the context of twisted bilayer graphene. In particular, both "layer-antiferromagnetic" (LAF) and QAH states are energetically favorable over bilayer ferromagnetic states. As in the main text, LAF states are defined as $|\boldsymbol{n}, -\boldsymbol{n}\rangle$, the subset of the states in Eq. (A.46) that have opposite spin polarization in opposite Chern sectors.

A.3 Additional Data for Phase Diagram at $\nu = 2$

In this Appendix we give additional details of the DMRG phase identification at the "undoped" filling of $\nu = 2$, which corresponds to filling two of the four low-lying narrow bands of the double Hofstadter model. Fig. A.5(a) recapitulates the phase diagram shown in the main text. At weak interactions, the half-filled narrow bands form Dirac semimetal (DSM) at large g and a metal at lower g, characterized by small electron/hole pockets. Meanwhile at high U_1, the LAF polarization

$$n^z_{\mathrm{LAF}} = \sum_{\mathbf{k}} \langle \hat{\varphi}^\dagger_{\mathbf{k}} \ell^z s^z \hat{\varphi}_{\mathbf{k}} \rangle \tag{A.78}$$

increase steadily towards 2, its maximal possible value, suggesting the state is the LAF insulator predicted by strong-coupling theory. To verify this, Fig. A.5(b) examines the phase diagram as a function of U_1 at fixed g. Since the LAF is strongly gapped, one expects electron-electron correlations to behave as

$$\langle \hat{\varphi}^\dagger_{x,k_y} \hat{\varphi}_{0,k_y} \rangle_{\mathrm{LAF}} \sim e^{-x/\xi_{1e}(k_y)}, \tag{A.79}$$

where the correlation length $\xi_{1e}(k_y)$ should be finite. By contrast, in the gapless metallic phase, one expects power-law correlations of $\langle \hat{\varphi}^\dagger_{x,k_y} \hat{\varphi}_{0,k_y} \rangle$, leading to diverging $\xi_{1e} \to \infty$ as $\chi \to \infty$. However, even in a gapped phase, ξ_{1e} may increase slowly with χ before converging to a finite value. Therefore, further analysis is needed to determine if its extrapolated value at infinite bond dimension is finite or likely infinite.

To this end, we employ a recently-developed method for extrapolating correlation lengths in DMRG [199, 205]. Namely, we compute several of the largest eigenvalues of the transfer matrix $TX_i = \lambda_i X_i$ in the electric charge $Q_E = 1$ sector for each k_y, and select those from the same "excitation branch" [205]. These are related to the correlation lengths as $\epsilon_i = 1/\xi_i = -\log|\lambda_i|$ with $\epsilon_i \leq \epsilon_{i+1}$, where we report ξ in units of the unit cell length $u = 4a$ (i.e., $q = 4$ square lattice sites). Correspondingly, ϵ is reported in units of u^{-1}. For a gapless system with a power-law correlation in charge sector Q, both $\epsilon^Q_1, \epsilon^Q_2 \to 0$ as $\chi \to \infty$. As a

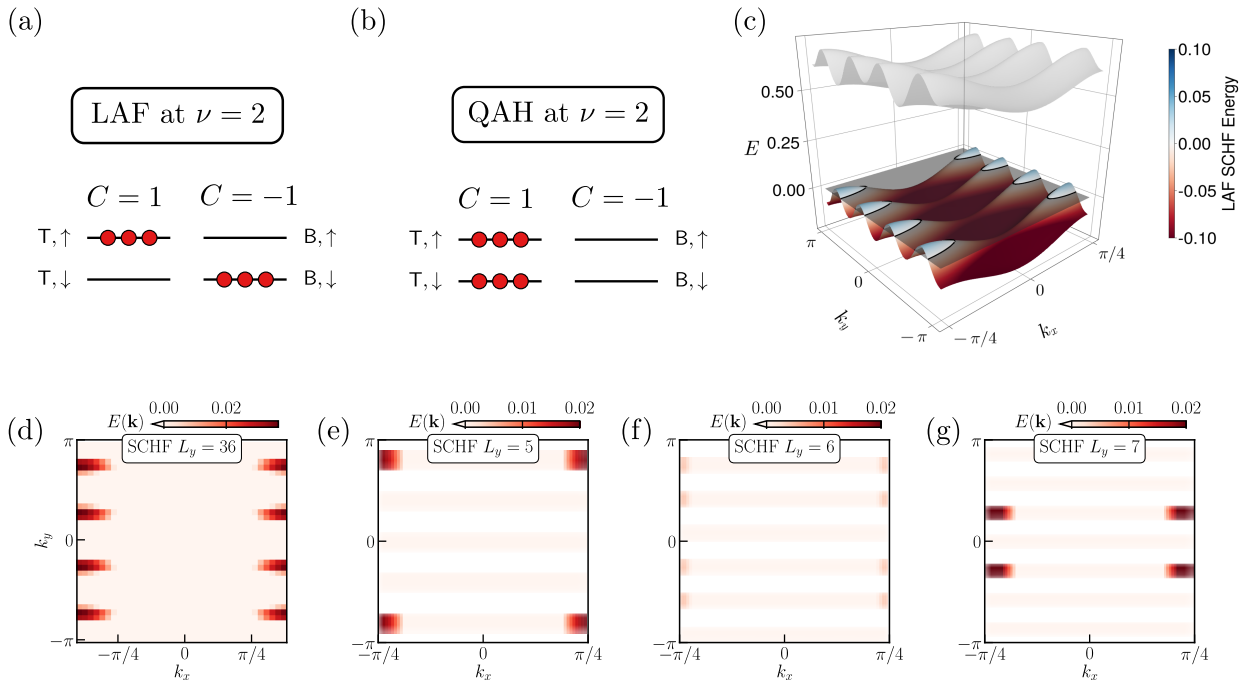

Figure A.4: **Strong Coupling Ground States**. (a) One possible LAF state that fills the $(\mathsf{T}, \uparrow)$ and $(\mathsf{B}, \downarrow)$ orbitals for each $\mathbf{k}$. (b) One possible quantized anomalous Hall state filling both T orbitals, with a total Chern number of $C = 2$. (c) The bandstructure of the LAF state within self-consistent Hartree Fock at filling $\nu = 1.8$ and $(g, U_1, U_2) = (0.15, 1.5, 0.0)$, matching the large-bond dimension superconductivity data. The horizontal plane at $E = 0$ is the chemical potential, and the top gray band is entirely unoccupied. Each band is doubly degenerate. Computed on 36×36 $\mathbf{k}$-points and linearly interpolated for display. (d) The lower band of the LAF band structure (c) without interpolation and only showing data above the Fermi level. (e,f,g) Same as (d) except with $L_y = 5, 6, 7$ and $\nu = 2 - 1/L_y$, yielding Fermi wavevectors $k_F^{L_y=5} = 0.59/a$, $k_F^{L_y=6} = 0.68/a$, $k_F^{L_y=7} = 0.59/a$.

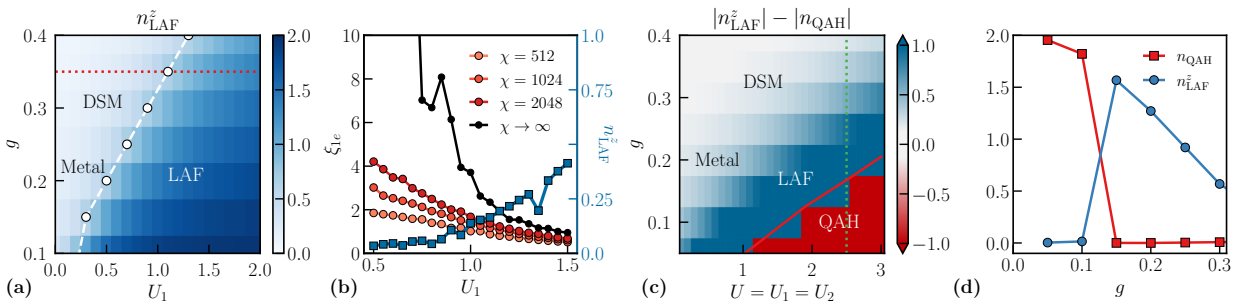

Figure A.5: **Additional Details for the Undoped Phase Diagram at $\nu = 2$.** (a) LAF polarization as a function of g and U_1 at $U_2 = 0$, $B_z = 10^{-2}$. (b) DSM-to-LAF phase transition at $g = 0.25$ [dotted red line in (a)]. The electron-electron correlation length ξ_{1e} is extrapolated to $\chi = \infty$ as described in the text. The LAF polarization (right axis) becomes significant near $U_1 = 1$, matching the divergence in ξ_{1e}. Here we take a smaller value of the Zeeman pinning field, namely $B_z = 10^{-4}$, to sharpen the transition. (c) Phase diagram as a function of g and $U = U_1 = U_2$ with $B_z = 10^{-2}$. (d) QAH-to-LAF transition as a function of g at fixed $U_1 = U_2 = 2.5$ with $B_z = 10^{-2}$ [dotted green line in (c)].

result, the quantity

$$\delta^Q = \epsilon_2^Q - \epsilon_1^Q \tag{A.80}$$

also vanishes at $\chi \to \infty$, serving as a good "scaling variable" that measures the deviation from the gapless state [199, 205]. To estimate $\xi(\chi \to \infty)$, we therefore compute $\epsilon(\delta)$ at each available $\epsilon(\chi), \delta(\chi)$ and extrapolate to $\delta = 0$ with a linear fit. This extrapolation is shown in Fig. A.5(b) for ξ_{1e} using numerical data at bond dimensions $\chi = 512, 1024, 2048$. At $U_1 \lesssim 1$, the extrapolated correlation length $\xi_{1e}(\chi \to \infty)$ apparently diverges—in concord with a metallic phase—while at larger U_1 the extrapolated value is finite and on the scale of a few unit cells. As a technical point, we note that taking a finite B_z broadens the transition region. To sharpen the transition (while still avoiding Hohenberg-Mermin-Wagner issues), we take $B_z = 10^{-4}$ in panel (b).

Fig. A.5(c,d) show the competition between the LAF and QAH phases when $U_1 = U_2$. At these parameters, the two phases are degenerate within strong coupling theory. Surprisingly, they are also exactly degenerate within self-consistent Hartree-Fock. DMRG, however, shows a clear transition near $g = 0.13$ at $U = 2.5$, with simultaneous and opposite jumps in n^z_{LAF} and the QAH polarization, namely

$$n_{\mathrm{QAH}} = \sum_{\mathbf{k}} \langle \hat{\varphi}^\dagger_{\mathbf{k}} \ell^z s^0 \hat{\varphi}_{\mathbf{k}} \rangle. \tag{A.81}$$

The transition therefore appears to be first order.

A.4 Additional Data for the Existence and Robustness of Superconductor

In the main text, we provided conclusive numerical evidence for the existence of superconductivity at $L_y = 5$ by performing a large bond dimension scaling analysis, and summarized the extent of evidence for this phase at higher circumferences $L_y = 6, 7$. We subsequently demonstrated that the superconductivity at $L_y = 5$ belongs to a robust superconducting phase that persists even upon including additional repulsive interactions. In this appendix, we provide additional numerical data and details supporting both of these claims.

In Subsection A.4, we provide a detailed account of our scaling analysis of the charge-$2e$ and charge-$1e$ correlations as a function of bond dimension and cylinder circumference. This includes a depiction of the superconducting correlation functions for each channel, a description of our procedure for obtaining a scaling collapse and the exponents of algebraic decay, a depiction of the $1e$ and $2e$ correlation lengths as a function of bond dimension, and our procedure for extrapolating the correlation lengths to infinite bond dimension. Crucially, we provide data for both the case of zero and non-zero interlayer repulsion U_2. Subsequently, in Subsection A.4, we provide the raw numerical data supporting the $L_y = 5$ superconducting phase diagrams shown in Fig. 5 of the main text.

Scaling Analysis of Correlations

In the main text, we claimed that we saw algebraic decay of the superconducting correlation function

$$C_{\alpha\beta}(x, k_y) = N_{2h}^{-1} \langle \hat{\Delta}^\dagger_{\alpha\beta}(x; 0, k_y) \hat{\Delta}_{\alpha\beta}(0; 0, k_y) \rangle \tag{A.82}$$

in the channels $\alpha\beta = xx, yy,$ and $x0$. There, in Fig. 4(a), we showed the superconducting correlation functions in the xx channel. In Fig. A.6(a, b), we show that the yy and $x0$ likewise exhibit clear signatures of algebraic decay, as claimed in the main text. In Fig. A.6(c), we compare the magnitudes of the correlation functions for the three different channels at $L_y = 5$. Since $C_{\alpha\beta}$ is normalized by the density of total hole pairs N_{2h}, then its value at $x = 0$ roughly corresponds to the average *fraction* of Cooper pairs occupying the $\alpha\beta$ channel. With this in mind, at $x = 0$ we find that the xx and yy channels have nearly equal magnitude, while $x0$ is roughly three times smaller, signaling a lower number density of Cooper pairs in the latter channel. This justifies our treatment of the $x0$ channel as subdominant.

Collapse to Algebraic Scaling Hypothesis

In the main text, we performed a finite-entanglement scaling collapse to quantitatively demonstrate the approach to algebraic decay. To this end, we adopted the scaling ansatz:

$$C^{(\chi)}_{\alpha\beta}(x, k_y) = \xi^{-\eta} g_{\alpha\beta}(x/\xi_{2e,\chi}, k_y). \tag{A.83}$$

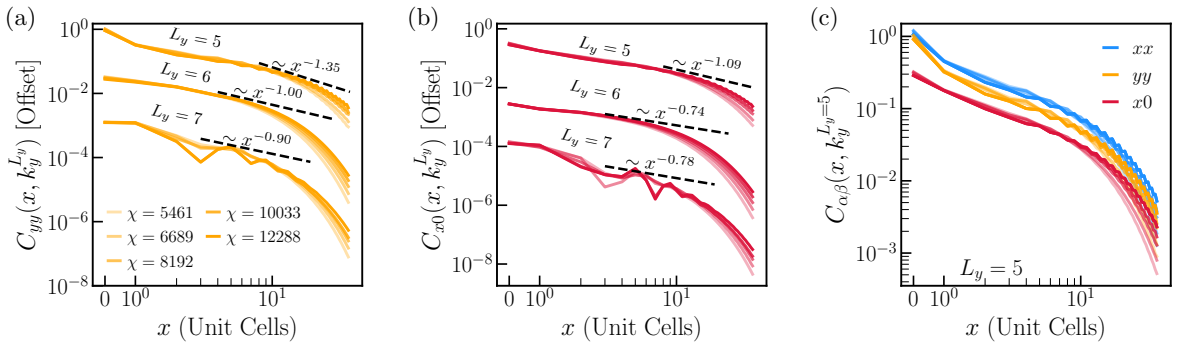

Figure A.6: **Additional Superconducting Correlations Functions.** In panels (a) and (b), we depict the superconducting correlation function for the yy and $x0$ channels, respectively, at circumferences $L_y = 5, 6, 7$. Similar to the the xx channel shown in the main text, clear signatures of algebraic decay are observed in these two channels. Likewise, an arbitrary vertical offset is added to $L_y = 6, 7$ for ease of viewing. In panel (c), the correlation functions at $L_y = 5$ for all three channels are shown without any vertical offset, allowing for the direct comparison of their magnitudes. While xx and yy are relatively close, especially at short distances, the $x0$ correlation function is notably smaller, a pattern that holds at all circumferences.

We now detail our precise quantitative procedure for performing this collapse and provide additional numerical data in support of our claims. In our numerics, the data for the superconducting correlation function is organized in the form of tuples $\{(x_i, C^\chi(x_i, k_y)\}$ for each simulated bond dimension χ and each position x_i. To perform the finite entanglement scaling collapse, the x-axis is first rescaled by the correlation length, yielding a data set $\{(x_i/\xi_\chi, C^{(\chi)}(x_i/\chi, k_y)\}$. Linearly interpolating this data, we obtain a continuous function $\widetilde{C}^{(\chi)}(x/\xi_\chi, k_y)$, which we can then scale and sample from. Namely, given this interpolation and Eq. (A.83), we posit the following cost function:

$$\mathcal{Q}(\eta) = \frac{1}{N_\chi(N_\chi - 1)} \sum_{\chi \neq \chi'} \int_{y_0}^{y_1} dy \, \frac{1}{\xi_\chi^\eta \xi_{\chi'}^\eta} \left| \widetilde{C}^{(\chi)}(y, k_y)\xi_\chi^\eta - \widetilde{C}^{(\chi')}(y, k_y)\xi_{\chi'}^\eta \right|^2 . \tag{A.84}$$

It is chosen based on the following principles: (i) it is positive semi-definite, (ii) it vanishes if and only if Eq. (A.83) holds, and (iii) its prefactor $(\xi_\chi^\eta \xi_{\chi'}^\eta)^{-1}$ makes the integrand dimensionless. More heuristically, it is more stable (compared to several considered alternatives) to the removal of some data from the fit, which suggests that it is more robust. A finite entanglement scaling collapse is achieved for the value of η that minimizes the cost function shown above, while the error in the optimal value $\eta = \eta^*$ is estimated from the inverse Hessian as

$$\delta\eta = \sqrt{Q(\eta^*) \left| \frac{\partial^2 Q}{\partial \eta^2} \right|^{-1}_{\eta=\eta^*}} . \tag{A.85}$$

$L_y \backslash \alpha\beta$	xx	yy	$x0$
5	1.3 ± 0.2	1.4 ± 0.3	1.1 ± 0.2
6	1.02 ± 0.04	1.00 ± 0.07	0.74 ± 0.07
7	0.9 ± 0.3	0.9 ± 0.3	0.7 ± 0.4

Table A.2: **Extracted Power Law Exponents from Scaling Collapse.** The table shows the exponents $\eta(L_y)$ extracted for each channel $\alpha\beta$ by collapsing under the finite entanglement scaling hypothesis of Eq. (A.83). The exponents here were obtained using the data at $\nu = 2 - 1/L_y$ and $(g, U_1, U_2, d) = (0.15, 1.8, 0, 0)$.

We remark that $y = x/\xi_\chi, y_0$ and y_1 are chosen to isolate the algebraic "shelf" of the correlation function — clearly visible in Fig. A.6 as the region over which multiple curves coincide with the algebraic fit — and to ensure that the function $Q(\eta)$ is convex at the obtained minimum. We remark that, when performing the optimization procedure for $L_y = 6, 7$, we discarded certain low bond dimension correlation functions, as including them inhibited the discovery of a convex solution. This suggests that these bond dimensions were not yet in the 'scaling regime' at $\chi \gtrsim e^{O(L_y)}$ and could therefore not be collapsed appropriately under the scaling hypothesis. In particular, for $L_y = 6$, the bond dimensions taken were $\chi \geq 8192$ and for $L_y = 7$, only the last two bond dimensions could be used $\chi \geq 10033$. With these choices of χ, we have ensured that this optimization problem is convex, and we have further ensured that our method is robust to changing the values of y_0, y_1. Fig. A.7 shows the scaling collapses for all channels. The collapses have generally high quality, both in terms of $Q(\eta)$ and to the eye. This constitutes strong evidence that superconducting correlations are gapless in all three channels $xx, yy, x0$ at all systems sizes $L_y = 5, 6, 7$ studied. The extracted exponents are also tabulated in Table A.2.

Correlation Lengths and Extrapolation

We now study the correlation lengths as a function of bond dimension at each cylinder circumference. By performing a quantitative extrapolation in bond dimension, we attempt to ascertain if the system is gapped or gapless in each sector. It is worthwhile to review the possible options. If the system is a Luttinger liquid, then one expects gapless excitations in both the one-electron ($1e$) and two-electron ($2e$) sectors, whose corresponding correlation lengths ξ would diverge as $\chi \to \infty$. Equivalently, $1/\xi_{1e}$ and $1/\xi_{2e}$ would vanish. By contrast, for a Luther-Emery (i.e. a 1D superconductor), there should be a gap to single-electron excitations, so $1/\xi_{1e}$ would remain positive as $\chi \to \infty$.

Clearly it is impossible to actually take this limit, so we are obliged to extrapolate in χ. Such a procedure is always fraught, due to the presence of finite χ phase transitions where the properties of the state change dramatically as a function of bond dimension. And indeed we

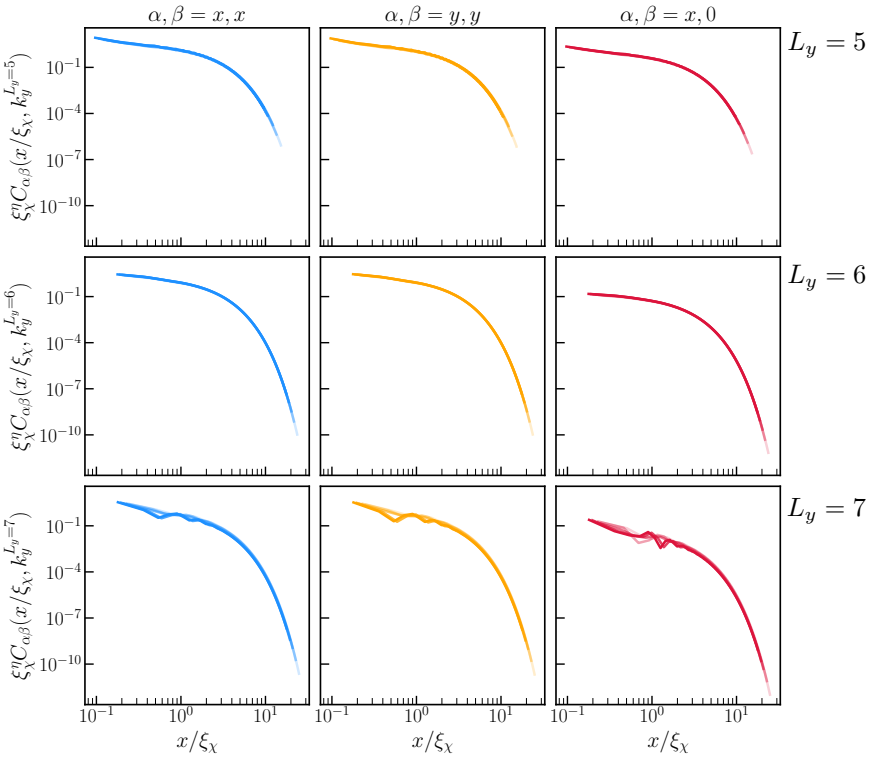

Figure A.7: **Additional Scaling Collapses for Superconducting Correlation Functions.** Here, we depict the results of the finite entanglement scaling collapse for each circumference ($L_y = 5, 6, 7$ for the top, middle, and bottom row) and condensed channel (x, x, y, y, and $x, 0$; labeling the columns). We find an excellent scaling collapse for each correlation function shown and the exponents η are shown in Fig. 4(c) of the main text. Data is shown for $\chi = 5461, 6689, 8192, 10033, 12288$.

often observe such a transition at $L_y = 5$ from a LAF-metal state at low χ to a Luther-Emery liquid at high χ. If one *assumes* that no such transition will occur beyond available bond dimensions, and further assumes that the available bond dimension is "close" to $\chi \to \infty$, then one may apply the scaling techniques pioneered in [199, 205], and described in App. A.3 above. We recall that describing a gapped state generically requires bond dimension $\chi \sim e^{O(L_y)}$, so describing a gapless state likely requires bond dimensions growing at least this fast. This suggests that studying extrapolation at fixed maximal bond dimension — a constraint imposed upon us by limited numerical resources — grows less reliable as L_y increases.

Nevertheless, we extrapolate using all available data in Fig. A.9, where we report ξ in units of the size of the unit cell, namely $u = 4a$, with δ accordingly being reported in units of u^{-1}. The data is clearest at $L_y = 5$. There, both ξ_{1e} and ξ_{2e} are increasing with χ.

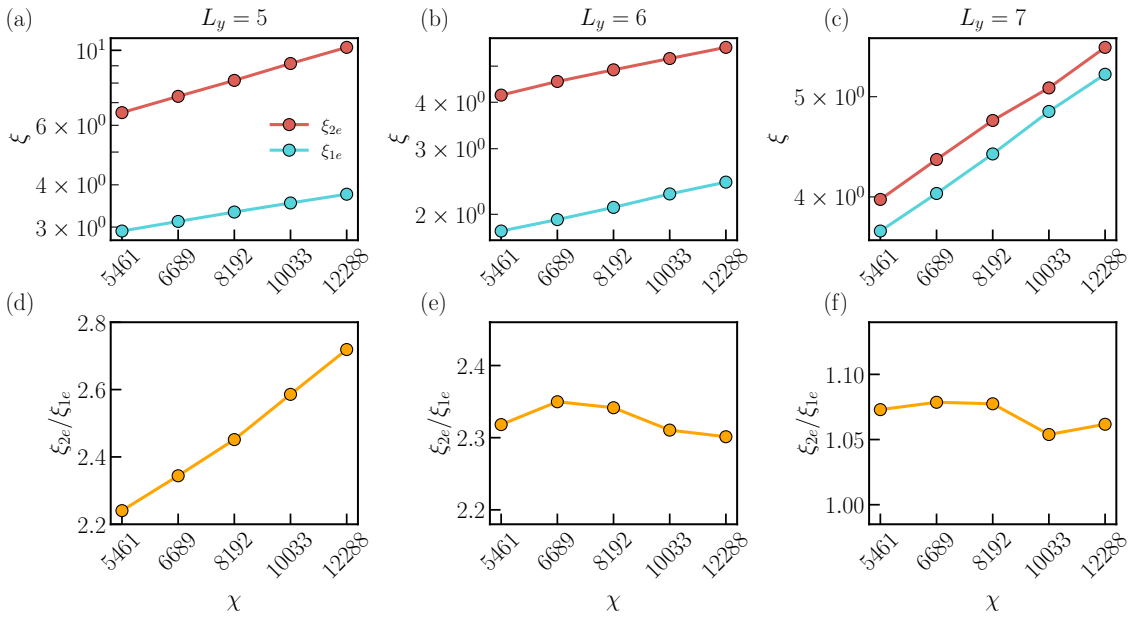

Figure A.8: **Bond Dimension Scaling of Correlation Lengths.** In panels (a, b, c), we depict the $2e$ and $1e$ correlation lengths as a function of bond dimension at a hole doping $\nu = 2 - 1/L_y$ for the parameter point $(g, U_1, U_2, d) = (0.15, 1.8, 0, 0)$ and circumferences $L_y = 5, 6, 7$. We find that for all circumferences, both correlation lengths grow linearly with χ. For $L_y = 5, 6$ [panels (a, b)], the $2e$ correlation lengths are substantially larger in magnitude suggesting non-trivial pair correlations in these states, while for $L_y = 7$, the difference in magnitude is not substantial. In panels (d, e, f), we check the ratio of these correlation lengths, which distinguishes a Luttinger Liquid from a Luther-Emery liquid based on the theory of finite entanglement scaling (See Section V.A of the main text). We find that for $L_y = 5$ [panel (d)], the ratio of the correlation lengths increases as a function of bond dimension strongly suggesting a Luther-Emery liquid. For $L_y = 6, 7$, this ratio does not increase suggesting that we cannot rule out the possibility of a Luttinger liquid at these circumferences.

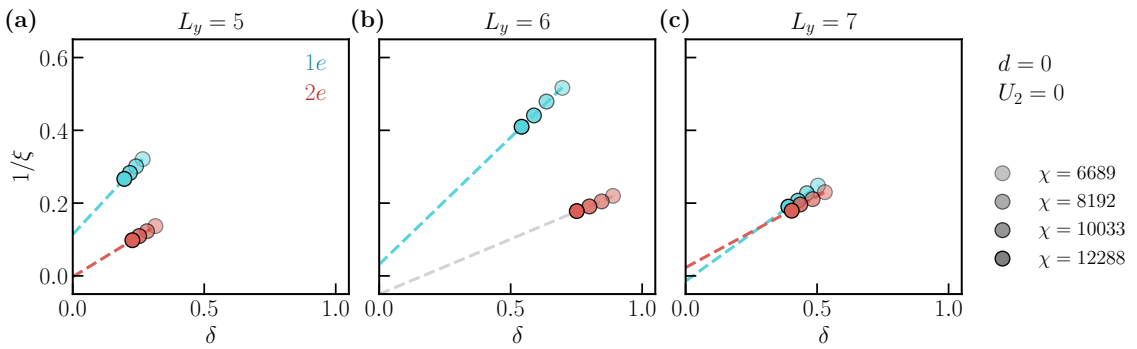

Figure A.9: **Extrapolation of Inverse Correlation Lengths.** Attempted extrapolation of the inverse correlation lengths $1/\xi_Q$ in the $Q = 1e$ and $2e$ charge sectors. (a) At circumference $L_y = 5$, we find that ξ_{1e} extrapolates to a finite value while $\xi_{2e} \to \infty$, the hallmark of a Luther-Emery liquid. (b) Though we find that ξ_{2e} substantially exceeds ξ_{1e} at $L_y = 6$, the former extrapolates to a negative value (therefore marked in gray), signaling the state is too far from convergence to confidently identify it as a Luther-Emery liquid or Luttinger liquid. (c) At $L_y = 7$, we find that the $1e$ and $2e$ excitations extrapolate close to zero with the former slightly negative and the latter appearing gapped. While these observations could arise from a Luttinger liquid, the changing behavior of the correlation functions (Fig. A.6 and Fig. 4(a) in the main text) as a function of bond dimension (e.g., short-distance behavior changing non-monotonically in χ) suggest that this state is also too far from convergence to derive any sharp conclusions.

Extrapolating the inverse correlation lengths versus δ [see Eq. (A.80)] by a linear fit implies that $1/\xi_{2e}$ is consistent with zero in the $\delta \to 0$ limit, whereas $1/\xi_{1e}$ is strictly positive. Taken in conjunction with the clear power law behavior for superconducting correlations discussed above, we thus identify the $L_y = 5$ state as a Luther-Emery liquid. For $L_y = 6$, the extrapolated $1/\xi_{2e}$ inverse is negative — a non-physical result since $\xi_{2e} > 0$. This fitting difficulty suggests the correlations are still changing non-linearly and may not be in the "almost infinite χ" regime required by scaling theory. So although the extrapolated value of $1/\xi_{1e}$ is slightly positive, consistent with an electronic gap for a Luther-Emery liquid, we cannot confidently rule out a Luttinger liquid at $L_y = 6$. Finally at $L_y = 7$ the extrapolated values of both inverse correlation lengths are close to zero (with $1e$ slightly negative). This behavior is consistent with a Luttinger liquid.

Let us make a few observations on the distance to the "scaling regime" at asymptotically large χ. It is instructive to consider how changing L_y changes the 'normal state' — the non-superconducting metal obtained by doping the LAF bandstructure. This is shown in Fig. A.4(d-g). There one can see that at asymptotically large L_y there are four Fermi pockets (wrapping around the right to left edges of the Brillouin zone). At $L_y = 5, 6, 7$ the wires

intersect only some of these cuts, resulting in $2, 4$ and 2 Fermi pockets, respectively. It is striking that the minimal δ at fixed bond dimension is roughly proportional to the number of Fermi pockets, in accord with the idea that it measures the "distance to infinite bond dimension". Moreover, these Fermi pockets have slightly different Fermi momenta, namely $k_F^{L_y=5} = 0.15u^{-1}, k_F^{L_y=6} = 0.17u^{-1}, k_F^{L_y=7} = 0.15u^{-1}$ (see Fig. A.4), which provide a natural inverse length scale against which to evaluate the smallness of δ. In particular, we find that δ greatly exceeds $k_F^{L_y}$ for each of the larger circumferences. Taken with the arguments above, this suggests that $L_y = 6, 7$ remain far from convergence and that vastly larger bond dimensions may be required to resolve the nature of their ground states definitively.

Scaling Analysis of Correlations With Additional Repulsion

In the main text and above, we detailed our scaling analysis of the charge-$2e$ and charge-$1e$ correlations as a function of bond dimension and cylinder circumference at the fixed parameters $(g, U_1) = (0.15, 1.5)$. In particular, this quantitative analysis was performed in the absence of additional repulsion d, U_2. To demonstrate that the superconductor that appears is not a consequence of a vanishingly small attractive interaction generated between the layers, we now examine the effect of adding additional long-range interactions in inter-layer channels:

$$\hat{V} = \sum_{\mathbf{r}} e^{-\frac{|\mathbf{r}-\mathbf{r}'|^2}{2d^2}} : \left[\frac{U_1}{2} (\hat{n}^2_{\mathbf{r}\mathsf{T}} + \hat{n}^2_{\mathbf{r}\mathsf{B}}) + U_2 \hat{n}_{\mathbf{r}\mathsf{T}} \hat{n}_{\mathbf{r}\mathsf{B}} \right] : \tag{A.86}$$

where U_2 controls the strength of interlayer repulsion and d controls their range. We perform the same scaling analysis as before at parameters $(g, U_1, U_2, d) = (0.1, 1.4, 0.2, 0.358)$. This point is marked with a star in Fig. 5(c) of the main text and crucially has inter-layer repulsion.

Similar to the analysis in the main text, let us start by examining the structure of the superconducting (charge-$2e$) correlation functions with increasing bond dimension and cylinder circumference. In particular, in Fig. A.10(a), we show the superconducting correlation function for $L_y = 5, 6$, finding that they both show a clear tendency to algebraic decay, similar to the case at $d = U_2 = 0$. We demonstrate this quantitatively once more via a finite entanglement scaling collapse in Fig. A.10(b) and show the extracted exponents for the two L_y's in Fig. A.10(c). Our results indicate that at finite repulsion $(U_2, d) = (0.2, 0.358)$, our system has algebraically decaying $2e$ correlations at $L_y = 5, 6$ but, unlike the case without repulsion, its exponents of algebraic decay do not clearly decrease with cylinder circumference. We largely suspect that this is due to the fact that the fillings and locations of Fermi pockets are qualitatively different at the two circumferences, preventing a direct comparison of the two circumferences.

We next turn to the analysis of the correlation lengths. The raw correlation lengths are given in Fig. A.11(a,b). At $L_y = 5$, both ξ_{1e} and ξ_{2e} are increasing with χ, but their ratio grows rapidly as a function of bond dimension, apparently without bound [see Fig. A.11(d)]. In particular, it greatly exceeds the value $1/2$ expected from Wick's theorem in the limit of a weakly-interacting metallic state. This is suggestive, but does not conclusively show on

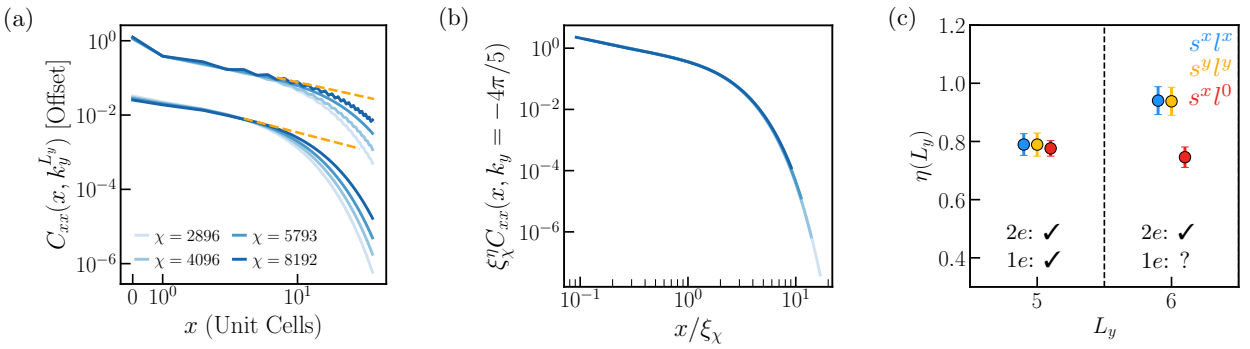

Figure A.10: **Superconducting Correlations at Finite Repulsion.** We perform a scaling analysis on the superconducting correlations in the ground state at $(g, U_1, U_2, d) = (0.1, 1.4, 0.2, 0.358)$ and doping $\nu = 2 - 1/L_y$. In panel (a), we show the correlation functions for the xx channel at circumferences $L_y = 5, 6$, finding a clear tendency to algebraic decay. We remark that an arbitrary vertical offset has been added to circumference $L_y = 6$ for ease of viewing. In panel (b), we verify the tendency to algebraic decay quantitatively by performing a finite entanglement collapse to the form Eq. (A.83). Finally, in panel (c), we report the exponent of algebraic decay extracted for $L_y = 5, 6$ for each condensed channel $\alpha\beta = xx, yy,$ and $x0$. At the bottom of the panel, we summarize our data indicating if the $2e$ correlations are gapless and $1e$ correlations are gapped at each circumference with a ✓. These panels demonstrate that our results from the main text are qualitatively unchanged as we introduce finite inter-layer repulsion U_2 and finite interaction range.

its own, that there is a gap to electronic excitations. The situation is similar at $L_y = 6$ but here the ratio, although above two, is not as large at the bond dimensions we can access.

To gain greater clarity about the nature of the state, e.g. the existence of a charge gap, we again attempt to extrapolate both the $2e$ and $1e$ correlation lengths. Fig. A.11(c,f) shows linear extrapolations of $1/\xi$ versus δ for $L_y = 5, 6$. At $L_y = 5$, $1/\xi_{2e}$ extrapolates to zero, in accord with the power law superconducting correlations above, where as $1/\xi_{1e}$ is positive. This is consistent with a charge gap, and we may again confidently identify the $L_y = 5$ at finite (d, U_2) as a Luther-Emery liquid, i.e. a superconductor. In fact, the indications of superconductivity here, such as $1/\xi_{1e}$, appear to be larger or more clear than the $(d, U_2) = (0, 0)$ case studied above. Unfortunately this clarity does not extent to the $L_y = 6$ case, where both extrapolations are consistent with zero. Given the ratio $\xi_{2e}/\xi_{1e} \gg 1/2$, ordinarily a good heuristic indication of pairing, and that the smallest attainable δ remains much larger than the Fermi wavevector (see Sec. A.4), this evidence does not yet yield a firm conclusion for $L_y = 6$. As usual, higher bond dimensions could resolve this issue. Due to computational expense, $L_y = 7$ was not studied in detail here.

In summary, adding finite (d, U_2) does not have a clear effect at $L_y = 6$, but appears to further stabilize superconductivity at $L_y = 5$. This success at $L_y = 5$ invites us to determine

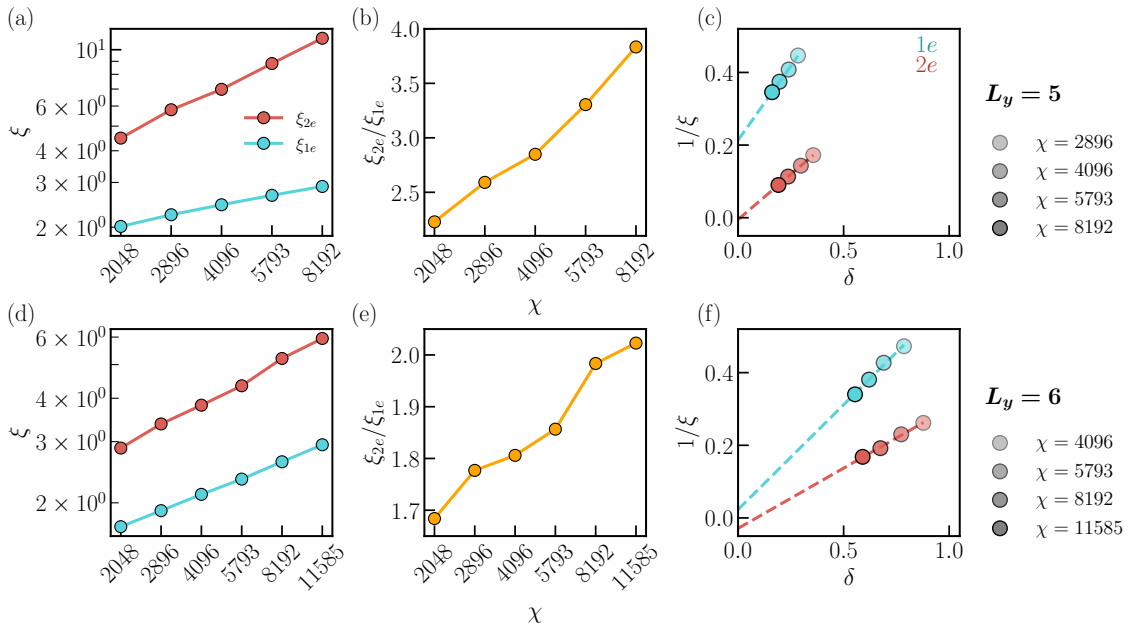

Figure A.11: **Bond Dimension Scaling of Correlation Lengths at finite (d, U_2).** In panels (a) and (d), we show the one-electron and two-electron correlation lengths as a function of bond dimension for $L_y = 5, 6$ at a parameter point $(g, U_1, U_2, d) = (0.1, 1.4, 0.2, 0.358)$ with finite inter-layer repulsion. We find that both appear to be growing linearly but the one-electron correlation lengths generally grow much slower. This is easiest to see from panels (b) and (e) where the ratio of ξ_{2e}/ξ_{1e} is found to be growing with bond dimensions for both $L_y = 5, 6$. From the discussion of Section V.A of the main text, this suggests that both parameter points are a Luther-Emery liquid. For $L_y = 5$, this is corroborated in panel (c) by performing an extrapolation to infinite bond dimension as we find a gapped $1e$ correlations and gapless $2e$ correlations. However, for $L_y = 6$, panel (e) yields negative correlation lengths for $\xi^{-1}_{2e,\infty}$ and $\xi^{-1}_{1e,\infty}$ close to zero suggesting that we are too far from a "scaling regime" for $L_y = 6$ to distinguish a Luther-Emery liquid from a Luttinger Liquid.

the boundaries of the superconducting phase at this circumference. This is the topic of the next section.

Robustness of Superconductivity at $L_y = 5$

We now focus on circumference $L_y = 5$ cylinders and study the extent of the superconducting phase in terms of several parameters: (i) interlayer tunneling g, (ii) in-layer interactions U_1, (iii) interlayer interactions U_2, (iv) interaction range d, (v) electron filling ν, and (vi) spin-layer Zeeman field B_z. We will show that the superconducting phase is at least perturbatively stable to each of these parameters, and has a large phase extent in most parameters. This

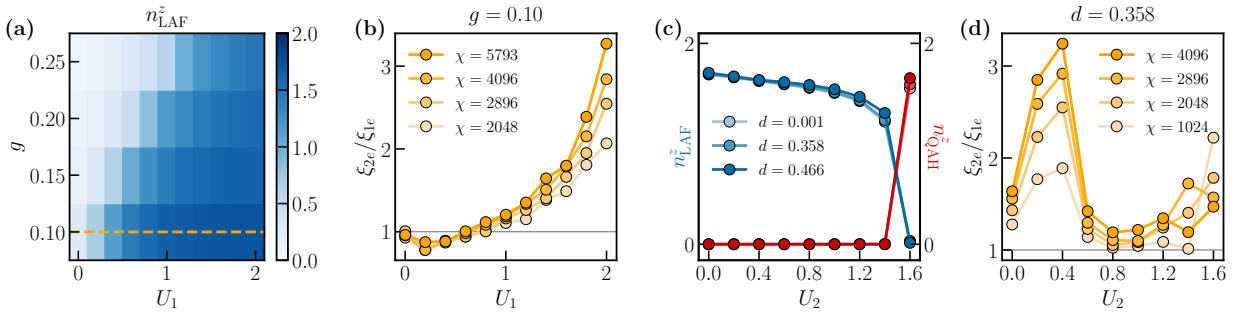

Figure A.12: **LAF Polarization of the Superconductor and Robustness to Additional Repulsion.** (a) LAF polarization of the doped state, which exhibits a widespread LAF phase in the strong coupling regime at fixed $d = U_2 = 0$. To diagnose superconducting order, we take a cut at fixed g (orange line) and, in (b), plot the ratio ξ_{2e}/ξ_{1e}. Its growth with bond dimension and substantial magnitude (i.e., in excess of unity at the largest available bond dimension) suggests the presence of superconductivity at $U_1 \gtrsim 0.6$. (c) Plot of the LAF and QAH (i.e. layer) polarization as a function of U_2 at fixed $(g, U_1) = (0.1, 1.4)$. For each value of the interaction range d, the doped state remains substantially LAF-polarized until U_2 exceeds U_1, at which the phase abruptly transitions to QAH. Fixing $d = 0.358$, in (d) we plot the superconducting diagnostic ξ_{2e}/ξ_{1e}, finding evidence for superconducting correlations at $U_2 \lesssim 1.2$. All plots at $L_y = 5$ and $\nu = 2 - 1/5$.

justifies our referring to the superconductor as "robust" in the main text.

To start, we examine the effect of g and U_1. Fig. A.12(a) shows the LAF polarization in the (g, U_1) plane from DMRG at filling $\nu = 1.8$. Comparing to Fig. A.5(a) above, the LAF polarization appears in essentially the same region of parameter space; doping the LAF does not destroy the order. Fig. 5(a) of the main text showed that the superconducting phase persists over almost the whole region. To corroborate this claim, Fig A.12(b) plots the ratio ξ_{2e}/ξ_{1e} at fixed $g = 0.1$ as a function of U_1. We adopt the heuristic that the state is superconducting if ξ_{2e}/ξ_{1e} is growing and exceeds unity at the largest available bond dimension. In the line cut, one can see this clearly holds at large U_1, but there is a small region near $U_1 = 0.2$ that is most LAF polarized but does not have significant superconducting correlations. At these bond dimensions, these states appear to be metallic and we refer to them as a LAF metal. However, larger bond dimensions tend to increase the superconducting correlations in a finite χ transition, albeit at larger χ at parameters close to the edge of the LAF-polarized region. We therefore cannot determine if the LAF metal is a finite bond dimension artifact or a genuine phase. Either way, the vast majority of the LAF polarized region is clearly adiabatically connected to the state at $(g, U_1) = (0.15, 1.5)$ that we previously determined to be a Luther-Emery liquid.

Next, we examine the effect of additional repulsive interactions (d, U_2), corresponding to

Fig. 5(c) of the main text. Fig. A.12(c) shows the LAF and quantum anomalous Hall (QAH) polarizations as a function of U_2 for each d at $\nu = 2 - 1/5$. As before, the polarizations hew closely to their respective values at $\nu = 2$ (not shown), with a transition from the LAF insulator to a Chern-polarized QAH insulator when U_2 exceeds U_1. Fig. A.12(d) shows the ratio ξ_{2e}/ξ_{1e} on the same axes, which exceeds unity and grows with bond dimension for $U_2 \lesssim 1.2$. By our heuristic, this suggests all these points lie in the superconducting phase, and in fact the largest superconducting correlations are at $U_2 \sim 0.4$ at the largest available bond dimension. However, the ratio drops off precipitously around $U_1 \approx 0.6$. This might signal a drop in the superconducting gap (perhaps even to zero) that would only be apparent at much larger bond dimensions, or might simply be a regime where more entanglement is required to adequately describe the state. Altogether, this demonstrates both that the superconductor is stable to significant additional repulsion, and that such interactions may accelerate the convergence of the superconducting state in bond dimension.

The superconductivity is also stable across a range of electronic densities below $\nu = 2$. Fig. A.4(a) shows that the LAF polarization is stable to significant hole doping, decreasingly almost linearly with filling down to $\nu = 1.5$, whereupon the behavior becomes more irregular. We remark that the states at $\nu \leq 1.5$ may be translation-breaking, though careful consideration of different circumferences would be necessary to draw any firm conclusions. Comparing to Fig. 5(b) of the main text, we see that superconductivity appears to persist down to $\nu = 1.6$. In particular, these data suggest that the superconductor is resilient to significant changes in the Fermi velocity of the underlying LAF band structure, which increases with decreasing density — recall from Fig. A.4 the structure of the LAF Fermi surface.

Finally we discuss the subtle role of B_z. Recall from Appendix A.1 that we have added a small field $-B_z \sum_{\mathbf{r}} \hat{\psi}^\dagger_{\mathbf{r}} s^z \ell^z \hat{\psi}_{\mathbf{r}}$, with a typical value of $B_z = 10^{-2}$ in our numerics. Briefly, the reason for this is that Hohenberg-Mermin-Wagner considerations forbid spontaneous symmetry breaking of a continuous symmetry in quasi-1D, a prerequisite for the formation of the LAF. Without this pinning field, one would expect a quantum disordered phase with extremely long but ultimately decaying LAF fluctuations, just as in the Haldane model [193]. To be able to realize a truly polarized ground state without a huge entanglement cost, we add this B_z field at an energy scale significantly below the other microscopic scales in the problem. Another choice would have been to add the square of the LAF order parameter, which has the advantage that it does not pick out a particular quantization axis.

To confirm that B_z is innocuous to the superconducting physics, we examine the effect of tuning it. Fig. A.4(b) shows the ratio ξ_{2e}/ξ_{1e} as a function of B_z. This quantity appears to increase without bound, all the way from $2 \cdot 10^{-2}$ (on the order of the value $B_z = 10^{-2}$ fixed in the main text), down to 10^{-3}, with a decrease in B_z appearing to accelerate convergence at fixed bond dimension. This strongly suggests that the value of B_z we used here only serves to stabilize the LAF order, but does not play a critical role in pairing on top of it. Working at non-zero (d, U_2) to circumvent convergence issues, in Fig. A.4(c) we show that superconductivity apparently persists to at least moderately larger $B_z \approx 0.1$, though a suppression in ξ_{2e}/ξ_{1e} at fixed bond dimension suggests that the larger-B_z states are more difficult to converge. In fact, the longer-range interactions appear necessary to avoid norm

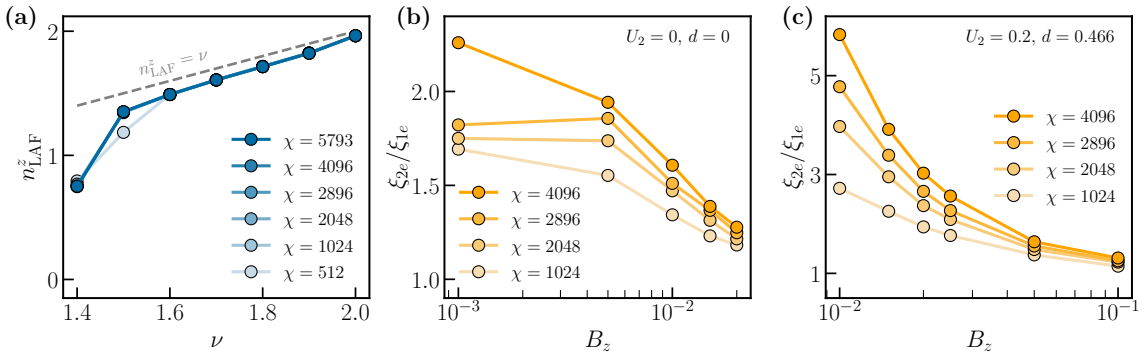

Figure A.13: **Additional data for the ν and B_z scans.** (a) The LAF polarization vs. the total electronic density at fixed $(g, U_1) = (0.1, 1.8)$ and $d = U_2 = 0$. Over a significant range of densities that subsumes the putative superconducting region $1.7 \lesssim \nu < 2$, the LAF polarization is near-maximal, decreasing approximately linearly with the density of hole dopants (i.e. $2 - \nu$). (b) Plot of ξ_{2e}/ξ_{1e} as a function of the Zeeman pinning field at $d = U_2 = 0$ and $(g, U_1) = (0.1, 1.4)$. Its large magnitude and continued growth with bond dimension signals the prevalence of superconducting correlations down to very small values, namely $B_z = 10^{-3}$ (an order of magnitude smaller than 10^{-2}, the value taken in the main text). (c) Plot of the same quantity at a finite amount of additional repulsion, enabling the numerical stabilization of DMRG simulations up to $B_z = 10^{-1}$, at which the state may still be superconducting. All plots are at $L_y = 5$.

errors at these larger B_z values. We conclude that the particular value of B_z is incidental to the superconducting phase at $L_y = 5$, and are therefore justified in treating it as a small perturbation used for numerical convenience.

In summary, we have found that the Luther-Emery liquid at $L_y = 5$ is resilient to six independent perturbations. This underscores the theme that doping the LAF insulator leads to a robust superconducting phase at this circumference.

A.5 Additional Details of Pairing Symmetry Analysis

In this appendix, we provide the theoretical details underlying our characterization of the pairing symmetry. To do so, we provide a brief reminder regarding how one formally characterizes pairing symmetry in a superconducting state. In particular, we describe how the pairing symmetry, in systems with both unitary and anti-unitary symmetries, is characterized by the induced co-representation of the symmetry group on the pair wavefunction. Subsequently, we use this formalism to determine the pairing symmetry of the double Hofstadter model.

Characterizing Pairing Symmetry: Induced Co-Representations on the Pair Wavefunction

In this subsection, we detail systematically how to characterize the pairing symmetry of a superconducting ground state. In particular, the pairing symmetry refers to the representation of the magnetic space group G under which the pair wavefunction $\Delta_{\alpha\beta}(\mathbf{k})$ transforms. To be a bit more precise, let us start by noting that the pair wavefunction $\Delta_{\alpha\beta}(\mathbf{k})$ lives in the vector space $\mathbb{C}^{4\times4}\otimes\mathcal{F}_{\mathrm{BZ}}$ where the 4×4 comes from the different channels $\alpha\beta$ and $\mathcal{F}_{\mathrm{BZ}}$ is the space of functions over the Brillouin zone. Our goal will be to first determine an action of the magnetic space group on the pair wavefunction such that it transforms under a *co-representation* of the group— the generalization of the notion of a representation to include both unitary and anti-unitary symmetries.[3] We recall the definition for convenience. Let G be a group with group elements $g\in G$ that are either linear or anti-linear. Following Ref. [363], define a function s such that $s(g)=\pm1$ for linear (anti-linear) group elements. We write $F^{s(g)=+1}=F$ and $F^{s(g)=-1}=F^*$ for complex numbers F. Then, a co-representation of G is a homomorphism from the group to the space of operators on a vector space V defined over the complex numbers:

$$g\to\begin{cases}\nu_g & s(g)=+1\\ \nu_g\mathsf{K} & s(g)=-1,\end{cases} \tag{A.87}$$

where $\nu_g\in\mathsf{GL}(V,\mathbb{C})$ (i.e. the group of automorphisms of V), K indicates complex conjugation, and where ν_g matrices must satisfy a characteristic composition property:

$$\nu_{gh}=\nu_g\nu_h^{s(g)} \tag{A.88}$$

Below we will show the action of our symmetry group on the pair wavefunction and demonstrate that it forms a co-representation. We will then organize the vector space $\mathbb{C}^{4\times4}\otimes\mathcal{F}_{\mathrm{BZ}}$ into a direct sum of irreducible co-representations. The subspaces the pair wavefunction we find lives in determines its pairing symmetry. The irrep that the pair wavefunction belongs to determines its pairing symmetry.

To define the action of the symmetry group G on the pair wavefunction, let us take $\hat{g}$ to be the (anti-)unitary operator corresponding to group element $g\in G$. Let us make the assumption (which will be relevant to the case at hand; see Subsection A.5) that *generators* of our magnetic space group $\hat{g}$ act on our Cooper pair operators $\Delta_{\alpha\beta}(\mathbf{k})$ by acting on the momentum label only:

$$\hat{g}^\dagger\hat{\Delta}^\dagger(\mathbf{k})\hat{g}=\hat{\Delta}^\dagger(g^{-1}\mathbf{k}), \tag{A.89}$$

where we have suppressed the $\alpha\beta$ indices, and $g^{-1}\mathbf{k}$ is the action of the symmetry on the momentum label. Define the action of the element on the pair wavefunction $\Delta(\mathbf{k})\equiv\langle\psi,\hat{\Delta}^\dagger(\mathbf{k})\psi\rangle$ as:

$$(g\cdot\Delta)(\mathbf{k})=\langle\hat{g}\psi,\hat{\Delta}^\dagger(\mathbf{k})\hat{g}\psi\rangle=\langle\psi,\hat{g}^\dagger\hat{\Delta}^\dagger(\mathbf{k})\hat{g}\psi\rangle^{s(g)}=\Delta^{s(g)}(g^{-1}\mathbf{k}), \tag{A.90}$$

[3]For a short but lucid review see Appendix B of Ref. [363], or Ref. [394] for a more comprehensive treatment.

where we have used the notation $\langle a, b\rangle = \langle a|b\rangle$ to denote the inner product as it will be more convenient for working with anti-unitary operators. While this action is derived from the quantum mechanical data, we can now think of $\Delta(\mathbf{k})$ as an element of the space of functions on the Brillouin zone $\mathcal{F}_{\text{Bz}}$, on which the action of the group is $(g \cdot F)(\mathbf{k}) = F^{s(g)}(g^{-1}\mathbf{k})$. On the vector space of such functions, this map is manifestly a group homomorphism and is anti-linear. To demonstrate that this action indeed does form a co-representation, it is helpful to decompose functions $F(\mathbf{k})$ into "irreducible" functions that are real and transform definitely under the action of $\mathbf{k} \to g^{-1}\mathbf{k}$. Explicitly, we have that:

$$F(\mathbf{k}) = \sum_{\Gamma \in \text{Irrep}(G)} \sum_{\mu=1}^{\dim(\Gamma)} \eta_F^{\Gamma,\mu} Y_{\Gamma,\mu}(\mathbf{k}), \tag{A.91}$$

where $Y_{\Gamma,\mu}(\mathbf{k}) \in \mathbb{R}$ and $Y_{\Gamma,\mu}(g^{-1}\mathbf{k}) = \mathbb{V}_{\mu\nu}^{\Gamma,g} Y_{\Gamma,\nu}(\mathbf{k})$. In this basis, the action of our group can be expressed as:

$$(g \cdot F)(\mathbf{k}) = F^{s(g)}(g^{-1}\mathbf{k}) = \nu_g \mathsf{K}^{s(g)} F(\mathbf{k}), \tag{A.92}$$

where ν_g is a block diagonal matrix whose rows and columns are labeled by Γ and μ that rotates the coefficients $\eta^{\Gamma,\mu}$ and $\mathsf{K}^{s(g)=+1} = 1$ and $\mathsf{K}^{s(g)=-1} = \mathsf{K}$. Its blocks are precisely the matrices $\mathbb{V}_{\mu\nu}^{\Gamma,g}$ labeled above. We now demonstrate that the ν_g's above form a co-representation. In particular, note that $(gh \cdot \Delta)(\mathbf{k}) = \nu_{gh}\mathsf{K}^{s(gh)}\Delta(\mathbf{k})$, by definition. However,

$$(gh \cdot F)(\mathbf{k}) = (g \cdot (h \cdot F))(\mathbf{k}) = \nu_g \mathsf{K}^{s(g)} (h \cdot F)(\mathbf{k}) = \nu_g \mathsf{K}^{s(g)} \nu_h \mathsf{K}^{s(h)} F(\mathbf{k}) = \nu_g \nu_h^{s(g)} \mathsf{K}^{s(gh)} F(\mathbf{k}). \tag{A.93}$$

As such, the ν matrices satisfy the characteristic algebra of a co-representation $\nu_{gh} = \nu_g \nu_h^{s(h)}$. As a remark, a change of basis $Y(\mathbf{k}) \to \mathbb{W}^\dagger Y(\mathbf{k})$, generates similarity transformations on the ν's:

$$\nu_g \to \mathbb{W}^\dagger \nu_g \mathbb{W}^{s(g)}. \tag{A.94}$$

Two co-representations are said to be *equivalent* if they are related by such a similarity transformation.

Pairing Symmetry

Generalities out of the way, we now focus on the specific case at hand. Recall that the magnetic space group of our model is generated by:

$$m_x \qquad m_y \qquad C_{2z} \qquad C_{2x} \qquad \mathcal{I} \tag{A.95}$$

as discussed in Appendix A.1. Note that, because our Cooper pairs carry zero momentum and charge-$2e$, the action of m_y on such objects is trival and the remaining generators mutually commute (c.f. Table A.1) and square to the identity. As such, the group acts on the pair wavefunction as $(\mathbb{Z}_2)^3 \times \mathbb{Z}_2^{\mathsf{K}}$, where $\mathbb{Z}_2^{\mathsf{K}}$ is anti-unitary. This fact greatly simplifies the possible representations that the pair wavefunction can live in. Since the group is abelian,

the ν_g's are constrained to be numbers and since they square to the identity, this implies that the index ν^g defined in Eq. (A.87) satisfies:

$$1 = \begin{cases} \nu_g^2 = 1 & s(g) = +1 \\ |\nu_g|^2 = 1 & s(g) = -1, \end{cases} \tag{A.96}$$

which follows from the algebra of the co-representation Eq. (A.88). This constrains:

$$\nu_g = \begin{cases} \nu_g = \pm 1 & s(g) = +1 \\ \nu_g = e^{i\theta} & s(g) = -1. \end{cases} \tag{A.97}$$

Finally, note that under basis transformations $\mathbb{W} = e^{i\phi/2}$,

$$\nu_g \to \begin{cases} \nu_g & s(g) = +1 \\ e^{-i\phi}\nu_g & s(g) = -1 \end{cases} \tag{A.98}$$

This implies that there is only one possible regular co-representation of the pair wavefunction under the $\mathbb{Z}_2^K$ as they are all related by a similarity transformation. Therefore, the pairing symmetry is characterized by three "symmetry indices" (or characters) ν_g for $g \in \{C_{2z}, C_{2x}, m_x\}$. To determine ν_g for these generators, let us tabulate the action of the symmetry operators on the Cooper pair operators $\Delta^\dagger_{\alpha\beta}(\mathbf{k})$ for the dominant condensed channels $\alpha\beta = xx$ and yy, which follows from Eqs. (A.26)-(A.29):

$$\hat{C}_{2z}\hat{\Delta}^\dagger_{\alpha\beta}(\mathbf{k})\hat{C}^{-1}_{2z} = \hat{\Delta}^\dagger_{\alpha\beta}(C_{2z}\mathbf{k}) \tag{A.99}$$

$$\hat{C}_{2x}\hat{\Delta}^\dagger_{\alpha\beta}(\mathbf{k})\hat{C}^{-1}_{2x} = \hat{\Delta}^\dagger_{\alpha\beta}(C_{2x}\mathbf{k}) \tag{A.100}$$

$$\hat{m}_x\hat{\Delta}^\dagger_{\alpha\beta}(\mathbf{k})\hat{m}^{-1}_x = \hat{\Delta}^\dagger_{\alpha\beta}(\mathbf{k} + \mathbf{G}_2/2) \tag{A.101}$$

$$\hat{\mathcal{I}}\hat{\Delta}^\dagger_{\alpha\beta}(\mathbf{k})\hat{\mathcal{I}}^{-1} = \hat{\Delta}^\dagger_{\alpha\beta}(\mathbf{k}). \tag{A.102}$$

Symmetry actions in hand, we can extract the ν_g's directly from the pair wavefunction. From the data shown in Fig. A.14 below, we can extract the symmetry indices directly, as shown Table A.3. Note that $x0$ has a different symmetry index under the magnetic translation $\hat{m}_x$, which is consistent with it having a different algebraic exponent η_{L_y} (see Fig. A.10c).

$L_y \backslash \alpha\beta$	xx	yy	$x0$
5	$(-1,-1,\boldsymbol{\times})$	$(-1,-1,\boldsymbol{\times})$	$(-1,-1,\boldsymbol{\times})$
6	$(-1,-1,-1)$	$(-1,-1,-1)$	$(-1,-1,+1)$
7	$(-1,-1,\boldsymbol{\times})$	$(-1,-1,\boldsymbol{\times})$	$(-1,-1,\boldsymbol{\times})$

Table A.3: **Pairing Symmetry of the Superconductor.** Symmetry Indices $(\nu_{C_{2z}}, \nu_{C_{2x}}, \nu_{m_x})$ for the different condensed channels and circumferences. An ✗ indicates that m_x is not a symmetry for odd circumferences, so that ν_{m_x} is not well defined.

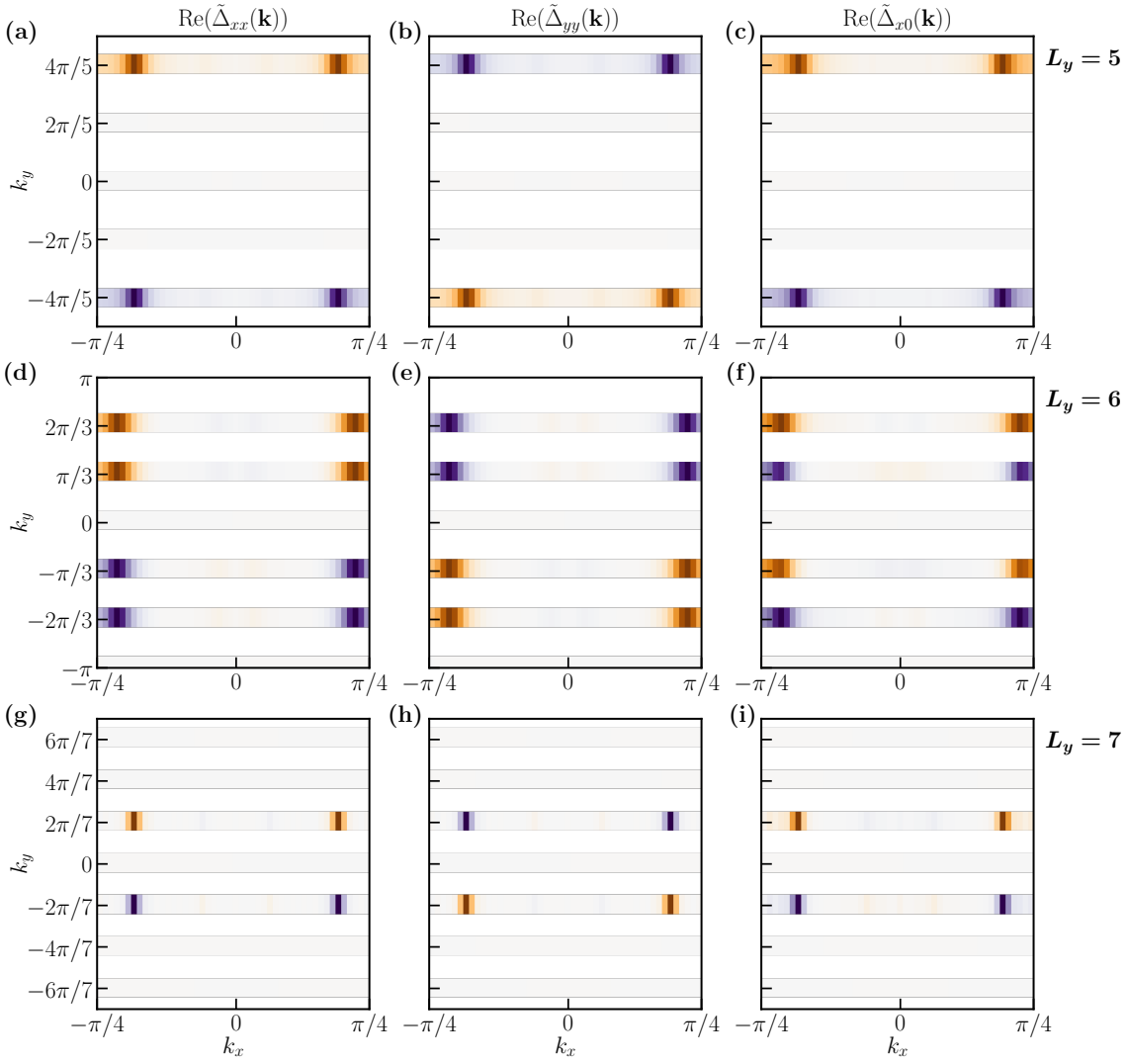

Figure A.14: **Momentum Space Structure of the Pair Wavefunction.** Plot of the proxy pair wavefunction for the two dominant superconducting channels $\alpha\beta = xx, yy$ at all three circumferences $L_y = 5, 6, 7$, extracted from charge-conserving iDMRG using the methods described in the text. Each function is manifestly odd under C_{2x} and C_{2z}, with the latter indicating p-wave pairing symmetry. At $L_y = 6$, where the magnetic translation m_x is a symmetry of the finite-circumference system, the pair wavefunction in the xx and yy channels is odd under shifts $k_y \to \pi$, where it is even in the sub-dominant $x0$ channel. We remark that the overall normalization of the pair wavefunction—which we have argued is proportional to the true pair wavefunction—is set arbitrarily. In each case, its imaginary part is smaller by orders of magnitude and is therefore omitted. Each plot is computed at $\chi = 12288$.

A.6 Additional Details on Relationship to Chiral TBG

In the main text, we described the similarities between the double Hofstadter model and chiral models of twisted bilayer graphene (TBG). In this section, we provide additional details regarding these similiarities. To do so, let us briefly review the form of the interacting Hamiltonian in chiral models of TBG. For a more complete and pedagogical review, we refer the reader to Ref. [32].

Brief Review of Chiral TBG

Recall that electrons in TBG carry a conserved electronic spin ($s = \Uparrow, \Downarrow$) and valley ($\tau = K, K'$) and can occupy one of two energetically close but distinct bands. The narrow bandwidth of the flat band subspace suggests that other linear combinations of these bands, distinct from the single-particle energy eigenbasis, may be more relevant for studying the interacting physics of TBG. One natural choice recognized in Refs. [31, 63] is the sublattice polarized basis which distinguishes bands in the subspace based on their weight on the two sites $\sigma = A, B$ of the honeycomb lattice of graphene. This sublattice polarization becomes maximal in the non-physical limit where intervalley hopping can only occur between opposite sublattices (i.e. only between A sites on the top layer to B sites on the bottom, or B on top to A on the bottom). This is called the "chiral limit of TBG" [32, 74, 75].

A crucial property of these sublattice polarized bands is that they carry a definite Chern number. In particular, let $\sigma^\alpha, \tau^\alpha, s^\alpha$ for $\alpha = 0, x, y, z$ correspond to the Pauli matrices of the sublattice, valley, and spin respectively. Then, the Chern number is labeled by $\mathcal{C} = \sigma^z\tau^z$. This motivates organizing the bands by their Chern sector $\sigma\tau$, their valley τ, and their electronic spin s. A complete set of commuting Pauli matrices, that define how to measure and flip each such degree of freedom independently, can then be defined as:

$$\boldsymbol{\eta} = (\sigma^x\tau^x, \sigma^x\tau^y, \tau^z) \qquad \widetilde{\boldsymbol{\eta}} = (s^x, s^y, s^z) \qquad \boldsymbol{\gamma} = (\sigma^x, \sigma^y\tau^z, \sigma^z\tau^z), \tag{A.103}$$

corresponding to a valley pseudospin, the electronic spin, and the Chern label. In this "strong coupling basis" of the flat bands, the band-projected Hamiltonian of chiral-limit TBG takes a particularly simple form:

$$\hat{H}_{\text{TBG}} = \hat{h}_{\text{TBG}} + \hat{\mathcal{V}}_{\text{TBG}}, \tag{A.104}$$

$$\hat{h}_{\text{TBG}} = \sum_{\mathbf{k}\in\text{BZ}} \hat{\varphi}^\dagger_{\mathbf{k}} \left[\gamma^x h_x^{\text{TBG}}(\mathbf{k}) + \gamma^y h_y^{\text{TBG}}(\mathbf{k})\right] \hat{\varphi}_{\mathbf{k}}, \tag{A.105}$$

$$\hat{V}_{\text{TBG}} = \frac{1}{2A} \sum_{\mathbf{q}\in\mathbb{R}^2} V_{\mathbf{q}} \delta\hat{\rho}_{\mathbf{q}} \delta\hat{\rho}_{-\mathbf{q}}, \tag{A.106}$$

where $\varphi^\dagger$ is a fermionic creation operators organized into a spinor in the Chern, spin, and valley pseudospin, evidently the dispersion is purely off-diagonal in the Chern sector, A is

the area of unit cell of TBG, and the interactions are written in terms of relative densities $\delta\hat{\rho}_{\mathbf{q}} = \rho_{\mathbf{q}} - \bar{\rho}_{\mathbf{q}}$. Here, the relative densities are defined from:

$$\hat{\rho}_{\mathbf{q}} = \sum_{\mathbf{k}} \hat{\varphi}^{\dagger}_{\mathbf{k}} \Lambda_{\mathbf{q}}(\mathbf{k}) \hat{\varphi}_{\mathbf{k}+\mathbf{q}}, \qquad \bar{\rho}_{\mathbf{q}} = \frac{1}{2} \sum_{\mathbf{k},\mathbf{G}} \delta_{\mathbf{q},\mathbf{G}} \operatorname{Tr}\left[\Lambda_{\mathbf{G}}(\mathbf{k})\right], \qquad \Lambda_{\mathbf{q}}(\mathbf{k}) = F^{S}_{\mathbf{q}}(\mathbf{k}) e^{i\Phi^{S}_{\mathbf{q}}(\mathbf{k})\gamma^{z}}, \tag{A.107}$$

where the form of the density operator arises from projecting the microscopic number density operator into the flat bands. Note that, manifestly, the interacting portion of the Hamiltonian is diagonal in the Chern number and is independent of spin or valley pseudospin. As a consequence, this term in the Hamiltonian has a $U(4)_+ \times U(4)_-$ symmetry corresponding to independent rotations of both the spin and valley pseudospin in either Chern sector. At the magic angle, when the dispersion $\hat{h}_{\mathrm{TBG}}$ identically vanishes, this enlarged symmetry is precisely the symmetry of the chiral TBG Hamiltonian. However, a departure from the magic angle re-introduces the dispersion which, while independent of both spin or valley pseudospin, mixes the two Chern sectors. As such, its inclusion breaks the $U(4)_+ \times U(4)_-$ symmetry down to a single $U(4)$.

As stated in the text, a number of experiments in TBG suggest some degree of flavor polarization. As such, in literature, this $U(4) \times U(4)$ symmetric model is typically reduced to a $U(2) \times U(2)$ symmetric model with half the number of degrees of freedom. Here $U(2)$ describes rotations of the unpolarized degree of freedom, which are generated by either $\boldsymbol{\eta}$ for "Route 1" or $\tilde{\boldsymbol{\eta}}$ for "Route 2". The form of this $U(2) \times U(2)$ symmetric model is identical to Eq. (A.104) but where the electrons $\hat{\varphi}^{\dagger}_{\mathbf{k}\gamma\eta\tilde{\eta}}$ are replaced with $\hat{\varphi}^{\dagger}_{\mathbf{k}\gamma\eta}$ or $\hat{\varphi}^{\dagger}_{\mathbf{k}\gamma\tilde{\eta}}$.

Comparison Between the Double Hofstadter Model and Chiral TBG

In this section, we establish a correspondence between the chiral TBG Hamiltonian and that of the band-projected double Hofstadter model. Recall from Sec. A.2 that the latter can be expressed in the "strong-coupling" form

$$\hat{\mathcal{H}} = \delta\hat{h} + \hat{\mathcal{V}}, \tag{A.108}$$

$$\delta\hat{h} = \sum_{\mathbf{k}\in\mathrm{BZ}} \hat{\varphi}^{\dagger}_{\mathbf{k}} \left\{ \underbrace{\left[l^{x} h_{x}(\mathbf{k}) + l^{y} h_{y}(\mathbf{k})\right]}_{\delta h_{g}(\mathbf{k})} + \underbrace{l^{0} h_{0}(\mathbf{k})}_{\delta h_{0}(\mathbf{k})} \right\} \hat{\varphi}_{\mathbf{k}}, \tag{A.109}$$

$$\hat{\mathcal{V}} = \sum_{\mathbf{q}\in\mathrm{EBZ}} V_{\ell\ell'}(\mathbf{q}) \delta\hat{\rho}_{\mathbf{q},\ell} \delta\hat{\rho}_{-\mathbf{q},\ell'}, \tag{A.110}$$

where the interactions are written in terms relative densities $\delta\hat{\rho}_{\mathbf{q}\ell} = \hat{\rho}_{\mathbf{q}\ell} - \bar{\rho}_{\mathbf{q}\ell}$ defined from:

$$\hat{\rho}_{\mathbf{q}\ell} = \sum_{\mathbf{k}} \hat{\varphi}^{\dagger}_{\mathbf{k}} \Lambda_{\mathbf{q}\ell}(\mathbf{k}) \hat{\varphi}_{\mathbf{k}+\mathbf{q}}, \qquad \bar{\rho}_{\mathbf{q}\ell} = \frac{1}{\sqrt{qN}} \sum_{\mathbf{k},\mathbf{G}} \delta_{\mathbf{q},\mathbf{G}} \operatorname{Tr}\left[\Lambda_{\mathbf{G}\ell}(\mathbf{k})\right]. \tag{A.111}$$

When $U_1 = U_2$ and $g = 0$, the Hamiltonian is greatly simplified. In particular, it can be re-expressed as

$$\hat{\mathcal{H}} = \sum_{\mathbf{k}\in \mathrm{BZ}} \hat{\varphi}^\dagger_{\mathbf{k}} l^0 h_0(\mathbf{k}) \hat{\varphi}_{\mathbf{k}} + \sum_{\mathbf{q}\in \mathrm{EBZ}} V(\mathbf{q}) \delta\hat{\rho}_{\mathbf{q}} \delta\hat{\rho}_{-\mathbf{q}}, \tag{A.112}$$

where $\delta\hat{\rho}_{\mathbf{q}} = \sum_\ell \delta\hat{\rho}_{\mathbf{q}\ell}$ and the corresponding layer-summed form factor is constrained to have the following structure:

$$\Lambda_{\mathbf{q}}(\mathbf{k}) = \sum_\ell \Lambda_{\mathbf{q}\ell}(\mathbf{k}) = F^S_{\mathbf{q}}(\mathbf{k}) e^{i\Phi_{\mathbf{q}}(\mathbf{k}) l^z}. \tag{A.113}$$

If we neglect the small bare Hofstadter dispersion $h_0(\mathbf{k})$, the resulting Hamiltonian has *precisely* the same form as the chiral TBG Hamiltonian at the magic angle under the mapping

$$\boldsymbol{l} \longleftrightarrow \boldsymbol{\gamma}, \qquad \mathbf{s} \longleftrightarrow \begin{cases} \eta & \text{Map 1} \\ \tilde{\eta} & \text{Map 2.} \end{cases} \tag{A.114}$$

Both models have a $U(2) \times U(2)$ symmetry corresponding to (pseudo)-spin rotations in distinct Chern sectors. As an added remark, in both models, those Chern sectors are related by a spacetime inversion symmetry $\mathcal{I}$, which in TBG is written in the literature as $C_{2z}\mathcal{T}$. The effect of introducing g into the double Hofstadter model restores the terms $\delta h_g(\mathbf{k})$ in the dispersion and modifies the form factors to $\Lambda_{\mathbf{q}}(\mathbf{k}) = F^S_{\mathbf{q}}(\mathbf{k}) e^{i\Phi_{\mathbf{q}}(\mathbf{k}) l^z} + F^A_{\mathbf{q}}(\mathbf{k}) l^x e^{i\Phi_{\mathbf{q}}(\mathbf{k}) l^z}$. The analog of δh_g is already present in chiral TBG (not necessarily at the magic angle) as a dispersion. However, the additional term $F^A_{\mathbf{q}}(\mathbf{k}) l^x e^{i\Phi_{\mathbf{q}}(\mathbf{k}) l^z}$ in the form factor has no direct analog in chiral TBG and scales linearly with g. Nonetheless, provided that g is small, the double Hofstadter model at $U_1 = U_2$ can be thought of as being "perturbatively related" to chiral TBG, even away from the magic angle.

Appendix B

Appendix to Chapter 3

B.1 Hamiltonian construction at all rational fluxes

YC Lattice Parameterization

We first describe two coordinate parameterizations of the **underlying triangular lattice**, beginning in the 2D limit. In the "YC" parameterization of the 2D plane, the $\hat{y}$ site-to-site distance is the nearest-neighbour distance a. This corresponds to the Bravais vectors

$$\boldsymbol{a}_1 = a\left(\frac{\sqrt{3}}{2}\hat{x} + \frac{1}{2}\hat{y}\right), \qquad \boldsymbol{a}_2 = a\hat{y} \qquad \text{(YC)}, \tag{B.1}$$

and the corresponding reciprocal lattice vectors

$$\boldsymbol{b}_1 = \frac{4\pi}{\sqrt{3}a}\hat{x}, \qquad \boldsymbol{b}_2 = \frac{2\pi}{a}\left(-\frac{\hat{x}}{\sqrt{3}} + \hat{y}\right) \qquad \text{(YC)}. \tag{B.2}$$

This leads to a natural cylinder compactification: one may identify each point

$$\boldsymbol{r} = x\boldsymbol{a}_1 + y\boldsymbol{a}_2 \tag{B.3}$$

with points $\boldsymbol{r}'$ for which $y \equiv y' \pmod{L_y}$ and also $x = x'$. We refer to L_y as the "circumference" of the cylinder. Doing so for the YC lattice, one obtains the canonical "YC-L_y" cylinder geometry [107], whose circumference is $L_y a$.

Choosing the magnetic unit cell

The following applies to the YC lattice geometry. Let the flux per *parallelogram* be

$$\Phi = \frac{p}{q}\Phi_0, \tag{B.4}$$

where $\Phi_0 = \frac{2\pi\hbar}{e} \sim 2\pi$ in units where $\hbar/e = 1$. The above definition of flux is convenient for defining the geometry, but we briefly remark that the flux $\Phi/2$ per triangle — which is the smallest traversable plaquette — is the quantity with respect to which physical behavior (*e.g.*, the Hofstadter spectrum) must be Φ_0-periodic. In any case, the corresponding magnetic field strength is

$$B = \frac{\Phi}{A_{\text{par}}} = \frac{p\Phi_0/q}{\frac{\sqrt{3}}{2}a^2} = \frac{2p\Phi_0}{\sqrt{3}q}a^{-2}. \tag{B.5}$$

Regardless of the parity of q, there will be q magnetic sublattice sites in the magnetic unit cell. When q is **even**, the magnetic Bravais vectors are

$$\boldsymbol{R}_1 = q\boldsymbol{a}_1 - \frac{q}{2}\boldsymbol{a}_2 \propto \hat{x}, \qquad \boldsymbol{R}_2 = \boldsymbol{a}_2 \propto \hat{y}, \qquad (q \text{ even}), \tag{B.6}$$

whose total area A_{muc} is precisely that of $2q$ triangles of area $\frac{\sqrt{3}}{4}a^2$. The associated reciprocal lattice vectors are

$$\boldsymbol{G}_1 = \frac{1}{q}\boldsymbol{b}_1 \propto \hat{x}, \qquad \boldsymbol{G}_2 = \frac{1}{2}\boldsymbol{b}_1 + \boldsymbol{b}_2 \propto \hat{y}, \qquad (q \text{ even}). \tag{B.7}$$

As a sanity check, the total of the magnetic Brillouin zone (mBZ) is then

$$A_{\text{mBZ}} = |\boldsymbol{G}_1 \times \boldsymbol{G}_2| = (2\pi)^2\frac{2}{q\sqrt{3}a^2} = \frac{(2\pi)^2}{A_{\text{muc}}}. \tag{B.8}$$

When q is **odd**, the enclosing magnetic unit cell again contains exactly $2q$ triangles, but we take

$$\boldsymbol{R}_1 = q\boldsymbol{a}_1 - \frac{q-1}{2}\boldsymbol{a}_2, \qquad \boldsymbol{R}_2 = \boldsymbol{a}_2 \propto \hat{y}, \qquad (q \text{ odd}), \tag{B.9}$$

whose total area is once again

$$|\boldsymbol{R}_1 \times \boldsymbol{R}_2| = q|\boldsymbol{a}_1 \times \boldsymbol{a}_2| = \frac{q\sqrt{3}}{2}a^2 = A_{\text{muc}}. \tag{B.10}$$

The reciprocal lattice vectors are now

$$\boldsymbol{G}_1 = \frac{1}{q}\boldsymbol{b}_1, \qquad \boldsymbol{G}_2 = \frac{q-1}{2q}\boldsymbol{b}_1 + \boldsymbol{b}_2, \qquad (q \text{ odd}), \tag{B.11}$$

which also satisfy the inverse area relationship, Eq. (B.8). For both even and odd denominator q, note that the enclosing magnetic unit cell contains exactly $2q$ triangles, so $2\pi p \in 2\pi\mathbb{Z}$ total flux.

Hamiltonian and choice of vector potential

In all cases, we adopt the standard convention for the on-site Hubbard repulsion:

$$H_{\text{int}} = U \sum_{\boldsymbol{r}} n_{\boldsymbol{r}\uparrow} n_{\boldsymbol{r}\downarrow}, \qquad U \geq 0. \tag{B.12}$$

Now we discuss the hoppings. Placing the underlying triangular lattice on the cylinder as described in Sec. B.1, let the resulting system have circumference L_y, *i.e.*, the points $\boldsymbol{r} \sim \boldsymbol{r} + L_y \boldsymbol{a}_2$ are geometrically identified. Let the lattice sites be indexed as in Eq. (B.3), which defines a set of coordinate coefficients $(x, y) \in \mathbb{Z}^2$. Since $\boldsymbol{a}_2$ is purely vertical in both the YC and XC geometries, then x indexes the cylinder "rings", and y is an integer-valued spatial index within each ring. To generate complex hoppings and modify the translation algebra into a magnetic translation algebra, we introduce an external $U(1)$ vector potential. We assume that it is linear and that its curl is the magnetic field:

$$\boldsymbol{A}(\boldsymbol{r}) = M\boldsymbol{r}, \qquad \nabla \times \boldsymbol{A}(\boldsymbol{r}) = B\hat{z}, \tag{B.13}$$

where B is as in Eq. (B.5). The hoppings are obtained from the vector potential via the Peierl's substitution, for which we adopt the following sign convention:

$$t_{\boldsymbol{r}' \leftarrow \boldsymbol{r}} = t \exp\left(i \int_{\boldsymbol{r}}^{\boldsymbol{r}'} \boldsymbol{A}(\boldsymbol{\ell}) \cdot d\boldsymbol{\ell} \right) = t \exp\left(i \boldsymbol{A}\left(\frac{\boldsymbol{r}' + \boldsymbol{r}}{2} \right) \cdot (\boldsymbol{r}' - \boldsymbol{r}) \right), \tag{B.14}$$

where the second equality is due to linearity of $\boldsymbol{A}(\boldsymbol{r})$. Our convention is that the single-particle Hamiltonian is (note the minus sign):

$$\hat{h} = -\sum_{\boldsymbol{r}', \boldsymbol{r}} c^\dagger(\boldsymbol{r}') t_{\boldsymbol{r}' \leftarrow \boldsymbol{r}} c(\boldsymbol{r}), \tag{B.15}$$

where we only include nearest-neighbour hopping on the triangular lattice, for which

$$t_{\boldsymbol{r}' \leftarrow \boldsymbol{r}} = t e^{i \boldsymbol{A}\left(\frac{\boldsymbol{r}' + \boldsymbol{r}}{2}\right) \cdot (\boldsymbol{r}' - \boldsymbol{r})}. \tag{B.16}$$

To constrain the form of the vector potential, we remark that the terms $x\hat{x}$ and $y\hat{y}$ are curl-free, whereas $Bx\hat{y}$ and $-By\hat{x}$ (the standard Landau gauge potentials on the rectangular lattice) have the correct curl. We therefore reason that the most general permissible M in Eq. (B.13) is given by

$$M = B \begin{pmatrix} \alpha & \gamma - 1 \\ \gamma & \beta \end{pmatrix}, \tag{B.17}$$

where $\alpha, \beta, \gamma \in \mathbb{R}$. We will now demand that the choice of vector potential is compatible with our chosen geometry of magnetic Bravais vectors. Specifically, we ask that the Peierl's hoppings generated by $\boldsymbol{A}$ are *periodic* in the chosen magnetic Bravais vectors. This allows

us to place the system easily on a torus or cylinder, provided the system is an integer tiling of magnetic unit cells. Quantitatively, we demand that the RHS of Eq. (B.14) is invariant under shifts of the argument of $\boldsymbol{A}$ by the magnetic Bravais vectors $\boldsymbol{R}_1$ and $\boldsymbol{R}_2$, for all bond vectors $\boldsymbol{r}' - \boldsymbol{r}$. By linearity of the vector potential, and since the bond vectors are linear combinations of $\boldsymbol{a}_1$ and $\boldsymbol{a}_2$, it suffices to require that

$$\boldsymbol{a}_i \cdot \boldsymbol{A}(\boldsymbol{R}_j) \in 2\pi\mathbb{Z}, \tag{B.18}$$

for all i, j. Following Ref. [395], an elegant solution can be found in terms of the reciprocal vectors of the underlying triangular lattice. We take the following since $\boldsymbol{b}_1 \propto \hat{x}$ for both YC and XC geometries, and we want the vector potential to be independent of y:

$$\boldsymbol{A}(\boldsymbol{r}) = \frac{\Phi}{(2\pi)^2}(\boldsymbol{r} \cdot \boldsymbol{b}_1)\boldsymbol{b}_2, \tag{B.19}$$

where Φ is the flux per *parallelogram*. Noting the vector identity

$$[\nabla \times ((\boldsymbol{r} \cdot \boldsymbol{Q})\boldsymbol{P})]_i = \epsilon_{ijk}\partial_j \left(\boldsymbol{r}_\ell \boldsymbol{Q}_\ell \boldsymbol{P}_k\right) = \epsilon_{ijk}\boldsymbol{Q}_j\boldsymbol{P}_k = (\boldsymbol{Q} \times \boldsymbol{P})_i, \tag{B.20}$$

then

$$\boldsymbol{B}(\boldsymbol{r}) = \nabla \times \boldsymbol{A}(\boldsymbol{r}) = \frac{\Phi}{(2\pi)^2}\boldsymbol{b}_1 \times \boldsymbol{b}_2 = \frac{\Phi}{(2\pi)^2}\frac{(2\pi)^2}{A_{\text{par}}}\hat{z} = \frac{\Phi}{A_{\text{par}}}\hat{z}. \tag{B.21}$$

Moreover, it can be shown to have the required periodicity property. Note that

$$\boldsymbol{a}_i \cdot \boldsymbol{A}(\boldsymbol{R}_j) = \frac{\Phi}{(2\pi)^2}(\boldsymbol{R}_j \cdot \boldsymbol{b}_1)\boldsymbol{b}_2 \cdot \boldsymbol{a}_i = \delta_{i,2}\frac{2\pi p/q}{2\pi}(\boldsymbol{R}_j \cdot \boldsymbol{b}_1) = \delta_{i,2}\frac{p}{q}\boldsymbol{R}_j \cdot \boldsymbol{b}_1, \tag{B.22}$$

which clearly vanishes when $j = 2$. Otherwise,

$$\boldsymbol{a}_i \cdot \boldsymbol{A}(\boldsymbol{R}_1) = \delta_{i,2}\frac{p}{q}\left(\begin{cases} \left(q\boldsymbol{a}_1 - \frac{q}{2}\boldsymbol{a}_2\right) \cdot \boldsymbol{b}_1 & q \text{ even} \\ \left(q\boldsymbol{a}_1 - \frac{q-1}{2}\boldsymbol{a}_2\right) \cdot \boldsymbol{b}_1 & q \text{ odd} \end{cases}\right) = 2\pi p\delta_{i,2}, \tag{B.23}$$

so that, indeed, in either case:

$$\boldsymbol{a}_i \cdot \boldsymbol{A}(\boldsymbol{R}_j) \in 2\pi\mathbb{Z}. \tag{B.24}$$

Specializing to the case $(p, q) = (1, 2)$ relevant to the main text, we plot the resulting hopping amplitudes Eq. (B.16) in Fig. B.1(a) for the YC parameterization of the 2D lattice. The hoppings only take values in $\{\pm 1, \pm i\}$ and are evidently periodic in both $\boldsymbol{R}_1$ and $\boldsymbol{R}_2$.

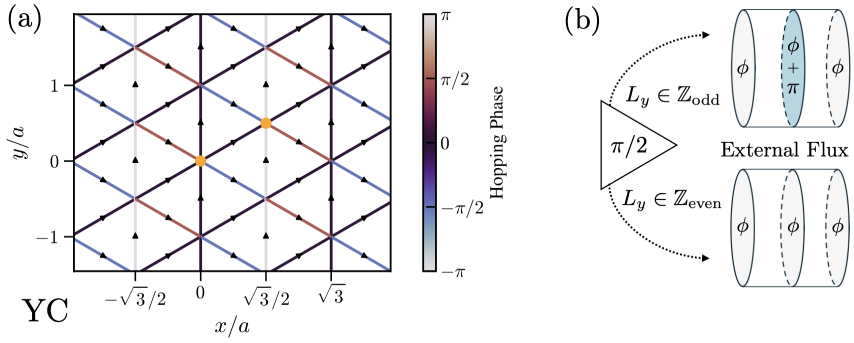

Figure B.1: (a) Graphical depiction of the complex phases of the nearest-neighbor hopping amplitudes of Eq. (B.16) for the $(p, q) = (1, 2)$ two-band Hamiltonian in the *2D plane*, where the orientation of the plane is consistent with the YC coordinate system specified by Eqs. (B.1,B.6). The two orange dots indicate the two sites in the magnetic unit cell. Note that the top/bottom and right/left edges are *not* implicitly identified. (b) Graphical depiction of the fluxes through adjacent loops of the YC-L_y cylinder defined in Sec. B.1. The outside surface of each cylindrical segment has a total area of $2L_y$ triangles, each of which has $\pi/2$ flux [pictured]. When L_y is odd [upper scenario], this leads to a π-staggering of the flux through each ring due to Gauss' law. When L_y is even [lower scenario], the flux through each ring is the same.

B.2 Threading flux

Affine-linear vector potential implementation

When dimensionally-reducing the lattice system to the cylinder, the charge and spin flux through the cross sections of the cylinder distinguish gauge-inequivalent systems. This additional flux can be implemented by adding a constant offset to the vector potential:

$$\boldsymbol{A}(\boldsymbol{r}) \longrightarrow \boldsymbol{A}_\phi(\boldsymbol{r}) = \boldsymbol{A}(\boldsymbol{r}) + \phi \frac{\boldsymbol{b}_2}{2\pi L_y}, \tag{B.25}$$

where

$$\phi = \phi_q + \frac{\sigma_z}{2}\phi_s. \tag{B.26}$$

This modifies the hopping elements by

$$t_{\boldsymbol{r}+\boldsymbol{\delta}\leftarrow\boldsymbol{r}} \longrightarrow t^{\phi}_{\boldsymbol{r}+\boldsymbol{\delta}\leftarrow\boldsymbol{r}} = t_{\boldsymbol{r}+\boldsymbol{\delta}\leftarrow\boldsymbol{r}} \exp\left(i\frac{\phi}{2\pi}\frac{\boldsymbol{b}_2\cdot\boldsymbol{\delta}}{L_y}\right). \tag{B.27}$$

Since we made the choice $\boldsymbol{A} \propto \boldsymbol{b}_2$ for the original vector potential (in the absence of flux threading), then this is equivalent to a shift in the origin:

$$\boldsymbol{A}_\phi(\boldsymbol{r}) = \boldsymbol{A}(\boldsymbol{r} + \boldsymbol{X}_\phi) = \boldsymbol{A}(\boldsymbol{r}) + \frac{\Phi}{(2\pi)^2}(\boldsymbol{X}_\phi \cdot \boldsymbol{b}_1)\boldsymbol{b}_2, \tag{B.28}$$

where

$$\boldsymbol{X}_\phi = \frac{\phi \boldsymbol{a}_1}{\Phi L_y}. \tag{B.29}$$

Twisted boundary condition implementation

For the purposes of numerical implementation, particularly in hybrid space where we trade y for k_y, it is convenient to instead implement flux threading via a twist in the boundary conditions. Starting with periodic boundary conditions for the fermion operators at $\phi = 0$, namely $c^\dagger(\boldsymbol{r} + L_y\boldsymbol{a}_2) = c^\dagger(\boldsymbol{r})$, we define a new set of operators

$$c^\dagger_\phi(\boldsymbol{r}) = c^\dagger(\boldsymbol{r}) \exp(iy\phi/L_y) = c^\dagger(\boldsymbol{r}) \exp\left(i\phi \frac{\boldsymbol{b}_2 \cdot \boldsymbol{r}}{2\pi L_y}\right). \tag{B.30}$$

Then instead of implementing Eq. (B.25), we can instead replace every instance of c in the second-quantized interacting Hamiltonian with c_ϕ. This does not affect terms that depend solely on charge and spin densities, *e.g.*, the Hubbard interaction. However, it modifies the hoppings in a way that is equivalent to Eq. (B.25). Under the operator replacement, the hoppings are replaced by

$$c^\dagger(\boldsymbol{r} + \boldsymbol{\delta}) t_{\boldsymbol{r}+\boldsymbol{\delta}\leftarrow\boldsymbol{r}} c(\boldsymbol{r}) \longrightarrow c^\dagger_\phi(\boldsymbol{r} + \boldsymbol{\delta}) t_{\boldsymbol{r}+\boldsymbol{\delta}\leftarrow\boldsymbol{r}} c_\phi(\boldsymbol{r}) \tag{B.31}$$

$$= c^\dagger(\boldsymbol{r} + \boldsymbol{\delta}) \exp\left(i\phi \frac{\boldsymbol{b}_2 \cdot (\boldsymbol{r} + \boldsymbol{\delta})}{2\pi L_y}\right) t_{\boldsymbol{r}+\boldsymbol{\delta}\leftarrow\boldsymbol{r}} \exp\left(-i\phi \frac{\boldsymbol{b}_2 \cdot \boldsymbol{r}}{2\pi L_y}\right) c(\boldsymbol{r}) \tag{B.32}$$

$$= c^\dagger(\boldsymbol{r} + \boldsymbol{\delta}) \exp\left(i \frac{\phi}{2\pi} \frac{\boldsymbol{b}_2 \cdot \boldsymbol{\delta}}{L_y}\right) t_{\boldsymbol{r}+\boldsymbol{\delta}\leftarrow\boldsymbol{r}} c(\boldsymbol{r}), \tag{B.33}$$

which is exactly equivalent to Eq. (B.27). To see that Eq. (B.30) corresponds to a twisting of the boundary condition on the fermion operators, we note that

$$c^\dagger_\phi(\boldsymbol{r} + L_y\boldsymbol{a}_2) = c^\dagger(\boldsymbol{r} + L_y\boldsymbol{a}_2) \exp\left(i\phi \frac{\boldsymbol{b}_2 \cdot (\boldsymbol{r} + L_y\boldsymbol{a}_2)}{2\pi L_y}\right) = c^\dagger_\phi(\boldsymbol{r}) \exp(i\phi). \tag{B.34}$$

The utility of this alternative formulation is that it leads to a clean numerical implementation upon fourier transforming $y \to k_y$. In particular, note that $(x, y) = (\boldsymbol{r}\cdot\boldsymbol{b}_1/2\pi, \boldsymbol{r}\cdot\boldsymbol{b}_2/2\pi)$ and define

$$c^\dagger_\phi(x, k_y) = \frac{1}{\sqrt{L_y}} \sum_y e^{-ik_y y} c^\dagger_\phi(x, y) \iff c^\dagger_\phi(x, y) = \frac{1}{\sqrt{L_y}} \sum_{k_y} e^{ik_y y} c^\dagger_\phi(x, k_y). \tag{B.35}$$

Note that this is the Fourier convention of TeNPy. When we express the Hamiltonian in the hybrid xk_y representation, we find that all that is required is to *shift the allowed values of* k_y. To see this, we impose the twisted boundary condition Eq. (B.34) on the Fourier-expanded operators:

$$\frac{1}{\sqrt{L_y}}\sum_{k_y} e^{ik_y(y+L_y)}c_\theta^\dagger(x,k_y) = \frac{1}{\sqrt{L_y}}\sum_{k_y} e^{ik_y y}c_\theta^\dagger(x,k_y)e^{i\phi}, \tag{B.36}$$

so that

$$e^{ik_y L_y} = e^{i\phi}. \tag{B.37}$$

The allowed values of momenta are therefore quantized to

$$k_y = \frac{2\pi}{L_y}\left(n + \frac{\phi_q}{2\pi} + \frac{\sigma_z\phi_s}{4\pi}\right), \qquad n \in \mathbb{Z}, \tag{B.38}$$

which are shifted relative to the $\phi = 0$ case. When the original Hamiltonian $\hat{H}_{\phi=0}$ is written in hybrid space, some coefficients will depend on k. The only effect of the replacement Eq. (B.30) is then for those coefficients to instead be evaluated on these shifted set of allowed values [107].

B.3 Two-band hopping Hamiltonian

Hamiltonian at $(p, q) = (1, 2)$

Now let us specialize to the YC lattice geometry and to the case $(p, q) = (1, 2)$, which corresponds to $\Phi_\triangle = \pi/2$. To specify the unit cells (which each contain two sites), we write $x = \tau + 2u$, where $u \in \mathbb{Z}$, while $\tau \in \{0, 1\}$ specifies the even/odd rings. With periodic boundary conditions and absent any flux insertion, the hoppings Eq. (B.16) take the particular form

$$\begin{aligned} t_{(x,y+1)\leftarrow(x,y)} &= t\exp\left(i\boldsymbol{A}\left(x\boldsymbol{a}_1 + y\boldsymbol{a}_2 + \frac{\boldsymbol{a}_2}{2}\right)\cdot\boldsymbol{a}_2\right) \\ &= t\exp\left(\frac{i}{4\pi}\left(x\boldsymbol{a}_1 + y\boldsymbol{a}_2 + \frac{\boldsymbol{a}_2}{2}\right)\cdot\boldsymbol{b}_1\boldsymbol{b}_2\cdot\boldsymbol{a}_2\right) \\ &= t\exp\left(i\pi x\right), \end{aligned} \tag{B.39}$$

$$\begin{aligned} t_{(x+1,y)\leftarrow(x,y)} &= t\exp\left(i\boldsymbol{A}\left(\frac{\boldsymbol{a}_1}{2} + x\boldsymbol{a}_1 + y\boldsymbol{a}_2\right)\cdot\boldsymbol{a}_1\right) \\ &= t, \end{aligned} \tag{B.40}$$

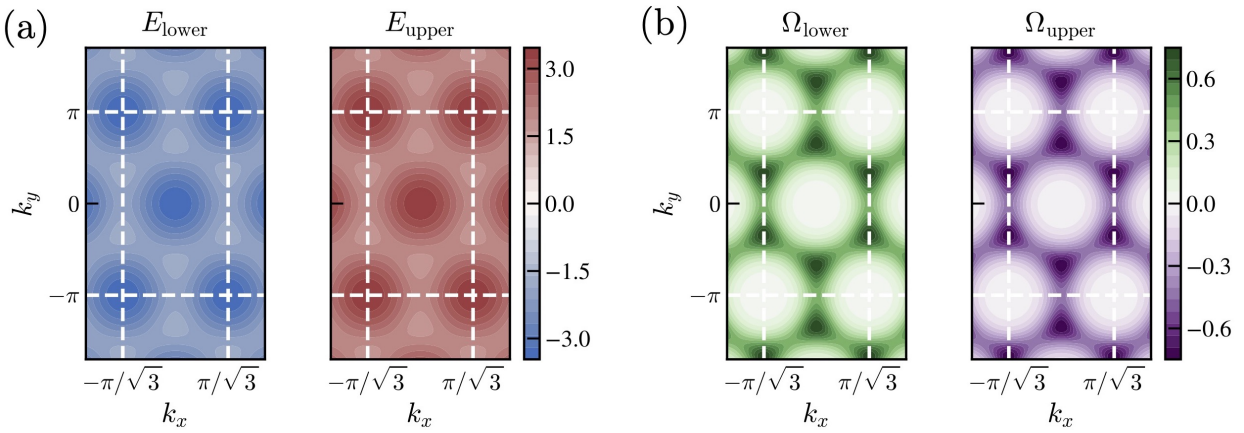

Figure B.2: (a) Plot of the lower and upper energy bands of the Hofstadter system with $(p, q) = (1, 2)$, corresponding to the case with $\Phi_\triangle = \pi/2$ considered throughout the main text. Momenta are given within the first "magnetic" Brillouin zone, defined with respect to the magnetic reciprocal vectors of Eq. (B.7) in the 2D planar YC coordinate system of Eq. (B.2). (b) Plot of the Berry curvature of the aforementioned bands which, like their energy, is equal and opposite at every momentum. The bands carry opposite Chern numbers ± 1.

$$\begin{aligned} t_{(x+1,y-1)\leftarrow(x,y)} &= t \exp\left(i\boldsymbol{A}\left(\frac{\boldsymbol{a}_1 - \boldsymbol{a}_2}{2} + x\boldsymbol{a}_1 + y\boldsymbol{a}_2 \right) \cdot (\boldsymbol{a}_1 - \boldsymbol{a}_2) \right) \\ &= t \exp\left(-i\boldsymbol{A}\left(\frac{\boldsymbol{a}_1 - \boldsymbol{a}_2}{2} + x\boldsymbol{a}_1 + y\boldsymbol{a}_2 \right) \cdot \boldsymbol{a}_2 \right) \\ &= t \exp\left(-i\pi(x + 1/2) \right), \end{aligned} \tag{B.41}$$

as shown graphically in Fig. B.1(a). We depict the resulting energy bands $E_{\text{lower/upper}}(\boldsymbol{k})$ in Fig. B.2, as well as their corresponding Berry curvature $\Omega_{\text{lower/upper}}(\boldsymbol{k})$, in the YC coordinate system consistent with Eqs. (B.2) and (B.7). The energies are equal and opposite at every momentum and are gapped everywhere in the Brillouin zone. The Berry curvature is also everywhere equal and opposite, with the Chern numbers evaluating to $+1$ for the lower band and -1 for the upper band.

Symmetries in the 2D plane

Magnetic translations

Recall that we designed the vector potential so that the Hamiltonian would be invariant under T_y translations, *i.e.*, in the circumferential direction $\boldsymbol{a}_2$, defined as

$$T_y c^\dagger_{\boldsymbol{r}} T_y^{-1} = c^\dagger_{\boldsymbol{r}+\boldsymbol{a}_2}. \tag{B.42}$$

To see this, note that

$$t_{\boldsymbol{r}+\boldsymbol{a}_2+\boldsymbol{\delta}\leftarrow\boldsymbol{r}+\boldsymbol{a}_2} = t\exp\left(i\boldsymbol{A}\left(\boldsymbol{r}+\boldsymbol{a}_2+\boldsymbol{\delta}/2\right)\cdot\boldsymbol{\delta}\right) \tag{B.43}$$
$$= t\exp\left(i\boldsymbol{A}\left(\boldsymbol{r}+\boldsymbol{\delta}/2\right)\cdot\boldsymbol{\delta}\right) \tag{B.44}$$
$$= t_{\boldsymbol{r}+\boldsymbol{\delta}\leftarrow\boldsymbol{r}}, \tag{B.45}$$

since $\boldsymbol{A}(\boldsymbol{a}_2) = 0$ by design. On the other hand, translation along $\boldsymbol{a}_1$ introduces an additional term:

$$t_{\boldsymbol{r}+\boldsymbol{a}_1+\boldsymbol{\delta}\leftarrow\boldsymbol{r}+\boldsymbol{a}_1} = t\exp\left(i\boldsymbol{A}\left(\boldsymbol{a}_1+\boldsymbol{r}+\boldsymbol{\delta}/2\right)\cdot\boldsymbol{\delta}\right) \tag{B.46}$$
$$= \exp\left(i\boldsymbol{A}\left(\boldsymbol{a}_1\right)\cdot\boldsymbol{\delta}\right)t_{\boldsymbol{r}+\boldsymbol{\delta}\leftarrow\boldsymbol{r}} \tag{B.47}$$
$$= \exp\left(\frac{i}{2}\boldsymbol{b}_2\cdot\boldsymbol{\delta}\right)t_{\boldsymbol{r}+\boldsymbol{\delta}\leftarrow\boldsymbol{r}}. \tag{B.48}$$

This affects the hoppings in directions with some weight along $\boldsymbol{\delta} = \boldsymbol{a}_2$ and, by comparison to Eq. (B.29) above, corresponds to threading $\phi = \pi L_y$ through the cylinder. In the 2D plane geometry—and on cylinder geometries of even circumference as we'll later show—the Hamiltonian can be restored by composing the bare T_x with a large gauge transformation. In particular, define the magnetic translation operation by

$$T_x c^\dagger_{\boldsymbol{r}}(T_x)^{-1} = c^\dagger_{\boldsymbol{r}+\boldsymbol{a}_1}\exp\left(\frac{i}{2}\boldsymbol{b}_2\cdot\boldsymbol{r}\right) = c^\dagger_{\boldsymbol{r}+\boldsymbol{a}_1}(-1)^y, \tag{B.49}$$

so that

$$T_x\hat{h}(T_x)^{-1} = T_x\left(\sum c^\dagger_{\boldsymbol{r}+\boldsymbol{\delta}}t_{\boldsymbol{r}+\boldsymbol{\delta}\leftarrow\boldsymbol{r}}c_{\boldsymbol{r}}\right)(T_x)^{-1} \tag{B.50}$$
$$= \sum\exp\left(\frac{i}{2}\boldsymbol{b}_2\cdot(\boldsymbol{r}+\boldsymbol{\delta})\right)c^\dagger_{\boldsymbol{r}+\boldsymbol{a}_1+\boldsymbol{\delta}}t_{\boldsymbol{r}+\boldsymbol{\delta}\leftarrow\boldsymbol{r}}c_{\boldsymbol{r}+\boldsymbol{a}_1}\exp\left(-\frac{i}{2}\boldsymbol{b}_2\cdot\boldsymbol{r}\right) \tag{B.51}$$
$$= \sum c^\dagger_{\boldsymbol{r}+\boldsymbol{a}_1+\boldsymbol{\delta}}\left(\exp\left(\frac{i}{2}\boldsymbol{b}_2\cdot\boldsymbol{\delta}\right)t_{\boldsymbol{r}+\boldsymbol{\delta}\leftarrow\boldsymbol{r}}\right)c_{\boldsymbol{r}+\boldsymbol{a}_1} \tag{B.52}$$
$$= \sum c^\dagger_{\boldsymbol{r}+\boldsymbol{a}_1+\boldsymbol{\delta}}t_{\boldsymbol{r}+\boldsymbol{a}_1+\boldsymbol{\delta}\leftarrow\boldsymbol{r}+\boldsymbol{a}_1}c_{\boldsymbol{r}+\boldsymbol{a}_1} \tag{B.53}$$
$$= \hat{h}, \tag{B.54}$$

where the second-last equality follows from Eq. (B.48) above.

Particle-hole

Consider the most naive definition of the particle-hole operation:

$$\tilde{\mathcal{P}}c^\dagger(\boldsymbol{r})\tilde{\mathcal{P}}^{-1} = c(\boldsymbol{r}), \qquad \tilde{\mathcal{P}}i\tilde{\mathcal{P}}^{-1} = +i, \tag{B.55}$$

where the second condition specifies that it is a linear (as opposed to anti-linear) unitary many-body operator. If 1 and 2 denote an adjacent pair of sites, then this naive particle-hole operation acts as

$$\tilde{\mathcal{P}}(t_{12}c_1^\dagger c_2 + t_{12}^* c_2^\dagger c_1)\tilde{\mathcal{P}}^{-1} = t_{12}c_1 c_2^\dagger + t_{12}^* c_2 c_1^\dagger \tag{B.56}$$

$$= -t_{12}c_2^\dagger c_1 - t_{12}^* c_1^\dagger c_2 \tag{B.57}$$

$$= -t_{12}^* c_1^\dagger c_2 - t_{12}c_2^\dagger c_1, \tag{B.58}$$

so that it reverses the Peierl's phase and shifts it by π. On the triangular lattice, this modifies the flux through each elementary triangular plaquette as follows:

$$\Phi_\triangle \to -\Phi_\triangle + \pi. \tag{B.59}$$

Requiring that this operation leave the flux invariant modulo 2π, we find that we need

$$2\Phi_\triangle = \pi\,(2n+1)\,, \qquad n \in \mathbb{Z}. \tag{B.60}$$

This is consistent with the observation that the Hofstadter spectrum on the triangular lattice only has bands with opposite energy for these values of $\Phi_\triangle$. In particular, in this work we consider $\Phi_\triangle = \pi/2$. We find at each momentum $\boldsymbol{k}$ that both the energy and Berry curvature are exactly opposite, with the bands having Chern number ± 1.

For a generic choice of Peierls' hopping phases consistent with this uniform magnetic flux, the naive particle-hole operation must be composed with a gauge transformation in order to exactly restore all the hopping elements. Given the particular form of the hoppings Eq. (B.39) to Eq. (B.41) for the two-band model, one may easily confirm that the following form of the particle-hole operation leaves the Hamiltonian invariant:

$$\mathcal{P}c^\dagger(\boldsymbol{r})\mathcal{P}^{-1} = (-1)^{x+y}c^{\mathsf{T}}(\boldsymbol{r}), \qquad \mathcal{P}i\mathcal{P}^{-1} = +i, \tag{B.61}$$

where T is the transposition operation on the row vector of electronic annihilation operators (indexed by spin).

To obtain the form of the particle-hole symmetry presented in the main text, we compose the version in Eq. (B.61) with a conventional spin rotation:

$$\mathcal{P}c_{x,y}^\dagger\mathcal{P}^{-1} = (-1)^{x+y}c_{x,y}^{\mathsf{T}}(i\sigma_y), \quad \mathcal{P}i\mathcal{P}^{-1} = +i. \tag{B.62}$$

The spin rotation is chosen so that the spin operator

$$S_\alpha(\boldsymbol{r}) = \frac{1}{2}c^\dagger(\boldsymbol{r})\sigma_\alpha c(\boldsymbol{r}) \tag{B.63}$$

is left invariant. To see this, we note that the unitarity of $\mathcal{P}$ implies that $\mathcal{P}c(\boldsymbol{r})\mathcal{P}^{-1} = (-1)^{x+y}(-i\sigma_y)c^{\dagger\mathsf{T}}(\boldsymbol{r})$. This allows us to explicitly compute:

$$\mathcal{P}S_\alpha(\boldsymbol{r})\mathcal{P}^{-1} = \frac{1}{2}\mathcal{P}c^\dagger(\boldsymbol{r})\mathcal{P}^{-1}\sigma_\alpha\mathcal{P}c(\boldsymbol{r})\mathcal{P}^{-1} = \frac{1}{2}c^{\mathsf{T}}(\boldsymbol{r})\sigma_y\sigma_\alpha\sigma_y c^{\dagger\mathsf{T}}(\boldsymbol{r}). \tag{B.64}$$

When $\alpha \in \{x, z\}$ we acquire a minus sign but then obtain another from fermion anti-commutation when undoing the transposes. On the other hand, when $\alpha = y$ the Pauli matrices commute but the minus sign from fermion anti-commutation cancels with the fact that σ_y is an anti-symmetric matrix:

$$\mathcal{P} S_y(\boldsymbol{r}) \mathcal{P}^{-1} = \frac{1}{2} c_s(\boldsymbol{r}) (\sigma_y)_{ss'} c^\dagger_{s'}(\boldsymbol{r}) = -\frac{1}{2} c^\dagger_{s'}(\boldsymbol{r}) (\sigma_y)_{ss'} c_s(\boldsymbol{r}) = +S_y(\boldsymbol{r}). \tag{B.65}$$

Fate of Symmetries on Cylinder

Particle-hole

Let us interrogate whether placing the system on a YC-L_y cylinder explicitly breaks particle-hole symmetry. We may use the naive definition of particle-hole Eq. (B.55) because the fluxes in question are gauge-invariant quantities. Focusing on a particular cylinder ring r penetrated with Φ_r flux, note that

$$\tilde{\mathcal{P}} : \Phi_r \mapsto \begin{cases} -\Phi_r & L_y \text{ even}, \\ -\Phi_r + \pi & L_y \text{ odd}. \end{cases} \tag{B.66}$$

Therefore, $\tilde{\mathcal{P}}$ is a symmetry (up to a gauge transformation) when, for all rings r, we have that

$$\Phi_r \in \begin{cases} \pi\mathbb{Z} & L_y \text{ even}, \\ \frac{\pi}{2} + \pi\mathbb{Z} & L_y \text{ odd}, \end{cases} \tag{B.67}$$

When L_y is even, Gauss's law dictates that the fluxes Φ_{r_1} and Φ_{r_2} through two adjacent rings $r_{1,2}$ must be equal. Note that this allows T_x to be a symmetry (up to a gauge transformation). Therefore, possibly after threading ϕ external flux through each ring of the cylinder, it is possible to tune all the Φ_r simultaneously (to 0 or π) so that $\tilde{\mathcal{P}}$ is respected. Only in those cases is $T_x \tilde{\mathcal{P}}$ also a symmetry (up to gauge).

On the other hand, when L_y is odd, Gauss's law instead dictates that

$$\Phi_{r_2} - \Phi_{r_1} = \pi \qquad \mod 2\pi. \tag{B.68}$$

This always rules out T_x as a symmetry. However, so long as Φ_{r_1} is $\pi/2$ or $-\pi/2$, both Eqs. (B.67) and (B.68) can be respected, so that $\tilde{\mathcal{P}}$ is a symmetry (up to gauge). However, odd L_y is special in that if we tune Φ_{r_1} to 0 or π, then $T_x \tilde{\mathcal{P}}$ is a symmetry (up to gauge) even though neither T_x nor $\tilde{\mathcal{P}}$ is individually a symmetry.

Magnetic translations

As discussed above, when L_y is even, the external magnetic flux through all the plaquettes and loops of the cylinder are consistent with a translation symmetry. In particular, this

generally requires composing a bare translation with a gauge transformation. In contrast, the effect of translations on the fluxes through loops cannot be gauged away when L_y is odd (see Fig. B.1b). Mathematically, this manifests in the fact that T_x [see Eq. (B.49)] is ill-defined, *i.e.*, not single-valued in the coordinate y. Thus, any gauge transformation which modifies T_x and T_y while preserving the property that they anti-commute will also fail to be single-valued.

B.4 Operators in the Hybrid xk_y Representation

Ring-Averaged Nearest-Neighbour Hopping

In our analysis of the transition, it is useful to study nearest-neighbour hoppings and their correlations. Since the states of interest are translation-invariant, namely around the cylinder circumference, we are motivated to study the *ring-averaged* correlation functions. For each nearest-neighbour lattice displacement

$$\boldsymbol{\delta} \in \{\pm\boldsymbol{a}_1, \pm\boldsymbol{a}_2, \pm(\boldsymbol{a}_1 - \boldsymbol{a}_2)\}, \tag{B.69}$$

let us define

$$d^\dagger_{\boldsymbol{\delta}}(x) = \frac{1}{L_y}\sum_y c^\dagger(x,y)c((x,y)+\boldsymbol{\delta}). \tag{B.70}$$

By Eq. (B.35),

$$d^\dagger_{\boldsymbol{\delta}}(x) = \frac{1}{L_y^2}\sum_y\sum_{k,k'} e^{iky}e^{-ik'(y+\delta_y)}c^\dagger(x,k)c(x+\delta_x,k') \tag{B.71}$$

$$= \frac{1}{L_y^2}\sum_y\sum_{k,k'} e^{i(k-k')y}e^{-ik'\delta_y}c^\dagger(x,k)c(x+\delta_x,k') \tag{B.72}$$

$$= \frac{1}{L_y}\sum_k e^{-ik\delta_y}c^\dagger(x,k)c(x+\delta_x,k), \tag{B.73}$$

so that

$$d^\dagger_{\boldsymbol{a}_1}(x) = \frac{1}{L_y}\sum_k c^\dagger(x,k)c(x+1,k) \tag{B.74}$$

$$d^\dagger_{-\boldsymbol{a}_1}(x) = \frac{1}{L_y}\sum_k c^\dagger(x,k)c(x-1,k) \tag{B.75}$$

$$d^\dagger_{\boldsymbol{a}_2}(x) = \frac{1}{L_y}\sum_k e^{-ik}c^\dagger(x,k)c(x,k) \tag{B.76}$$

$$d^\dagger_{-\boldsymbol{a}_2}(x) = \frac{1}{L_y}\sum_k e^{+ik}c^\dagger(x,k)c(x,k), \tag{B.77}$$

and similarly for $\boldsymbol{\delta} = \pm(\boldsymbol{a}_1 - \boldsymbol{a}_2)$.

Staggered Heisenberg Order Parameter

The following documents the numerical computation of the staggered Heisenberg order parameter in the hybrid xk_y fermion representation. The spin correlation operator $\vec{S}_i \cdot \vec{S}_j$ can be expressed in terms of fermionic operators by first noting that

$$S_i^+ = c_{i\uparrow}^\dagger c_{i\downarrow}, \quad S_i^- = c_{i\downarrow}^\dagger c_{i\uparrow}, \quad S_i^z = \frac{1}{2}(c_{i\uparrow}^\dagger c_{i\uparrow} - c_{i\downarrow}^\dagger c_{i\downarrow}). \tag{B.78}$$

The spin correlation operator $\vec{S}_i \cdot \vec{S}_j$ can then be written in terms of these fermion operators as:

$$\vec{S}_i \cdot \vec{S}_j = \frac{1}{2}\left(c_{i\uparrow}^\dagger c_{i\downarrow} c_{j\downarrow}^\dagger c_{j\uparrow} + c_{i\downarrow}^\dagger c_{i\uparrow} c_{j\uparrow}^\dagger c_{j\downarrow}\right) + S_i^z S_j^z. \tag{B.79}$$

Next, we express the staggered-Heisenberg order parameter in the hybrid (x, k_y) operator representation, where x indexes cylinder rings. Because of translation invariance around the cylinder, it is useful to define the y-averaged inter-ring NN Heisenberg operator

$$\mathcal{O}_{\mathrm{H}}(x) = \frac{1}{L_y}\sum_y \sum_{a=x,y,z} S^a(x,y) S^a(x+1,y), \tag{B.80}$$

where

$$S^a(x,y) = c^\dagger(x,y)\frac{\sigma^a}{2}c(x,y) = \frac{1}{L_y}\sum_{k,k'} e^{i(k-k')y} c^\dagger(x,k)\frac{\sigma^a}{2}c(x,k'). \tag{B.81}$$

Since both the IQH and CSL ground states exhibit a two-ring translation invariance (*i.e.*, are invariant under $(T_x)^2$ in addition to T_y) then we can measure the local order parameter

$$\mathcal{O}_0^{\delta\mathrm{Heis}} = \mathcal{O}_{\mathrm{H}}(0) - \mathcal{O}_{\mathrm{H}}(1). \tag{B.82}$$

In general, the hybrid representation reads

$$\begin{aligned}
\mathcal{O}_{\mathrm{H}}(x) &= \frac{1}{L_y}\sum_y \sum_{a=x,y,z} S^a(x,y) S^a(x+1,y) \\
&= \frac{1}{L_y^2}\sum_{a=x,y,z}\sum_{k,k'}\sum_{p,p'}\left(\frac{1}{L_y}\sum_y e^{i(k-k'+p-p')y}\right) \\
&\qquad \times c^\dagger(x,k)\frac{\sigma^a}{2}c(x,k')\cdot c^\dagger(x+1,p)\frac{\sigma^a}{2}c(x+1,p') \\
&= \frac{1}{L_y^2}\sum_{a=x,y,z}\sum_{k,k'}\sum_{p,p'} c^\dagger(x,k)\frac{\sigma^a}{2}c(x,k')\cdot c^\dagger(x+1,p)\frac{\sigma^a}{2}c(x+1,k-k'+p).
\end{aligned}$$

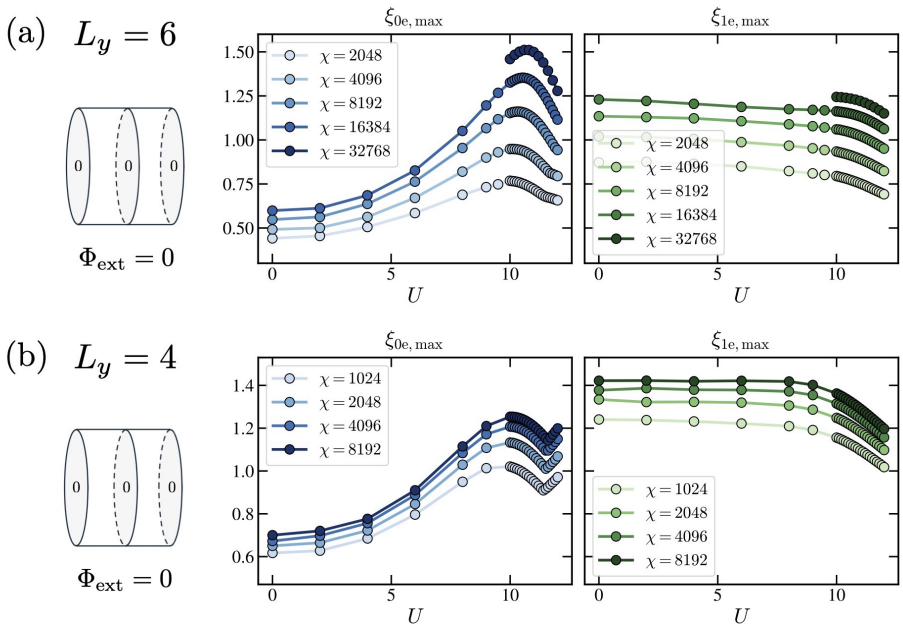

Figure B.3: (a) Plot of the maximum correlation length in the charge-0e [middle panel] and charge-1e [right panel] sectors of the ground state transfer matrix for the YC6 geometry, with bond dimensions increasing light-to-dark. Left illustration: depiction of the flux through the various cylinder rings, consistent with no externally-threaded magnetic flux. (b) Same for YC4.

B.5 Even-circumference Supplementary Data

Reproducing Correlation Lengths of Kuhlenkamp *et al.*

Here we briefly comment on additional data concerning the correlation lengths for geometries not already highlighted in the main text. In particular, Fig. B.3 shows correlation length data for the $L_y = 4$ and 6 cylinders which are not threaded by external flux. In particular, $L_y = 6$ reproduces the behavior presented in Kuhlenkamp *et al.*, [118], pushed here to bond dimension $\chi = 32768$. We remark that the correlation lengths are much smaller than those with $\Phi_{\text{ext}} = \pi/2$ external flux, investigated and shown in the main text. However, there is no reason these two sequences of geometries will not tend to the same limit in 2D.

Flux-threaded System: Correlation Length Extrapolation for Main Text

To obtain the extrapolated correlation lengths shown in the main text, we employ a recently-developed method for extrapolating correlation lengths in DMRG [199, 205]. Namely, we

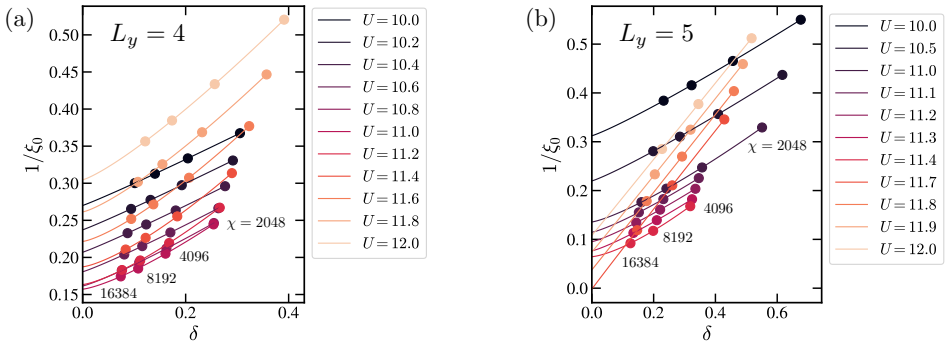

Figure B.4: (a) Inverse correlation length in the charge-neutral sector at $L_y = 4$ and $\Phi_{\text{ext}} = \pi/2$. The y-intercept of the fitted curve is the correlation length extrapolated to infinite bond dimension; the curve is obtained following the method in Ref. [205], as detailed in Sec. B.5, for a range of Hubbard strengths [different colors], sampled from a sequence of increasing bond dimensions [same-colored points moving sequentially to the left]. The extrapolated inverse correlation length saturates at a minimum value exceeding 0.15, *i.e.*, the correlation length is bounded above by 6.6 ring spacings. (b) The same for $L_y = 5$ and $\Phi_{\text{ext}} = 0$.

compute several of the largest eigenvalues of the transfer matrix $TX_i = \lambda_i X_i$ in the electric charge $Q_E = 1$ sector for each k_y, and select those from the same "excitation branch" [205], namely carrying a consistent complex phase. These are related to the correlation lengths as

$$\epsilon_i = 1/\xi_i = -\log|\lambda_i| \tag{B.83}$$

with $\epsilon_i \leq \epsilon_{i+1}$. We report ξ in units of cylinder rings, or equivalently $u = a\sqrt{3}/2$ where a is the lattice spacing of the underlying triangular lattice. Correspondingly, ϵ is reported in units of u^{-1}. For a system that is gapped in a charge sector $q = (Q, S_z, k_y)$, both $\epsilon_1^q, \epsilon_2^q$ converge to the same infinite value as $\chi \to \infty$, namely the finite inverse correlation length. As a result, the quantity

$$\delta^q = \epsilon_2^q - \epsilon_1^q \tag{B.84}$$

vanishes at $\chi \to \infty$, serving as a good "scaling variable" that measures the deviation from convergence. To estimate $\xi(\chi \to \infty)$, we therefore compute $\epsilon(\delta)$ at each available $\epsilon(\chi), \delta(\chi)$ and extrapolate to $\delta = 0$ with a polynomial fit, namely

$$\epsilon(\delta) = a + b\delta^c. \tag{B.85}$$

This extrapolation is shown in Fig. B.4 for both $L_y = 4$ at $\Phi_{\text{ext}} = \pi/2$ and $L_y = 5$ at $\Phi_{\text{ext}} = 0$, yielding the extrapolated values shown in the main text. In both cases, the correlation length is computed in the $(Q, S_z, k_y) = 0$, which hosts largest correlation length.

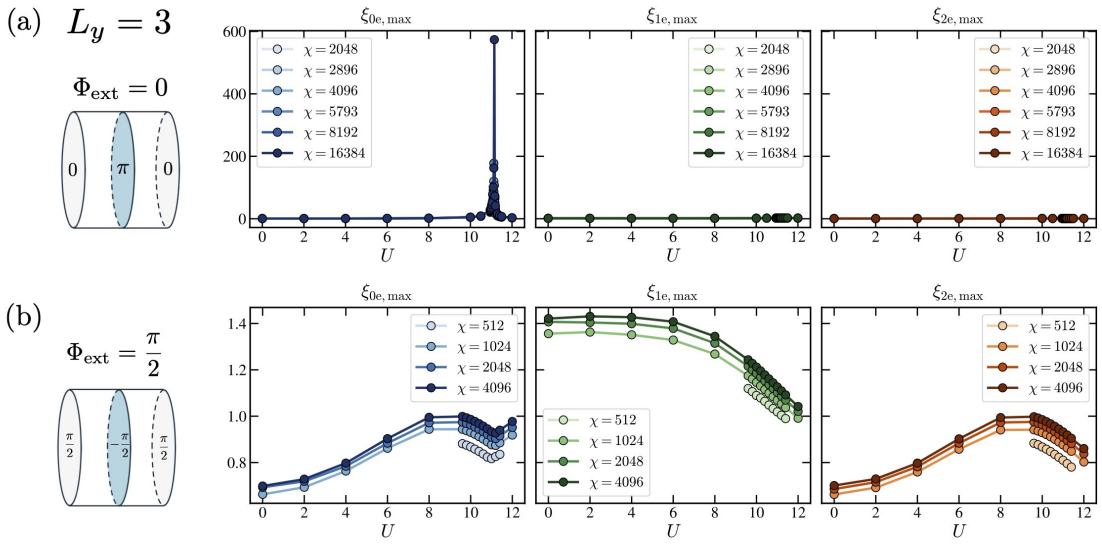

Figure B.5: (a) Plot of the maximum correlation length in the charge-0e, charge-1e, and charge-2e sectors of the ground state transfer matrix for the YC3 cylinder geometry, with bond dimensions increasing light-to-dark. Left illustration: depiction of the flux through the various cylinder rings, consistent with no externally-threaded magnetic flux, $\Phi_{\text{ext}} = 0$. (b) Same for the case $\Phi_{\text{ext}} = \pi/2$, for which the Hamiltonian explicitly breaks glide-PH symmetry and therefore does not exhibit SSB criticality.

B.6 Supplementary Odd-Circumference Analysis

YC3 Correlation Lengths

In Fig. B.5, we display the correlation lengths for the YC3 geometry. In particular, in panel (a) we provide data for the $\Phi_{\text{ext}} = 0$ case, which accompanies Fig. 3 of the main text. Here, the system respects glide-PH symmetry and, like the YC5 system with $\Phi_{\text{ext}} = 0$ studied in the main text, exhibits a symmetry-unbroken small-U phase and symmetry-broken larger-U phase. The transition between then is evidently continuous, featuring a diverging correlation length which reaches almost 600 ring spacings at the maximum bond dimension $\chi = 16384$ considered. In Fig. B.5(b), in contrast, threading Φ_{ext} explicitly breaks the glide-PH symmetry, which reduces the transition to a crossover with a small and wide peak in the correlation length.

Relation to Ionic Hubbard Chain

Here, we make more precise the relationship between the "ionic" Hubbard chain and our model on YC-L_y cylinders (with odd L_y and $\Phi_{\text{ext}} = 0$) *which possess glide-PH symmetry*. In particular, the former model can be thought of as a truly 1+1D version of the latter, *i.e.*,

a bipartite chain as opposed to a quasi-(1+1)D system with the hopping-connectivity of a cylinder. We first compare them at the level of symmetries. The ionic Hubbard Hamiltonian is defined as [396]:

$$H = -t \sum_{i,\sigma} (c^\dagger_{i,\sigma} c_{i+1,\sigma} + h.c.) + U \sum_i n_{i,\uparrow} n_{i,\downarrow} + \frac{\Delta}{2} \sum_{i,\sigma} (-1)^i n_{i,\sigma}. \tag{B.86}$$

The Hamiltonian is invariant under translation by two sites, with Δ being the potential energy difference between the two sublattice sites in the unit cell. Moreover, it is invariant under site-centered inversion (but not bond-centered inversion), time-reversal, and a "duality" symmetry that is the combination of particle-hole with a single-site translation [284]. These symmetries of the ionic Hubbard chain correspond to the following symmetries of our model: $(T_x)^2$, site-centered C_{2z}, $M_y\mathcal{T}$, and glide-PH $\mathcal{P}T_x$.

Remarkably, the two models are also similar at the level of their ground states. The small-U ground state phase of the ionic Hubbard chain is a fully-symmetric band insulator. Is it widely believed that the phase which appears next upon increasing U is a "spontaneously-dimerized" phase which spontaneously breaks the duality and site-centered inversion symmetries [284]. Moreover, as mentioned in the main text, it is believed that these two states are separated by a 2D Ising critical point. This Ising picture has been substantiated both by weak-coupling bosonization arguments [281, 282] and an effective strong-coupling effective spin model formulation [283]. However, at least one careful numerical study of the transition using finite DMRG finds features inconsistent with Ising criticality [397], though the numerical observations are still consistent with a gap to charged excitations and a gapless neutral sector [398]. These two phases should be identified with the odd-circumference (symmetry-respecting) IQH and (symmetry-breaking) CSL phases, respectively.

B.7 Correlation functions at even circumferences

In Fig. B.6 we show the even-L_y current-current, density-density, spin-spin, and electron-hole correlations specified in the main text. In Fig. 4 of the main text, we displayed these correlations on odd circumferences with $\Phi_{\text{ext}} = 0$, where we saw clear evidence of glide-PH SSB and associated critical correlations of the current, with more rapidly-decaying critical correlations of the charge density; the spin and electron correlators exhibited a clear gap.

Specifically, we study the $L_y = 4, 6$ systems with $\Phi_{\text{ext}} = \pi/2$ threaded flux, for which the MPS transfer matrix spectrum hosts a large correlation length for zero-momentum, charge-neutral correlations. Here we show that this is associated with significantly long-ranged (but still ultimately exponentially-decaying due to finite L_y) correlations of the circumferential current and charge density; see Fig. B.6(a,b). In the $L_y = 6$ case, the correlation function is still becoming significantly longer-ranged with bond dimension, in tandem with the continued rapid growth of the correlation length shown in Fig. 3 of the main text. Like at odd L_y, the spin-spin and electron-hole correlations decay exponentially, with no apparent enhancement from $L_y = 3$ to $L_y = 5$.

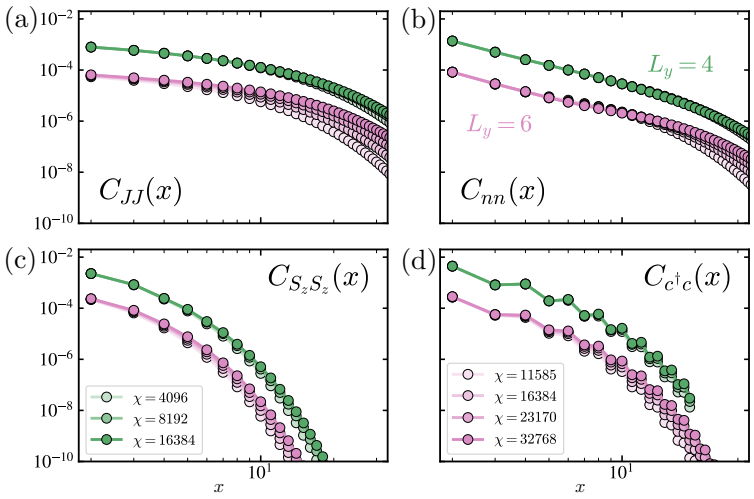

Figure B.6: For $L_y = 4, 6$ with $\Phi_{\text{ext}} = \pi/2$, and with the Hubbard interaction tuned to the values at which the correlation length is maximal at the largest available bond dimension (namely $U(L_y = 4) = 11.0$ and $U(L_y = 6) = 11.4$), we show the current-current, density-density, spin-spin, and electron-hole correlations, defined in the main text.

Appendix C

Appendix to Chapter 4

C.1 Coordinates, Gauge Choice and Symmetries

Triangular lattice coordinates

Here, we specify the Bravais vectors of the underlying triangular lattice (see Fig. 1(b) of the main text):

$$\boldsymbol{a}_1 = \hat{x}, \qquad \boldsymbol{a}_2 = \frac{\hat{x}}{2} + \frac{\hat{y}\sqrt{3}}{2} \tag{C.1}$$

where we've set the nearest-neighbour lattice bond length to unity, $a = 1$. The lattice points are then given by

$$\boldsymbol{r} = n_1\boldsymbol{a}_1 + n_2\boldsymbol{a}_2, \qquad n_i \in \mathbb{Z}, \tag{C.2}$$

We take the reciprocal lattice vectors to be

$$\boldsymbol{b}_1 = 2\pi\hat{x} - \frac{2\pi}{\sqrt{3}}\hat{y}, \qquad \boldsymbol{b}_2 = \frac{4\pi}{\sqrt{3}}\hat{y}. \tag{C.3}$$

Imaginary C_6 gauge

Fig. C.1(a) provides an electronic gauge in which the hoppings are purely imaginary *and* in which the C_6 symmetry acts in its bare form in real space:

$$C_6 c^\dagger_{\boldsymbol{r}} C_6^{-1} = c^\dagger_{C_6\boldsymbol{r}}, \tag{C.4}$$

provided that the (infinite 2D or torus) geometry is such that C_6 is well-defined. Thinking of a torus as a set of equivalence classes of points on the infinite plane, a well-defined spatial operation must map between equivalence classes. For example, by direction inspection, one can see that C_6 is ill-defined on the 4×2 torus.

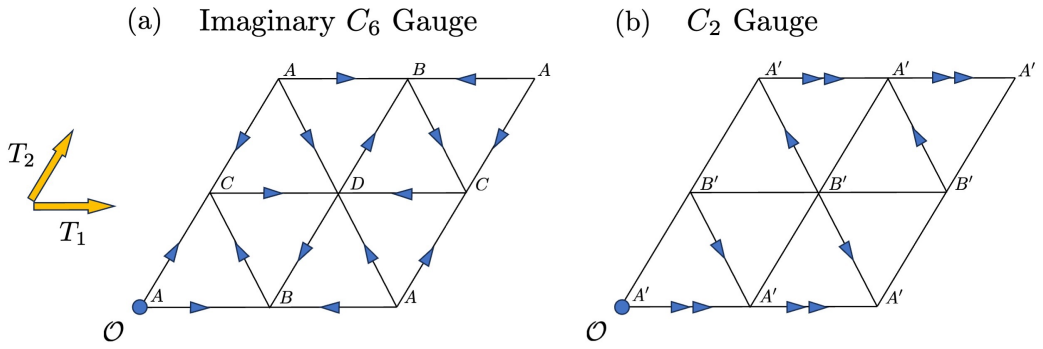

Figure C.1: Two gauge choices for the hopping Hamiltonian, in both cases giving rise to $\Phi_\triangle = \pi/2$ magnetic flux per triangular plaquette. (a) Hoppings in the "Imaginary C_6" gauge, which is manifestly C_6 symmetric about the origin [bottom left marked by $\mathcal{O}$]. The origin is chosen to coincide with the A sublattice (other sublattices B, C, D are also marked). Each arrow indicates a Peirel's phase of $+i$ in the direction of the arrow. This gauge choice is identical to that displayed in Fig. 1(b) of the main text, except there the origin is in the middle of the image. (b) Hoppings in the "C_2" gauge. All hoppings are either imaginary or real, with a single arrow again indicating a Peirel's phase of $+i$ in the direction of the arrow. There are two magnetic sublattices, A' and B'. For both (a) and (b): T_1 and T_2 (yellow arrows) denote translation symmetry in the unit directions $\boldsymbol{a}_1$ and $\boldsymbol{a}_2$, respectively. In App. C.1B we provide the explicit form of T_1 and T_2 in the Imaginary C_6 gauge.

By inspecting the phases of the hoppings in Fig. C.1(a), we read off

$$T_1 c^\dagger_{\boldsymbol{r}} T_1^{-1} = i(-1)^{n_1+n_2} c^\dagger_{\boldsymbol{r}+\boldsymbol{a}_1}, \qquad T_2 c^\dagger_{\boldsymbol{r}} T_2^{-1} = i(-1)^{n_2} c^\dagger_{\boldsymbol{r}+\boldsymbol{a}_2}, \tag{C.5}$$

where $\boldsymbol{r} = n_1\boldsymbol{a}_1 + n_2\boldsymbol{a}_2$ is the lattice point before the transformation. To see the former, note that only the hoppings parallel to $\boldsymbol{a}_1 - \boldsymbol{a}_2$ are left invariant by bare T_1, *i.e.*, the hoppings in the $\boldsymbol{a}_1$ and $\boldsymbol{a}_2$ directions pick up a minus sign that needs to be corrected. For the latter, bare T_2 instead negates the hoppings in the $\boldsymbol{a}_2$ and $\boldsymbol{a}_1 - \boldsymbol{a}_2$ directions. The factors i are chosen so that two-fold translation is a pure shift:

$$(T_j)^2 c^\dagger_{\boldsymbol{r}} (T_j)^{-2} = c^\dagger_{\boldsymbol{r}+2\boldsymbol{a}_j}. \tag{C.6}$$

But more importantly, the definitions (C.4) and (C.5) are chosen to be consistent with all the algebraic conditions laid out in Sec. 1 of the main text.

As a non-trivial check of correctness of these translations, we can show that they correctly anti-commute:

$$\begin{aligned}(T_1 \circ T_2)\cdot c^\dagger_{\boldsymbol{r}} &= -T_1 T_2 c^\dagger_{\boldsymbol{r}} T_2^{-1} T_1^{-1} && \text{(C.7)}\\ &= -(-1)^{n_2} T_1 c^\dagger_{\boldsymbol{r}+\boldsymbol{a}_2} T_1^{-1} && \text{(C.8)}\\ &= (-1)^{n_2}(-1)^{n_1+n_2} c^\dagger_{\boldsymbol{r}+\boldsymbol{a}_2+\boldsymbol{a}_1} && \text{(C.9)}\end{aligned}$$

compared to

$$(T_2 \circ T_1) \cdot c^\dagger_{\boldsymbol{r}} = -T_2 T_1 c^\dagger_{\boldsymbol{r}} T_1^{-1} T_2^{-1} \tag{C.10}$$
$$= -(-1)^{n_1+n_2} T_2 c^\dagger_{\boldsymbol{r}+\boldsymbol{a}_1} T_2^{-1} \tag{C.11}$$
$$= -(-1)^{n_1+n_2}(-1)^{n_2} c^\dagger_{\boldsymbol{r}+\boldsymbol{a}_1+\boldsymbol{a}_2}, \tag{C.12}$$

so that indeed $T_2T_1 = (-1)^{N_F} T_1T_2$.

The phases can be written in a more geometric form:

$$T_1 c^\dagger_{\boldsymbol{r}} T_1^\dagger = i e^{i\boldsymbol{r}\cdot(\boldsymbol{b}_1+\boldsymbol{b}_2)/2} c^\dagger_{\boldsymbol{r}+\boldsymbol{a}_1}, \qquad T_2 c^\dagger_{\boldsymbol{r}} T_2^\dagger = i e^{i\boldsymbol{r}\cdot\boldsymbol{b}_2/2} c^\dagger_{\boldsymbol{r}+\boldsymbol{a}_2}. \tag{C.13}$$

From these, we can also obtain

$$(T_1^\dagger T_2) c^\dagger_{\boldsymbol{r}} (T_1^\dagger T_2)^\dagger = e^{-i\boldsymbol{r}\cdot\boldsymbol{b}_1/2} c^\dagger_{\boldsymbol{r}-\boldsymbol{a}_1+\boldsymbol{a}_2}, \tag{C.14}$$

and by inverting the above three,

$$T_1^\dagger c^\dagger_{\boldsymbol{r}} T_1 = i e^{-i\boldsymbol{r}\cdot(\boldsymbol{b}_1+\boldsymbol{b}_2)/2} c^\dagger_{\boldsymbol{r}-\boldsymbol{a}_1} \tag{C.15}$$
$$T_2^\dagger c^\dagger_{\boldsymbol{r}} T_2 = i e^{-i\boldsymbol{r}\cdot\boldsymbol{b}_2/2} c^\dagger_{\boldsymbol{r}-\boldsymbol{a}_2} \tag{C.16}$$
$$(T_1^\dagger T_2)^\dagger c^\dagger_{\boldsymbol{r}} (T_1^\dagger T_2) = -e^{i\boldsymbol{r}\cdot\boldsymbol{b}_1/2} c^\dagger_{\boldsymbol{r}+\boldsymbol{a}_1-\boldsymbol{a}_2}. \tag{C.17}$$

From this we learn that $C_6 T_1 C_6^\dagger = T_2$:

$$(C_6 T_1 C_6^\dagger) c^\dagger_{\boldsymbol{r}} (C_6 T_1 C_6^\dagger)^\dagger = (C_6 T_1) c^\dagger_{C_6^{-1}\boldsymbol{r}} (C_6 T_1)^\dagger \tag{C.18}$$
$$= i C_6 e^{i C_6^{-1}\boldsymbol{r}\cdot(\boldsymbol{b}_1+\boldsymbol{b}_2)/2} c^\dagger_{C_6^{-1}\boldsymbol{r}+\boldsymbol{a}_1} C_6^\dagger \tag{C.19}$$
$$= i e^{i\boldsymbol{r}\cdot C_6(\boldsymbol{b}_1+\boldsymbol{b}_2)/2} c^\dagger_{\boldsymbol{r}+C_6\boldsymbol{a}_1} \tag{C.20}$$
$$= i e^{i\boldsymbol{r}\cdot\boldsymbol{b}_2/2} c^\dagger_{\boldsymbol{r}+\boldsymbol{a}_2} \tag{C.21}$$
$$= T_2 c^\dagger_{\boldsymbol{r}} T_2^\dagger. \tag{C.22}$$

Similarly, it can be shown that $T_3 = C_6 T_2 C_6^\dagger = (-i)^{N_F} T_1^\dagger T_2$ and $C_6 T_3 C_6^\dagger = T_1^\dagger$, which is altogether consistent with $C_2 T_j C_2 = (T_j)^\dagger$ for all j.

Closed-form composition of translation generators

Here we provide the closed form expression for powers of T_1 and T_2, namely

$$T_2^M c^\dagger_{\boldsymbol{r}} T_2^{-M} = i^M c^\dagger_{\boldsymbol{r}+M\boldsymbol{a}_2} \prod_{j=0}^{M-1} e^{i(\boldsymbol{r}+j\boldsymbol{a}_2)\cdot\boldsymbol{b}_2/2} \tag{C.23}$$
$$= i^M c^\dagger_{\boldsymbol{r}+M\boldsymbol{a}_2} e^{i\sum_{j=0}^{M-1}\boldsymbol{r}\cdot\boldsymbol{b}_2/2} e^{i\pi\sum_{j=0}^{M-1} j} \tag{C.24}$$
$$= i^M c^\dagger_{\boldsymbol{r}+M\boldsymbol{a}_2} e^{iM\boldsymbol{r}\cdot\boldsymbol{b}_2/2} e^{i\pi M(M-1)/2} \tag{C.25}$$
$$= c^\dagger_{\boldsymbol{r}+M\boldsymbol{a}_2} e^{iM\boldsymbol{r}\cdot\boldsymbol{b}_2/2} e^{i\pi M^2/2}, \tag{C.26}$$

and similarly

$$T_1^M c_{\boldsymbol{r}}^\dagger T_1^{-M} = i^M c_{\boldsymbol{r}+M\boldsymbol{a}_1}^\dagger \prod_{j=0}^{M-1} e^{i(\boldsymbol{r}+j\boldsymbol{a}_2)\cdot(\boldsymbol{b}_1+\boldsymbol{b}_2)/2} \tag{C.27}$$

$$= i^M c_{\boldsymbol{r}+M\boldsymbol{a}_1}^\dagger e^{iM\boldsymbol{r}\cdot(\boldsymbol{b}_1+\boldsymbol{b}_2)/2} e^{i\pi M(M-1)/2} \tag{C.28}$$

$$= c_{\boldsymbol{r}+M\boldsymbol{a}_1}^\dagger e^{iM\boldsymbol{r}\cdot(\boldsymbol{b}_1+\boldsymbol{b}_2)/2} e^{i\pi M^2/2}. \tag{C.29}$$

Then for two-electron operators, in particular, we obtain:

$$T_{\boldsymbol{M}} c_{\boldsymbol{r}}^\dagger c_{\boldsymbol{r}'}^\dagger T_{\boldsymbol{M}}^\dagger = T_2^{M_2} T_1^{M_1} c_{\boldsymbol{r}}^\dagger c_{\boldsymbol{r}'}^\dagger T_1^{-M_1} T_2^{-M_2} \tag{C.30}$$

$$= e^{i\pi M_1^2} e^{iM_1(\boldsymbol{r}+\boldsymbol{r}')\cdot(\boldsymbol{b}_1+\boldsymbol{b}_2)/2} T_2^{M_2} c_{\boldsymbol{r}+M_1\boldsymbol{a}_1}^\dagger c_{\boldsymbol{r}'+M_1\boldsymbol{a}_1}^\dagger T_2^{-M_2} \tag{C.31}$$

$$= e^{i\pi(M_1^2+M_2^2)} e^{iM_1(\boldsymbol{r}+\boldsymbol{r}')\cdot(\boldsymbol{b}_1+\boldsymbol{b}_2)/2} e^{iM_2(\boldsymbol{r}+M_1\boldsymbol{a}_1)\cdot\boldsymbol{b}_2/2} e^{iM_2(\boldsymbol{r}'+M_1\boldsymbol{a}_1)\cdot\boldsymbol{b}_2/2} c_{\boldsymbol{r}+\boldsymbol{M}}^\dagger c_{\boldsymbol{r}'+\boldsymbol{M}}^\dagger \tag{C.32}$$

$$= e^{i\pi(M_1^2+M_2^2)} e^{iM_1(\boldsymbol{r}+\boldsymbol{r}')\cdot(\boldsymbol{b}_1+\boldsymbol{b}_2)/2} e^{iM_2\boldsymbol{r}\cdot\boldsymbol{b}_2/2} e^{iM_2\boldsymbol{r}'\cdot\boldsymbol{b}_2/2} c_{\boldsymbol{r}+\boldsymbol{M}}^\dagger c_{\boldsymbol{r}'+\boldsymbol{M}}^\dagger. \tag{C.33}$$

C_2 gauge for XC geometries

Fig. C.1(b) displays the Hamiltonian hopping amplitudes that we employ for our calculations on the XC4 cylinder analyzed in the main text. In this gauge, the hoppings are real and imaginary. Moreover, the site-centered inversion symmetry is implemented as $C_2 c_{\boldsymbol{r}}^\dagger C_2^{-1} = c_{C_2\boldsymbol{r}}^\dagger$.

The lattice vector $\boldsymbol{a}_1$ points along the cylinder axis, while $2\boldsymbol{a}_2 - \boldsymbol{a}_1$ has length $\sqrt{3}$ and points along the circumference. For the XC4 infinite cylinder [107], the lattice and hoppings are repeated so that the cylinder has infinite length and circumference $2\sqrt{3}$. We also employ the hoppings of Fig. C.1(b) in Sec. C.4 below, where we calculate ground state correlation lengths on the XC4 and XC6 infinite cylinders at half filling.

C.2 U(1) Slave-Rotor Theory and Mean Field Estimate of the Transition Point

We utilize the slave-rotor approach [261, 326], introducing a U(1) rotor variable $e^{i\theta}$ and its conjugate integer-valued "angular momentum" L on each site and writing the electron operator as

$$c_{i,\sigma}^\dagger = f_{i,\sigma}^\dagger e^{i\theta_i}, \tag{C.34}$$

where f_σ is a fermionic "spinon" that carries the spin index. The Hilbert space redundancy introduced by the rotors is removed by requiring that each site satisfy a constraint:

$$L_i = \sum_\sigma \left(f_{i,\sigma}^\dagger f_{i,\sigma} - 1/2 \right). \tag{C.35}$$

Note that the singly-filled site is represented by $L_i = 0$, while the doublon/empty sites are $L_i = \pm 1$. The Hubbard model can then be rewritten as:

$$H = -\sum_{\langle ij\rangle,\sigma} t_{ij} e^{i(\theta_i-\theta_j)} f^\dagger_{i,\sigma} f_{j,\sigma} + \text{h.c.} + \frac{U}{2}\sum_i L_i^2, \tag{C.36}$$

supplemented with the constraint (C.35) and the commutation relation $\left[e^{i\theta_i},\, L_j\right] = -\delta_{ij} e^{i\theta_i}$.

Of course, treating everything exactly is tantamount to solving the original problem, but we can make progress by adopting a mean field approach, satisfying the constraint *on average* and assigning self-consistent expectation values to $\langle f^\dagger_{i,\sigma} f_{j,\sigma}\rangle$ and $\langle e^{i(\theta_i-\theta_j)}\rangle$. This gives us the mean field Hamiltonian:

$$\begin{aligned} H_{MF} &= H_f + H_\theta & \text{(C.37)}\\ H_f &= -\sum_{\langle ij\rangle,\sigma} t_{ij}\langle e^{i(\theta_i-\theta_j)}\rangle f^\dagger_{i,\sigma} f_{j,\sigma} + \text{h.c.} & \text{(C.38)}\\ H_\theta &= -\sum_{\langle ij\rangle,\sigma} t_{ij} e^{i(\theta_i-\theta_j)}\langle f^\dagger_{i,\sigma} f_{j,\sigma}\rangle + \text{h.c.} + \frac{U}{2}\sum_i L_i^2 & \text{(C.39)} \end{aligned}$$

Note that the constraint (C.35) implies gauge invariance, $\theta_i \to \theta_i + \epsilon_i$, $f_i^\dagger \to f_i^\dagger e^{-i\epsilon_i}$ which is broken by the mean field Hamiltonian. This is remedied by incorporating a fluctuating gauge field a on the links, though we shall not do that here.

In the limit of small Hubbard U, we expect the rotor fields to condense, $\langle e^{i\theta_i}\rangle = \sqrt{Z_i} \leq 1$, so that the spinons f are identified with the electron up to this prefactor. This phase possesses off-diagonal long-range order; at the mean-field level, we assume $\langle e^{i(\theta_i-\theta_j)}\rangle \approx \langle e^{i\theta_i}\rangle\langle e^{-i\theta_j}\rangle$. Thus, the gap to the electron excitation is obtained from the dispersion $t_{ij}\sqrt{Z_i Z_j} f_i^\dagger f_j$, which explains why the single-electron gap on the IQH side (*i.e.*, the condensed rotor phase) *decreases* on increasing U.

On the other side of the phase diagram, when U is sufficiently large, we have $\langle e^{i\theta_i}\rangle = 0$ and thus the electron excitation is distinct from the spinon. To create an electron, one must both create a spinon $f^\dagger$ *and* increase the rotor angular momentum by $\Delta L = 1$. Thus, due to the interaction term, this gap tracks U for large U. Despite the absence of an expectation value $\langle e^{i\theta_i}\rangle = 0$ on this side, there is virtual tunneling of the rotor quanta, so that $\langle e^{i(\theta_i-\theta_j)}\rangle = \beta_{ij} \neq 0$ for neighboring sites [399]. In fact, this expectation value is expected to scale as $|t|/U$, in the large U limit, implying that the dispersion of spinons in (C.39) is on the order of t^2/U, as is expected of magnetic excitations. On the other hand, if we assume that the expectation values β_{ij} are positive, consistent with the fact that the rotors see no net flux (while the electrons and spinons do), then we simply fill up the negative energy states of the band-structure shown in Fig. 1(c) of the main text, albeit with a smaller gap. This gives a non-zero value for the rotor hoppings, $\langle f^\dagger_{i,\sigma} f_{j,\sigma}\rangle = \alpha_{ij}$. We can find this expectation value from the ground state energy of the band Hamiltonian: writing $\alpha_{ij} = -t^*_{ij}\alpha/|t|$, we expect the average over the filled bands $\langle \epsilon^-(k)\rangle$ to determine $\alpha = \frac{|\langle \epsilon^-(k)\rangle|}{2z|t|}$, where $z = 6$ is the coordination number.

Now we can determine the transition, which amounts to analyzing the Bose-Hubbard model

$$H_B = -J \sum_{\langle ij \rangle} e^{i(\theta_i - \theta_j)} + \text{h.c.} + \frac{U}{2} \sum_i L_i^2. \tag{C.40}$$

A simple mean field theory locates the transition at $U^* = 4zJ$. This is done by taking a simple variational ansatz for each site, $|\psi\rangle = |0\rangle + \frac{\psi}{2}(|+1\rangle + |-1\rangle)$ in the L basis, which has the property $\langle\psi|e^{i\theta}|\psi\rangle = \psi$. Then $\langle H_B\rangle = N\psi^2(-zJ + \frac{U}{4})$. The condensate occurs when the coefficient in parentheses first turns negative.

Substituting $J = 2|t|\alpha$, where the factor of 2 is for the two spins of f, we get:

$$U^* = 4|\langle \epsilon^-(k)\rangle| \approx 9.60813\, t \tag{C.41}$$

where we averaged over the dispersion $\epsilon_-(k) = -2t\sqrt{\cos^2 k_1 + \cos^2 k_2 + \cos^2(k_1 + k_2)}$. This mean field result is to be compared to, and is indeed relatively close to, the iDMRG-obtained transition that occurs at $U^*/t \approx 11 - 12$ [114, 118].

Additionally, we can argue directly that the gap to the charge-$2e$ Cooper pair excitations vanishes at the transition. To access them one has to include coupling to the internal gauge field a. If we focus on the transition and integrate out the fermionic spinons f, this gives a Chern-Simons term [330]. Also, the rotor variables are at low energies and couple minimally to the gauge field. In the condensed phase of the rotors, we have the effective Lagrangian:

$$L = \frac{1}{4U}\left(\dot{\theta} + a_0\right)^2 - \frac{\rho_s}{2}\left(\nabla\theta + a\right)^2 + \frac{2}{4\pi} a \wedge da, \tag{C.42}$$

where the superfluid density ρ_s goes to zero at the transition. The vortices of the rotor condensate are the Cooper pairs. The fact that they carry 2π flux of da implies, via the Chern-Simons term, a gauge charge of 2. This is screened by two rotor fields, giving the vortex a global $\mathrm{U}(1)_c$ charge of 2 and no spin. The energy of such vortices vanishes as we approach the transition.

C.3 Chirality of Edge States from K-Matrix Formalism

In this appendix, we provide a more thorough account of the charge response, spin response, and edge states of the IQH, CSL, and superconductor phases within the framework of Chern-Simons K-matrix formalism [400]. We employ the following convention for the Chern-Simons Lagrangian:

$$\mathcal{L} = -\frac{K_{IJ}}{4\pi}\alpha_I \wedge d\alpha_J + \frac{t_J}{2\pi} A \wedge d\alpha_J + \frac{(t_s)_J}{2\pi} A_s \wedge d\alpha_J, \tag{C.43}$$

or in components:

$$\mathcal{L} = -\frac{1}{4\pi}\alpha_I^\mu K_{IJ}\epsilon_{\mu\nu\lambda}\partial^\nu\alpha_J^\lambda + \frac{1}{2\pi} A^\mu t_J \epsilon_{\mu\nu\lambda}\partial^\nu\alpha_J^\lambda + \frac{1}{2\pi}(A_s)^\mu (t_s)_J \epsilon_{\mu\nu\lambda}\partial^\nu\alpha_J^\lambda. \tag{C.44}$$

Here, α_I are dynamical U(1) gauge fields. On the other hand, A is a classical field that probes the charge response, while A_s probes the spin response. In order for this effective theory to describe a microscopic system of electrons, it must obey the "spin/charge relation", which is the following requirement on gauge-invariant *local* operators: those with odd electric charge must have fermionic statistics, while those with even electric charge have bosonic statistics [401]. Mathematically, this condition reads (see Section 2.3 of Ref. [401]):

$$t_I \equiv K_{II} \text{ (mod 2)}. \tag{C.45}$$

This relation will be satisfied by the K-matrix theories for the IQH, CSL, and superconductor described below.

On a spatial manifold of genus g, the ground state degeneracy is given by $|\det K|^g$, provided $\det K \neq 0$. Furthermore, the edge chiral central charge is given by the "signature" of K, *i.e.*, $c_- =$ the number of positive eigenvalues minus the number of negative eigenvalues [402]. Provided the K-matrix is invertible, the Hall conductivity is [400]

$$\sigma_{xy} = \frac{e^2}{h} \sum_{IJ} t_I (K^{-1})_{IJ} t_J. \tag{C.46}$$

and the spin quantum Hall conductivity (*i.e.*, spin current in response to a Zeeman gradient) is likewise

$$\sigma^s_{xy} = \frac{(\hbar/2)^2}{h} \sum_{IJ} (t_s)_I (K^{-1})_{IJ} (t_s)_J. \tag{C.47}$$

Moreover, within the K-matrix formalism, each quasi-particle excitation can be labeled by a $\boldsymbol{\ell}$, where ℓ_I denotes its charge under each of the dynamical gauge fields. The current of this quasi-particle is then a source for the dynamical gauge fields and has statistical angle

$$\theta(\boldsymbol{\ell}) = \pi \sum_{IJ} \ell_I (K^{-1})_{IJ} \ell_J, \tag{C.48}$$

electric charge

$$q(\boldsymbol{\ell}) = e \sum_{IJ} t_I (K^{-1})_{IJ} \ell_J, \tag{C.49}$$

(where e is the electron charge) and S_z spin quantum number

$$q_s(\boldsymbol{\ell}) = \frac{\hbar}{2} \sum_{IJ} (t_s)_I (K^{-1})_{IJ} \ell_J. \tag{C.50}$$

The spin-singlet integer quantum Hall phase (with total Chern number $C = 2$) is described by the data

$$K_{\text{IQH}} = \begin{pmatrix} 1 & 0 \\ 0 & 1 \end{pmatrix}, \qquad t_{\text{IQH}} = \begin{pmatrix} 1 \\ 1 \end{pmatrix}, \qquad t_{s,\text{IQH}} = \begin{pmatrix} 1 \\ -1 \end{pmatrix}. \tag{C.51}$$

One immediately verifies that it satisfies the expected properties. It has a unique gapped ground state, as well as $c_- = 2$, $\sigma_{xy} = 2 \cdot e^2/h$, and $\sigma^s_{xy} = 2 \cdot (\hbar/2)^2/h$. Moreover, no quasi-particles are fractionalized: since $K_{\rm IQH} = K^{-1}_{\rm IQH} = 1_{2\times 2}$, then $q(\boldsymbol{\ell}) = (\ell_1 + \ell_2)e$ and $q_s(\boldsymbol{\ell}) = (\ell_1 - \ell_2)\hbar/2$. Thus, in units of e and $\hbar/2$ respectively, $q(\boldsymbol{\ell})$ and $q_s(\boldsymbol{\ell})$ are both odd or both even.

The CSL phase is obtained by "gauging" the global charge U(1) of the IQH phase. Specifically, let us promote $A \to \alpha_3 + A$, where α_3 is a third dynamical U(1) gauge field and A is still a classical field. The resulting theory is described by the data

$$K_{\rm CSL} = \begin{pmatrix} 1 & 0 & -1 \\ 0 & 1 & -1 \\ -1 & -1 & 0 \end{pmatrix}, \qquad t_{\rm CSL} = \begin{pmatrix} 1 \\ 1 \\ 0 \end{pmatrix}, \qquad t_{s,\rm CSL} = \begin{pmatrix} 1 \\ -1 \\ 0 \end{pmatrix}. \tag{C.52}$$

The eigenvalues of $K_{\rm CSL}$ are $2, 1, -1$. Thus, the ground state degeneracy is 2^g and the chiral central charge is $c_- = 1$, as expected in the Kalmeyer-Laughlin CSL phase. Moreover, since

$$(K_{\rm CSL})^{-1} = \frac{1}{2}\begin{pmatrix} 1 & -1 & -1 \\ -1 & 1 & -1 \\ -1 & -1 & -1 \end{pmatrix}, \tag{C.53}$$

then this phase has the expected quantized Hall responses, $\sigma_{xy} = 0$ and $\sigma^s_{xy} = 2 \cdot (\hbar/2)^2/h$. Within this effective theory, the spin-up (spin-down) electron excitation is labeled by the first column $\boldsymbol{\ell}_{e\uparrow}$ (second column $\boldsymbol{\ell}_{e\downarrow}$) of $K_{\rm CSL}$, with charges

$$q(\boldsymbol{\ell}_{e,\uparrow/\downarrow}) = e, \qquad q_s(\boldsymbol{\ell}_{e,\uparrow/\downarrow}) = \pm\hbar/2. \tag{C.54}$$

On the other hand, there is a fractionalized charged semion excitation labeled by $\boldsymbol{\ell}_c = (0 \;\; 0 \;\; -1)^{\mathsf{T}}$, which carries $q(\boldsymbol{\ell}_c) = e, q_s(\boldsymbol{\ell}_c) = 0$, and a semionic statistical angle $\theta(\boldsymbol{\ell}_c) = -\pi/2$. The fractionalized spinful semion excitations correspond to $\boldsymbol{\ell}_{s,\uparrow/\downarrow} = \boldsymbol{\ell}_{e,\uparrow/\downarrow} - \boldsymbol{\ell}_c$, which indeed have $q(\boldsymbol{\ell}_s) = 0, q_s(\boldsymbol{\ell}_{s,\uparrow/\downarrow}) = \pm\hbar/2$, and a semionic statistical angle $\theta(\boldsymbol{\ell}_s) = +\pi/2$.

Now, let us turn to the anyon superconductor and the chirality of its edge modes. From the main text, recall that the main additional step was that the gauge field $a = \alpha_3$ now has a bIQH response $-\frac{2}{4\pi} a da$. With the sign convention of (C.43), adding this to $K_{\rm CSL}$ yields

$$K_{\rm SC} = \begin{pmatrix} 1 & 0 & -1 \\ 0 & 1 & -1 \\ -1 & -1 & 2 \end{pmatrix}, \qquad t_{\rm SC} = \begin{pmatrix} 1 \\ 1 \\ 0 \end{pmatrix}, \qquad t_{s,\rm SC} = \begin{pmatrix} 1 \\ -1 \\ 0 \end{pmatrix}. \tag{C.55}$$

We find $\det K_{\rm SC} = 0$, which signals that the gauge fields are not independent and that the system (absent A) is gapless. Performing the change of variables

$$\begin{pmatrix} \alpha_1 \\ \alpha_2 \\ \alpha_3 \end{pmatrix} = \begin{pmatrix} \alpha'_1 + \alpha'_3 \\ \alpha'_2 + \alpha'_3 \\ \alpha'_3 \end{pmatrix} = W \begin{pmatrix} \alpha'_1 \\ \alpha'_2 \\ \alpha'_3 \end{pmatrix}, \qquad W = \begin{pmatrix} 1 & 0 & 1 \\ 0 & 1 & 1 \\ 0 & 0 & 1 \end{pmatrix}, \tag{C.56}$$

we obtain the equivalent K-matrix theory

$$K'_{\mathrm{SC}} = W^{\mathsf{T}} K_{\mathrm{SC}} W = \begin{pmatrix} 1 & 0 & 0 \\ 0 & 1 & 0 \\ 0 & 0 & 0 \end{pmatrix}, \quad t'_{\mathrm{SC}} = W^{\mathsf{T}} t_{\mathrm{SC}} = \begin{pmatrix} 1 \\ 1 \\ 2 \end{pmatrix}, \quad t'_{s,\mathrm{SC}} = W^{\mathsf{T}} t_{s,\mathrm{SC}} = \begin{pmatrix} 1 \\ -1 \\ 0 \end{pmatrix}. \tag{C.57}$$

This theory obeys the spin/charge relation (C.45), so that W is a valid transformation. Moreover, we see that α'_3 has decoupled from the other gauge fields and is governed by its Maxwell dynamics. With $A = 0$, this leads to a single bulk gapless mode corresponding to the superfluid Goldstone mode of the spontaneously-broken $\mathrm{U}(1)_c$ symmetry. From the remaining fields, we see that there is no accompanying topological order and that the resulting phase is a chiral superfluid with edge chiral central charge $c_- = 2$.

Further insight into the topological properties of the superconductor is gained by replacing A with a 2+1D dynamical gauge field [359, 403]. This gaps out the Goldstone mode of the superfluid and gives rise to one of Kitaev's 16-fold way $\mathbb{Z}_2$ topological orders [86]. For instance, a topologically-trivial superfluid maps to the $m = 0$ member of the 16-fold way.[1] In fact, we only expect one of the eight *even* members of the 16-fold way since we will only describe Abelian topological orders via the K-matrix. Making $\alpha'_4 = A$ dynamical in (C.57) and discarding A_s, we obtain

$$K'_{\text{gauged SC}} = \begin{pmatrix} 1 & 0 & 0 & -1 \\ 0 & 1 & 0 & -1 \\ 0 & 0 & 0 & -2 \\ -1 & -1 & -2 & 0 \end{pmatrix}, \tag{C.58}$$

which has precisely the same topological order as the gauged, weak-pairing $d + id$ superconductors [359]. In particular, it corresponds to the member $m = 4$ of Kitaev's classification [86], which has $c_- = m/2 = 2$. However, recall from the main text that our superconductor is far from the weak-pairing limit (evidenced by electron pairing above the insulators), so that its pairing symmetry is not directly linked to its edge chiral central charge [360].

C.4 Correlation Lengths at Half-Filling from Cylinder iDMRG

In this section, we provide the transfer matrix correlation length data for the ground states at half-filling, for a range of Hubbard interaction strengths U and various system sizes. We consider both the YC-L_y and XC-$2L_y$ cylinder geometries [107].

[1] We use the symbol m instead of Kitaev's ν to avoid collision with the filling of the various quantum Hall phases.

Let us first discuss the YC cylinder geometries. In the gauge-invariant language of Sec. 1 of the main text, in the YC case with even L_y, we take $T = T_2$ to be a purely circumferential translation with $T^{L_y} = 1$. When L_y is odd, we instead thread $\pi/2$ flux so that $T^{L_y} = i^{N_F}$, which means that T can have eigenvalue -1 in the charge-$2e$ ($N_F = 2$) sector. In both cases, the fluxes through the rings are such that the system respects particle-hole symmetry.

The XC case proceeds the same way except that we take our circumferential translation to be $T = (T_2)^2 T_1^\dagger$, which translates by a distance $\sqrt{3}a$ instead of a. For our Hamiltonian hopping amplitudes, we specifically choose those shown in Fig. C.1(b).

The dominant correlation length ξ in a given charge sector of the transfer matrix is related to the dominant non-trivial transfer matrix eigenvalue λ by [375]:

$$1/\xi_i = -\log|\lambda_i|. \tag{C.59}$$

We report ξ in units of cylinder rings. For the YC cylinders, the distance between the cylinder rings is $a\sqrt{3}/2$, whereas it is $a/2$ in the XC case.

In Fig. C.2, we display the maximum correlation lengths for the YC3, YC4 and YC6 cylinders resolved by the electric charge sector of the ground state transfer matrix, namely $Q \in \{0e, 1e, 2e\}$, where we maximize over spin and momentum quantum numbers for simplicity. We note that due to the pseudospin SU(2) symmetry, the charge-$0e$ and charge-$2e$ sectors manifestly have equal correlation lengths, with the exception of the regime $U/t \gtrsim 11$ where the spin-*triplet* charge-$0e$ branch (known to be low-energy from the ED and DMRG excitation calculations in the main text) have quantitatively larger correlation length, at least for the YC3 and YC4 systems. The main numerical feature we point out here, consistent with Ref. [114] (though differentiated here since we strictly study the pseudospin-symmetric configurations), is that the correlation length peak and the sharpness of the peak is in the charge-$0e/2e$ sectors is increasing with system size while the charge-$1e$ sector does not see a similar enhancement. The same features are seen in the XC4 vs. XC6 data, shown in Fig. C.3.

C.5 Spin and Pseudospin SU(2) Formalism

Relation between spin and pseudospin generators

Here we present an alternative description, complementing the Majorana representation discussed in Sec. 1 of the main text, of how the presence of particle-hole symmetry and Hubbard interactions gives rise to the pseudospin $\mathrm{SU}(2)_c$ symmetry [404]. We begin with the familiar spin rotation generators:

$$S^+ = \sum_{\boldsymbol{r}} c^\dagger_{\boldsymbol{r}\uparrow} c_{\boldsymbol{r}\downarrow}, \qquad S^- = \sum_{\boldsymbol{r}} c^\dagger_{\boldsymbol{r}\downarrow} c_{\boldsymbol{r}\uparrow}, \qquad S^z = \frac{1}{2}\sum_{\boldsymbol{r}} (n_{\boldsymbol{r}\uparrow} - n_{\boldsymbol{r}\downarrow}). \tag{C.60}$$

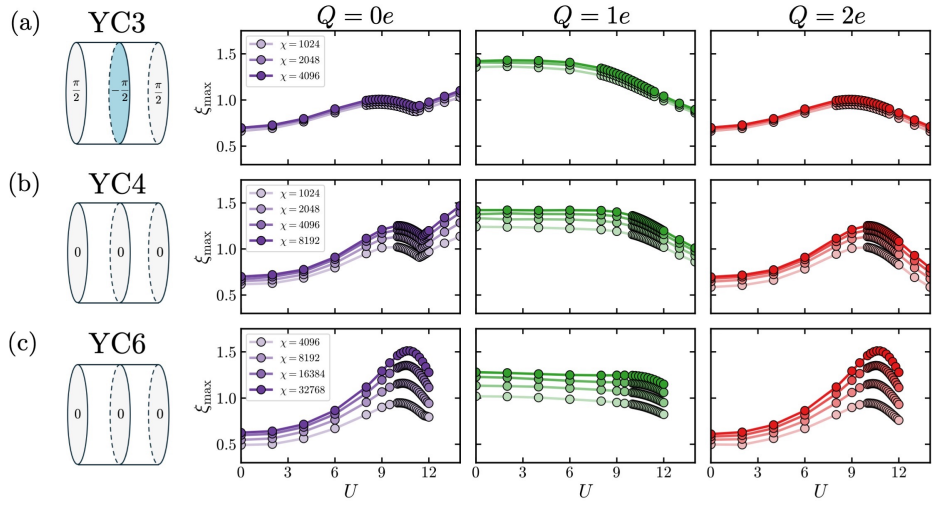

Figure C.2: (a) Maximum correlation length of the half-filled ground state transfer matrix on the infinite YC3 cylinder vs. Hubbard U in the charge sectors $Q \in \{0e, 1e, 2e\}$. The external flux is chosen so that the cylinder rings are pierced by fluxes $\pi/2, -\pi/2, \ldots$ which alternate between rings. Bond dimension, increasing with shade light-to-dark, indicated in legend. (b) Same for the YC4 infinite cylinder with zero flux through each ring. (c) Same for YC6 cylinder with zero flux through each ring.

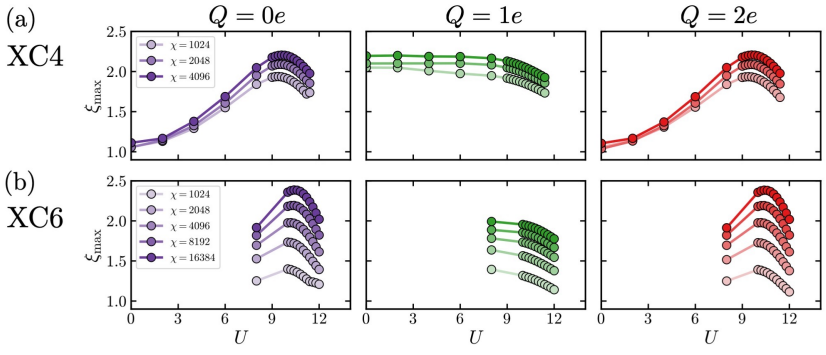

Figure C.3: (a) Maximum correlation length of the half-filled ground state transfer matrix on the infinite XC4 cylinder vs. Hubbard U in the charge sectors $Q \in \{0e, 1e, 2e\}$. Bond dimension, increasing light-to-dark with shade, indicated in legend. (b) Same for XC6 cylinder. For both the XC4 and XC6 cylinders, we make the choice of Hamiltonian hopping amplitudes specified in Sec. C.1.

Given a particle hole symmetry $\mathcal{P}c_{\boldsymbol{r}\sigma}\mathcal{P}^{-1} = e^{i\alpha_{\boldsymbol{r}}}c^\dagger_{\boldsymbol{r}\sigma}$, which commutes with the Hamiltonian, let us define the following *half*-particle-hole transformation:

$$\bar{\mathcal{P}}c_{\boldsymbol{r}\uparrow}\bar{\mathcal{P}}^{-1} = e^{i\alpha_{\boldsymbol{r}}}c^\dagger_{\boldsymbol{r}\uparrow}, \qquad \bar{\mathcal{P}}c_{\boldsymbol{r}\downarrow}\bar{\mathcal{P}}^{-1} = c_{\boldsymbol{r}\downarrow}. \tag{C.61}$$

Though the half-PH leaves the spin-rotation-symmetric hopping Hamiltonian invariant, it is not a symmetry of the interaction since it flips the sign of the Hubbard U:

$$\bar{\mathcal{P}}\left(U\sum_{\boldsymbol{r}}(n_{\boldsymbol{r}\uparrow}-1/2)(n_{\boldsymbol{r}\downarrow}-1/2)\right)\bar{\mathcal{P}}^{-1} = U\sum_{\boldsymbol{r}}(1-n_{\boldsymbol{r}\uparrow}-1/2)(n_{\boldsymbol{r}\downarrow}-1/2) \tag{C.62}$$

$$= -U\sum_{\boldsymbol{r}}(n_{\boldsymbol{r}\uparrow}-1/2)(n_{\boldsymbol{r}\downarrow}-1/2). \tag{C.63}$$

Since H_{-U} also commutes with the spin generators, then $\bar{\mathcal{P}}S^\alpha\bar{\mathcal{P}}^{-1}$ are symmetries of H_{+U}. In particular, note that

$$\eta^+ \equiv \bar{\mathcal{P}}S^+\bar{\mathcal{P}}^{-1} = \sum_{\boldsymbol{r}} e^{-i\alpha_{\boldsymbol{r}}}c_{\boldsymbol{r}\uparrow}c_{\boldsymbol{r}\downarrow}, \tag{C.64}$$

while

$$\eta^z \equiv \bar{\mathcal{P}}S^z\bar{\mathcal{P}}^{-1} = \frac{1}{2}\sum_{\boldsymbol{r}}(1-n_{\boldsymbol{r}\uparrow}-n_{\boldsymbol{r}\downarrow}) \tag{C.65}$$

is related to the total charge density. While the resulting symmetries seem unnatural (in that η^z includes a minus sign relative to the charge density and η^+ *lowers* the total charge by $2e$), we will show later that this convention is the most natural for implementing spin and pseudospin rotations simultaneously as left and right actions, respectively, in a way that is consistent with $\bar{\mathcal{P}}$ relating the generators, as in Eqs. (6-8) of Ref. [324]. Also, note that one can simply take $e^{i\alpha_{\boldsymbol{r}}} = 1$ when the hoppings are all imaginary, so that:

$$\mathcal{P}c_{\boldsymbol{r}\sigma}\mathcal{P}^{-1} = c^\dagger_{\boldsymbol{r}\sigma}. \tag{C.66}$$

Fermionic matrix structure in $\mathrm{SU}(2)_s \times \mathrm{SU}(2)_c$ formalism

In order to get an analytic handle on how various $0e$ and $\pm 2e$ objects transform into one another under the pseudo SU(2) symmetry, it is useful to establish several identities. In particular, here we motivate defining the 2×2 fermion construction where spin (pseudospin) rotations act on the left (right). We know that the column vector of fermion annihilation operators transforms as a spin doublet: defining

$$C_{\boldsymbol{r}} = \begin{pmatrix} c_{\boldsymbol{r}\uparrow} \\ c_{\boldsymbol{r}\downarrow} \end{pmatrix}, \tag{C.67}$$

then $[S_a, c_s] = -\frac{(\sigma_a)_{ss'}}{2} c_{s'}$, so that

$$[\boldsymbol{S}, C_{\boldsymbol{r}}] = -\frac{\boldsymbol{\sigma}}{2} C_{\boldsymbol{r}}, \qquad [\boldsymbol{S}, C^\dagger_{\boldsymbol{r}}] = C^\dagger_{\boldsymbol{r}} \frac{\boldsymbol{\sigma}}{2}. \tag{C.68}$$

Exponentiating these relations, we get

$$e^{i\boldsymbol{\theta}\cdot\boldsymbol{S}} C_{\boldsymbol{r}} e^{-i\boldsymbol{\theta}\cdot\boldsymbol{S}} = e^{-i\boldsymbol{\theta}\cdot\boldsymbol{\sigma}/2} C_{\boldsymbol{r}}. \tag{C.69}$$

Now it's easy to obtain the analogous relation for the pseudospin SU(2) generators via the mapping $\boldsymbol{\eta} = \bar{\mathcal{P}} \boldsymbol{S} \bar{\mathcal{P}}^\dagger$. We simply conjugate both sides by $\bar{\mathcal{P}}$ and use the fact that $\bar{\mathcal{P}} C_{\boldsymbol{r}} \bar{\mathcal{P}}^\dagger = \begin{pmatrix} c^\dagger_{\boldsymbol{r}\uparrow} \\ c_{\boldsymbol{r}\downarrow} \end{pmatrix}$. For the infinitesimal relations, we obtain $[\boldsymbol{\eta}, \begin{pmatrix} c^\dagger_{\boldsymbol{r}\uparrow} \\ c_{\boldsymbol{r}\downarrow} \end{pmatrix}] = -\frac{\boldsymbol{\sigma}}{2} \begin{pmatrix} c^\dagger_{\boldsymbol{r}\uparrow} \\ c_{\boldsymbol{r}\downarrow} \end{pmatrix}$, or by taking the Hermitian conjugate,

$$\left[\boldsymbol{\eta}, \begin{pmatrix} c_{\boldsymbol{r}\uparrow} & c^\dagger_{\boldsymbol{r}\downarrow} \end{pmatrix}\right] = \begin{pmatrix} c_{\boldsymbol{r}\uparrow} & c^\dagger_{\boldsymbol{r}\downarrow} \end{pmatrix} \frac{\boldsymbol{\tau}}{2}. \tag{C.70}$$

(we have relabeled the Pauli matrices as $\boldsymbol{\tau}$ when they act to the right as pseudospin rotations). Exponentiating gives

$$e^{i\boldsymbol{\theta}\cdot\boldsymbol{\eta}} \begin{pmatrix} c_{\boldsymbol{r}\uparrow} & c^\dagger_{\boldsymbol{r}\downarrow} \end{pmatrix} e^{-i\boldsymbol{\theta}\cdot\boldsymbol{\eta}} = \begin{pmatrix} c_{\boldsymbol{r}\uparrow} & c^\dagger_{\boldsymbol{r}\downarrow} \end{pmatrix} e^{i\boldsymbol{\theta}\cdot\boldsymbol{\tau}/2}. \tag{C.71}$$

Thus $\begin{pmatrix} c_{\boldsymbol{r}\uparrow} & c^\dagger_{\boldsymbol{r}\downarrow} \end{pmatrix}$ should be a row of the 2×2 fermion matrix. It turns out that completing this matrix with $-c^\dagger_{\boldsymbol{r}\uparrow}$ as the bottom right element makes both columns (rows) transform as spin (charge) doublets. Namely,

$$\Psi_{\boldsymbol{r}} = \begin{pmatrix} c_{\boldsymbol{r}\uparrow} & c^\dagger_{\boldsymbol{r}\downarrow} \\ c_{\boldsymbol{r}\downarrow} & -c^\dagger_{\boldsymbol{r}\uparrow} \end{pmatrix} = \begin{pmatrix} C_{\boldsymbol{r}} & i\sigma_y C^*_{\boldsymbol{r}} \end{pmatrix} \tag{C.72}$$

satisfies

$$e^{i\boldsymbol{\theta}\cdot\boldsymbol{S}} \Psi_{\boldsymbol{r}} e^{-i\boldsymbol{\theta}\cdot\boldsymbol{S}} = e^{-i\boldsymbol{\theta}\cdot\boldsymbol{\sigma}/2} \Psi_{\boldsymbol{r}} \tag{C.73}$$

and, on account of the relation $\bar{\mathcal{P}} C_{\boldsymbol{r}} \bar{\mathcal{P}}^\dagger = C^\dagger_{\boldsymbol{r}}$, also satisfies

$$e^{i\boldsymbol{\theta}\cdot\boldsymbol{\eta}} \Psi_{\boldsymbol{r}} e^{-i\boldsymbol{\theta}\cdot\boldsymbol{\eta}} = \Psi_{\boldsymbol{r}} e^{i\boldsymbol{\theta}\cdot\boldsymbol{\tau}/2}. \tag{C.74}$$

We also remark that the spin and charge generators can be neatly written in terms of this fermionic matrix. First:

$$\boldsymbol{S}_{\boldsymbol{r}} = \frac{1}{4} \mathrm{tr} \left(\Psi^\dagger_{\boldsymbol{r}} \boldsymbol{\sigma} \Psi_{\boldsymbol{r}} \right), \tag{C.75}$$

which naturally transforms as a vector under spin rotations. Using the half-PH change of basis, we directly obtain

$$\boldsymbol{\eta}_{\boldsymbol{r}} = \bar{\mathcal{P}}\boldsymbol{S}\bar{\mathcal{P}}^\dagger = \frac{1}{4}\mathrm{tr}\left(\Psi_{\boldsymbol{r}}\boldsymbol{\tau}\Psi_{\boldsymbol{r}}^\dagger\right), \tag{C.76}$$

where we have once again trivially rewritten the charge Pauli matrices as $\boldsymbol{\tau}$.

Finally, we note a useful implementation of the Hermitian conjugate:

$$\Psi_{\boldsymbol{r}}^\dagger = \begin{pmatrix} c_{\boldsymbol{r}\uparrow}^\dagger & c_{\boldsymbol{r}\downarrow}^\dagger \\ c_{\boldsymbol{r}\downarrow} & -c_{\boldsymbol{r}\uparrow} \end{pmatrix} = -\sigma_y \begin{pmatrix} c_{\boldsymbol{r}\uparrow} & c_{\boldsymbol{r}\downarrow} \\ c_{\boldsymbol{r}\downarrow}^\dagger & -c_{\boldsymbol{r}\uparrow}^\dagger \end{pmatrix} \sigma_y = -\tau_y \Psi_{\boldsymbol{r}}^{\mathsf{T}} \sigma_y. \tag{C.77}$$

This can be useful when contracting multiple $\Psi_{\boldsymbol{r}}$ under a trace, but one has to be careful about extra minus signs from fermion anti-commutation.

Hofstadter-Hubbard Hamiltonian

Suppose we are given a hopping model $h = -\sum_{\boldsymbol{r},\boldsymbol{r}'} t_{\boldsymbol{r}\boldsymbol{r}'} c_{\boldsymbol{r}}^\dagger c_{\boldsymbol{r}'}$ where $\boldsymbol{r}, \boldsymbol{r}'$ each run over all the sites in the triangular lattice. As usual, Hermiticity requires that

$$t_{\boldsymbol{r}\boldsymbol{r}'} = t_{\boldsymbol{r}'\boldsymbol{r}}^*. \tag{C.78}$$

If we further suppose that the *hoppings are all imaginary*, then

$$t_{\boldsymbol{r}\boldsymbol{r}'} = -t_{\boldsymbol{r}'\boldsymbol{r}}. \tag{C.79}$$

In particular, this means the Hamiltonian has the particle-hole symmetry $\mathcal{P} c_{\boldsymbol{r}} \mathcal{P}^{-1} = c_{\boldsymbol{r}}^\dagger$, like our $\Phi_\triangle = \pi/2$ Hofstadter model on the triangular lattice. In the general case, we claim that the hopping Hamiltonian can be written as

$$h = -\sum_{\boldsymbol{r} \leftarrow \boldsymbol{r}'} t_{\boldsymbol{r}\boldsymbol{r}'} \mathrm{tr}\left(\Psi_{\boldsymbol{r}}^\dagger \Psi_{\boldsymbol{r}'}\right), \tag{C.80}$$

where the sum is over *oriented* pairs of sites, which we denote by $\boldsymbol{r} \leftarrow \boldsymbol{r}'$, whose orientation we fix so that $t_{\boldsymbol{r}\boldsymbol{r}'} = +it$ (with $t > 0$) which gives

$$h = -it \sum_{\boldsymbol{r} \leftarrow \boldsymbol{r}'} \mathrm{tr}\left(\Psi_{\boldsymbol{r}}^\dagger \Psi_{\boldsymbol{r}'}\right). \tag{C.81}$$

The Hamiltonian is already Hermitian in this form. To see this, we explicitly compute its Hermitian conjugate:

$$h^\dagger = -\sum_{\boldsymbol{r} \leftarrow \boldsymbol{r}'} t_{\boldsymbol{r}\boldsymbol{r}'}^* \mathrm{tr}\left(\Psi_{\boldsymbol{r}'}^\dagger \Psi_{\boldsymbol{r}}\right) = +\sum_{\boldsymbol{r} \leftarrow \boldsymbol{r}'} t_{\boldsymbol{r}\boldsymbol{r}'} \mathrm{tr}\left(\left(-\tau_y \Psi_{\boldsymbol{r}'}^{\mathsf{T}} \sigma_y\right)\left(-\sigma_y (\Psi_{\boldsymbol{r}}^\dagger)^{\mathsf{T}} \tau_y\right)\right), \tag{C.82}$$

where we used (C.77). After the Pauli matrices and minus signs cancel, we anti-commute the two operators (they live on different sites) and confirm that

$$h^\dagger = -\sum_{\boldsymbol{r}\leftarrow\boldsymbol{r}'} t_{\boldsymbol{r}\boldsymbol{r}'}\mathrm{tr}\left((\Psi^\dagger_{\boldsymbol{r}})^{\mathsf{T}}\Psi^{\mathsf{T}}_{\boldsymbol{r}'}\right) = -\sum_{\boldsymbol{r}\leftarrow\boldsymbol{r}'} t_{\boldsymbol{r}\boldsymbol{r}'}\mathrm{tr}\left(\Psi^\dagger_{\boldsymbol{r}}\Psi_{\boldsymbol{r}'}\right) = h. \tag{C.83}$$

We note that it is manifestly spin- and pseudospin-rotation-invariant due to the trace. To verify that h is indeed the familiar hopping Hamiltonian, we explicitly expand out the expression:

$$h = -\sum_{\boldsymbol{r}\leftarrow\boldsymbol{r}'} t_{\boldsymbol{r}\boldsymbol{r}'}\mathrm{tr}\left(\begin{pmatrix} c^\dagger_{\boldsymbol{r}\uparrow} & c^\dagger_{\boldsymbol{r}\downarrow}\\ c_{\boldsymbol{r}\downarrow} & -c_{\boldsymbol{r}\uparrow}\end{pmatrix}\begin{pmatrix} c_{\boldsymbol{r}'\uparrow} & c^\dagger_{\boldsymbol{r}'\downarrow}\\ c_{\boldsymbol{r}'\downarrow} & -c^\dagger_{\boldsymbol{r}'\uparrow}\end{pmatrix}\right) \tag{C.84}$$

$$= -\sum_{\boldsymbol{r}\leftarrow\boldsymbol{r}'}\left(t_{\boldsymbol{r}\boldsymbol{r}'}c^\dagger_{\boldsymbol{r}s}c_{\boldsymbol{r}'s} + t_{\boldsymbol{r}\boldsymbol{r}'}c_{\boldsymbol{r}s}c^\dagger_{\boldsymbol{r}'s}\right) \tag{C.85}$$

$$= -\sum_{\boldsymbol{r}\leftarrow\boldsymbol{r}'}\left(t_{\boldsymbol{r}\boldsymbol{r}'}c^\dagger_{\boldsymbol{r}s}c_{\boldsymbol{r}'s} + t^*_{\boldsymbol{r}\boldsymbol{r}'}c^\dagger_{\boldsymbol{r}'s}c_{\boldsymbol{r}s}\right) \tag{C.86}$$

$$= -\sum_{\boldsymbol{r}\leftarrow\boldsymbol{r}'}\left(t_{\boldsymbol{r}\boldsymbol{r}'}c^\dagger_{\boldsymbol{r}s}c_{\boldsymbol{r}'s} + h.c.\right), \tag{C.87}$$

where we again used the fact that $\boldsymbol{r}\neq\boldsymbol{r}'$, and for the last equality we crucially used the imaginary condition, (C.79).

As for the Hubbard interaction, we reference Ref. [324]:

$$H_U = \frac{2U}{3}\sum_{\boldsymbol{r}}\left(\eta^2_{\boldsymbol{r}} - \frac{3}{8}\right), \tag{C.88}$$

which is clearly also invariant under both spin (because $[\boldsymbol{\eta},\boldsymbol{S}]=0$) and pseudospin rotations.

C.6 SU(2) Slave-Rotor Theory of IQH-CSL transition

The presence of both $\mathrm{SU}(2)_s$ and pseudospin symmetries $\mathrm{SU}(2)_c$ enables an SU(2) slave-rotor analysis of the IQH, CSL, and their critical point. The construction was introduced by Hermele in Ref. [324] in the context of Hubbard models on bipartite lattices, but applies in the present context with almost no modification. The main difference is that since the triangular lattice has no natural sublattice, we instead work in the Imaginary C6 gauge (with all imaginary hoppings), where the particle-hole acts as in (C.66) above. This means we don't need to keep track of a sublattice-dependent sign, *i.e.*, Hermele's $\epsilon_{A/B}=\pm 1$.

Physical Hilbert space from parton constraint

We begin by decomposing the electron operators into spinons and rotors:

$$\Psi_{\boldsymbol{r}} = F_{\boldsymbol{r}}Z_{\boldsymbol{r}}, \qquad F_{\boldsymbol{r}} = \begin{pmatrix} f_{\boldsymbol{r}\uparrow} & f^\dagger_{\boldsymbol{r}\downarrow}\\ f_{\boldsymbol{r}\downarrow} & -f^\dagger_{\boldsymbol{r}\uparrow}\end{pmatrix}, \qquad Z_{\boldsymbol{r}} = \begin{pmatrix} z_{\boldsymbol{r}1} & z_{\boldsymbol{r}2}\\ -z^\dagger_{\boldsymbol{r}2} & z^\dagger_{\boldsymbol{r}1}\end{pmatrix}. \tag{C.89}$$

The spinon operators are arranged like the electron operators, with spin acting by SU(2) rotations from the left, whereas gauge rotations act from the right. The rotor $Z_{\boldsymbol{r}}$ is an SU(2) matrix of operators (meaning $z^\dagger_{\boldsymbol{r}1} z_{\boldsymbol{r}1} + z^\dagger_{\boldsymbol{r}2} z_{\boldsymbol{r}2} = 1$), with gauge rotations acting from the left and pseudospin rotations acting from the right. The enlarged slave-rotor Hilbert space at each site is a product of that of the spin-1/2 spinons and that of the SU(2) rotor. Since the slave-rotor Hilbert space is much larger than the physical one, we have to specify which of its states are physical. Following Ref. [324], one projects to the subspace of gauge singlets, $\boldsymbol{J}_G(\boldsymbol{r}) = 0$, where:

$$\boldsymbol{J}_G(\boldsymbol{r}) = \frac{1}{4}\mathrm{tr}\left(F_{\boldsymbol{r}}\boldsymbol{\mu}F^\dagger_{\boldsymbol{r}}\right) + \frac{1}{4}\mathrm{tr}\left(Z^\dagger_{\boldsymbol{r}}\boldsymbol{\mu}Z_{\boldsymbol{r}}\right), \tag{C.90}$$

so that

$$e^{i\boldsymbol{\alpha}\cdot\boldsymbol{J}_G(\boldsymbol{r})} Z_{\boldsymbol{r}} e^{-i\boldsymbol{\alpha}\cdot\boldsymbol{J}_G(\boldsymbol{r})} = e^{-i\boldsymbol{\alpha}\cdot\boldsymbol{\mu}/2} Z_{\boldsymbol{r}}, \tag{C.91}$$

$$e^{i\boldsymbol{\alpha}\cdot\boldsymbol{J}_G(\boldsymbol{r})} F_{\boldsymbol{r}} e^{-i\boldsymbol{\alpha}\cdot\boldsymbol{J}_G(\boldsymbol{r})} = F_{\boldsymbol{r}} e^{i\boldsymbol{\alpha}\cdot\boldsymbol{\mu}/2}. \tag{C.92}$$

We have denoted the Pauli matrices acting in the gauge space by $\boldsymbol{\mu}$, reserving $\boldsymbol{\sigma}$ for the spin space and $\boldsymbol{\tau}$ for the pseudospin space, as in Sec. C.5 above.

Note that the F-Z Hamiltonian — obtained by writing the Hamiltonian in terms of partons — is a gauge-singlet operator. It therefore acts within the $\boldsymbol{J}_G(\boldsymbol{r}) = 0$ subspace and has the same matrix elements as the electronic Hamiltonian. To construct this subspace, which is four-dimensional at each site, we start with the slave-particle vacuum:

$$|0\rangle_{\mathrm{sp}} = |0\rangle_f \otimes |0\rangle_{\mathrm{rot}}, \tag{C.93}$$

where $|0\rangle_f$ is the spinon vacuum and $|0\rangle_{\mathrm{rot}} = |\ell_C = 0, \ell_G = 0, m_C = 0, m_G = 0\rangle$ is the unique rotationally-invariant state in the rotor Hilbert space (C stands for "charge" pseudospin and G stands for gauge); recall from Ref. [324] that only $\ell_G = \ell_C$ states are allowed to begin with. In particular, $\boldsymbol{J}_G(\boldsymbol{r})|0\rangle_{\mathrm{rot}} = 0$ by definition. Then it can be shown that while $|0\rangle_{\mathrm{sp}}$ is not a physical state, $f^\dagger_{\boldsymbol{r}\uparrow}|0\rangle_{\mathrm{sp}}$ is physical, *i.e.*, it is a gauge-singlet. Similarly, $f^\dagger_{\boldsymbol{r}\downarrow}|0\rangle_{\mathrm{sp}}$ is a physical state. We can then construct the fully-filled and empty states by applying electronic operators:

$$c^\dagger_{\boldsymbol{r}\uparrow} f^\dagger_{\boldsymbol{r}\downarrow}|0\rangle_{\mathrm{sp}} = (f^\dagger_{\boldsymbol{r}\uparrow} z^\dagger_{\boldsymbol{r}1} - f_{\boldsymbol{r}\downarrow} z_{\boldsymbol{r}2}) f^\dagger_{\boldsymbol{r}\downarrow}|0\rangle_{\mathrm{sp}} = (z^\dagger_{\boldsymbol{r}1} f^\dagger_{\boldsymbol{r}\uparrow} f^\dagger_{\boldsymbol{r}\downarrow} - z_{\boldsymbol{r}2})|0\rangle_{\mathrm{sp}}, \tag{C.94}$$

and

$$c_{\boldsymbol{r}\uparrow} f^\dagger_{\boldsymbol{r}\uparrow}|0\rangle_{\mathrm{sp}} = (f_{\boldsymbol{r}\uparrow} z_{\boldsymbol{r}1} - f^\dagger_{\boldsymbol{r}\downarrow} z^\dagger_{\boldsymbol{r}2}) f^\dagger_{\boldsymbol{r}\uparrow}|0\rangle_{\mathrm{sp}} = (z_{\boldsymbol{r}1} + z^\dagger_{\boldsymbol{r}2} f^\dagger_{\boldsymbol{r}\uparrow} f^\dagger_{\boldsymbol{r}\downarrow})|0\rangle_{\mathrm{sp}}. \tag{C.95}$$

Since the electron operators are invariant under gauge transformations, then both of these states are gauge singlets. We have therefore generated the full four-dimensional physical on-site Hilbert space.

Functional integral representation

Following the path integral construction outlined in Ref. [324], the electronic Hofstadter-Hubbard Hamiltonian can now be written in the slave-rotor representation:

$$H_{\rm HH} = -\sum_{\boldsymbol{r},\boldsymbol{r}'} \mathrm{tr}\left[(F_{\boldsymbol{r}} Z_{\boldsymbol{r}})^\dagger (F_{\boldsymbol{r}'} Z_{\boldsymbol{r}'})\right] + \frac{2U}{3}\sum_{\boldsymbol{r}} \eta_{\boldsymbol{r}}^2, \tag{C.96}$$

which must be accompanied by the aforementioned "gauge-singlet" constraint

$$\boldsymbol{J_G}(\boldsymbol{r}) = 0. \tag{C.97}$$

Working at zero temperature, we introduce imaginary time $\tau \in (-\infty, +\infty)$ and write the functional integral:

$$\mathcal{Z} = \int \mathcal{D}Z\mathcal{D}F\mathcal{D}\boldsymbol{a}_\tau e^{-S}, \qquad S = S_Z + S_F + S_t, \tag{C.98}$$

where

$$S_Z = \frac{3}{4U}\sum_{\boldsymbol{r}} \int d\tau\ \mathrm{tr}\left[Z_{\boldsymbol{r}}^\dagger \left(\overleftarrow{\partial}_\tau - \frac{i\boldsymbol{a}_\tau\cdot\boldsymbol{\mu}}{2}\right)\left(\partial_\tau + \frac{i\boldsymbol{a}_\tau\cdot\boldsymbol{\mu}}{2}\right) Z_{\boldsymbol{r}}\right], \tag{C.99}$$

$$S_F = \frac{1}{2}\sum_{\boldsymbol{r}} \int d\tau\ \mathrm{tr}\left[F_{\boldsymbol{r}}\left(\partial_\tau + \frac{i\boldsymbol{a}_\tau\cdot\boldsymbol{\mu}}{2}\right) F_{\boldsymbol{r}}^\dagger\right], \tag{C.100}$$

$$S_t = -it\int d\tau \sum_{\boldsymbol{r}\leftarrow\boldsymbol{r}'} \mathrm{tr}\left[(F_{\boldsymbol{r}} Z_{\boldsymbol{r}})^\dagger (F_{\boldsymbol{r}'} Z_{\boldsymbol{r}'})\right]. \tag{C.101}$$

Here and below, $\overleftarrow{\partial}$ denotes differentiation acting to the left, and the gauge field $\boldsymbol{a}_\tau$ has been introduced to enforce the on-site gauge constraint ((C.97)).

So far everything is exact and therefore intractable, so we pass to a mean-field approximation. The first step is to replace the constraint $Z_{\boldsymbol{r}}(\tau) \in \mathrm{SU}(2)$ with an equivalent Lagrange multiplier term:

$$S_\lambda = i\int d\tau \sum_{\boldsymbol{r}} \lambda_{\boldsymbol{r}}(\tau)\left[\frac{1}{2}\mathrm{tr}(Z_{\boldsymbol{r}}^\dagger Z_{\boldsymbol{r}}) - 1\right]. \tag{C.102}$$

The next step is to decouple the hopping term into separate spinon and rotor terms. This is done by introducing a complex Hubbard–Stratonovich field via the identity [149, 324]:

$$e^{\epsilon\alpha_{\boldsymbol{r}\boldsymbol{r}'}\beta_{\boldsymbol{r}\boldsymbol{r}'}} = \frac{\epsilon}{\pi}\int d\eta_{\boldsymbol{r}\boldsymbol{r}'} d\eta^*_{\boldsymbol{r}\boldsymbol{r}'}\ e^{-\epsilon(|\eta_{\boldsymbol{r}\boldsymbol{r}'}|^2 - \eta_{\boldsymbol{r}\boldsymbol{r}'}\alpha_{\boldsymbol{r}\boldsymbol{r}'} - \eta^*_{\boldsymbol{r}\boldsymbol{r}'}\beta_{\boldsymbol{r}\boldsymbol{r}'})}.$$

Since we have fixed the bond orientation for the hopping in (C.101) above, and since $S_t = t\int d\tau \sum_{\boldsymbol{r}\leftarrow\boldsymbol{r}'}(-Z_{\boldsymbol{r}'}Z_{\boldsymbol{r}}^\dagger)_{ab}(iF_{\boldsymbol{r}}^\dagger F_{\boldsymbol{r}'})_{ba}$, then we may assign $\epsilon = t\Delta\tau > 0$ and for each a, b assign

$\alpha^{ab}_{\boldsymbol{r}\boldsymbol{r}'} = -(Z_{\boldsymbol{r}'}Z^\dagger_{\boldsymbol{r}})_{ab}$ and $\beta_{\boldsymbol{r}\boldsymbol{r}'} = (iF^\dagger_{\boldsymbol{r}}F_{\boldsymbol{r}'})_{ba}$, which yields:

$$S_\eta = t\int d\tau \sum_{\boldsymbol{r}\leftarrow\boldsymbol{r}'} \mathrm{tr}\left[(\eta_{\boldsymbol{r}\boldsymbol{r}'})^\dagger \eta_{\boldsymbol{r}\boldsymbol{r}'}\right],$$
$$S_{tZ} = -t\int d\tau \sum_{\boldsymbol{r}\leftarrow\boldsymbol{r}'} \mathrm{tr}\left[Z^\dagger_{\boldsymbol{r}}\eta_{\boldsymbol{r}\boldsymbol{r}'}Z_{\boldsymbol{r}'}\right],$$
$$S_{tF} = it\int d\tau \sum_{\boldsymbol{r}\leftarrow\boldsymbol{r}'} \mathrm{tr}\left[F_{\boldsymbol{r}'}(\eta_{\boldsymbol{r}\boldsymbol{r}'})^\dagger F^\dagger_{\boldsymbol{r}}\right].$$

One obtains a real free energy at the saddle point provided that $\eta_{\boldsymbol{r}\boldsymbol{r}'} = \chi_{\boldsymbol{r}\boldsymbol{r}'}U_{\boldsymbol{r}\boldsymbol{r}'}$ is a real number times an SU(2) matrix, as can be shown using the identity (C.77) above. In particular, two of the saddle point equations read $(\eta_{\boldsymbol{r}\boldsymbol{r}'})^\dagger = \langle Z_{\boldsymbol{r}'}Z^\dagger_{\boldsymbol{r}}\rangle$ and $\eta_{\boldsymbol{r}\boldsymbol{r}'} = (t_{\boldsymbol{r}\boldsymbol{r}'}/|t_{\boldsymbol{r}\boldsymbol{r}'}|)\langle F^\dagger_{\boldsymbol{r}}F_{\boldsymbol{r}'}\rangle = i\langle F^\dagger_{\boldsymbol{r}}F_{\boldsymbol{r}'}\rangle$. We take an ansatz where $\langle F^\dagger_{\boldsymbol{r}}F_{\boldsymbol{r}'}\rangle$ is proportional to $\langle \Psi^\dagger_{\boldsymbol{r}}\Psi_{\boldsymbol{r}'}\rangle$ in the $U = 0$ IQH phase, producing a solution $\eta^*_{\boldsymbol{r}\boldsymbol{r}'}$ (at $\boldsymbol{a}_\tau = 0$).

Fluctuations about this solution are parameterized by an SU(2) gauge-field on the links $\boldsymbol{r} \leftarrow \boldsymbol{r}'$ and by a fluctuating $\boldsymbol{a}_\tau$ component. Integrating out the spinons while retaining these gauge field degrees of freedom, then in the continuum limit we obtain at leading order in the gauge fields [405]:

$$S_{\mathrm{CS}} = \frac{i}{4\pi}\int d^3x\ \epsilon^{\mu\nu\rho}\mathrm{tr}\left(a_\mu\partial_\nu a_\rho + \frac{2}{3}a_\mu a_\nu a_\rho\right),$$

which is an SU(2) Chern-Simons term at level 1 [406].

Low-energy $\mathrm{SU}(2)_1$ Higgs-Chern-Simons theory

To describe the IQH-CSL transition, we pass to a continuum description of the rotor bosons. We begin with the mean-field action

$$S^Z_{\mathrm{MF}} = -\sum_{\tau,\boldsymbol{r}}\left[\mathrm{tr}Z^\dagger_{x+\epsilon z}Z_x + h.c.\right] - \sum_\tau\sum_{\langle \boldsymbol{r},\boldsymbol{r}'\rangle}\left[\mathrm{tr}Z^\dagger_{\boldsymbol{r},\tau}Z_{\boldsymbol{r}',\tau} + h.c.\right] + \frac{r + r_{c0}}{2}\sum_{\tau,\boldsymbol{r}}\left[\mathrm{tr}Z^\dagger_x Z_x\right], \tag{C.103}$$

where r_{c0} is chosen so that the lowest boson mode goes gapless as $r \to 0^+$. Following Ref. [324], we take a spacetime lattice of triangular lattice sites separated by ϵ increments in imaginary time. For $r > 0$, diagonalizing the above spacetime-translation-invariant Hamiltonian gives a unique low-energy mode at $\boldsymbol{q} = 0$, consistent with the rotors experiencing no net flux. We write $\Theta(x) \sim Z_{\boldsymbol{r},t}$ with x now a continuous spacetime coordinate, which yields:

$$\mathcal{L}^\Theta_0 = \frac{1}{2}\mathrm{tr}(\Theta^\dagger \overleftarrow{\partial}_\nu \partial_\nu \Theta) + \frac{r}{2}\mathrm{tr}(\Theta^\dagger\Theta), \tag{C.104}$$

where $\overleftarrow{\partial}$ denotes differentiation to the left. Note that demanding invariance under global SU(2) gauge transformations and pseudospin rotations precludes a linear time-derivative

term $\sim \mathrm{tr}(\Theta^\dagger \partial_\tau \Theta)$. This entirely fixes the form at $\mathcal{L}_0^\Theta$ quadratic order. Now we add the gauge field fluctuations by promoting the derivative to the covariant derivative

$$\partial_\nu \to \partial_\nu + \frac{i\boldsymbol{a}_\nu \cdot \boldsymbol{\mu}}{2}, \tag{C.105}$$

giving

$$\mathcal{L}_{\mathrm{kin}}^\Theta = \frac{1}{2}\mathrm{tr}\left[\Theta^\dagger \left(\overleftarrow{\partial}_\mu - \frac{ia_\mu^j \sigma^i}{2}\right)\left(\overrightarrow{\partial}_\mu + \frac{ia_\mu^j \sigma^i}{2}\right)\Theta\right], \tag{C.106}$$

where $\boldsymbol{\mu}$ is again the Pauli matrix vector in the gauge space. Reintroducing the $\mathrm{SU}(2)_1$ Chern-Simons term from integrating out the spinons, and the symmetry-allowed quartic term, the full SU(2) Higgs-Chern-Simons theory is:

$$\mathcal{L}_{\mathrm{eff}} = \mathcal{L}_{\mathrm{CS}} + \mathcal{L}_{\mathrm{kin}}^\Theta + \frac{1}{2}\mathrm{tr}(\Theta^\dagger\Theta) + \frac{\lambda}{4}\left[\mathrm{tr}(\Theta^\dagger\Theta)\right]^2 + \ldots \tag{C.107}$$

Conserved current

As spin excitations are gapped across the IQH-CSL transition, and neither the spin nor pseudospin symmetries are broken, then the closing of the charge gap is associated with gapless bosonic modes that transform as spin-singlet pseudospin-triplets. We now compute the conserved Noether current associated with the pseudospin rotation $\mathrm{SU}(2)_c$ symmetry. The important Lagrangian term for the current is the coupling $\mathcal{L}_{\mathrm{kin}}^\Theta$ between the low-energy bosonic field Θ and the SU(2) gauge field in (C.106) above. Under the pseudospin SU(2) rotation

$$\Theta' = \Theta e^{i\boldsymbol{\alpha}\cdot\boldsymbol{\tau}/2} \approx \Theta + \Theta\frac{i\boldsymbol{\alpha}\cdot\boldsymbol{\tau}}{2}, \tag{C.108}$$

this term transforms to

$$(\mathcal{L}_{\mathrm{kin}}^\Theta)' = \frac{1}{2}\mathrm{tr}\left[\left(\Theta^\dagger - \frac{i\boldsymbol{\alpha}\cdot\boldsymbol{\tau}}{2}\Theta^\dagger\right)\left(\overleftarrow{\partial}_\mu - \frac{ia_\mu^j\sigma^i}{2}\right)\left(\vec{\partial}_\mu + \frac{ia_\mu^j\sigma^i}{2}\right)\left(\Theta + \Theta\frac{i\boldsymbol{\alpha}\cdot\boldsymbol{\tau}}{2}\right)\right] \tag{C.109}$$

$$= \mathcal{L}_{\mathrm{kin}}^\Theta + \frac{1}{2}\mathrm{tr}\left[\left(-\frac{i\boldsymbol{\alpha}\cdot\boldsymbol{\tau}}{2}\Theta^\dagger\right)\left(\overleftarrow{\partial}_\mu - \frac{ia_\mu^j\sigma^i}{2}\right)\left(\vec{\partial}_\mu + \frac{ia_\mu^j\sigma^i}{2}\right)\Theta\right] \tag{C.110}$$

$$+ \frac{1}{2}\mathrm{tr}\left[\Theta^\dagger\left(\overleftarrow{\partial}_\mu - \frac{ia_\mu^j\sigma^i}{2}\right)\left(\vec{\partial}_\mu + \frac{ia_\mu^j\sigma^i}{2}\right)\left(\Theta\frac{i\boldsymbol{\alpha}\cdot\boldsymbol{\tau}}{2}\right)\right]. \tag{C.111}$$

When α is constant, then $(\mathcal{L}_{\mathrm{kin}}^\Theta)' = \mathcal{L}_{\mathrm{kin}}^\Theta$ to all orders. When it varies in spacetime, on the other hand

$$(\mathcal{L}_{\mathrm{kin}}^\Theta)' - \mathcal{L}_{\mathrm{kin}}^\Theta = \frac{1}{2}\mathrm{tr}\left[\left(-\frac{i\boldsymbol{\alpha}\cdot\boldsymbol{\tau}}{2}\Theta^\dagger\right)\left(\overleftarrow{\partial}_\mu - \frac{ia_\mu^j\sigma^i}{2}\right)\left(\vec{\partial}_\mu + \frac{ia_\mu^j\sigma^i}{2}\right)\Theta\right] \tag{C.112}$$

$$+ \frac{1}{2}\mathrm{tr}\left[\Theta^\dagger\left(\overleftarrow{\partial}_\mu - \frac{ia_\mu^j\sigma^i}{2}\right)\left(\vec{\partial}_\mu + \frac{ia_\mu^j\sigma^i}{2}\right)\left(\Theta\frac{i\boldsymbol{\alpha}\cdot\boldsymbol{\tau}}{2}\right)\right]. \tag{C.113}$$

After expansion and simplification, the two terms above reduce to:

$$\frac{1}{2}\mathrm{tr}\left[\Theta^\dagger\left(\overleftarrow{\partial}_\mu - \frac{ia_\mu^j\sigma^i}{2}\right)\left(\vec{\partial}_\mu + \frac{ia_\mu^j\sigma^i}{2}\right)\left(\Theta\frac{i\boldsymbol{\alpha}\cdot\boldsymbol{\tau}}{2}\right)\right] \tag{C.114}$$

$$= \frac{1}{2}\mathrm{tr}\left[\Theta^\dagger\left(\overleftarrow{\partial}_\mu - \frac{ia_\mu^j\sigma^i}{2}\right)\Theta\frac{i\partial_\mu\boldsymbol{\alpha}\cdot\boldsymbol{\tau}}{2}\right] \tag{C.115}$$

$$+ \frac{1}{2}\mathrm{tr}\left[\Theta^\dagger\left(\overleftarrow{\partial}_\mu - \frac{ia_\mu^j\sigma^i}{2}\right)\left(\vec{\partial}_\mu + \frac{ia_\mu^j\sigma^i}{2}\right)\Theta\times\frac{i\boldsymbol{\alpha}\cdot\boldsymbol{\tau}}{2}\right], \tag{C.116}$$

and likewise

$$\frac{1}{2}\mathrm{tr}\left[\left(-\frac{i\boldsymbol{\alpha}\cdot\boldsymbol{\tau}}{2}\Theta^\dagger\right)\left(\overleftarrow{\partial}_\mu - \frac{ia_\mu^j\sigma^i}{2}\right)\left(\vec{\partial}_\mu + \frac{ia_\mu^j\sigma^i}{2}\right)\Theta\right] \tag{C.117}$$

$$= -\frac{1}{2}\mathrm{tr}\left[\frac{i\partial_\mu\boldsymbol{\alpha}\cdot\boldsymbol{\tau}}{2}\Theta^\dagger\left(\vec{\partial}_\mu + \frac{ia_\mu^j\sigma^i}{2}\right)\Theta\right] \tag{C.118}$$

$$- \frac{1}{2}\mathrm{tr}\left[\frac{i\boldsymbol{\alpha}\cdot\boldsymbol{\tau}}{2}\times\Theta^\dagger\left(\overleftarrow{\partial}_\mu - \frac{ia_\mu^j\sigma^i}{2}\right)\left(\vec{\partial}_\mu + \frac{ia_\mu^j\sigma^i}{2}\right)\Theta\right]. \tag{C.119}$$

By cyclicity of the trace, what remains after cancellation is:

$$(\mathcal{L}_{\mathrm{kin}}^{\Theta})' - \mathcal{L}_{\mathrm{kin}}^{\Theta} = \partial_\mu\alpha^j\cdot\frac{1}{2}\mathrm{tr}\left[\Theta^\dagger\left(\overleftarrow{\partial}_\mu - \frac{ia_\mu^j\sigma^i}{2}\right)\Theta\frac{i\tau^j}{2} - \frac{i\tau^j}{2}\Theta^\dagger\left(\vec{\partial}_\mu + \frac{ia_\mu^j\sigma^i}{2}\right)\Theta\right], \tag{C.120}$$

so that the conserved current is

$$\boldsymbol{\mathcal{J}}_\mu \propto \mathrm{tr}\left[\frac{\boldsymbol{\tau}}{2}\frac{\Theta^\dagger\left(\vec{\partial}_\mu + \frac{ia_\mu^j\sigma^i}{2}\right)\Theta - \Theta^\dagger\left(\overleftarrow{\partial}_\mu - \frac{ia_\mu^j\sigma^i}{2}\right)\Theta}{2i}\right] = \mathrm{tr}\left[\frac{\boldsymbol{\tau}}{2}\frac{\Theta^\dagger\vec{D}_\mu\Theta - \Theta^\dagger\overleftarrow{D}_\mu\Theta}{2i}\right]. \tag{C.121}$$

Because of the pseudospin Pauli vector $\boldsymbol{\tau}/2$, this bosonic object transforms as a vector under global pseudospin rotations $\Theta \to \Theta e^{i\boldsymbol{\theta}\cdot\boldsymbol{\tau}/2}$. Indeed, its τ^z component is like the density of low-energy Cooper pairs, while $\tau^\pm$ serve as Cooper pair annihilation/creation operators. Moreover, it is gauge-invariant since $D_\mu\Theta$ is gauge-covariant. Finally, since it is the conserved current, then at the critical point all components will have protected scaling dimension 2. Altogether, this SU(2) formulation confirms the physical conclusions made in Ref. [344], by working here in a formalism manifestly invariant under the pseudospin symmetry.